MASS SPECTROMETRY CHARACTERISATION OF LASER PRODUCED PRODUCTS

by

Hendrik Johannes Strydom

Submitted in partial fulfilment of the

requirements for the degree of

Doctor of Philosophy,

in the

Department of Physics,

University of Natal.

Durban,

December 1999

Abstract

Mass spectrometers are analytical instruments that convert neutral atoms and molecules into gaseous ions and separate those ions according to the ratio of their mass to charge, *m/z*. The measurement is reported as a mass spectrum: a plot of relative intensity vs. *m/z* that can be used to deduce the chemical structure and composition of materials and compounds. Initially, the use of mass spectrometers was restricted to the analysis of volatile compounds. Recent advances in the development of ionisation techniques to produce intact molecules directly from samples in the liquid or solid phase, has extended the powerful use of mass spectrometry to compounds of increasingly higher molecular mass.

The aim of this study was twofold: develop diagnostic techniques for the in-situ measurement of isotope ratios in laser isotope separation experiments; and to correlate it with the measured isotope ratios on the collected product. The outcome is a thesis that can be divided into two distinct fields of application: Firstly; the Atomic Vapour Laser Isotope Separation (AVLIS) of lithium, and secondly the Molecular Laser Isotope Separation (MLIS) of uranium.

In both AVLIS and MLIS pulsed laser systems were used to ionise and/or dissociate atomic or molecular beams. The pulsed nature of the lasers is ideally suited to in-situ time-of-flight detection of the produced ions.

Different types of inter-changeable ion sources are common to the same TOF mass spectrometer. Each of these sources is selected according to its application. For instance, applications vary from photo- and multiphoton ionisation (laser ionisation) to surface analysis (laser desorption or particle bombardment) to chromatography (electron impact ionisation). Four different source configurations were considered in this study:

(i) Atomic Laser Isotope Separation (AVLIS) of lithium;

(ii) Multiphoton Ionisation (MPI) of UF_6 gas;

(iii) Non-resonant ionisation during Laser Desorption (LDI) of solids; and

(iv) Matrix-Assisted Laser Desorption (MALD) of biopolymers.

The design of each of these sources will be discussed in detail in chapters to follow. Bulk analysis of harvested laser-produced products needs to be in correlation with in-situ analysis. Three different characterisation methods were used in this study:

(i) Laser Desorption Time-of-Flight Mass Spectrometry (LD-TOF-MS)

(ii) Quadrupole-based Secondary Ion Mass Spectrometry (SIMS); and

(iii) TOF-MS-based Secondary Ion Mass Spectrometry (TOF-SIMS).

Chapter I describes the principles of time-of-flight mass spectrometry, design parameters, as well as the instrumentation that were designed and constructed for the purposes of this study. Chapter II describes the

principles of Secondary Ion Mass Spectrometry (SIMS). In particular, research done on the establishment of tools to the non-expert user of SIMS to select analyses conditions, is described. Chapter III reports on the application of TOF-MS and SIMS during the AVLIS of lithium. Chapter IV reports on the application of the different combinations of TOF-MS, LD-TOF-MS, SIMS, and TOF-SIMS during the MLIS of uranium.

Preface

The work described in this thesis was carried out at the CSIR, formerly known as the Council for Scientific and Industrial Research, the Atomic Energy Corporation of South Africa (AEC) and at the Department of Physics, University of Natal in Durban. The research was done from March 1990 to December 1997 under the supervision of Prof. M M Michaelis. The fundamental research on the sputtering yield theory was done in 1983-1984 under the guidance of Dr W H Gries.

This study represents original work by this author and has not been submitted in any form to another University, although parts of this work have been published as conference proceedings and as journal publications. Where use was made of the work of others it has been duly acknowledged in the text.

This thesis can be described as a roller coaster ride through two large scale enrichment projects (yearly budgets exceeding tens of millions of Rand), that spanned over seven years during which time the employment of mass spectrometric methods in the measurement of enrichment experiments guided the development of both projects.

The commercial nature of both the Atomic Vapour Laser Isotope Separation (AVLIS) and the Molecular Laser Isotope Separation (MLIS) projects, requires that knowledge of integral parts of the enrichment processes be kept secret. I therefore apologise in advance for the lack of detail in some chapters. Several internal reports were compiled which are classified and not available to the reader.

Although the author was responsible for the irradiation test facility where all the enrichment experiments were performed, this thesis concentrates on the demands, solutions and performance of mass spectrometric instruments.

Acknowledgements

I would like to extend my sincere thanks to the following people, without whose contribution this thesis would not have been possible:

- Prof. Max Michaelis my supervisor for his guidance and encouragement.
- Dr Werner Gries for introducing me to the field of mass spectrometry.
- Dr Einar Ronander for his enthusiastic support and practical suggestions.
- Prof. Egmont Rohwer who has been a consultant to project all along.
- My wife Rentia for never giving up hope to seeing the thesis completed.
- My parents for their support and unquestioning belief in me.
- Christo Green for technical assistance on the LD-TOFMS, without whom most of this would not have been possible.
- Martin van Staden and Dr Wynand Louw for performing the SIMS analysis.
- Dr Fraser Reich for performing the TOF-SIMS analysis.
- My colleagues at the CSIR and the AEC, for creating the opportunities to complete this work.

Finally, I would like to thank both the CSIR and the AEC for the financial support and the opportunity to use the facilities for a part of this thesis.

Contents

1. Time-of-Flight Mass Spectrometry 1

1.1. Introduction 1

1.2. The TOF Principle of Mass Analysis 2

1.3. TOF Mass Spectrometers 4

1.4. TOFMS Design Criteria 8

1.5. Linear TOFMS 9

1.5.1. Time-of-Flight Equations 10

1.5.2. Mass Resolution 12

1.5.3. Two-Stage Extraction (Wiley-McLaren Instrument) 13

1.5.4. Laser Desorption from Surfaces 16

1.6. Reflectron TOFMS 19

1.7. Ion Detection for TOFMS 21

1.7.1. Microchannel Plate (MCP) Detectors 22

1.7.1.1. Principle of Operation 24

1.7.1.2. Detector Efficiency 27

1.7.1.3. Dead Time 28

1.8. The LD-TOFMS Instrument used in this Study 30

1.8.1. LD-TOFMS Instrument Specifications 31

1.8.2. LD-TOFMS Mass Spectra 34

1.8.3. LD-TOFMS High-Mass Capability 38

2. Secondary Ion Mass Spectrometry **42**

2.1. Introduction 42

2.2. The Principle of SIMS Analysis 43

2.3. Theory of SIMS 45

2.4. SIMS Analysis Formula 48

2.5. Normalised Sputtering Yields 49

2.5.1. Calculation of α_{eff} Values 50

2.5.2. A Comparison of Three Versions of Sigmund's Model of Sputtering using Experimental Results 60

2.5.3. Dependence of Sputtering Yield on Incident Angle 64

2.5.4. Sputtering Rate 65

2.6. SIMS Instrumentation 66

2.6.1. Magnetic Sector SIMS 67

2.6.2. Quadrupole SIMS 68

2.6.3. Time-of-Flight SIMS 70

2.6.4. Ion Detection 70

2.7. SIMS Instruments used in this Study 71

2.7.1. VG ESCALAB II QUAD-SIMS 71

2.7.2. PHI TRIFT II TOF-SIMS 72

3. AVLIS of Lithium **74**

3.1. Introduction 74

3.2. Principles of Laser Isotope Separation 75

3.3. Atomic Vapour Laser Isotope Separation 77

3.4. AVLIS of Lithium 79

3.4.1. Spectroscopy of Lithium 80

3.4.2. Photoionisation routes for Lithium 83

3.4.3. Lithium Vaporisation 85

3.4.4. The Laser System 88

3.4.4.1. Copper Vapour Laser (CVL) 88

3.4.4.2. Dye Laser 91

3.4.4.3. Integrated Laser System 96

3.4.5. The Separator System 98

3.4.5.1. Time-of-Flight Mass Spectrometer 99

3.5. Conclusion 108

4. MLIS of Uranium 110

4.1. Introduction 110

4.2. Molecular Laser Isotope Separation 111

4.3. MLIS of UF_6 113

4.3.1. UF_6 Flow Cooling 114

4.3.2. Selective Photodissociation of UF_6 116

4.3.3. The Laser System 116

4.3.3.1. Carbon Dioxide Laser (CO_2) 118

4.3.3.2. Raman Conversion 119

4.3.3.3.Integrated Laser System 120

4.4. In-line TOFMS 122

4.5. LD-TOFMS Instrument 128

4.6. SIMS Instrument 132

4.6.1. SIMS Mass Resolution 135

4.6.2. SIMS Analysis of MLIS Produced Product 142

4.6.3. SIMS Analysis of Enrichment Standards 147

4.7. LD-TOFMS and SIMS Results 153

4.8. TOF-SIMS Analysis of Collected MLIS Product 162

4.9. Conclusion 209

5. References 211

A. Ion Implantation Theory 218

A.1.Introduction 218

A.2.Basic Concepts 218

A.3.Energy Loss 220

A.4.Ion Range 221

A.5.Summary of LSS Theory 222

B. Table of Measured Sputtering Yields (S) for Polycrystalline Targets 226

C. Predicted Normalised Sputtering Yields for Mono-elemental Polycrystalline Targets .246

Chapter 1

Time-of-Flight Mass Spectrometry

1.1 Introduction

Mass Spectrometry is a powerful and versatile technique for the identification and measurement of atomic and molecular species. Because of its high mass resolution capability, the magnetic sector has been the dominant instrument design. Of the alternative techniques the quadrupole has found a niche for itself in the ease of interfacing with other analytical techniques, but the time-of-flight mass spectrometer (TOF-MS) has until recently been neglected.

The operating principle of the TOF-MS has been known since J J Thomson (1913) carried out his experiments on ionised particles. The first successful TOF-MS was developed in the mid-1950s [Wiley and McLaren (1955)], but was limited by low mass resolution and poor sensitivity. This was to change only during the 1970s with two new inventions. Mamyrin et al (1973) published the first account of a mass reflectron device, which boosted the resolving power of the TOF-MS far beyond that of the quadrupole and well into the regime of the magnetic sector. At about the same time McFarlane et al (1974) announced the detection of high mass

ions resulting from plasma desorption. The TOF-MS was ideal for this application, as it was the only instrument capable of providing the required mass analysis per ionisation event. Subsequently, laser ionisation used initially for surface analysis and then for multiphoton ionisation in the gas phase, has also benefited from this particular feature of TOF-MS.

1.2 The TOF Principle of Mass Analysis

The simplest time-of-flight mass spectrometer (Fig 1.1) consists of a short source-extraction region (*s*, usually of the order of a few centimetres), a drift region (*D*, from 0.3 to 4m in length), and a detector.

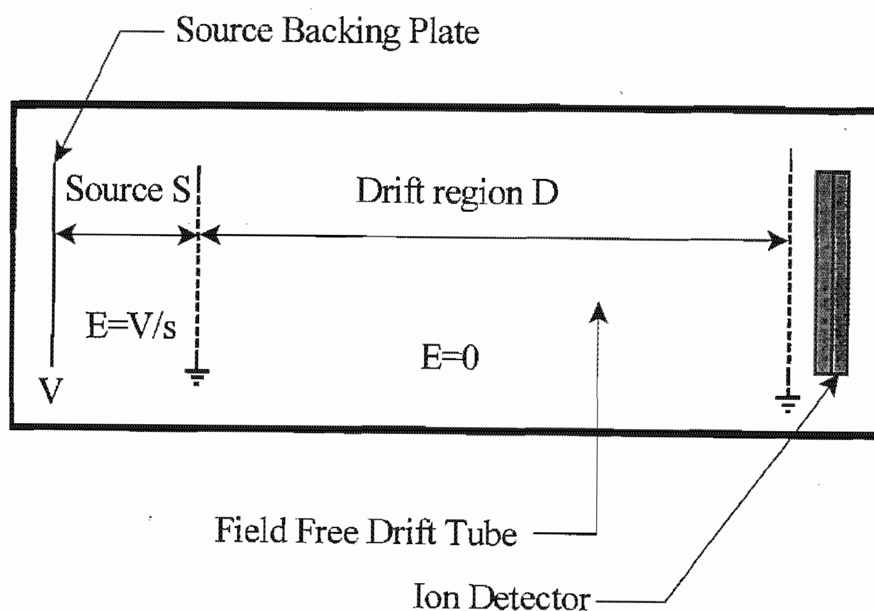

Fig 1.1 A simple time-of-flight mass spectrometer, consisting of a source region, a field free drift region and an ion detector.

In the source region, the electrical field ($E=V/s$) is defined by a voltage V, placed on the source backing plate, and is used to accelerate ions in the source region to a constant energy. The drift region is field free and is bounded by an extraction grid and a second grid placed just before the detector, both of which are at ground potential. TOF-MS operates on the principle: if a group or packet of ions (of differing mass to charge (m/e) ratios) is formed on the surface of the backing plate, they are accelerated through the entire source-extraction region to the same final kinetic energy:

$$\frac{mv^2}{2} = eV \tag{1.1}$$

and cross the drift region with velocities:

$$v = \left(\frac{2eV}{m}\right)^{1/2} \tag{1.2}$$

Consequently ions that are allowed to traverse a fixed distance D to the detector, separate in time according to their m/e ratio, the lightest ions, having the highest velocity, reach the detector first. Their flight times is given by

$$t = \left(\frac{m}{2eV}\right)^{1/2} D \tag{1.3}$$

To utilise this time-of-flight separation the ion packets must be pulsed into the flight tube. Each packet of ions detected yields a series of output pulses at various mass dependent arrival times within the TOF time scale, typically less than 1ms. Hence, each packet or ionisation event yields a complete mass spectrum. The mass range is limited only by the ability of heavy ions to be created from the sample, the time available for collection and the detector to detect them.

1.3 TOF Mass Spectrometers

An ionisation region, ion extraction, a field-free flight tube, an ion detector and a computer system for data collection, manipulations and output characterise a TOF-MS.

To evaluate TOF mass spectrometers, one has to compare their mass accuracy and mass resolution with other types of mass spectrometers. Mass accuracy is a measure of the accuracy of which the mass of a given signal can be assigned, whilst mass resolution $R = m/\Delta m$ is a measure of an instrument's capability to distinguish between adjacent peaks. The width of the peak observed by the detector is determined by:

(i) The finite time of ion formation;

(ii) the finite volume of ion formation; and

(iii) the initial ion velocity distribution.

Further limitations in mass resolution are due to electronics (i.e. ion detector), space charge effects and transmission grids. However, these factors are inherent to the instrument design and effort was made to keep their influence to a minimum. The three mentioned effects can be reduced to pure initial temporal or initial spatial distributions:

(i) The finite time of ion formation is due to the finite laser pulse length and therefore is a pure **initial temporal** effect;

(ii) A finite volume of ion formation is due to the finite laser focus size and therefore a pure **spatial distribution** effect;

(iii) An initial velocity distribution entails initial forward and backward velocity distributions, coupled with differences in magnitude they can be separated into **initial temporal and initial spatial distribution** effects.

In summary, for an improvement of the final mass resolution, one has to minimise initial distributions of time and space.

TEMPORAL DISTRIBUTIONS

Temporal distributions caused by finite pulse length of the laser can only be compensated for as far as the choice of lasers with nanosecond and less

pulse widths are allowed for. In contrast, increasing the potential in the source can decrease the time distribution due to initial velocities (the turn around time needed for backward velocities). Although this would reduce temporal time distribution it would on the other hand, because of increased potential energy, increase broadening effects due to spatial distribution.

Many different techniques have been proposed to overcome this problem. Back in the 1950s time-lag-focussing was introduced [Wiley and McLaren (1955)] where the ions were allowed to spread out in the field-free ion source before the extraction field is switched on. By choosing a delay time between ion formation and extraction, different velocities give rise to different spatial positions in the final extraction field and therefore two different ion kinetic energies. The resulting variation of the flight time can partially compensate the flight-time effect of the initial velocities. A detailed description is given in section 1.4. Browder et al (1981) used impulse-field-focussing to rapidly accelerate the ions to very high velocities, before the normal acceleration field is switched on. Möller and Holmid (1984) improved on this technique by employing rapid field reversal. Finally, post-source focussing has also been used to compensate for initial temporal distributions (see section 1.4).

SPATIAL DISTRIBUTION

Initial spatial distributions of ion formation results in a spread of ion kinetic energies in the field-free region. This energy spread is the main limiting factor for the mass resolution in simple linear TOF instruments, but can be compensated for by flight-time correcting methods. There is a point in the field-free drift region, called the first-order space focus, where the flight-time decrease due to the larger velocity of the ions, is compensated for by the increase due to the longer acceleration length. This includes the real initial spatial distribution due to the spatially distributed ion formation as well as the pseudo-initial spatial distribution due to the initial velocity distribution. Such flight-time corrections are only of first order. Weinkauf et al (1989) demonstrated that a second-order space focus with increased mass resolution is also achievable, however, since a long flight path is needed, very weak acceleration electric fields were needed, inducing a large spread in flight times due to the turn around effect, which is counteracting.

A better solution is to use the space focus of an ion source as pseudo-ion origin with minimised spatial distribution. The ions then start from here with only a distribution in kinetic energy. Flight-time broadening in the drift region behind the space focus due to the pure kinetic effect can then be corrected by a second energy compensating means, such as an ion reflector or a reflectron mass spectrometer.

1.4. TOFMS Design Criteria

The detail design of a time-of-flight mass spectrometer (TOFMS) depends entirely on its application. The design criteria, however, is apparent if one considers the advantages/disadvantages of TOFMS.

TOF mass spectrometry has three main advantages:

(i) A unique advantage is the speed with which a spectrum can be obtained - typically less than 1ms. This allows the study of ion species in a source with rapidly changing ionisation conditions.

(ii) Secondly an entire mass spectrum can be recorded for each ionisation event. Therefore allowing for the accurate measurement of relative intensity occurring, even though source conditions might vary unpredictably, provided that the variation affects each mass spectrum in the same way. In particular, the determination of isotopic abundance of elements is met with great success (Chapters 3 and 4).

(iii) The third major advantage is that the mass accuracy of the TOF mass spectrometer depends on electronic switching/triggering, rather than mechanical alignment. The freedom from stringent geometric conditions simplifies construction. Furthermore, it is found that the absence of narrow slits in the ion source and ion detector provides for

higher transmission than in the case of quadrupole and magnetic sector mass spectrometers.

The main disadvantage of TOF mass spectrometers was initially its limited mass resolution. However, with the advent of reflectron ion mirrors, mass resolutions far exceeding that of quadrupole mass spectrometers have been reported. Mass resolutions of up to 20 000 [Grix, et al, (1988)] put TOF mass spectrometers within reach of magnetic sector instruments - at appreciably lower cost.

1.5. Linear TOF-MS

The simplest TOF mass spectrometer consists of an ion source and an ion collector situated at opposite ends of a linear evacuated tube (Figure 1.1). A constant electric field extracts ions formed in the ionisation region of the source. At the end of the ion source all ions have the same kinetic energies. The ions are then allowed to travel down the field-free flight tube, the velocity of all the ions are then a function of their mass m to charge q ratio. Ions would therefore arrive at the detector in bunches corresponding to the same m/q ratio. For single charged ions, the lightest group would reach the detector first, followed by groups of successively heavier mass. Thus each ionisation pulse results in a mass spectrum, which can easily be displayed with an oscilloscope (Fig 1.2).

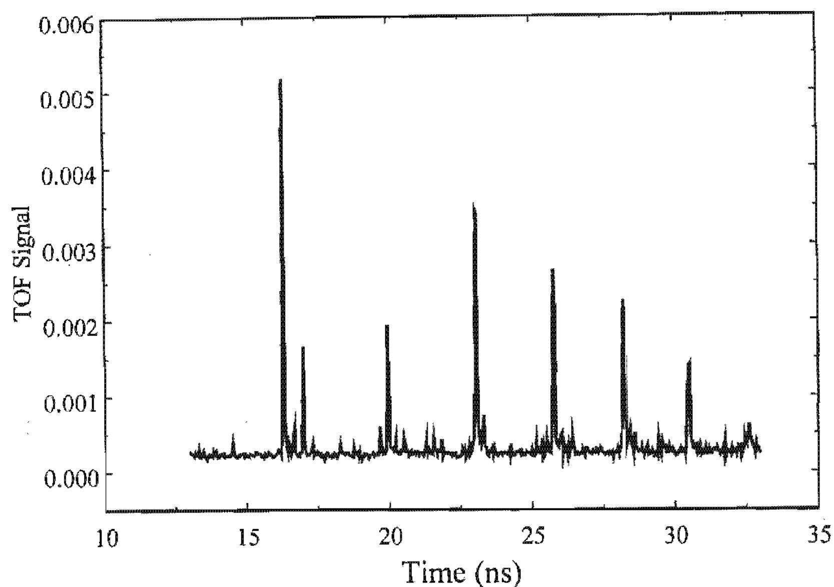

Fig 1.2 A typical time-of-flight mass spectrum. The light masses arrive first at the detector surfaces.

1.5.1. Time-of-Flight Equations

Ions are either formed in the gas phase, generally in the centre of the source, or directly on the backing plate. Let us consider that the ions are formed at some distance s between the backing plate and the extraction plate/grid (see fig 1.3). Furthermore, the extraction field is strong enough to ensure that the ions spend a short time (t_s) in the source region, where their velocities are not constant. The ions are accelerated through the entire source-extraction region to the same final kinetic energy:

$$\frac{mv^2}{2} = eV \tag{1.4}$$

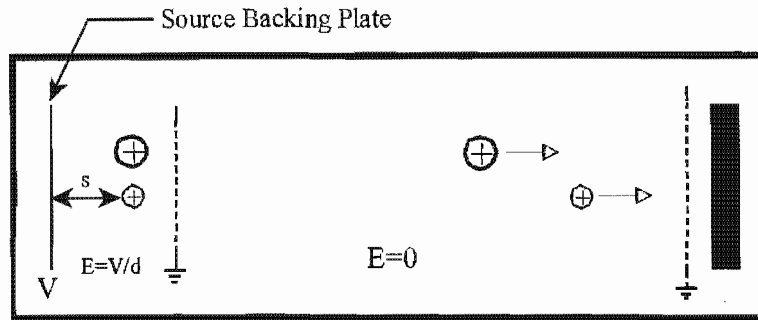

Fig 1.3 A time-of-flight mass spectrometer with a source region, a field free drift region, and an ion detector.

The velocity at each point *s* in the source is then given by

$$v = \left(\frac{2\,eEs}{m} \right)^{1/2} \tag{1.5}$$

Where $v = ds/dt$, and integrating:

$$\int_0^{t_s} dt = \int_0^s \left(\frac{m}{2\,eE} \right)^{1/2} \frac{ds}{s^{1/2}}$$

$$t_s = \left(\frac{m}{2eE} \right)^{1/2} 2s^{1/2} = \left(\frac{m}{2eEs} \right)^{1/2} 2s \tag{1.6}$$

In addition, the flight time in the drift region, t_D becomes:

$$t_D = \left(\frac{m}{2eEs} \right)^{1/2} D \qquad (1.7)$$

And the total flight time is then given by:

$$t = t_s + t_D = \left(\frac{m}{2eEs} \right)^{1/2} (2s + D) \qquad (1.8)$$

The time-of-flight of ions are clearly dependent on the square root of their masses, regardless of the relative sizes of the extraction and drift regions. This simplifies the calibration of the mass spectrum tremendously – by measuring the flight times of two known masses to determine the constants a and b in the following equation:

$$t = am^{1/2} + b \qquad (1.9)$$

where b takes into account any time offsets due to laser triggering time, triggering of the recording devices, etc.

1.5.2. Mass Resolution

The mass resolution is defined as $m/\Delta m$: in a TOF mass spectrometer in which the ions are accelerated to constant energy this is given by:

$$\frac{m}{\Delta m} = \frac{t}{2 \Delta t} \qquad (1.10)$$

where Δt is measured as the full width at half maximum (FWHM) of the peak.

Linear time-of-flight mass spectrometers typically have mass resolutions of 300 to 800 but often appear to be dependent upon the nature of the sample or the laser power. Exceptional mass resolutions of up to 25,000 have been demonstrated using reflectrons [Grix, et al, (1988)], but have been by no means the routine. As said before, the uncertainties in the time of ion formation, its initial location in the extraction field, its initial kinetic energy, and metastable fragmentation, gives rise to temporal, spatial, and kinetic energy distributions that contribute to poor mass resolution.

1.5.3. Two-stage Extraction (Wiley-McLaren Instrument)

The Wiley and McLaren instrument utilised pulsed, time-delayed, two-stage extraction as an approach to simultaneously time, space, and energy focusing. A schematic is shown in Fig 1.4. In a two-stage extraction instrument, the second extraction field (E_1 typically 1200V/cm) is much larger than the first (E_0 typically 300V/cm). With large E_1/E_0 ratios ions of different initial velocity directions are all allowed to turn towards the detector (direction of extraction) after which they are vigorously accelerated into the drift free region. With this configuration, ions having initial velocity differences of up to 5eV can be compensated for.

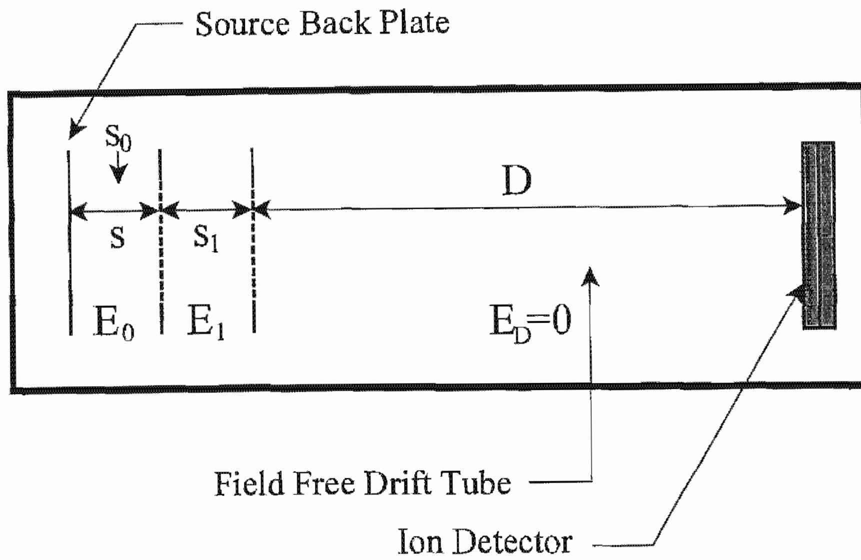

Fig 1.4 A Schematic of the Wiley and McLaren two-stage extraction time-of-flight mass spectrometer.

For ions formed at a position s_0, in the source region, the flight time is:

$$t_0 = \left(\frac{m}{2eE_0 s_0}\right)^{1/2} 2s_0 \qquad (1.11)$$

where the field strength $E_0=(V_0-V_1)/s$. The time spent in the second extraction region is determined from its average velocity. When an ion enters this region its initial velocity is:

$$v_i = \left(\frac{2eE_0 s_0}{m}\right)^{1/2} \qquad (1.12)$$

Its final velocity is determined by its final kinetic energy $eE_0s_0 + eE_1s_1$:

$$v_f = \left(\frac{2e}{m}\right)^{1/2} \left(E_0 s_0 + E_1 s_1\right)^{1/2} \tag{1.13}$$

where $E_1 = V_1/s_1$. Thus the time in the second region is:

$$t_1 = \left(\frac{m}{2e}\right)^{1/2} \left[\frac{2s_1}{\left(E_0 s_0 + E_1 s_1\right)^{1/2} + \left(E_0 s_0\right)^{1/2}}\right] \tag{1.14}$$

The time spent in the field free drift region is again:

$$t_D = \left(\frac{m}{2e}\right)^{1/2} \left[\frac{D}{\left(E_0 s_0 + E_1 s_1\right)^{1/2}}\right] \tag{1.15}$$

The total flight time of an ion formed at position s_0 is:

$$t = t_0 + t_1 + t_D \tag{1.16}$$

$$t = \left(\frac{m}{2e}\right)^{1/2} \left[\left(\frac{s_0}{E_0}\right)^{1/2} + \frac{2s_1}{\left(E_0 s_0 + E_1 s_1\right)^{1/2} + \left(E_0 s_0\right)^{1/2}} + \frac{D}{\left(E_0 s_0 + E_1 s_1\right)^{1/2}}\right] \tag{1.17}$$

When designing a TOF instrument with a two-stage extraction, one first chooses the value of the drift length (D) and the lengths of the source (s) and the extraction region (s_1). If one then chooses a value for the acceleration voltage (V_0 on the backing plate), then this will uniquely determine the voltage (V_1) on the first extraction grid. The voltage V_1 can then be adjusted experimentally to provide the best focus – which is focussed at the detector surface/plane.

1.5.4 Laser Desorption from Surfaces

In laser desorption from a surface the design of the time-of-flight mass spectrometer is significantly simplified, since both the time- and spatial-distribution problems are eliminated. The lasers used in laser desorption instruments generally have pulse widths of less than 10ns. Ionisation times are, therefore, considerably shorter than the drawout pulse in the Wiley and McLaren instrument. The initial temporal distribution, Δt_0, is therefore greatly reduced. Furthermore, since the ions are desorbed from a well-defined, equipotential surface, the initial spatial distribution, Δs_0, is also minimised.

Let us therefore, consider a single extraction source (length s), with the ions formed on the source backing plate. The ions are formed with an initial kinetic energy U_0. The final kinetic energy of an ion as it enters the drift region is:

$$\frac{mv^2}{2} = U_0 + eEs \tag{1.18}$$

The final velocity again depends upon mass and is:

$$v = (U_0 + eEs)^{1/2}\left(\frac{2}{m}\right)^{1/2} \tag{1.19}$$

To determine the flight time in the source-extraction region, consider that the velocity is not constant, and integrate between the time of formation (t_0) and the time that the ion leaves the source (t_s):

$$\int_{t_0}^{t_s} dt = \int_0^s \left(\frac{m}{2}\right)^{1/2} \frac{ds}{(U_0 + eEs)^{1/2}} \tag{1.20}$$

$$t_s = \frac{(2m)^{1/2}}{eE}\left[(U_0 + eEs)^{1/2} \mp U_0^{\ 1/2}\right] + t_0 \tag{1.21}$$

In the drift region the velocity is constant, so the time spent is:

$$t_D = \frac{(2m)^{1/2} D}{2(U_0 + eEs)^{1/2}} \tag{1.22}$$

The total flight time is then:

$$t = \frac{(2m)^{1/2}}{eE}\left[(U_0 + eEs)^{1/2} \mp U_0^{\ 1/2}\right] + \frac{(2m)^{1/2} D}{2(U_0 + eEs)^{1/2}} + t_0 \tag{1.23}$$

If the potential difference over the source-extraction region is V, all ions receive the same energy (eV) because of acceleration. $E = V/s = eV$. Furthermore, since the short pulse length lasers (3-60ns) are used, the initial temporal distribution is negligible therefore the flight time is given by:

$$t = \frac{(2m)^{1/2}\left[(U_0 + eV)^{1/2} \mp U_0^{1/2}\right]s}{eV} + \frac{(2m)^{1/2} D}{2(U_0 + eV)^{1/2}} \tag{1.24}$$

The equation simplifies even further if the drift tube D is much longer than the source length s, because the flight time of an ion with $KE=U_0+eV$ is then:

$$t = \frac{(2m)^{1/2} D}{2(U_0 + eV)^{1/2}} \tag{1.25}$$

The space-focus plane, the point at which $\Delta t/\Delta s_0 = 0$, that is when the initial spatial difference during the ion formation, equals the resultant temporal difference is given by. To obtain space-focussing the source length should be:

$$d = 2\sigma^{3/2}\left[\frac{1}{s_0^{1/2}} - \frac{2s_1}{s_0^{1/2}\left(\sigma^{1/2} + s_0^{1/2}\right)^2}\right] \tag{1.26}$$

with $\sigma = s_0 + (E_1/E_0)s_1$.

If the accelerating voltage, V, is very large, then the flight times will be insensitive to initial kinetic energies. The difference between the arrival times of an ion with kinetic energy U_0, and an ion with no kinetic energy is:

$$\Delta t = D\left(\frac{m}{2}\right)^{1/2}\left[\frac{1}{(eV)^{1/2}} - \frac{1}{(eV + U_0)^{1/2}}\right] \tag{1.27}$$

The mass resolution $\Delta m/m = 2\Delta t/t$. If $eV \gg U_0$, then the mass resolution is given by:

$$\frac{\Delta m}{m} \approx 2\left[\frac{(eV + U_0)^{1/2} - (eV)^{1/2}}{(eV)^{1/2}}\right] \tag{1.28}$$

Expanding $(eV+U_0)^{1/2}$ to first order, yields:

$$\frac{\Delta m}{m} \approx 2\left[\frac{(eV)^{1/2} + \frac{U_0}{2(eV)^{1/2}} - (eV)^{1/2}}{(eV)^{1/2}}\right] \tag{1.29}$$

$$\frac{\Delta m}{m} \approx \frac{U_0}{eV} \tag{1.30}$$

This implies that mass resolution is improved by using very high accelerating voltages, i.e., $eV \gg U_0$. Furthermore, if the drift tube is much longer than the source length, $D \gg s$, then the mass resolution is not improved by lengthening the flight tube further. In practice, the initial kinetic energy is of the order of 0.1 to 10eV. To obtain a mass resolution exceeding 100, the acceleration voltage should be at least 1000eV.

1.6. Reflectron TOFMS

The design of any time-of-flight mass spectrometer should strive to improve the mass resolution. Eliminating or minimising the initial conditions (time, space, and kinetic energy distributions) does this. Initial kinetic energy distributions are perhaps the most difficult to cater for, because they are such an inherent part of the ionisation process. For the same instrument configuration, the initial kinetic energy distribution that is observed from one sample matrix to the next, could differ significantly,

even though the laser ionisation and ion extraction parameters are kept the same.

Ion extraction provides an opportunity for improving the mass resolution by compensating for the effects of initial conditions, in particular then for the initial kinetic energy distribution. The kinetic energy distributions (particularly in the case of MALDI) can be rather severe, which is beyond the capability of static field correction.

In 1973 Mamyrin et al published a design for a high-resolution time-of-flight mass spectrometer that included a reflectron for kinetic energy focussing. Their instrument used electron impact ionisation, whereby ions were extracted by means of a dual-stage system in which the first grid was pulsed. Their reflectron instrument consisted of two linear drift regions and the reflectron itself. The reflectron was a two-stage design consisting of a retarding region, in which the ions are slowed down, and a reflection region, in which the ions are turned around before reaching the back of the reflectron. The ions exit the reflectron and drift off to the detector. The geometry was chosen so that the ions enter the reflectron at an angle of 2° off the centre, and exit the reflectron a further 2° off the centre – a total reflectron angle of 4°. This angle allows for the detector to be located alongside the source region. The Mamyrin instrument yielded a mass resolution exceeding 1 part in 3000.

A simpler arrangement to the dual-stage reflectron is the single-stage reflectron, also known as an ion mirror. In this case the extracted ions are retarded and turned around in the same reflectron region. The single-stage reflectron provides a first-order correction for the kinetic energy distribution. The penetration depth into the single-stage reflectron is obviously longer than in the Mamyrin case where the dual-stage reflectron, providing for a more compact design. Second-order, dual stage reflectrons provide energy focussing over a broad range of kinetic energies, for example a 5-keV instrument will tolerate energy spreads of ±125eV.

1.7. Ion Detection for TOFMS

In time-of-flight mass spectrometry ions are created, accelerated in synchrony to a constant kinetic energy, and permitted to separate in time due to differences in their velocities. The time of arrival at a fixed detector surface yields information regarding their mass-to-charge (*m/z*) ratio. The amplitude of the detector signal at a given arrival time indicates the number of ions of the corresponding *m/z* value. Thus, the detector output signal is a transient waveform that contains all of the data needed to produce a mass spectrum (a plot of ion intensity versus *m/z*). The difference in arrival time between the ions of *m/z* values of 15 and 1000 is typically 80μs. To clearly distinguish ions of *m/z* values 999 and 1000, resolution along the time

(mass) axis should be at least 5ns. Hence, the acquisition of this waveform requires a transient recorder with a 200 MHz sampling rate and a memory that can hold 16k data points. A high speed, high gain and low noise detector is therefore needed. Two different detector systems were used. The first system contains two microchannel plates mounted in a chevron configuration, whilst the second system was a combination of one microchannel plate followed by an electron multiplier.

1.7.1. Microchannel Plate (MCP) Detectors

A microchannel plate (MCP) is an array of thousands to millions of miniature electron multipliers orientated parallel to one another. These channel diameters are in the range 10-100μm and have length to diameter ratios between 40 and 100.

A MCP begins as a specially formulated lead glass tube and solid core assembly that is drawn and fused to form a monofibre. A bundle of monofibers, stacked in a hexagonal array, is drawn to form a multifiber.

These multifibers are then stacked and fused to form a billet, which is sliced into wafers at specific bias angles, ground and polished to an optical finish. The solid core is etched away, yielding a honeycomb structure of millions of tiny holes. A thin SiO_2 electron emissive layer is deposited on

the inner walls of each of these tubes/holes. Each hole then functions as a single channel electron multiplier, relatively independent of adjacent channels. Finally, a thin metal electrode (nichrome or inconel) is vacuum deposited on both input and output surfaces to connect all channels in parallel.

For normal operation, less than 1kV bias voltage is applied across the MCP (output positive with respect to input). The bias current flowing through the resistive layer supplies electrons necessary to continue the secondary emission process. The total resistance between electrodes is in the order of $10^9\ \Omega$. When used singly or in a cascade, they allow electron multiplication factors of 10^4-10^7 coupled with ultra-high time resolution (<100ps) and spatial resolution limited only by the channel dimensions and spacing; 12μm diameter channels with 15μm centre-to-centre spacing are typical.

Originally developed as an amplification element for image intensification devices, MCPs have direct sensitivity to charged particles and energetic photons. This has extended their usefulness to such diverse fields as X-ray (Kellogg et al, 1976) and UV (Lampton et al, 1977) astronomy, e-beam fusion studies (Dolan and Chang, 1977) and nuclear science, where to date most applications have capitalised on the superior MCP time resolution characteristics (Green et al, 1975; Girard and Bolore, 1977; Boutot et al,

1977). Wiley and Hendee (1962) built the first operational MCPs between 1959 and 1961 at Bendix Research Laboratories.

1.7.1.1.Principle of Operation

The theory of channel multiplication has been adequately covered (J Adams and B W Manley, 1966; G Eschard and B W Manley, 1971; P Schagen, 1974). In this section merely the important parameters needed for understanding optimum MCP performances, will be highlighted. These entail the phenomena of ion feedback, space charge saturation and dimensional scaling.

THE STRAIGHT CHANNEL ELECTRON MULTIPLIER; ION FEEDBACK

The simplified mechanism for electron multiplication in a straight channel electron multiplier is as follows: an incident electron produces δ secondary electrons. The kinematics are such that δ^2 secondary electrons are produced in the second stage, δ^3 in the third, etc., so that the overall gain G after n stages is given by

$$G = \delta^n \qquad (1.31)$$

Assuming that the secondary electron emission is normal to the channel walls Schagen (1974) derived the following expression for the gain

$$G = \left[\frac{AV}{2\alpha\sqrt{V_o}} \right]^{\frac{4V_o\alpha^2}{V}} \tag{1.32}$$

where

V is the total channel voltage,

V_0 is the initial energy of an emitted secondary electron ~ 1eV,

α is the length diameter ratio, and

A is the proportionality constant in the assumed relation

$$\delta = A\sqrt{V_c} \tag{1.33}$$

where eV_c is the electron collision energy in eV, and A~0.2

Straight channel multipliers typically operate at gains of 10^3-10^5, the upper limit being set by the onset of ion feedback and the resulting performance instabilities. As the gain increases, so does the probability of producing positive ions in the high charge density region at the output of the channel. The ions are produced by electron collisions with residual gas molecules at ambient pressures greater than 10^{-6} torr and with gas molecules desorbed from the channel walls under electron bombardment. Such ions can drift back to the channel input, producing ion after pulses. In the case of a

vacuum tube with a proximity focus photocathode, these ions can produce additional secondary electrons at the photocathode, resulting in a regenerative feedback situation. In the case of large single channels, simply bending or twisting the channels can suppress ion feedback.

THE CURVED CHANNEL ELECTRON MULTIPLIER; SPACE CHARGE SATURATION

As the suppression of ion feedback allowed operation of single channel multipliers at higher gains, it was found that the charge pulse height distribution changed radically from a negative exponential to a quasi-Gaussian shape with FWHM of 50% or better at a peak gain of 10^8 or more. Such behaviour is the result of space charge saturation near the channel output. At high enough gains, the charge density at the rear of the channels reduces the kinetic energy of electrons as they interact with the channel walls until the secondary electron yield δ is reduced to unity. Thus, the channel gain is limited by the space charge density which itself is defined by the channel geometry and the overall channel voltage.

Loty (1971) has shown that the maximum gain for a space charged saturated channel, for a fixed V and α, is proportional to the channel diameter. Therefore, since a 1mm diameter channel saturates at a gain of 10^8, a 10μm diameter channel should saturate at 10^6. Therefore,

microchannel plates (~25μm pore size), suitably engineered to suppress ion feedback should exhibit saturated gains in the low 10^6 ranges, which have indeed been found to be the case (Timothy and Bybee, 1977).

The phenomena of space charge saturation and the resulting quasi-Gaussian pulse height distribution allows an integral discriminator to be set for event counting so that the measured count rates are relatively insensitive to gain shifts. Therefore count rate vs. bias voltage characteristic exhibits a reasonably flat plateau; the latter cannot be obtained with a negative exponential charge distribution.

As suggested earlier, ion feedback suppression may be achieved in single multipliers by the simple expedient of curving the channel. This is difficult for a thin (~0.5mm) microchannel plate. Instead a commonly used method of obtaining high gain space charge saturated output pulses is MCP Chevron configuration. Two MCPs, with channel bias angles of typically 8° or 15°, are placed so that their channel bias angles provide a sufficiently large directional change so as to inhibit positive ions produced at the output of the rear plate from reaching the input of the front plate.

1.7.1.2. Detector Efficiency

Hill (1976) reported that the secondary electron emission coefficient δ for lead glasses typically used in channel plates reaches a maximum of about 2 at incident primary electron energy of 300 eV. At low energies, where the incident electrons do not have a range sufficient for multi-channel excitation, the detection efficiency should approach the open area ratio of the MCP, which is typically 50%. However, electron striking the interstitial electrode material produces secondaries, which can excite neighbouring channels. A variation in efficiency is also dependent on the angle of incidence, for instance, if the electron trajectories are almost parallel to the channel axis, there is a high probability for deep penetration into the channels before a primary interaction; this results in low gain output pulses near 0°.

Most positive ion detection measurements reported in the literature have been with single channels, and quantitative results only exist for energies less than 30keV. However, measured efficiencies are of the same order of magnitude as those for electrons.

1.7.1.3. Dead Time

The number of channels in a 25mm diameter MCP with 25μm diameter channels is about 5.5×10^5. The total plate resistance, electrode to electrode, is typically $3 \times 10^8\,\Omega$, so that each channel has an associated resistance of $R_c = 2.75 \times 10^{14}\Omega$.

If one considers the MCP to be a parallel plate capacitor, 1mm thick, with half the volume between electrodes filled with Corning 8161 glass (dielectric constant $\varepsilon = 8.3$), then the total plate capacitance is ~ 200pF or 3.7×10^{-16} F per channel. After a channel is used, the charge in the channel walls must be replenished, and because of the exponential nature of channel multiplication, most of the charge is depleted from the last 20% of the channel length. Therefore, an effective channel capacitance $C_c = 7.4 \times 10^{-17}$ F, must be recharged through a channel resistance $R_c = 2.75 \times 10^{14}\,\Omega$. This channel recharge or recovery time is given by

$$T_c = R_c C_c \approx 20\ ms \tag{1.34}$$

In general, this recovery time can be written as

$$T_c = Kd \tag{1.35}$$

where K is a proportionality constant which depends on the open area ratio of the MCP and the glass dielectric constant. For MCPs made of Corning 8161 glass the constant $K \sim 4 \times 10^{-13}$.

Although each channel of an MCP has a dead time on the order of 10ms, the fact that there are 10^5 to 10^6 channels in a plate, which operate more or less independently, makes the effective dead time of an MCP on the order of 10-100ns. This is provided that no single channel is excited more frequently than once every 10 ms - uniformly distributed incident flux over the active area of the MCP.

1.8. The LD-TOFMS Instrument used in this Study

The laser desorption time-of-flight mass spectrometer used, was a Wiley-McLaren type linear instrument. The instrument was designed and built in-house. Due to the small amount of uranium product (nanogram quantities) that is collected during three hour irradiation experiments at 2-10Hz laser repetition rates, a sensitive instrument was needed that could measure isotopic ratios at low material consumption rates.

Having successfully implemented in-line time-of-flight mass spectrometers in both the lithium and the UF_6 contact cells, a mature technology was at hand. Furthermore, utilisation of the same mass separation principle (TOF-MS), seemed to have the advantages for comparison of in-line and bulk measurements. The decision to design and build the system in-house was also motivated by the fact that none of the commercially available systems at that time allowed for routine analyses involving highly reactive uranium

products. For example the bearings of the turbo pumps had to be modified to run on sealed fomblin oil bearings, the o-ring seals had to be changed to viton, the microchannel plate detectors and electron multipliers had to be differentially pumped, etc.

1.8.1 LD-TOFMS Instrument Specifications

The initial system design consisted of a two-stage source-extraction region, lengths 1 and 2 cm, respectively. The field free flight pipe was 1.2m long. A schematic of the instrument is shown in Fig 1.5.

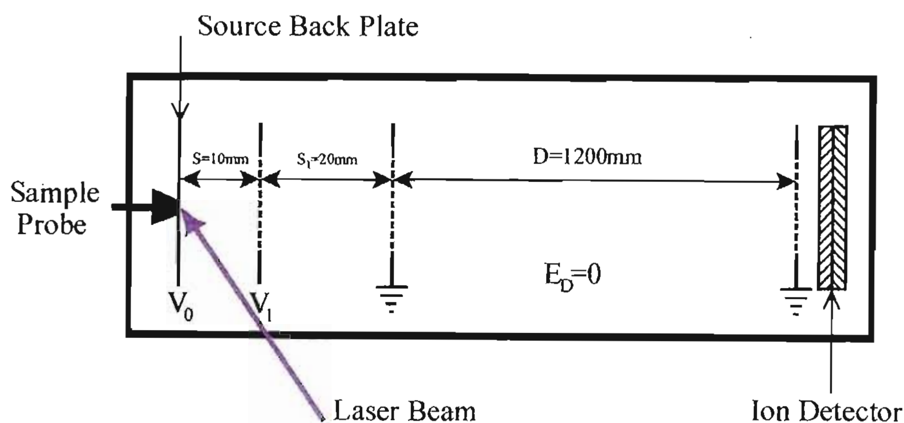

Fig 1.5 In-house designed and built Wiley-McLaren type lasers desorption time-of-flight mass spectrometer.

The sample platelets are mounted onto a 5mm diameter stainless steel probe with a conductive carbon adhesive. The probe design is such that

when inserted into the mass spectrometer, the surface of the sample platelet was flush with the source backing plate to ensure a homogeneous acceleration field. Laser desorbed ions were accelerated in two stages with total acceleration voltage of up to ±35kV.

To operate the TOF instrument under the Wiley-McLaren conditions to obtain simultaneous time, space, and energy focusing, the approach was as follows:

Fixed Parameters:

$s_0 = 1$ cm

$s_1 = 2$ cm

$D = 120$ cm

Set the voltage on the back plate at 4500V, and then solve equation (1.26) for V_1 such that d=D=120. For the present values of s_0, s_1, D, and V_0 the solution for V_1on the first grid is 4438.6V, then:

$E_0 = (4500 - 4438.6)/0.1 = 614$V/cm;

$E_1 = 4438.6/0.2 = 22193$V/cm;

$\sigma = s_0 + (E_1/E_0)s_1 = 7.329$; and

$$d = 2\sigma^{3/2}\left[\frac{1}{s_0^{1/2}} - \frac{2s_1}{s_0^{1/2}\left(\sigma^{1/2} + s_0^{1/2}\right)^2}\right] = 119.995$$

The detector consists of a combined microchannel plate, electron multiplier configuration. The microchannel plate (MCP) of 32mm diameter, liberates electrons in response to the incidence of an ion, as well as multiplies such

electrons by a factor of ~1000 over its thickness of 0.5mm. Special measures had to be taken to ensure a linear dynamic range large enough to accommodate the 1:140 intensity ratio of the two main uranium isotopes at natural abundance. The double MCP system in a chevron configuration, usually employed for detection of ions in a TOF-MS, does not allow such a dynamic range. Instead of the second MCP, an electron multiplier (Hamamatsu R2362) was used as secondary signal amplifier. The total amplification of this detector configuration is 10^6 at 3500V supply. The electron multiplier was modified to enable the supply of large current pulses in short bursts by connecting capacitors of 220pF over the last four dynodes. These capacitors serve as reservoirs of electrons, making them available during the pulse. The large resistance of the 24-dynode chain (24MΩ) limits the peak current attainable. The signal from the electron multiplier is fed via a feed-through to an external fast amplifier (EG&G Ortec 9305) with 50Ω load resistance and 10x amplification. A fast digital oscilloscope is used to record the pulses.

A pulsed UV laser (N_2) of 337nm wavelength, 1.4mJ energy per pulse and 600ps pulse width type LN1000 (Laser Photonics) was used for ion desorption. The laser beam was focussed (focal length 25cm) onto the target surface at a 75° angle of incidence. The oval spot illuminated on the target had the approximate dimensions of $0.5x3mm^2$. The output of the

laser was attenuated with a combination of neutral density filters of different transmissions.

The laser pulse, the trigger being obtained from a beam splitter and a fast UV-grade silicon pin detector, determined the starting time of the data system. The spectra were accumulated on a digitising oscilloscope with 250MHz bandwidth, 1Gsa/s sampling rate, and a time resolution as low as 1ns. Data was read from the oscilloscope using a 486 IBM compatible computer via an IEEE interface with custom software.

1.8.2 LD-TOFMS Mass Spectra

Many of the limitations of isotopic abundance measurements in mass spectrometers arise from the requirement that the complete mass spectrum should be obtained from a single ionisation event. The time-of-flight mass spectrometer is well suited for this purpose since it produces a time separation at the detector for ions of different mass to charge ratios that were formed at the same moment.

The reproducibility of isotopic abundance of the same element measured with laser desorption TOF-MS is much better than the reproducibility of elemental abundance ratios. This is because inter-isotope effects in the ionisation

process are much less sensitive than inter-elemental effects (similar to the "matrix"-effect in SIMS) to variables such as laser power deposition.

The feasibility of LD-TOF-MS to perform isotopic analysis was tested on a solder sample containing 10% tin, Sn, with natural isotopic composition. Sn is an ideal test sample, as it has 10 stable isotopes bunched between the masses of 112 to 124 – an excellent test of mass resolution. The relative intensities vary from as little as 0.65 to 32.6% - an excellent test of the sensitivity and linearity of the instrument. Fig 1.6 shows a typical mass spectrum obtained from the solder sample. Nine of the Sn peaks are clearly resolved, indicating a mass resolution of well in excess of 120.

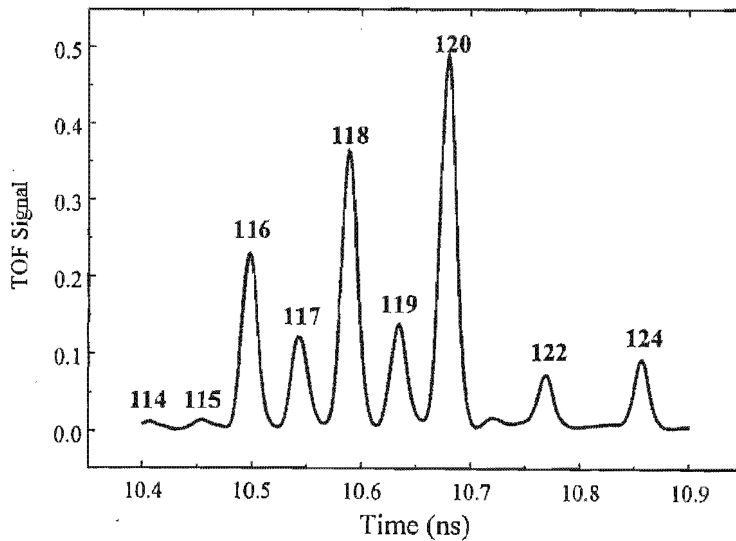

Fig 1.6 Laser desorption TOF-MS spectrum of the Sn isotopes present in a commercial solder.

The peak areas were measured. Table 1.1 gives a comparison of the natural isotopic abundance versus the LD-TOF-MS measurements.

Sn (amu)	Natural abundance (%)	LD-TOF-MS measured
112	0.97	1.1
114	0.65	0.7
115	0.36	0.5
116	14.5	14.5
117	7.7	7.9
118	24.2	24.4
119	8.6	8.6
120	32.6	32.5
122	4.6	4.2
124	5.8	5.6

Table 1.1 Laser desorption TOFMS measured values for the isotopes of Sn vs. published isotopic abundance.

During the concept design of the LD-TOFMS instrument it was also noted that although the measurement of the 235 to 238 isotopes of uranium was the primary focus, it was more than likely that the analyses of the MLIS product would involve UF_x molecules, where x=0,1,..6. It turned out that UF, UF_2, UOF, UOF_2, U_2, etc. species were in fact measured. For that reason the instrument design had to accommodate measurements at much higher masses than the 235/238 elemental isotopes of uranium. Hence the choice of a 1.2m long drift tube and the 35kV extraction voltage supply.

Fig 1.7 shows a typical LD-TOFMS spectrum obtained from a MLIS sample. The peak intensities of the UO and UF species are comparable to

that of the elemental ^{238}U-peak. The UO_2, UFO, and UF_2 peaks can clearly be seen.

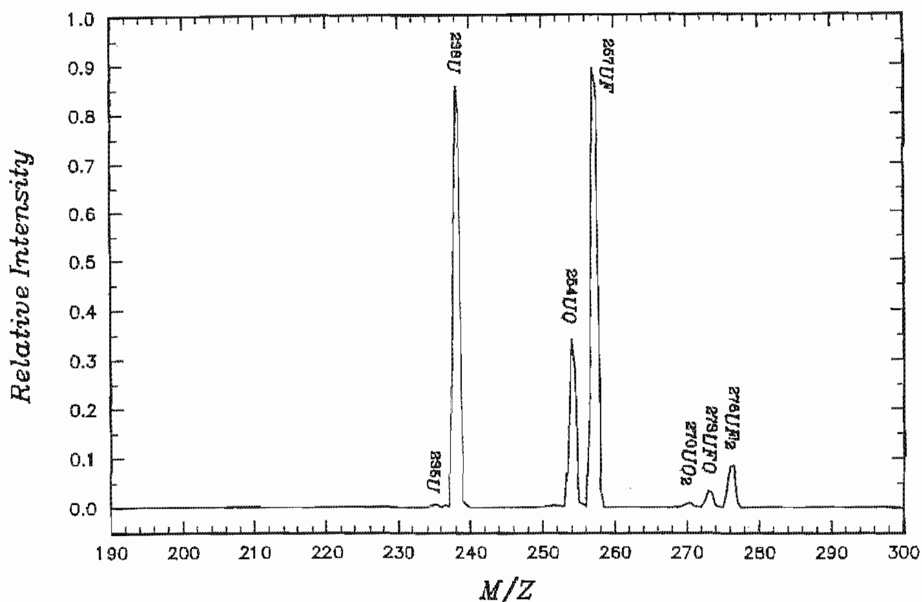

Fig 1.7 A LD-TOFMS spectrum obtained from a MLIS product sample. The peak intensities for UO and UF species are comparable to that of the U-elemental peak.

The mass resolution of the instrument is clearly more than sufficient to resolve masses up to 300. It was at this point in time that the measurement of High Mass proteins (>1000 amu) was a hot topic in the scientific literature. The LD-TOFMS instrument capability of measuring High Mass proteins had to be tested.

1.8.3 LD-TOFMS High-Mass Capability

With the advent of matrix-assisted laser desorption/ionisation (MALDI) in 1988, molecular weights of biological macromolecules such as proteins, carbohydrates and oligonucleotides, exceeding 100,000 Da, have been recorded. Initial success with oligonucleotide mixtures has encouraged future contributions in mapping the human genome.

In MALDI a low concentration of analyte molecules is embedded in either a solid or a liquid matrix consisting of a small, highly absorbent species. The matrix therefore retains the property of efficient and controlled energy transfer, while the analyte molecules are spared from excessive energy that would lead to fragmentation. A laser pulse with sufficient irradiance causes the mixture of matrix and analyte molecules to undergo gas phase transition. Suitable matrices enhance quasi-molecular ion formation of the analyte molecules by proton transfer reactions in the gas phase.

Fig 1.8 shows an MALDI spectrum of horse heart cytochrome C (HHCC) with molecular mass 12360amu. A 50mM solution of sinapinic acid was mixed with the HHCC to give 1pM/μl analyte concentration. A few μl (a couple of drops) are deposited on the sample probe, allowed to dry in air, before loading into the vacuum system.

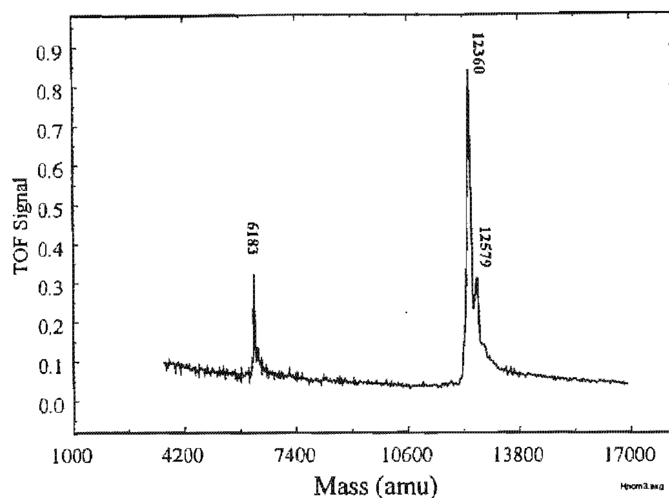

Fig 1.8 A MALDI TOFMS spectra of Horse Heart Cytochrome C (HHCC). The high mass peaks at 12360 and 12579 can clearly be resolved. The peaks at 6180-6280 are the double charged species.

A high-resolution scan of the peaks at 12360 is shown in Fig 1.9. A mass resolution of 320 was measured. The peaks at masses 12573 and 12782 are assigned to the addition n-sinapinic acid to the horse heart protein.

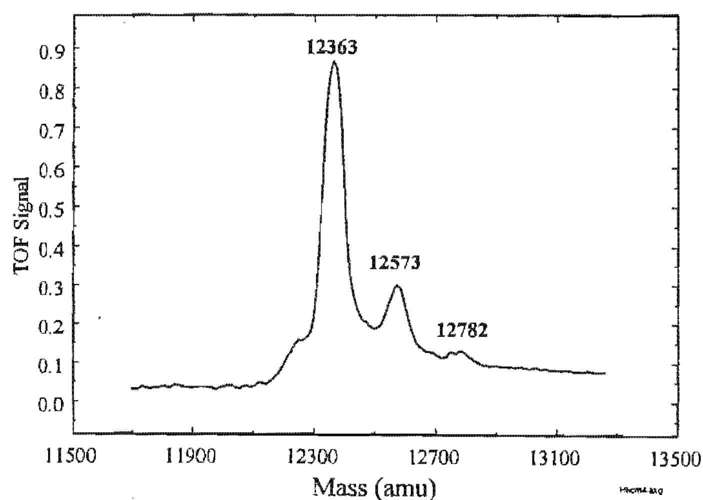

Fig 1.9 High mass resolution MALDI TOFMS spectra of HHCC.

The sensitivity of the technique is shown in Fig 1.10 where 75 femtomoles/μl of HHCC could still be measured with ease.

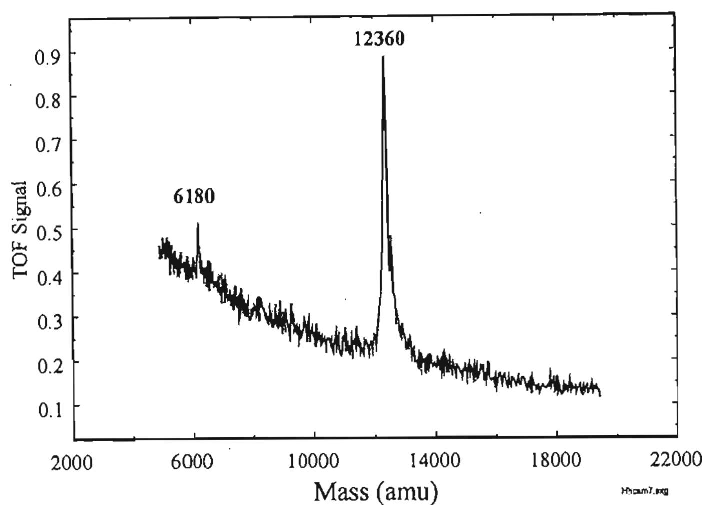

Fig 1.10 A MALDI TOFMS spectrum of 75 femtomoles of HHCC.

The mass accuracy can be seen in Fig 1.11 where a known mass standard bovine lung protein at 6500, was used as internal mass calibration. Using this known internal mass the flight times are converted to mass, resulting in a mass measurement of the HHCC peak at 12364. The absolute value should be 12360. The 4 mass differences constitute a 0.03% mass accuracy.

Table 1.2 summarises the proteins and peptides that were successfully analysed with the LD-TOFMS instrument.

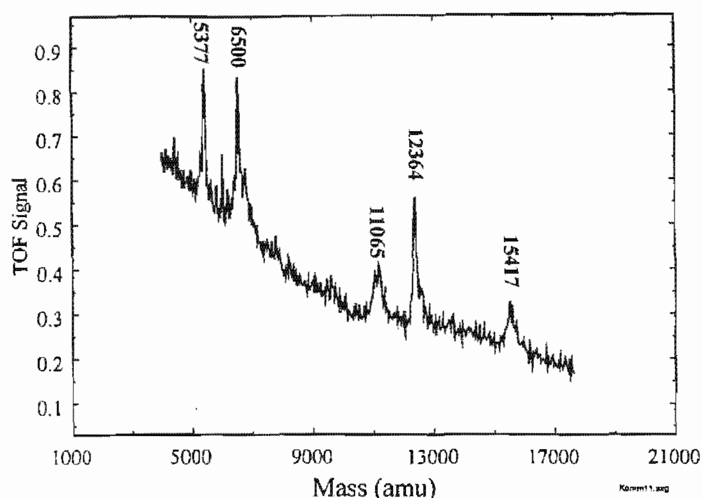

Fig 1.11A MALDI TOF spectrum of HHCC, showing an internal mass calibrates at masses 5377 and 6500. Using the known mass of the internal standard, the mass calibration is done, resulting in a measurement of the HHCC peak at 12364.

Proteins and Peptides	Mol.wt.		Proteins and Peptides	Mol. wt
Ala_4Val	401.5		Human milk lysozyme	14,693
Leucine enkephalin	555.6		Horse heart apomyoglobin	16,951
Methionine enkephalin	573.8		Bovine pancreas-trypsin	23,290
$Ala_{10}Val$	827.9		Bovine trypsin	23,311
Gramicidine S	1141.5		Porcine pepsin1	34,504
Substance P	1347.7		Porcine pepsin2	34,688
Ammonium octathymidylate	2568		Yeast alcohol dehydrogenase	36,740
Human β-endophin	3465		Yeast alcohol dehydrogenase	36,766
Bovine insulin	5733.5		Bovine albumin	66,267
Porcine proinsulin	9082		Rabbit phosphorylase B	97,093
Human apolipoprotein $CIII_1$	9421		Rhodabacter capsulates	112,154
Pig-heart cytochrome C	12,224		E coli β-galactosidase	116,336
Bovine ribonuclease A	13,682		Mouse monoclonal antibody	149,190
Lysozyme from egg-white	14,306		Glucose isomerase	172,000

Table 1.2 Summary of proteins and peptides successfully measured with LD-TOFMS instrument.

Chapter 2

Secondary Ion Mass Spectrometry

2.1 Introduction

The original roots of secondary ion mass spectrometry (SIMS) go back to the beginning of the century. J J Thomson carried out his experiments on the "particle nature" of the electron. He observed the effect of ions in a discharge tube on a metal plate. He deduced that secondary particles were emitted in all directions and these were, for the most part, neutrals, but that a small fraction was positively charged. Early SIMS instruments of type suitable for analysis were developed from 1949 by Herzog and Viehböck (1949) and from 1950 by the workers of RCA Laboratories based on Honig's 180° magnetic sector spectrometer.

In the sixties a number of workers added more knowledge about the general features of secondary ion emission. At the time the emphasis was mainly on bulk analysis. A number of specialised SIMS instruments were developed for microanalysis. In 1967 the application of SIMS to thin film analysis was urged and quantitative analysis of depth profiles was reported. Not only was the ion current measured as a function of bombardment time, but also the concentration (number of particles per cm^3) was given in terms

of depth (Å) and diffusion coefficients were determined. Today a number of companies offer commercial SIMS instruments with applications in diverse fields.

In this chapter the theory of SIMS is presented. The emphasis is on the application of SIMS, rather than on the design of instrumentation. Fundamental research on the establishment of a practical table of sputtering yields, for the non-expert user, is detailed. These findings form the basis of selecting SIMS parameters in the analyses of collected laser-produced products, e.g. lithium deposits (Chapter 3) and uranium fluoride deposits (Chapter 4).

2.2 The Principle of SIMS Analysis

SIMS operates on the principle that a target is bombarded with a beam of primary ions having energies of several keV. Target particles are sputtered due to this ion impact, mostly as neutrals, and only a small portion as ions (positive or negative), either in the ground or the excited state. These sputtered (secondary) ions are extracted from the target region and passed through a mass analyzer, where they are separated on a basis of mass-to-charge ratio. These mass-to-charge separated ions are detected by suitable means and the information fed to a recorder or computer. The end result is a mass spectrum, starting at mass 1, H^+, up to several hundreds of mass

units. The highest achievable mass unit is dependent on the type of mass spectrometer.

Qualitative and semi-quantitative survey analyses of all elements from hydrogen to uranium can be carried out with SIMS. The minimum detectable concentrations are element and matrix dependent, typically between 1ppm to 1ppb. Minimum detectable concentrations are related to the material consumption, as SIMS is a destructive technique.

SIMS can be used for the detection of surface contamination and impurities (Marais, Strydom, et al, 1988; Tullmin, Strydom, et al, 1989 & 1990), or for studying surface and interfaces of semiconductor materials (Demanet and Strydom, 1985; and Demanet, Strydom, et al, 1986; Barnard, Strydom, et al, 1988; Strydom et al, 1989), or catalytic reactions. It can also be used to carry out depth analyses. In this case, comparison of the spectra obtained after ten minutes and after three hours allows one to visualise how the composition of the sample as a function of bombardment time (proportional to depth) changes with depth. Quantification of these measured depth profiles is possible by means of implanted standards (Botha, Strydom, and Marais, 1988; Strydom, Botha, and Barnard, 1989; Strydom, 1989; Strydom, Botha, and Vermaak, 1991).

2.3 Theory of SIMS

The *sputter process* forms the basis of SIMS. Energetic primary ions penetrate the solid target, where binary collisions with target atoms occur, and yielding recoil target atoms. Primary particles will finally come to rest after a slowing down time at the so-called *penetration depth.* Meanwhile the first second, and n^{th} generation target recoils yield a dense cascade. These cascades replace the target atoms. If they are close enough to the outer surface of the target, and their velocity vectors are pointing outside the target, they can be emitted from the surface – a process called sputtering. Sputtering is an event caused by a number of cascades. Sputtering by direct ejection of target atoms by primary ions occurs relatively scarcely.

The *information depth* is the depth at which the particles, which are sputtered, were present prior to the emission process. The information depth depends on the mass and energy of the primary ions and on the mass and energy of the recoil atoms. The majority of atoms are emitted from zones immediately below the surface with a mean escape depth of about 6Å. The escape depth of cluster ions, i.e. two or more atoms emitted as one unit, is restricted to one or two atomic layers, since the dimensions of cluster particles are large compared to the average distance between two target atoms.

There is no complete theory at the moment, which accounts for all the processes from the very beginning right up to the emission of particles. However, a number of theories, which describe details of the above, mentioned processes have been attempted. In many cases these theories hold for certain experimental conditions only or they relate to secondary ions of given kinetic energy. Six models are worth mentioning:

(i) *The Kinetic model* refers to ions emitted with kinetic energies greater than 30eV, from pure metals under bombardment by noble gas ions. Secondary ion emission takes place in several steps: penetration of the primary ion into the target and emission of secondary particles via collision cascades. During the violent collisions between particles in the dense cascade, electrons of inner shells are excited. The target atom is then emitted as an excited neutral particle and de-excites outside the metal into an ion via an Auger effect.

(ii) *The Autoionisation model* is valid for rare gas ion bombardment, assumes inner shell excitation into autoionisation state and relaxation of the latter in vacuum via an Auger process, yielding a secondary ion and an Auger electron.

(iii) The *Surface effect model* assumes that all processes relevant to the formation of ions take place at or near the surface of the target. According to this, a particle while being ejected will change its electron structure from that of the bulk target to the free atomic or ionic level. The ion yield is then calculated as the probability of finding an ion at a great distance from the surface.

(iv) The *Bond breaking model* considers all elements in the target to be present as ionic compounds. Upon ejection of the target elements the ionic compound is broken, and the element retains its charge.

(v) The *Thermodynamic model* assumes that a plasma in complete thermodynamic equilibrium is generated locally in the solid by ion bombardments. The ratio of the number of ions generated in the plasma to the number of particles present in the plasma in any state is assumed to be unchanged during the emission.

(vi) The *Collision cascade model* has been developed from the thermodynamic model. Sputtering and ionisation are described in terms of collision cascades initiated by penetration of primary particles. Peter Sigmund (1969, 1993) spent a lifetime in refining this topic. From his work, the process can be described in terms of sputtering yields and erosion rates.

2.4. SIMS Analysis Formula

SIMS analysis is aimed at determining the concentration of element M from the measured secondary ion current I_S. Furthermore, the isotopic abundance of the element of mass M should be taken into account, and corrected for. The principle formula is:

$$I_S = I_p S \beta^+ cf = I_p S^+ cf \tag{2.1}$$

where

I_P is the primary ion current;

I_S is the measured secondary ion current;

S is sputter yield (number of particles sputtered, N_S^k, per number of impinging primary ions, N_P);

S^+ is the ion yield (number of sputtered ions per number of impinging primary ions);

β^+ is the degree of ionisation (number of particles sputtered as ions per the number of particles which have been sputtered in a state k).

c is the fractional concentration actually present per cm^3; and

f is the mass spectrometer transmission.

2.5. Normalised Sputtering Yields

Sputtering is the most important consequence of ion bombardment of a solid target, and the sputtering yield, defined as the average number of target atoms removed for each incident ion, is the quantitative measure thereof. Despite the large number of sputtering yields, which have been measured and published over the years, by 1990 no comprehensive compilation has yet been made that provides the non-expert user of the sputtering process with a quick estimate of the yield. This is of paramount importance in SIMS, since the choice of ion species, ion energy and fluence determine the amount of target material removed. The amount of target material removed determines the minimum sensitivity achievable as well as the depth of information in time (sputter time).

The various models of sputtering from which the yield can be calculated are even less useful to such a person because the calculation requires expert knowledge and time. Moreover, the models employ idealised assumptions, which are not necessarily applicable in a real situation. With these users in mind the author and Werner Gries embarked on presenting a universal table of sputtering yields of monoelemental polycrystalline targets (Strydom and Gries, 1984; Gries and Strydom, 1984 a & b).

The table is based on an adaptation of Sigmund's well-known model of sputtering (1969) to the results of 620 yield measurements, which were taken from literature (given in Appendix B). These measurements were a combination of different primary ion beams on different target materials. In other words, the Sigmund model is used to supply structure to the experimental results so that other sputtering yields, which have not yet been measured or published, can be predicted realistically. The table consists of these predicted values for any combination of bombarding element ion and sputter element target for ion energies within the range $0.001 < \varepsilon < 100$, where ε denotes the dimensionless universal energy of the well-known LSS range theory [Lindhard, Scharff, and Schiϕtt (1963)] – see Appendix A for a summary of ion implantation theory. To simplify the table, all sputtering yields were calculated for an atomic surface binding energy of 1eV. These normalised values can easily be converted to real sputtering yields by division by the actual atomic surface binding energy (which can be presented by the sublimation enthalpy).

2.5.1. Calculation of α_{eff} Values

Sigmund's sputtering model was formulated for perpendicular incidence of monoenergetic and monoatomic ions on amorphous (and electrically conductive) monoelemental and defect-free smooth-surfaced clean solid targets. Since most real targets are polycrystalline rather than amorphous

(as shown also by the very small number of "amorphous" sputtering yields published compared to the number of "polycrystalline" sputtering yields), all 620 real sputtering yields used were of the "polycrystalline" variety.

Little was known of the cleanliness, topography and defect density of most of the targets. From the relatively high residual gas pressure at which some of the measurements were made, it must be assumed, however, that cleanliness (in the sense of no gas coverage) was the exception rather than the rule. Also, medium-to-high defect densities are assumed to have been prevalent (if only for the radiation damage induced by the ion bombardment). Moreover, a smooth topography, even if present at the beginning, is unlikely to persist throughout most sputtering yield determinations where sputter removal of a substantial surface layer is involved. In these cases, the monoelemental character of the target is not maintained, because of incorporation of substantial quantities of the bombarding ion species in the target. Finally, preferential rather than random orientation of crystallites (as is expected for the typical polycrystalline target) cannot be ruled out in some of the targets. Overall this may be ineffectual (because the sputtering yield can increase as well as decrease as a result of preferential sputtering).

In summary therefore, the adjusted model should be representative for sputtering of ion species-contaminated polycrystalline targets with a

relatively high defect density and a gas-coverage surface topography of sub-micron roughness by perpendicularly incident monoenergetic and monoatomic ions.

According to Sigmund the sputtering yield S (for the ideal situation) can be calculated from the formula

$$S = \frac{0.042\alpha S_n}{B} \tag{2.2}$$

where

- S is the sputter yield (atoms/ion)
- α is a dimensionless number which expresses the relative availability of the deposited energy arising from the incident ion for sputtering
- S_n is the nuclear stopping power (in eV.A^2) of the LSS-theory, of the target for the incident ion, and
- B is the average surface binding energy (in eV/atom) of the atoms to be sputtered.

Values of α have been provided by Sigmund as a function of the mass number ratio M_2/M_1 (where *1* refers to the incident ion, and *2* to the target element) and S_n is calculated from the LSS theory (1963) as a function of the incident ion energy E.

Sigmund's α can be replaced by a best-fit plot to yield "effective" α values (designated α_{eff}), by substitution of the 620 measured sputtering yields, S_{real} mentioned above, into equation 2.2:

$$\alpha_{eff} = \frac{S_{real} \cdot B}{0.042 \cdot S_n} \tag{2.3}$$

The nuclear stopping power values were calculated from

$$S_n = 84.7 \frac{Z_1 Z_2}{\left(Z_1^{2/3} + Z_2^{2/3}\right)^{1/2}} \frac{M_1}{M_1 + M_2} s_n(\varepsilon) \tag{2.4}$$

where Z_1 and Z_2 are the atomic numbers of the incident ion and the target elements, respectively and $s_n(\varepsilon)$ denotes the dimensionless universal nuclear stopping cross-section $(d\varepsilon/d\rho)_n$ of the LSS theory. The cross-section $s_n(\varepsilon)$, in the numerical form provided by Schiφtt (1966), is approximated by the following set of expressions:

$$s_n(\varepsilon) = \begin{cases} -0.0205(\log\varepsilon)^3 - 0.106(\log\varepsilon)^2 - 0.0188\log\varepsilon + 0.435 & for\ 0.001 \le \varepsilon \le 0.2 \\ +0.0583(\log\varepsilon)^3 - 0.110(\log\varepsilon)^2 - 0.175\log\varepsilon + 0.356 & for\ \ 0.2 \le \varepsilon \le 10 \\ 0.5[\ln(1.294\varepsilon)]/\varepsilon & for\ \ 10 \le \varepsilon \le 100 \end{cases} \tag{2.5}$$

The relationship between ε and E (in keV) is given by

$$\frac{\varepsilon}{E} = 32.5 \frac{1}{Z_1 Z_2 \left(Z_1^{2/3} + Z_2^{2/3}\right)^{1/2}} \frac{M_2}{M_1 + M_2} \tag{2.6}$$

The 620 values of α_{eff}, calculated using equation 2.3 were fitted with a best-fit, α_{eff}* vs. log(M_2/M_1) graph (where α_{eff}* denotes an approximation function) by the procedure sketched below.

(i) Smoothing Step: This step consists of 2 stages, viz. firstly the replacement of all α_{eff} values at (M_1, Z_1, M_2, Z_2) by a representative average value α_{eff}^*. Each of these average points ($\log(M_2/M_1)$, α_{eff}^*) is given a statistical weight which is equal to the original number of points which the average point represents. The second stage consists of a replacement of these average points by a new set of points ($\log(M_2/M_1)$, α_{eff}^{**}), which carry equal statistical weight of an arbitrary pre-set magnitude. This is done by a procedure in which a replacement point is chosen so that the sum of moments of two average points must equal the pre-set value. If this value is exceeded, one or both of the average points are split into a doublet point so that the constraint is satisfied.

(ii) Curve Fitting Step: This step consists of fitting a curve to the almost smooth string of points ($\log(M_2/M_1)$, α_{eff}^{**}) by any least-square procedure. For this study, Chebyschev polynomials of different degrees were tried for the least-square fit and the following set of three smoothly interlinking expressions was obtained:

$$\alpha_{eff} = \begin{cases} 0.120 & for \quad L \le -1.2 \\ 0.0857L^5 + 0.289L^4 + 0.402L^3 + 0.35L^2 + 0.22L + 0.189 & for \; -1.2 \le L \le -0.144 \\ 0.0499L^6 - 0.107L^5 - 0.209L^4 + 0.314L^3 + 0.207L^2 + 0.156L + 0.183 & for \; -0.144 \le L \le 1.8 \end{cases} \tag{2.7}$$

where $L = log(M_2/M_1)$.

Fig 2.1 shows the 620 α_{eff}^* values as well as the graph of α_{eff}^* as a function of $\log(M_2/M_1)$. The vertical lines indicate the spread of the associated α_{eff} values. The best quality fit in the different M_2/M_1 sub-ranges was obtained by optimising value $g_{i,n}$, given by:

$$g_{i,n} = \frac{1}{n+1} \sum_{i}^{i+n} \left[1 - (\alpha^*_{eff} / \alpha_{eff})_i \right] \qquad (2.8)$$

where i is summed over all samples. By means of this simple test it was established that the fit of the α_{eff}^* graph to the α_{eff}^* values is equally good throughout most of the M_2/M_1 range.

The best-fit normalised sputtering yield (S^*B) can be calculated from

$$S^*B = 0.042\alpha^*_{eff} S_n \qquad (2.9)$$

Thus, the sputtering yield is normalised to an atomic surface binding energy of 1eV, from which the real sputter yields are obtained upon division by the actual atomic surface binding energy of the target solid (represented by the sublimation enthalpy).

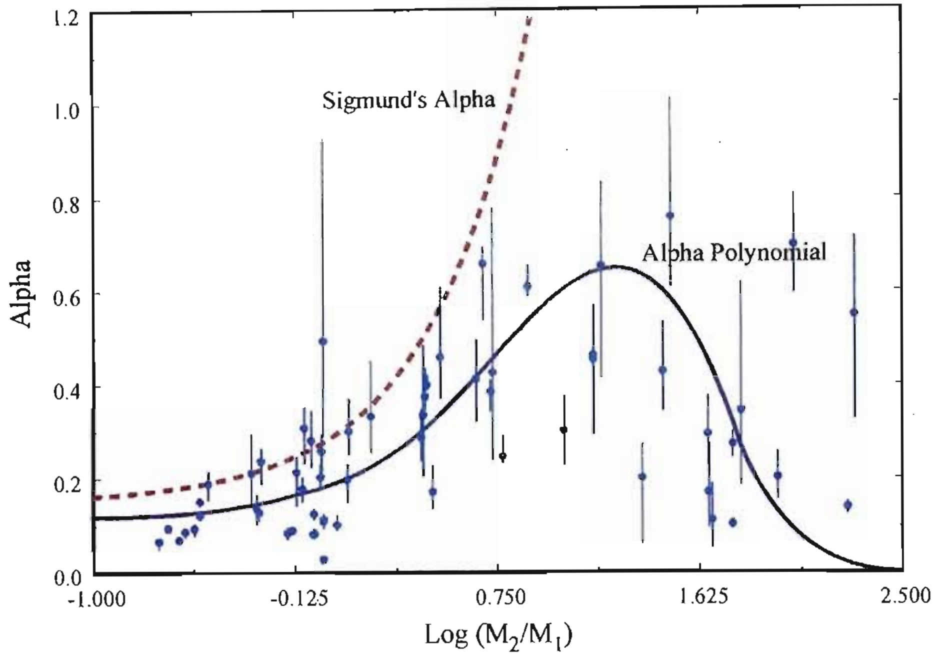

Fig. 2.1 *Graph of α_{eff} values as a function of $\log(M_2/M_1)$. The vertical lines are indicative of the spread in measured values for that specific M_2/M_1 combination. Clearly, Sigmund's formulation for α (broken line) is inadequate to describe the measured values. The polynomial fit, equation 2.7, gives a better representation.*

The *SB* values were tabulated (Gries and Strydom, 1984a and 1984b) for Z_1 and Z_2 ranging from 1 to 90 in intervals of 2 or 5, and for *E* values ranging from 0.1 to 1000keV, provided these fall within the interval $0.001 \leq \varepsilon \leq 100$. As this table is somewhat elaborate (given in Appendix C), some of the *SB* values are shown in Figs 2.2 - 2.6.

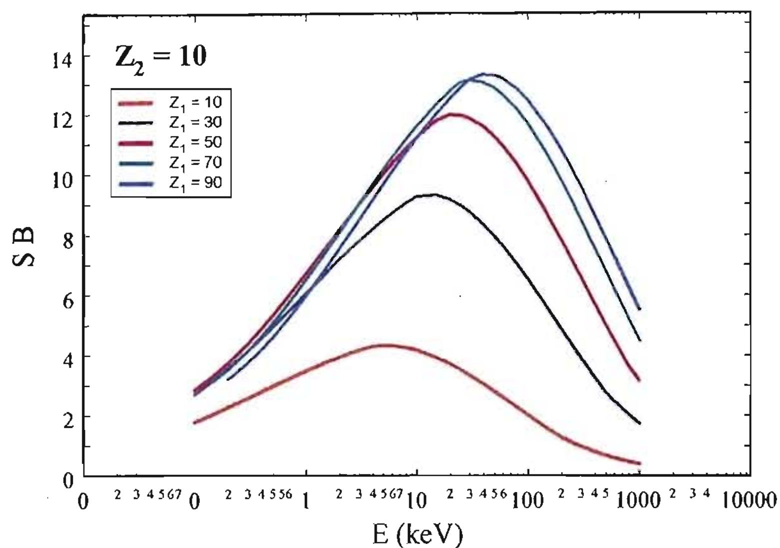

Fig 2.2 Normalised sputter yield SB as a function of ion energy E with the atomic number Z_1=10, 30, 50, 70, and 90 of the incident ion species, as parameter of the target species represented by atomic number Z_2=10.

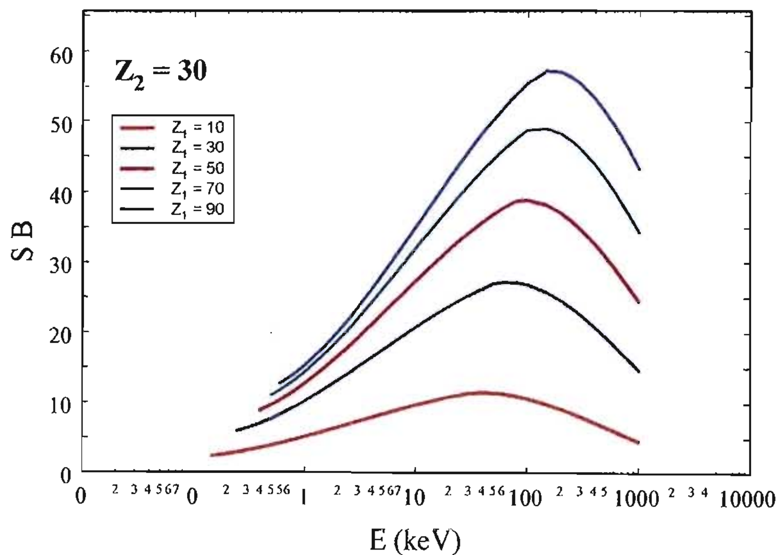

Fig 2.3 Normalised sputter yield SB as a function of ion energy E with the atomic number Z_1=10, 30, 50, 70, and 90 of the incident ion species, as parameter of the target species represented by atomic number Z_2=30.

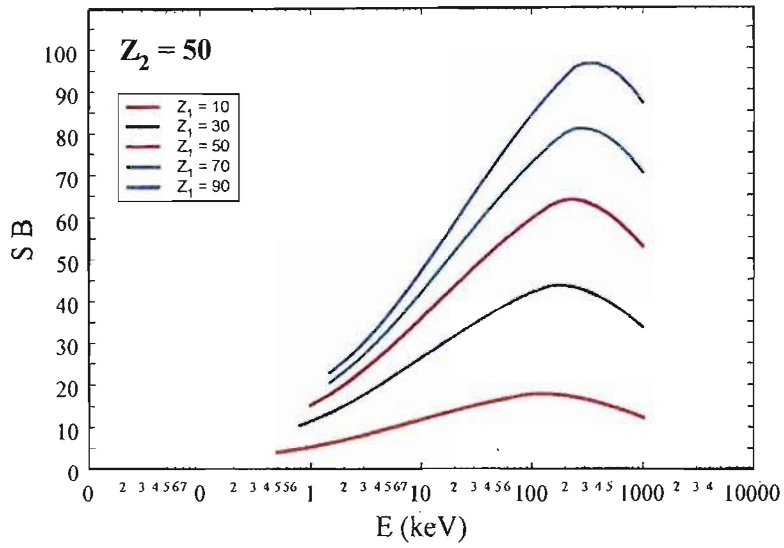

Fig 2.4 Normalised sputter yield SB as a function of ion energy E with the atomic number Z_1=10, 30, 50, 70, and 90 of the incident ion species, as parameter of the target species represented by atomic number Z_2=50.

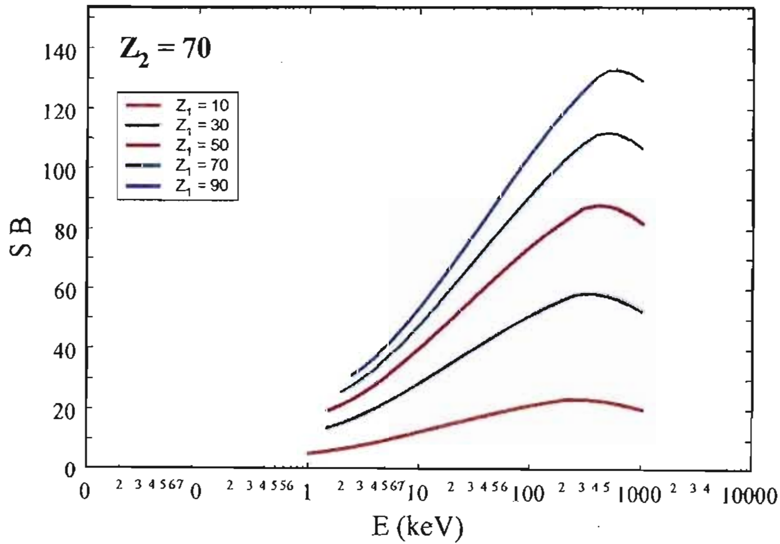

Fig 2.5 Normalised sputter yield SB as a function of ion energy E with the atomic number Z_1=10, 30, 50, 70, and 90 of the incident ion species, as parameter of the target species represented by atomic number Z_2=70.

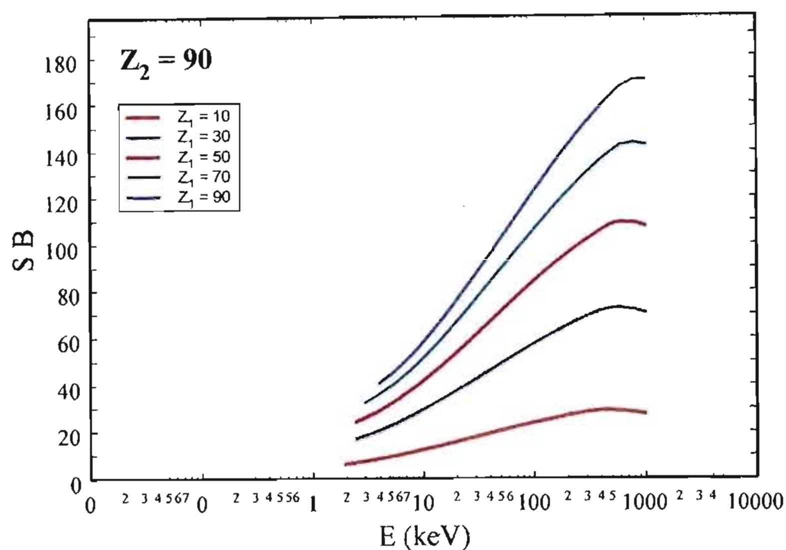

Fig 2.6 Normalised sputter yield SB as a function of ion energy E with the atomic number Z_1=10, 30, 50, 70, and 90 of the incident ion species, as parameter of the target species represented by atomic number Z_2=90.

When deciding on which parameters to use in a SIMS experiment, the available primary ion species and the instrument used prescribe primary ion energy, primary ion current and analyses area. The *SB* table or graphs forecast the *SB*-values for a given primary ion/target combination as a function of primary ion energy. Knowing the sublimation enthalpy of the target, the sputtering yield, *S* can be estimated. In section 2.5.3 the effect of angle of incidence, if not normal to the sample surface, can be included. Finally selecting the primary ion current and the size of the area to be analysed can estimate the sputter rate. This is done in section 2.5.4. Chapters 3 and 4 shows in detail how these graphs/table were used to

estimate sputter rates on lithium and uranium samples for a given SIMS instrument.

2.5.2. A Comparison of Three Versions of Sigmund's Model of Sputtering using Experimental Results

The application of Sigmund's formulation of the sputtering yield in practical SIMS analysis can be a daunting task. Attempts have been made to modify (simplify) Sigmund's theory for easy day-to-day application. This was done by means of a simple α-adaptation of the original model. Bohdansky (1983) and Yamamura et al. (1982) suggested two different modifications of the sputter yield formula for normal incidence of mono-energetic ions on single-element targets. Strydom and Gries (1984) have investigated their effectiveness in providing a better fit between theory and experiment.

For this purpose the α-values were calculated using each of the three formulae, for 620 measured sputtering yields (published in 24 papers) see (Gries and Strydom, 1984b) and these values compared. Because of the scarcity of sputtering data for amorphous targets to which Sigmund's model applies, sputter yields for polycrystalline targets were used instead. The three formulae are as follows:

Sigmund (1969), as given before

$$S = \frac{0.042\alpha S_n(E)}{B} \tag{2.10}$$

Bodansky (1983)

$$S = \frac{0.042\alpha}{B}\frac{R_p}{R}S_n(E)g(E/E_{th}) \tag{2.11}$$

with

$$g(E/E_{th}) = \left[1-(E_{th}/E)^{2/3}\right](1-E_{th}/E)^2 \tag{2.12}$$

Yamamura et al. (1982)

$$S = \frac{0.042\alpha}{B}\frac{S_n(E)}{1+0.35Bs_e(\varepsilon)}\left[1-(E_{th}/E)^{1/2}\right]^2 \tag{2.13}$$

Where the symbols have their usual meaning:

- S is the sputter yield (atoms/ion)
- α is a dimensionless function of the mass ratio M_2/M_1 (where M_1 and M_2 are the mass numbers of the ion species and the target respectively)
- $S_n(E)$ is the nuclear stopping power (in eV.A^2) of the LSS-theory (1963), which is a function of the incident ion energy E,
- B is the atomic surface binding energy (in eV/atom),
- R_P/R is the ratio of the projected range to the range of the ion species in the target,
- E_{th} is the threshold ion energy below which no sputtering occurs,

- $s_e(\varepsilon)$ is the dimensionless universal electronic stopping cross-section of the LSS-theory, which is a function of the dimensionless energy ε.

Each of the three equations was solved for α, with S being substituted by the 620 measured sputter yields mentioned above. To distinguish the α-values according to their origin, they were designated α_{eff} (i.e. effective α, Sigmund), α_{Bo} (Bodansky) and α_{Ya} (Yamamura). The same standard sublimation enthalpies were used for B in all cases.

Figs 2.7 and 2.8 shows a plot of the α_{eff}^* vs. α_{Bo}^* and α_{Ya}^* as a function of M_2/M_1, respectively.

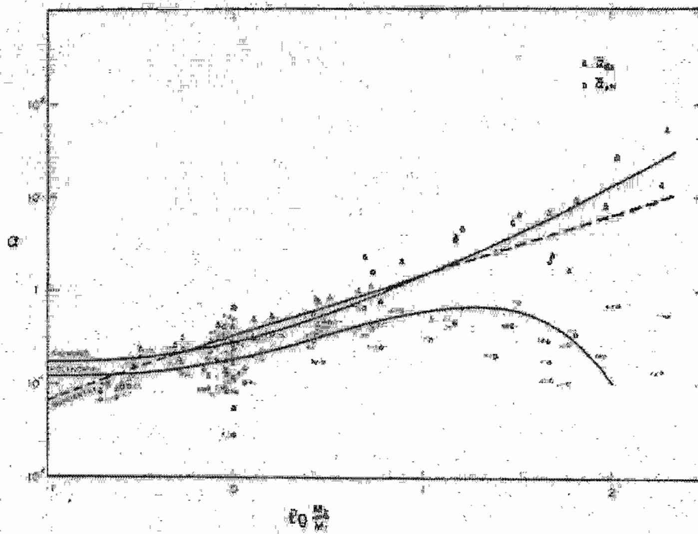

Fig. 2.7 Values of α_{eff}^* (circles) and α_{Bo}^* (triangles) and associated approximation graphs α_{eff}^* (Polynomial) and α_{Bo}^* (Bohdansky). The graph of α-values proposed by Sigmund is also shown.

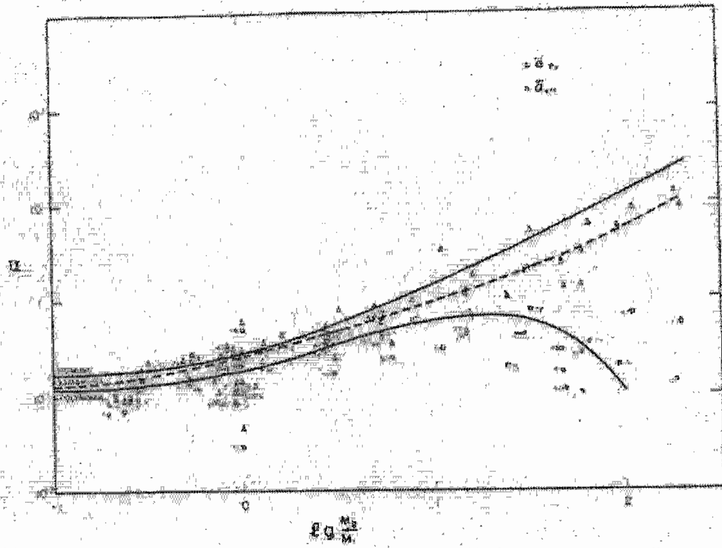

Fig 2.8 Values of α_{eff}^* (circles) and α_{Bo}^* (triangles) and associated approximation graphs α_{eff}^* (Polynomial) and α_{Ya}^* (Yamamura). The graph of α-values proposed by Sigmund is also shown.

Satisfactory average results are provided by both the Bohdansky's and Yamamura's modification of Sigmund's model in the mass ratio range $M_2/M_1<3$ when compared with the 620 measured sputter yields used in the investigation. However, these results are not more general, than that which can be obtained by use of an empirical α-approximation such as the polynomial of equation 2.7 in Sigmund's original formula. This is shown by the fact that the scatter of α^* values is not reduced by either of the two modifications.

2.5.3. Dependence of Sputtering Yield on Incident Angle

On the basis of the Sigmund theory the dependence of the sputtering yield on the angle of incidence is contained in the dimensionless energy factor α. For polycrystalline and isotropic substances the theory gives an angular dependence of the sputtering yield:

$$\frac{S(\psi)}{S(0)} = (\cos\psi)^{-f} \tag{2.14}$$

where ψ is the angle of incidence with respect to the surface normal;

$S(0)$ is the sputtering yield under normal incidence; and

f is a constant depending mainly on the mass ratio M_2/M_1 and only weakly on the constant m in the scattering cross-section:

$$f = \begin{cases} 5/3 & M_2/M_1 < 3 \\ 1 & M_2/M_1 > 3 \end{cases} \tag{2.15}$$

For large values of ψ, equation (2.13) is expected to break down because the assumption of an infinite isotropic medium, on which Sigmund's theory relies, is not strictly valid due to the very presence of a surface, particularly when most of the recoils are generated in the vicinity of the surface (as in the case of glancing incidence). In addition, as the angle of incidence increases, the reflection coefficient of the primary ions also increases, and

above a certain angle total reflection takes place, at least for a perfectly smooth surface.

The SIMS instruments used in this study all have angles of incidence that vary from 30° to 70°, all within the assumptions of the theory. As a result, the sputtering yields that are calculated for the specific measurements have taken equation (2.14) into account.

2.5.4 Sputtering Rate

Although it is essential to know the sputtering yield, one still has to express this in terms of erosion or sputtering *rate* that is the consumption of material per unit time. The higher the primary ion current density (for a given beam cross-section), the higher the elemental secondary ion current for a given concentration but also the higher the erosion rate. A compromise must therefore be made between primary ion current density, beam cross-section, desired sensitivity, and the speed at which the mass spectrum is scanned, particularly in the analysis of thin films.

The erosion rate can be estimated [Werner and De Grefte (1968)]:

$$\dot{z} = 3.755 \times 10^{-4} \frac{M}{\rho j S} \tag{2.16}$$

where $\dot{z}$ is the material thickness of material removed in μm per hour.

M is the average mass number;

ρ the density in g/cm^3;

S the total sputtering yield of the target; and

j the effective primary ion current density in μA/cm^2.

2.6. SIMS Instrumentation

All SIMS instruments have a vacuum chamber, primary ion source, a sample holder, an analyser and a detector for the secondary ions, followed by equipment for automatic data acquisition and processing, and instrument control. Ion guns and detectors do not differ essentially from instrument to instrument. The main distinction is based on the choice of analyser, namely quadrupole, sector, or time-of-flight.

Primary ion sources on the earlier SIMS instruments consist mainly of duoplasmatron ion guns, producing Ar, O_2, and N_2 primary ions. Later development included surface ionisation sources producing Cs^+ ions for improved negative SIMS. These primary ions could be focussed down to 1-10μm beam diameters. The advent of liquid metal ion sources (LMIS) in the early 80's, producing Ga^+ and In^+ primary ions, allowed for primary ion beams to be focussed down to 100-1000nm in diameter – a powerful tool in sub-micron semiconductor technology.

2.6.1. Magnetic Sector SIMS

Ions subjected to a voltage difference U obtain a kinetic energy

$$E_k = \frac{1}{2}mv^2 = eU \quad (2.17)$$

where m is the mass of the ions, and v their velocity. When these ions enter into a magnetic field B, they describe circular trajectories, and the Lorenz force and the centripetal force are in equilibrium:

$$F_L = evB = \frac{mv^2}{r} = F_C \quad (2.18)$$

The ions then move in circles with radius

$$r = \frac{mv}{eB} \quad (2.19)$$

Ions with different momentum mv move along circles with different radii. Introducing a collector slit at the exit of the magnetic field allows for the detection of specific masses. If the magnetic field is varied as a function of time, one mass after the other can pass the collector slit and by recording the collector current as a function of time, one obtains a mass spectrum. Insertion of equation (2.18) in (2.19) gives:

$$r(cm) = \frac{144\sqrt{\frac{M}{n}U(volts)}}{B(G)} \qquad (2.20)$$

where M is the mass in amu;

B is the magnetic field in G ($1G = 10^{-4}\ Vs/m^2 = 10^{-4}\ T$); and

$n = 1, 2, \ldots$. counts the charge state of the ion.

Mass resolutions routinely achievable with magnetic sector instruments are of the order of thousands. However, to achieve this the collector slit has to be small, resulting in high loss of transmission through the spectrometer. In order to obtain reasonable spectra, the magnetic field has to be scanned slowly, or alternatively, accumulation of spectra has to be performed. Since the sputtering process is continuous and destructive, long acquisition times lead to extensive sample consumptions. This seriously limits the use of this type of spectrometer in the analyses of thin surfaces and interface studies. Furthermore, it rules out any application in single event ionisation studies, as is the case with in-situ analyses during pulsed laser isotope separation experiments.

2.6.2. Quadrupole SIMS

For quadrupole mass spectrometers no magnetic field is necessary for mass separation. The mass separation occurs in a system consisting of four hyperbolic rods to which a voltage is applied. The potential obtained

between the rods is the result of applying simultaneously an electrostatic DC voltage, U, and a high frequency voltage (zero to peak value V):

$$\Phi(x,y,t)=\left[\frac{(U-V\cos\varpi t)}{2r_0^2}\right](x^2+y^2)=\left(\frac{\Phi_0}{2r_0^2}\right)(x^2-y^2) \qquad (2.21)$$

where $\Phi_0=(U-V)\cos\varpi t$

Ions injected into the rod configuration move along oscillatory trajectories through the rod system. Depending on the value of U/V, only ions in a given mass-interval have amplitudes of oscillations in the x-y plane, which do not become infinitely large, i.e. they move on "stable trajectories." These ions can therefore pass the rod system and be collected at a collector at the end of the rods.

The amplitudes of the other ions grow rapidly when passing through the rod system, the ions are finally intercepted by the rods. A mass spectrum is obtained by variation of U and V with time, with the U/V ratio kept constant at all times. Mass resolutions of several hundred are achievable. As is the case with the magnetic sector instruments, it takes time to acquire a mass spectrum due to the fact that the U/V field has to be scanned. Typical transmissions of up to 7% have been reported. Due to the absence of magnetic fields, interfacing a quadrupole mass spectrometer with other analytical techniques such as Auger electron spectroscopy (AES) and X-ray

photoelectron spectroscopy (XPS) is easily achieved. The majority of SIMS measurements performed in this study were done on a quadrupole-based instrument that was interfaced with an XPS.

2.6.3. Time-of-Flight SIMS

Time-of-flight mass spectrometers have been employed because of their great transmission (better than 95%). The principle here is that the primary ions source is pulsed, and the resulting pulsed sputtered ions are mass analysed in a time-of-flight mass spectrometer, as described in Chapter 1. Liquid metal ion sources are easily pulsed, with energies of up to 30keV. The choice of either linear, reflectron or electrostatic mass spectrometers exists. As seen before, the quest for improved mass resolution makes electrostatic spectrometers the analyser of choice.

2.6.4. Ion Detection

Detection of ion currents between $10^{-8} - 10^{-14}$ A is achieved with a Faraday cup followed by a DC amplifier. Nowadays, electron multipliers are commonly used for ion detection between $10^{-12} - 10^{-19}$ A. The higher upper limit of detection with the multiplier ensures an overlap with signals obtained from the DC amplifier. The principle of the electron multiplier is that the ions to be detected strike the conversion dynode of the multiplier

and release secondary electrons. These electrons in turn strike a following dynode, which is at a positive potential with respect to the first dynode, and release further secondary electrons. A series of discrete dynodes can be used to obtain the required amplification. Current amplification of up to 10^6 is achieved.

Channeltron multipliers have been developed, consisting of continuously distributed dynodes. They are made of glass tubes coated internally with a thin metallic layer (continuous electrode) to provide secondary electrons. Current amplifications of between 10^4 and 10^8 are achieved. The VG-ESCALAB used in this study was fitted with a channeltron detector.

2.7. SIMS Instruments used in this Study

2.7.1. VG ESCALAB II QUAD-SIMS

The secondary ion mass spectrometry analysis was conducted at the CSIR, Pretoria, on a commercial Vacuum Generators ESCALAB Mk II, fitted with a VG SIMSLAB. The SIMSLAB consisted of a DP50B duoplasmatron ion source ($^{16}O^+$, $^{16}O^-$, and $^{40}Ar^+$) inclined at 70^0 to the sample normal, and a MIG 100 liquid metal ion source ($^{69.72}Ga^+$) at 45^0. The detection of the secondary ions was done with an MM12-12S quadrupole fitted with a HTO100 acceleration lens assembly capable of 0-

800amu mass range. Both primary ion sources were operated at 10keV and rastered over a target area of 300x300μm^2. The beam intensity was kept below 2nA/cm^2 to enable slow sputtering rates. A small percentage of this sputtered material was ionised. The ions were extracted into the quadrupole, and by scanning from low to high masses, a spectrum of ion counts vs. mass could be produced. In addition, the QMS could be operated in a Depth Profile mode, where specific masses were selected, and only counts of these masses were recorded.

The mass resolution of the quadrupole mass spectrometer was typically 300, in other words at mass 300 the mass analyser could resolve mass 300 from mass 301.

2.7.2. PHI TRIFT II TOF-SIMS

The TOF-SIMS analysis of uranium products was conducted at the PHI, USA and France, on a commercial Physical Electronics Systems TRIFT II time-of-flight mass spectrometer. This was part of an evaluation of a new series of instrumentation that entered the market. The PHI TRIFT II TOF-SIMS employed energy compensating time-of-flight mass spectrometry consisting of three spherical electrostatic analysers. The spectrometer had a 2m nominal flight path. A pulsed ^{69}Ga field emission was used as primary ion source. Ion energies of 3-25keV were available, with a maximum beam

current of 20nA. The minimum beam diameter was 120nm. The detector system consisted of dual microchannel plates with a phosphor screen.

The TRIFT II had a Low Mass resolution of ≥ 9000 at $m/z = 28$ (Si^+) on silicon wafer, and a High Mass resolution of ≥ 15000 at $m/z \geq 200$ on a hydrocarbon-covered silicon wafer. The transmission through the spectrometer was ~40% for atomic species, and >90% for molecular species.

Chapter 3

AVLIS of Lithium

3.1. Introduction

Most chemical elements, be they oxygen or uranium, naturally occur with a few slightly different masses, called isotopes. Lithium, for example, is most abundant as an atom with three protons and four neutrons, giving it an atomic weight of 7. But about 7.5 percent of Lithium have one neutron less and a molecular weight of 6. These special forms of elements, called isotopes, are often very useful for things like medical tracers, speciality materials and nuclear fuel. But sorting something as small as atoms by weight has always been a tremendous technical problem.

Traditional gaseous diffusion isotope separation, in addition to being costly, time consuming, and dirty, has also become politically controversial. Sorting out the various weights of isotopes in a gas or plasma has always required carefully tuned magnetic fields and centrifuges. Since the early 70's laser isotope separation has been investigated by a number of groups.

In this chapter the basic principles of atomic vapour laser isotope separation (AVLIS) is presented. In particular, the AVLIS of lithium is described. The design and performance of an in-line time-of-flight mass spectrometer for the in-situ analyses of the ^{6}Li and ^{7}Li isotope ratio during laser irradiation experiments, is given. In-situ enrichment factors are correlated with measurements done by secondary ion mass spectrometry on collected products.

3.2. Principles of Laser Isotope Separation

Gaseous mixtures of various particles (atoms, molecules), that differs little or not at all in chemical properties is difficult or impossible to separate by ordinary chemical methods. If the quantum levels of the particles differ just somewhat one can, in principle, excite certain particles selectively by monochromatic laser radiation, leaving the other particles aside. The criterion for selective excitation is not very rigid. It is enough to have at least one absorption line of a particle shifted with respect to the spectral lines of the other particles.

The excitation of selected particles results in a change in their chemical and physical properties, and hence, may be used to separate substances by any method based on differences in the characteristics of excited and unexcited particles. The excitation energy must be much higher than the thermal

energy kT_o of the particles that is responsible for non-selective thermal excitation of the lower-energy states of all particles in the plasma.

This is the most general idéa of substance separation by a laser at the atomic/molecular level. Three conditions are required for selective atomic and molecular photo separation:

(i) At least one absorption line of the particle exists that does not overlap all absorption lines of other particles in the plasma.

(ii) The chosen frequency of the selected absorption line should be accessible for monochromatic radiation specified by the separation method in use.

(iii) The selectivity of particles should be maintained in the ensuing secondary photoionization processes of separation.

The spectral line widths of atomic and molecular absorption in plasmas are rather small. Therefore the spectral criterion of particle difference is very sensitive to the slightest details in atomic and molecular structures.

One or more of the following effects cause spectral differences in atoms:

(i) Difference in atomic number (number of protons Z).

(ii) Difference in the number of neutrons

(iii) Difference in the excitation energy (the nuclear spin, causing an isomeric effect in the hyperfine structure of the atomic spectrum).

One or more of the following effects cause spectral differences in molecules:

(i) Difference in the molecular chemical composition (number and type of atoms in a molecule, causing differences in electronic and vibrational molecular spectra).

(ii) Difference in the isotopic composition of molecules.

(iii) Difference in the three-dimensional structure of molecules.

(iv) Difference in the nuclear spin orientation of atoms in a molecule.

3.3. Atomic Vapour Laser Isotope Separation

The selectivity obtained with Atomic Vapour Laser Isotope Separation (AVLIS) in a single step, is much higher than that obtained with conventional separation processes. AVLIS is based on the fact that different isotopes of the same element, while chemically identical, have different electronic energies. As a result, each isotope absorbs different colours of light, such that each has its own distinct colour signature. When illuminated by a laser beam containing the colour signature, an atom of the selected isotope emits an electron and becomes a positively charged ion. The ion can then be separated from the neutral atoms of the other isotopes by an electromagnetic field.

Conventional isotope separation techniques - gaseous diffusion and gas centrifuge - depend on mass differences of isotopic species. The most common used technique, gaseous diffusion, operates on the principle that lighter molecules move faster than heavy ones through porous membranes. Using a cascade of porous barriers through which the lighter isotope is statistically more likely to pass can separate the lighter isotope. The separation per barrier pass is small, which results in the need for multiple stages in very large plants and large requirements for power consumption.

The gas centrifuge spins a gaseous material compound in a rotating cylinder, throwing the heavier isotope to the cylinder wall where it is scooped away from the lighter isotope. These processes require significantly less power than do gaseous diffusion, but equally as large a plant. The mass differences on which gaseous diffusion and gas centrifuge depend are about 0.01 for uranium. In contrast, fundamental selectivity of the AVLIS process by means of the colour signature process is extremely high, greater than 10 000. As a result AVLIS can achieve a high degree of isotopic enrichment on a single pass and requires relatively little equipment to achieve enrichment. The bottom-line result is low capital and operating cost.

The AVLIS process includes four major component processes: vaporisation of the metal, selective excitation of one isotope, photo-ionisation of the

excited isotope and separation of the ions from the neutral plasma. Each of these will be discussed in detail in the next section.

3.4. AVLIS of Lithium

In nature, the stable lithium isotopes, ^{6}Li and ^{7}Li, exist at a proportion of 7.52: 92.48. Recently, ^{6}Li has become of interest as the source of tritium, T, which is used as the fuel for thermonuclear fusion furnaces. On the earth, tritium is extremely rare and exists in a proportion of only 10^{-18} to 1 with respect to ordinary hydrogen. In view of such extremely meagre natural presence of tritium, it is readily appreciated that the isotope must be artificially manufactured on a commercial scale.

One of the simplest methods available is by a nuclear reaction of the following formula, which is caused by irradiation of ^{6}Li with thermal neutrons

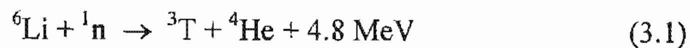

$$^{6}Li + {}^{1}n \rightarrow {}^{3}T + {}^{4}He + 4.8\ MeV \qquad (3.1)$$

This nuclear reaction permits ready production of tritium. Also, tritium can be produced from ^{7}Li as follows:

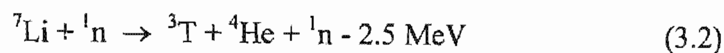

$$^{7}Li + {}^{1}n \rightarrow {}^{3}T + {}^{4}He + {}^{1}n - 2.5\ MeV \qquad (3.2)$$

In this case the reaction does not occur unless the neutrons have a sufficient high energy level. For this reason ^{7}Li is used as the absorbent for thermal neutrons and as the pH adjuster for preventing hydrogen embrittlement in nuclear fission light water reactors.

Separating the two isotopes is therefore of importance for the nuclear power industry. The financial incentive is provided by the fact that natural lithium metal cost ~R500/kg, whilst ^{7}Li, enriched to more than 99.9%, is worth more than R30 000/kg.

3.4.1. Spectroscopy of Lithium

Lithium is the lightest of all metals and, being only the third element in the periodic table, has been the centre of extensive theoretical and experimental spectroscopy studies. Only those elements of spectroscopy that underlie its photoionisation will be covered in this study.

The ground state electron configuration is $1s^2 2s^1$, placing the atom in the $2s^2S_{1/2}$ state. The energy levels increase with the principal quantum number n, with $42p^2P^0$, the highest lying state reported. For a given principal quantum number the energy also increases with the orbital quantum number l. These energy differences become rather minute at large n and l. For these high lying states the valence electron is physically at large

distances from the nucleus. Therefore these different states experience virtually the same electric field.

The ionisation level for lithium is given at 43487.150 cm^{-1} or 5.392 eV at which point the valence electron takes its leave. Laser photoionization of lithium is but one means of relieving the atom of its valence electron. The particular advantage of laser isotope separation is its isotopic selectivity.

The possible use of a single photon to reach an autoionisation state or the continuum directly is met with poor selectivity and exceedingly small ionisation cross sections (less than 10^{-18} cm^2), respectively. Furthermore, single photon ionisation would need a tuneable laser in the region of 200nm (to overcome the 5.392eV binding energy). Frequency-doubled dye lasers can be used, but at very high cost.

Alternatively, multistep resonant excitation may be used, with subsequent ionisation routes. Two distinct routes can be followed: the first involves multistep ionisation directly into the continuum, whereas with the second route a state just below the ionisation limit is reached, with subsequent ionisation methods still needed.

Photoionisation from an intermediate state into the continuum is characterised by a very small cross section; less than 10^{-17} cm^2. Atoms with

more than one valence electron provide autoionisation states just beyond the ionisation limit; excitation cross-section ~10^{-15} cm^2. Although more attractive than the previous scenario, difficulty is experienced in the ionisation step to ensure resonance with the autoionisation state.

In the second route, three different ionisation methods can be used for excitation to high lying states (also referred to as Rydberg atoms/states). For a Rydberg state the binding energy of an electron is proportional to the inverse square of the principal quantum number n; for $n=20$ it is only 0.0025 eV. Removing the electron is therefore comparatively easily by either collisional, infrared field or electric field ionisation.

In collisional ionisation a variety of mechanisms may be active, depending on the chemical interaction between the excited atom and the carrier gas. However, loss of selectivity rules this method out of contention.

Ionisation by means of an IR laser is also not favoured due to low ionisation cross sections ~10^{-16} cm^2.

In applying an electric field, either pulsed or DC fields may be used. Pulsed fields are only used if DC fields induce line broadening with resultant loss in selectivity. However, higher ionisation yields are obtained with DC

fields since the continuous ionisation of high lying states is guaranteed. The mechanism of electric field ionisation remains the same for the two options.

An electric field distorts the classical potential well that houses the valence electron to be removed. The magnitude of the electric field is critical; at some critical field value it is possible to excite a specific Rydberg state to an autoionisation state with a high decay rate to the continuum (also referred to as forced-autoionisation). Too large a field will push the Rydberg state directly into the continuum with a low ionisation cross section, whilst, too low a field would leave the electron with a large potential barrier separating it from the continuum. Ionisation cross sections of $5x10^{-13}$ cm^2 have been reported (Letokhov, 1987).

3.4.2. Photoionisation routes for Lithium

Many different transitions for lithium exist between the ground state and high lying Rydberg states. However, the availability of lasers with outputs in the range 550nm to 1μm, high isotopic selectivity and high ionisation efficiency, has limited the choice of transitions routes.

As mentioned before, the ground state is $2s^2S$. The $2p^2P^0$ level is 1.848 eV above the ground level. This level can be reached with a laser output of 670.8nm. Furthermore, a negligible thermal population of this level is

observed, even at 700 ^{0}C. Being the first transitional level above the ground state would therefore imply that all atoms are in the ground state and accessible to laser excitation:

$$2s^2S \xrightarrow{670nm} 2p^2P^0 \quad (3.3)$$

This transition has a lifetime of ~27ns. This implies an enormous absorption cross section (~5x10^{-12} cm^2) with a very small saturation intensity of only 10W/cm^2. The isotopic selectivity of this transition yields isotope shift of 15pm between ^{6}Li and ^{7}Li. Being still 3.544 eV from the ionisation limit, two further photons are needed.

The next level reachable with a 610.4nm laser is 3d^{2}D. Its lifetime is 14ns with an even higher absorption cross section of ~10^{-11} cm^2. The isotopic selectivity of this transition is much smaller than that of the first transition, less than 1pm.

From the previous section it is obvious that the third transition should be to a high lying Rydberg state (n=10-15) with subsequent electric field ionisation. The 3d^{2}D level is still 1.513 eV from the continuum, needing a laser of wavelength 820nm to bridge the gap. The Rydberg states with n=10-15 are situated 0.0604 - 0.136 eV below the ionisation level, requiring the third step laser to be tunable between 854 and 900nm.

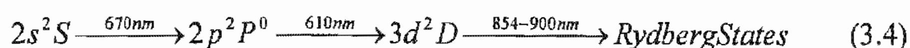

$$2s^2S \xrightarrow{670nm} 2p^2P^0 \xrightarrow{610nm} 3d^2D \xrightarrow{854-900nm} RydbergStates \quad (3.4)$$

3.4.3. Lithium Vaporisation

The separator system serves a three-fold purpose of generating an atomic lithium beam, providing the laser irradiation zone, and collecting the enriched and depleted products. The system is operated at a vacuum of 10^{-6} to 10^{-7} mbar so that the mean-free path will allow straight travelling of the lithium atoms.

Lithium metal is vaporised in a thermally heated crucible inside the separator. The metal melts at 180 °C. Fig 3.1 shows the equilibrium vapour pressure of lithium as a function of temperature. The pressure-temperature domain to the left of the curve is associated with the liquid phase, whilst that to the right indicates the vapour phase.

At the working point of 700 °C the atomic vapour leaves the crucible in all possible directions. Optimal laser irradiation and isotope selectivity require a well-defined and collimated atomic beam.

Fig 3.2 shows a side view of the separator system used in this study. Three sets of collimating slits ensured an atomic beam of width 5mm in the irradiation zone.

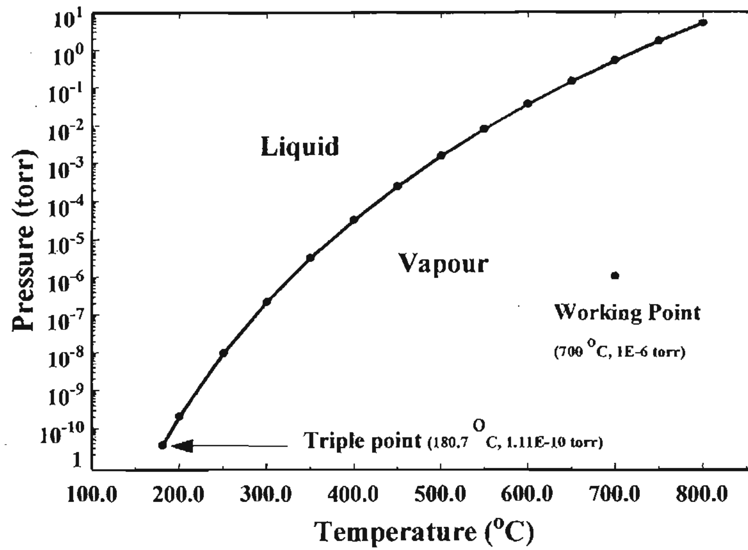

Fig 3.1 Lithium vapour pressure curve. All the AVLIS laser irradiation measurements were done at 700 ^0C, with a vapour pressure of 10^{-6} torr (indicated as the "Working Point").

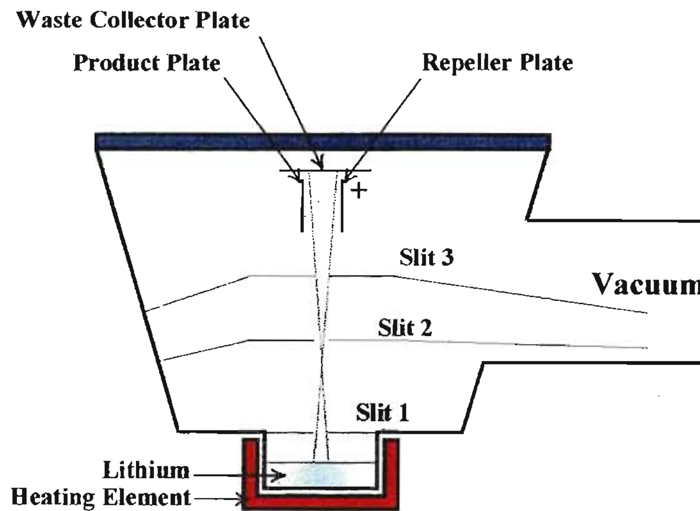

Fig 3.2 A side view of the separator system. The lithium is heated in a crucible to 700 ℃, the vapour expands upwards through a series of slit plates to prevent non-selective pick up on the product collector plate.

The number of lithium atoms contributing to the atomic beam in the irradiation zone is a minuscule fraction of that leaving the crucible. This resulted in a low mass throughput of 3mg/hour. At high crucible temperatures (700 °C) the lithium is in the vapour phase. Assuming thermal equilibrium, the Maxwell velocity distribution applies:

$$G(v)dv = 4\pi v^2 \left(\frac{m}{2\pi kT}\right)^{3/2} e^{-\frac{mv^2}{2kT}} dv \qquad (3.5)$$

where m is the atomic and M the molar mass. The average velocity is given by:

$$\langle v \rangle = \left(\frac{8RT}{\pi M}\right)^{1/2} \qquad (3.6)$$

Accordingly the average velocity of the ^{6}Li and ^{7}Li isotopes at 700 °C is 1853 and 1715m/s, respectively. Not only does the extremely high velocity pose a challenge to the irradiation/monitoring setup, but also does the difference in isotopic velocity add to the complexity of the experiment. To ensure that all atoms will be irradiated, the height of the irradiation volume was taken as the distance that lithium atoms travel at this average velocity during the laser pulse period.

3.4.4. The Laser System

The selective Photoionisation scheme for lithium enrichment, as set out in section 3.3.2 requires three-photon ionisation with wavelengths tunable in the range 600-900nm. With the isotopic shift between ^{6}Li and ^{7}Li of the order of 15pm, the lasers should be tunable in picometer increments to ensure exact resonance with atomic transitions. Furthermore, a narrow line width of less than 15pm is essential to maintain selectivity. Optimal efficiency of the enrichment process demands further that the laser intensity should be sufficient for saturation of each of the transitions; pulsed lasers are therefore required. Organic dye lasers were used. These lasers need to be optically pumped by either copper vapour lasers (CVLs) or excimer lasers. CVL's were used in this study.

3.4.4.1.Copper Vapour Laser (CVL)

The layout of a copper vapour laser is shown in Fig.3.3. Copper metal nuggets are evenly spaced inside an alumina tube, typically 1.5-2 m long and inside tube diameter of 40 mm. This ceramic tube is surrounded by a ceramic fiber insulating material, and fitted inside a Pyrex tube. At both ends the Pyrex tube seals against water-cooled, elongated flanges, allowing evacuation of the laser volume. Electrode gas fittings and laser windows are attached to the ends. Finally a metal water jacket surrounds the laser,

acting as a thermal reference surface and as a coaxial current return for the laser discharge.

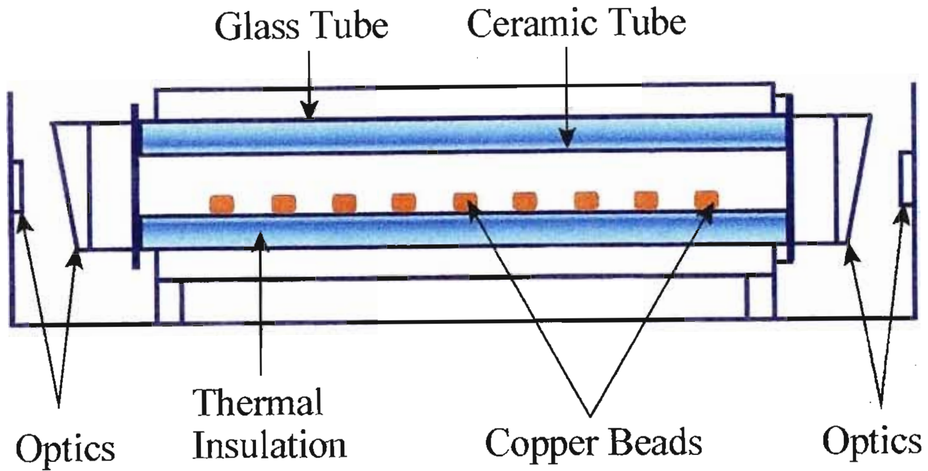

Fig 3.3 Layout of a copper vapour laser head.

The laser tube is filled with 20 Torr Neon buffer gas. A voltage discharge between the two end electrodes heat the copper metal to temperatures of around 1300 °C with subsequent copper vapour densities of ~$5x10^{13}$ cm^{-3}. A power supply capability of 5-8 kW average power at 15kV, with 1kA currents rising in less than 100ns is required.

Laser action takes place in a three level system between the two top most vibrational levels of copper (see Fig 3.4.). There are no states in between and those above the upper laser level are far removed, facilitating effective pumping. The lower laser level is metastable, thereby self-terminating the laser action. Since the upper laser level is also resonant it is preferentially

excited in an electric discharge. Laser action takes place between the doublets $3d^{10}(^1S)4p\ ^2P^0$ and $3d^94s^2\ ^2D$. The transition between the innermost levels is a 578.2nm (yellow) and that between the top and bottom levels in the green at 510.6nm.

Laser mirrors on both sides of the laser tube complete the setup. The optical resonator was either a plane-plane or an unstable cavity. Plane optics consisted of a back mirror coated for maximum reflectance at the laser wavelengths and a common glass flat to the front as an output coupler. It's 8% reflectance is sufficient since the laser is super radiant. Plane optics, however, cause a high divergence in the output beam; ~6mrad for a 40mm tube diameter. A confocal unstable resonator, on the other hand, comprising a small convex high reflectance mirror in front and a normal sized concave mirror at the back, provides less than 1mrad divergence, but at the expense of ~25% loss in output power.

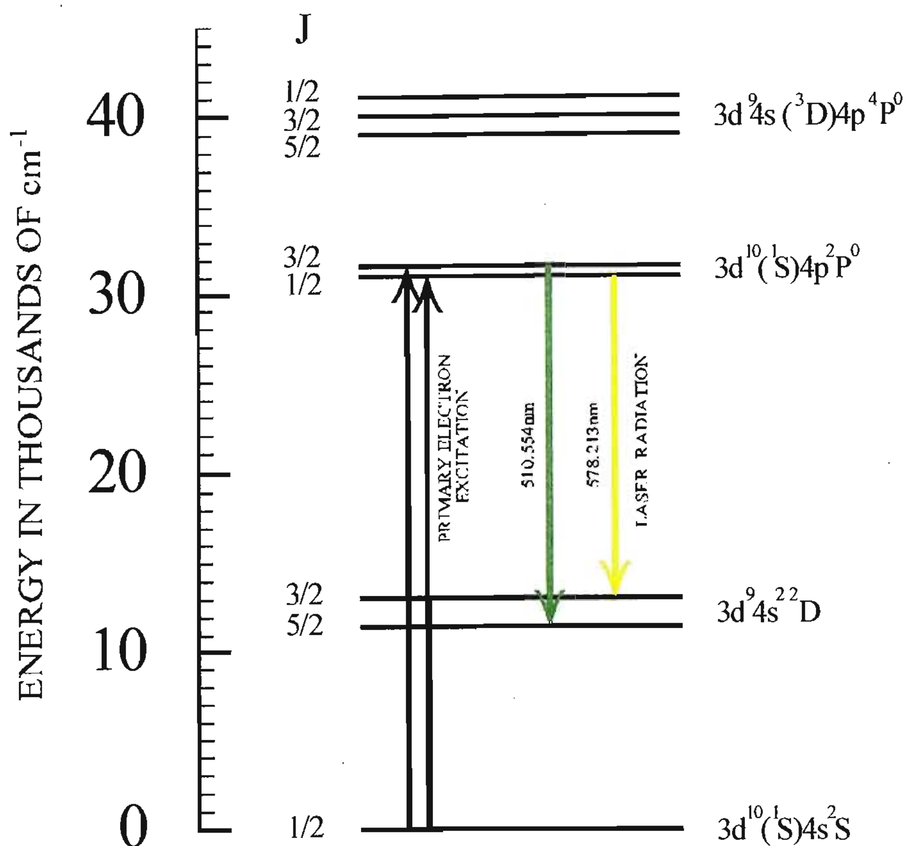

Fig 3.4 The three level laser system of copper.

3.4.4.2.Dye laser

A dye laser derives its capability from its laser medium, a fluorescent organic dye dissolved in a liquid solvent. The dye itself consists of large molecules with multiple ring structures, having complex spectra. Usually there are two major absorption bands, one in the UV and one in the visible. The second partially overlaps the fluorescent band, inside which the laser

gain curve appears. The width of the gain curve (tunable range) is determined by operating conditions; just above the threshold it will be narrow and centred at the peak of the fluorescent band.

Using a number of the dye solutions, output is tunable from the near-UV to the near IR. Tuneable outputs down to 216nm could furthermore be achieved with frequency doubling crystals. The laser is capable of producing very narrow bandwidths and ultrashort pulses, which however, are extremely sensitive to optical alignment of the pump beam and the dye laser cavity.

The dye lasers used in this study are based on the design of Hecht (1986), shown in Fig 3.5. The dye oscillator cavity is formed between the diffraction grating and output mirror. The grating is the wavelength dispersive element that can be aligned so as to reflect a small wavelength range along the laser axis. In this way it serves to both select a certain wavelength and to restrict oscillation to a narrow bandwidth. A stepper motor from the laser's front panel computer control tunes the grating angle. Further reduction of the laser line width can be achieved with an intra-cavity etalon.

Beam expanding optics in the oscillator cavity ensure that the grating area is fully utilised, thereby maximising its resolving power. The dye medium

is a removable flow cuvette with dye reservoir and circulation pump to remove excess heat deposited in the dye solution. A typical energy level diagram of a laser dye is shown in figure 3.6.

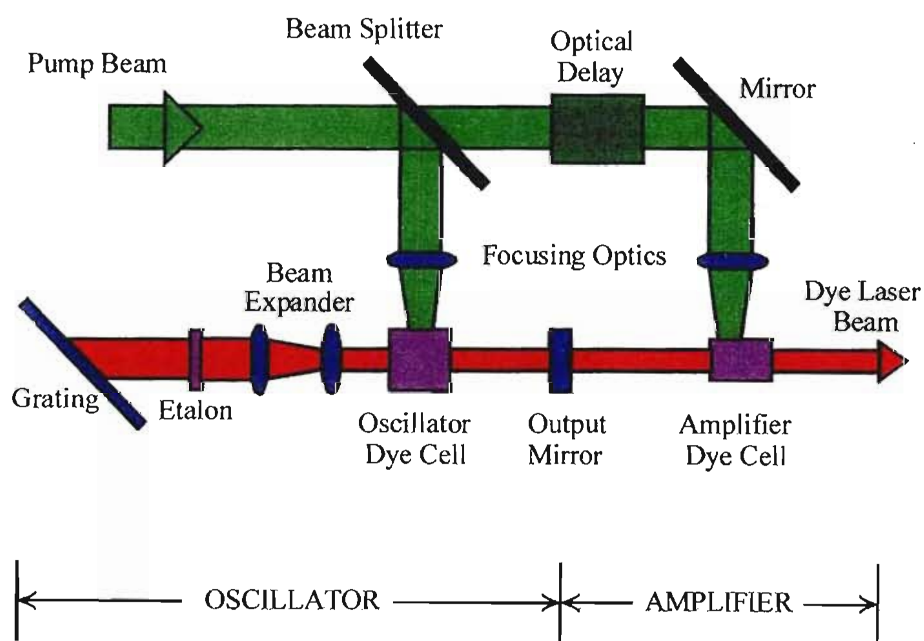

Fig 3.5 Diagram of a pulsed dye laser.

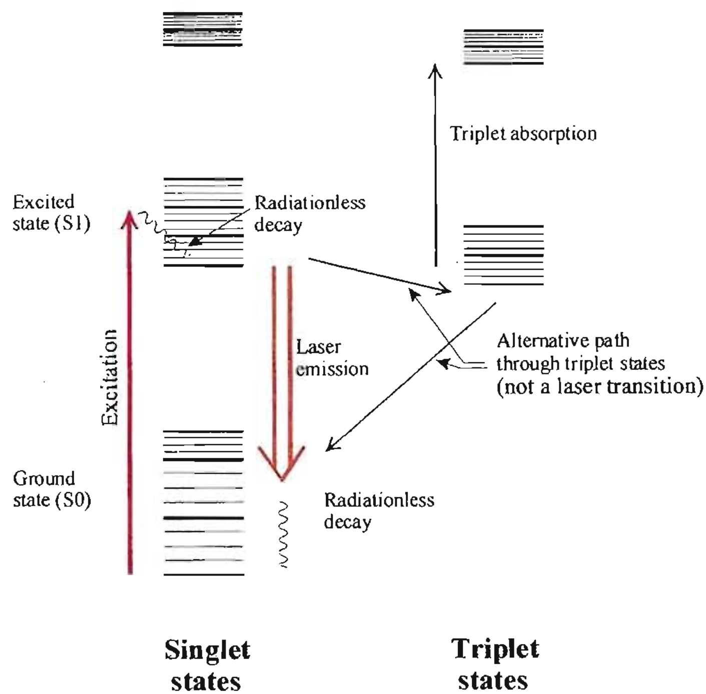

Fig 3.6 Typical energy level diagram of a dye laser.

On the left, three electronic levels are shown, each with a host of vibrational (bold lines) and rotational states (thin lines) superimposed. In the presence of normal line broadening mechanisms, these substrates merge into a continuum. Photons from a pump source are absorbed, causing a transition from the bottom of the lower band anywhere into the upper bands. Transitions to the highest band are responsible for UV absorption, whereas the middle one causes the absorption feature adjacent to the spontaneous emission curve shown in Fig 3.7.

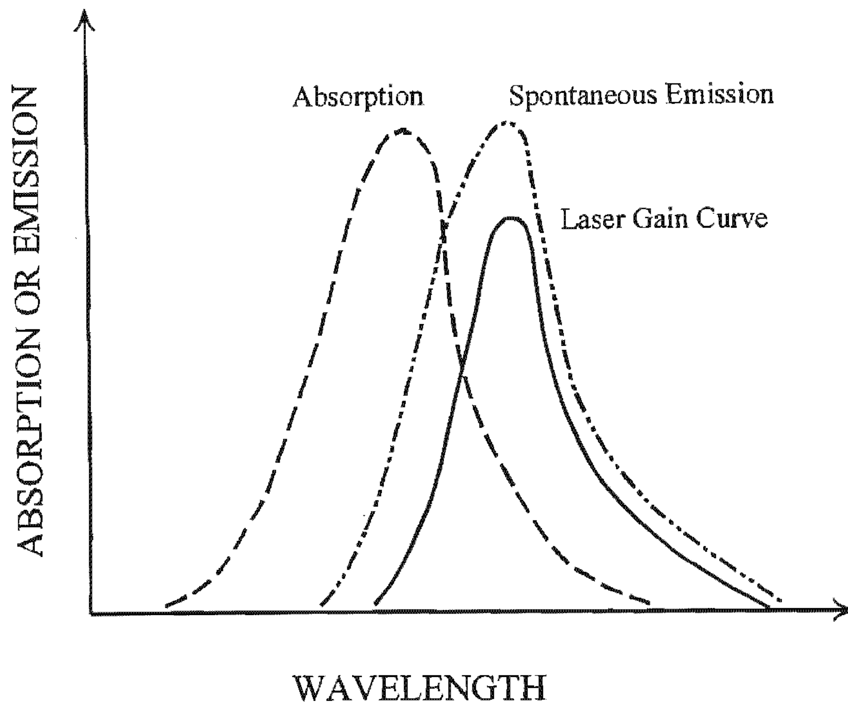

Fig 3.7 The spectral characteristics of a dye laser.

Excitation is followed by non-radiative decay to the bottom of the middle band, which acts as the upper laser level. It has a lifetime of a few nanoseconds, after which a transition into the bottom band takes place. The wide choice of lower laser levels is the origin of the broad laser gain curve. Transitions to the middle of the lower band are favoured, as can be seen in the shape of the spontaneous emission curve. The cavity design limits the reflection of only a particular wavelength through the dye cuvette. Back and forth reflections would therefore amplify the output intensity through spontaneous emission.

3.4.4.3.Integrated Laser System

The layout of CVL's, dye lasers and separator is shown in figure 3.8. The laser path starts at the centre 25W CVL oscillator, which generates a high quality beam. The beam is amplified with a 40W CVL amplifier after which the beam is split with a partial reflector. Two 40W CVL amplifiers again amplify both beams respectively. The beam on the left acts as an optical pump for λ_3 dye emitting ~820nm, whilst the beam on the right is separated on a dichroic beam splitter into its green (510.6nm) and yellow (578.2nm) components. These two beams on their own optically pump the dye lasers delivering λ_1 (670nm) and λ_2 (610nm). λ_1 and λ_2 are combined and focussed into the separator. The path lengths of the three dye laser pulses are virtually equal and therefore overlap in the separator at the same moment in time.

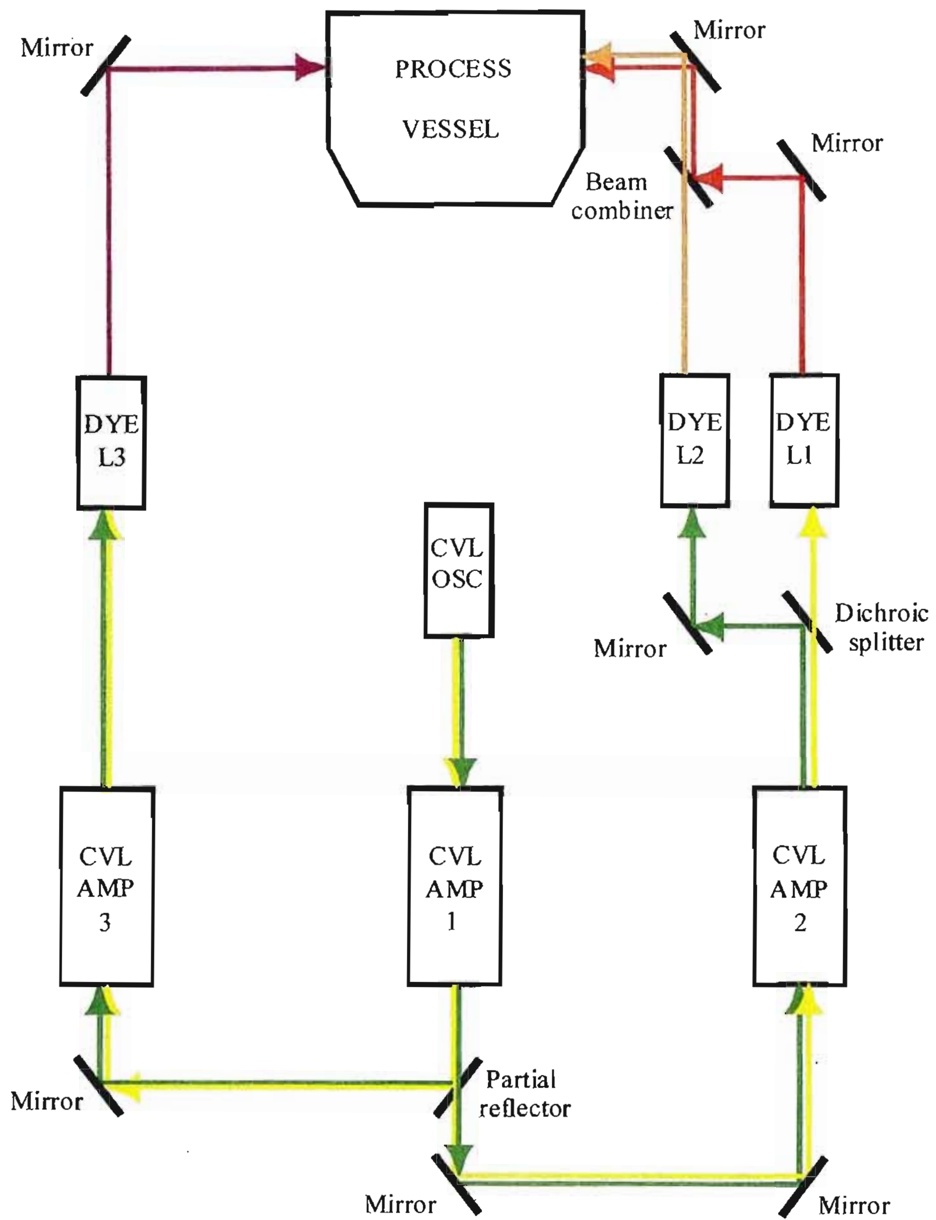

Fig 3.8 Layout of integrated laser system.

3.4.5. The Separator System

After ionisation the ions of the selected lithium isotope are separated from the neutral particles by applying both a pulsed electric field and a continuous magnetic field generating magneto-hydrodynamic cross-field forces on the electrons and ions. The divergent ion orbits caused by crossed-field acceleration make it possible to collect the ions separately from the other components of the vapour stream.

In order to determine and optimise enrichment efficiencies, samples of the collected product are mass analysed. These measured enrichments (given as an enrichment factor, α) are a convolution of the laser-selected ionisation and the non-selective deposition of non-radiated lithium vapour on the collection plates. In the event of the latter contribution being dominant, a low α would obscure possible high laser selectivity. Furthermore, it is a time consuming exercise of irradiation, sample collection and mass analysis.

The introduction of an on-line time-of-flight mass spectrometer provided instant shot-for-shot information on the ion formation and isotope selectivity. Laser alignment, wavelength tuning and synchronisation could be optimised using the TOF output. Once optimised, irradiation for product collection could begin and be monitored with the TOF.

3.4.5.1.Time-of-Flight Mass Spectrometer

A linear in-situ time-of-flight mass spectrometer was used. The TOF utilises a double acceleration plate system of the Wiley-McLaren type. The pulsed laser irradiation used for the selective ionisation of either one of the lithium isotopes, initiates the start of each TOF spectrum to be recorded. The process vessel, housing the lithium crucible/evaporator, electrostatic extraction plates, and the TOF mass spectrometer, is shown in Fig 3.9.

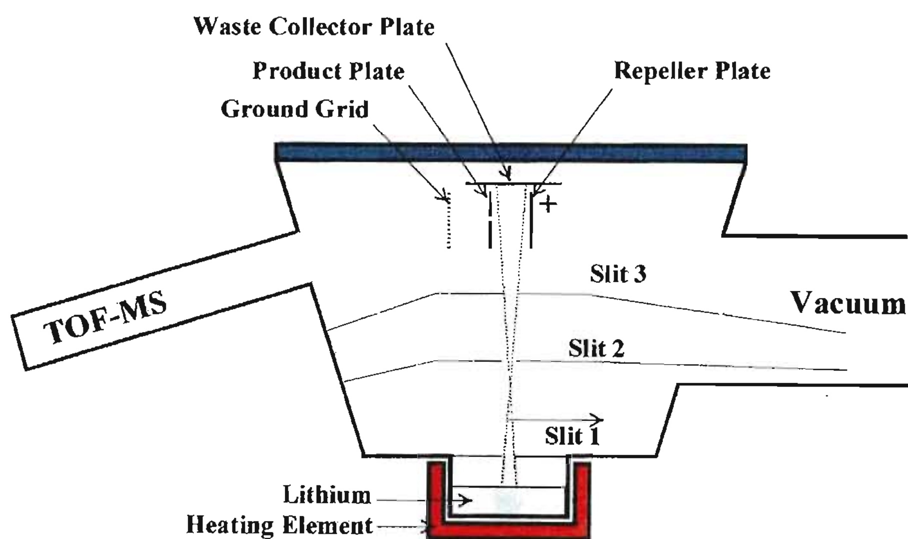

Fig 3.9 End view of the process vessel shows the TOF-MS.

The atomised lithium beam expands upwards through a series of collimating slits into the interaction zone. The interaction zone lies between a set of electrostatic extraction plates of different potential, 22mm apart. The negative plate collects all the selectively ionised lithium isotopes of positive charge. This forms the first region of the dual accelerating TOF mass spectrometer. The ions exit the product plate through a small hole, 2mm in diameter, into the second stage of the dual accelerating source, also 22mm long, into the field-free flight pipe, with total flight length of 456mm. Ion detection is done with a chevron microchannel plate detector.

Typical electrical fields of 1200V/cm and 500V/cm were used for the first and second extraction regions, respectively. With these values flight times of t_6 = 4.40μs and t_7 = 4.85μs were measured. The time difference is 450ns. Fig 3.10 shows a typical time-of-flight mass spectrum obtained during laser irradiation of natural lithium. Clearly the $^6Li/^7Li$ ratio is not that of the natural isotopic abundance of the starting material – indicating selective ionisation/separation of the ^{6}Li isotope.

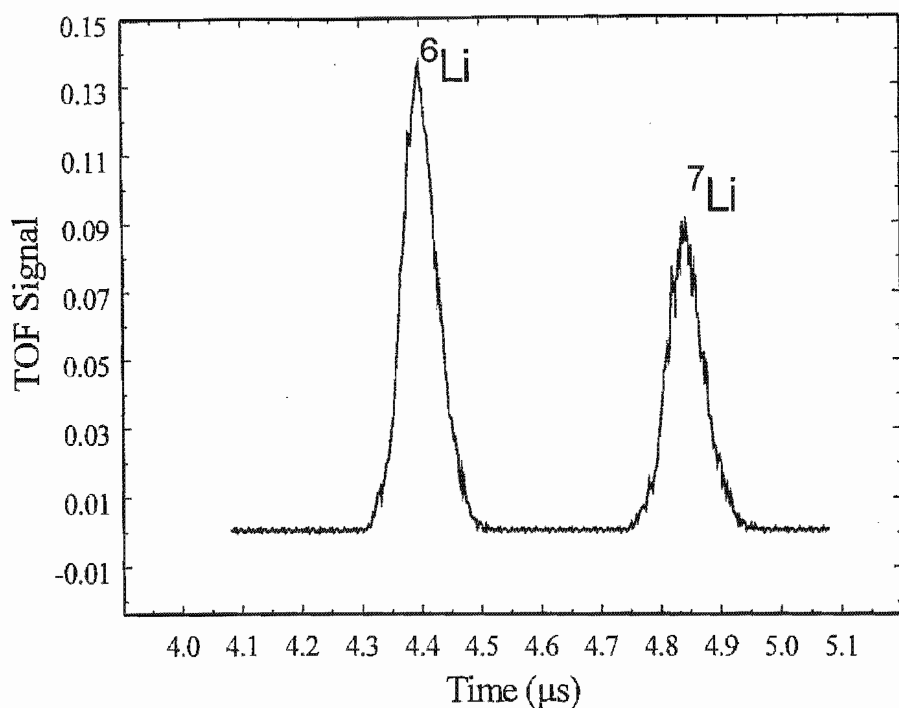

Fig 3.10A typical time-of-flight mass spectrum of lithium acquired during laser irradiation experiments.

Fig 3.11 shows a sequence of measured spectra. This is the result of a two-colour experiment, where the first wavelength was set at 610.82nm. The second wavelength was scanned from 670.84nm downwards. Fig 3.11a contains signals of both isotopes with that of ^{6}Li very prominent, with an associated alpha of 112. Fig 3.11b shows an increase in the ^{7}Li signal as the λ_2 wavelength is decreased, resulting alpha is 76.2. Continuing decrease in λ_2 wavelength shows the steady increase in the ^{7}Li isotope, until eventually no ^{6}Li is visible – Fig 3.11f. In this case the enrichment alpha is 108.

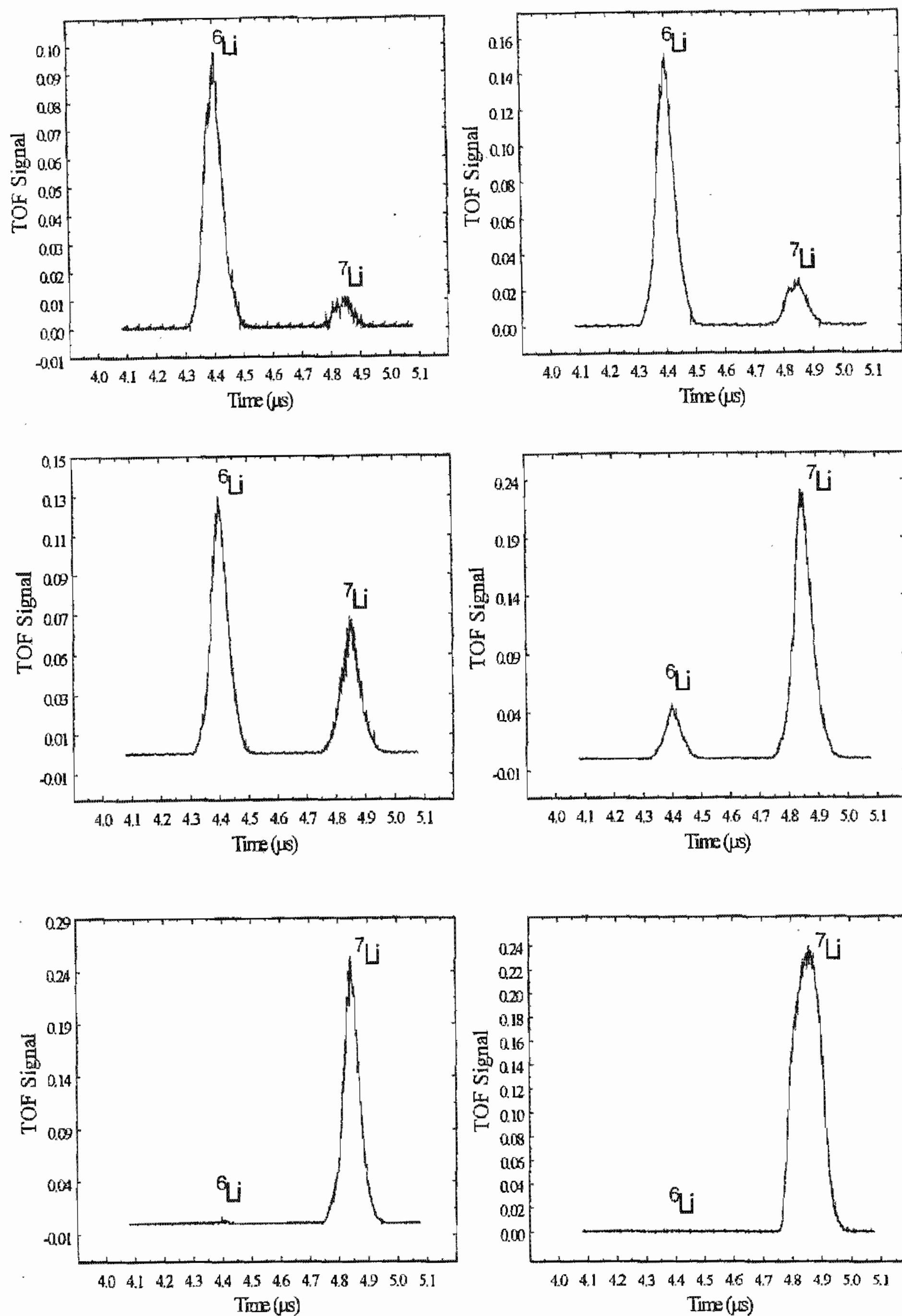

Fig 3.11 In-line TOF measured alpha's for different two-colour selective irradiation measurements. The measured enrichment alpha's varied from 112, 76.2, 24.3, to 2.4 for ^{6}Li, to 59 and 108 on ^{7}Li, shown in (a) – (f), respectively.

The maximum selectivity for ^{7}Li was found at 670.780nm. In this case the peak for ^{6}Li cannot be seen. From the TOF-MS spectra the enrichment factor can be calculated, by using the simple equation:

$$\alpha = \frac{\left|{}^7Li/{}^6Li\right|_{PRODUCT}}{\left|{}^7Li/{}^6Li\right|_{FEED}} \tag{3.7}$$

where either the ratio of the peak intensities or the peak areas in the TOF spectra can be used. Table 3.1 summarises the calculated α-values, reported in Fig 3.11.

Wavelengths (nm)	Alpha(7)	Alpha(6)
(670.840, 610.380)	0.009	112.00
(670.811, 610.380)	0.014	72.50
(670.813, 610.380)	0.041	24.30
(670.800, 610.380)	0.417	2.40
(670.812, 610.380)	59.00	0.017
(670.780, 610.380)	108.00	0.009

Table 3.1 Summary of TOF-MS measured α-values for different irradiation wavelengths.

The values in Table 3.1 show that enrichment alphas in excess of a 100 could be obtained on either the 6 or the 7 isotope. The in-line TOF-MS could easily measure differences in enrichment as a function of the laser wavelength.

The next step was to correlate the enrichment of the collected product with that of the in-line TOF-MS. For this purpose product collector plates (thin aluminium sheets) were attached on the collector plate adjacent to the hole to the TOF mass spectrometer. These product plates were removed, and analysed with a secondary ion mass spectrometer.

The SIMS analyses were done on the VG SIMS/ESCALAB II, described in Chapter 2. The option of either the Ga liquid metal ion source or the O/Ar duoplasmatron ion source had to be considered. Using the modified Sigmund's formula, described in Chapter 2, the product of the sputtering yield and surface binding energy is given in Fig 3.12 for Ga, O and Ar primary ions.

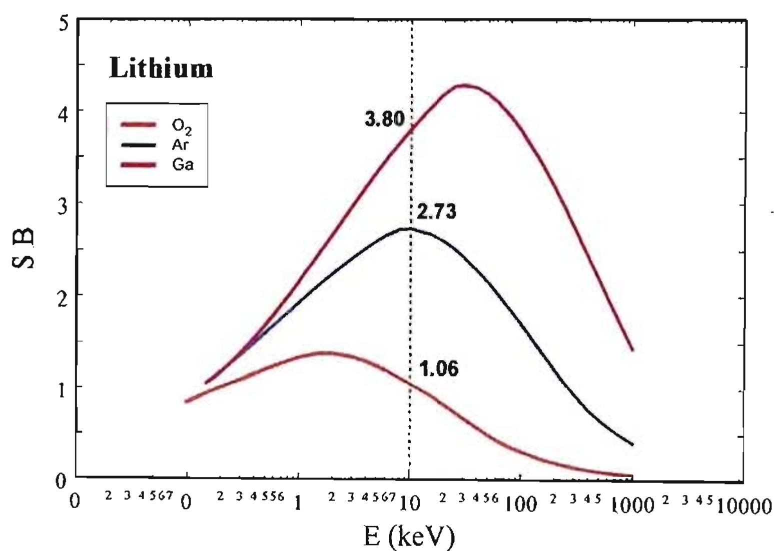

Fig 3.12 Calculated sputtering yields for Li using Ga, Ar or O primary ions. The values at 10keV are 3.8, 2.73 and 1.06 respectively.

Both ion sources were operated at 10keV, the calculated *SB*-values for Ga, Ar and O are 3.8, 2.73 and 1.06, respectively. However, the angle of incidence with respect to the sample normal was 45^0 and 70^0 for the Ga and Ar and O ion sources, respectively. Using the angle dependence relationship given by equation (2.13) in Chapter II, the calculated SB-values for Ga, Ar and O are 1.3, 1.28 and 0.5, respectively. The enthalpy of sublimation at room temperature for lithium is 1.65eV/atom, resulting in sputtering yields of 0.79, 0.77 and 0.30 atoms/incident ion, respectively. Ga and Ar have the highest sputtering yields. Ga was selected because the source could operate stable at less than a tenth of the beam current of the duoplasmatron source. Furthermore, the superior beam quality of the Ga liquid metal ion source allowed area selection on the samples.

Equation (2.15) was used to estimate the sputtering rate:

$$\dot{z}[\mu m/h] = 3.755\times10^{-4}\frac{M[amu]}{\rho[g/cm^3]j[\mu A/cm^2]S}$$

For values of $\rho = 0.534 g/cm^3$;

$j = 2x10^{-3}\mu A/3x10^{-4}cm^2 = 6.67\mu A/cm^2$; and

$S(45^0) = 0.79$atoms/incident ion,

the sputtering rate is estimated at :

$$\dot{z}[\mu m/h] = 3.755\times10^{-4}\frac{6.92}{0.534\times6.67\times0.79} = 9.29\times10^{-4}$$

$$\therefore \dot{z} = 5.54 \times 10^{-2} \mu m / \min = 3.32 \mu m / s$$

The estimated sputtering rate is 3.32μm per second. To acquire a SIMS spectrum from mass 1 to 10 the quadrupole is typically scanned in mass steps of 0.05 amu, counting secondary ions for 200ms per step. This implies a total scanned time of 36 seconds per spectrum. The material consumption per single scanned spectrum is therefore 120μm. Alternatively, there is only ~290 seconds available to acquire ~8 consecutive spectra before 1mm thick lithium material is removed!

In the first AVLIS experiment, lithium was evaporated without any laser irradiation. The vapour was allowed to deposit on SIMS sample plates. Fig 3.13 shows a typical SIMS spectra obtained from these plates. The ^{7}Li / ^{6}Li ratio measured with the SIMS agrees with the 92.48/7.52 ratio of the feeding material to within 2% accuracy. The SIMS sputter rate that was selected was slow enough to allow for the collection of spectra, before all of the sample material was consumed. Furthermore, it is clear that the mass resolution of the quadrupole mass spectrometer is more than ample to resolve the ^{6}Li and ^{7}Li peaks.

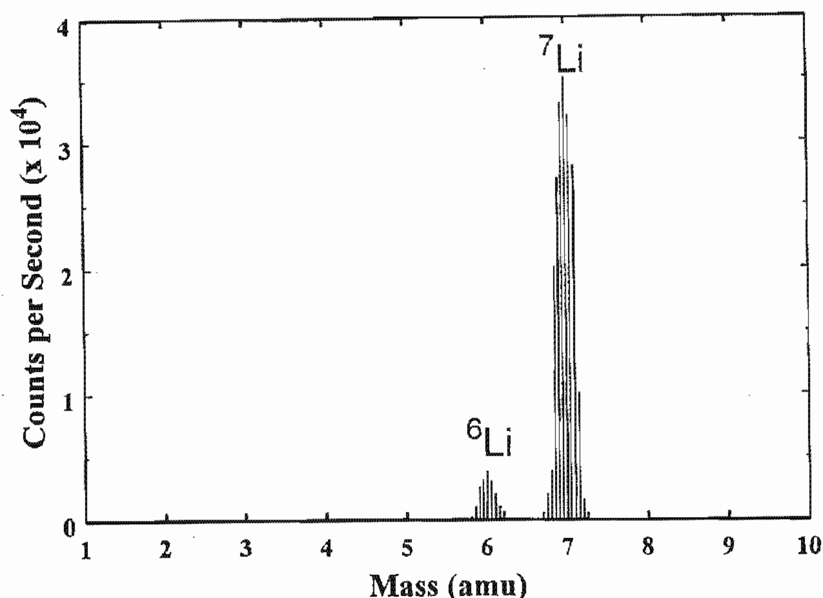

Fig 3.12 A typical SIMS spectrum of deposited lithium of natural isotopic abundance.

Fig 3.13 shows a spectrum obtained from collected material where the selective laser irradiation was used. During the collection of the product, the in-line TOF-MS measured an alpha(^{6}Li) of higher than 50. This does not compare well to the SIMS measured alpha of ~4. One of the more difficult problems to overcome in the AVLIS of lithium was the non-selective pickup of non-radiated vapour that deposited on the collector plates. If the amount of enriched product were small compared to the non-selective pickup, no matter how high the spectroscopic selectivity, the average enrichment of the product would be low. This problem was minimised by the introduction of a series of shutters and skimmer slits to prevent reflections and back streaming of non-selective material. With this

in place correlation between in-line spectroscopic enrichment factors (measured with TOF-MS) and enrichment factors of collected product (measured with SIMS) was better than 80%.

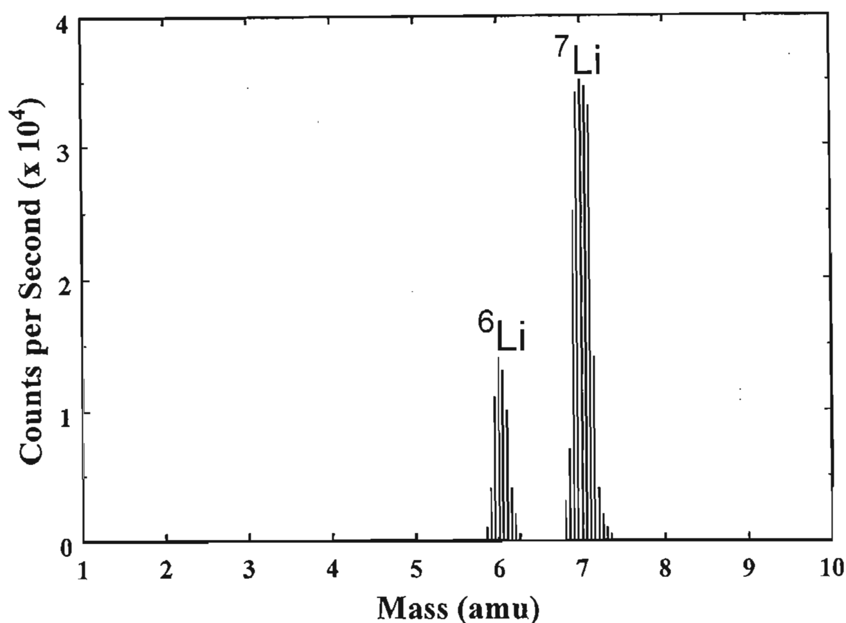

Fig 3.13A SIMS spectra of enriched lithium product.

3.5. Conclusion

A time-of-flight mass spectrometer was successfully developed to measure in-line the relative abundance of the lithium 6 and 7 isotopes on a shot-to-shot basis. With this in-line diagnostic tool, it was possible to optimise the irradiation parameters, viz. wavelength, fluence, delays and irradiation

geometry to yield the maximum TOF signal strength on the required isotope at the highest possible selectivity.

Collected AVLIS products for different irradiation experiments were characterised with secondary ion mass spectrometry for isotopic abundance. Poor correlation with the in-line TOF-MS measurements was initially obtained. This was due to a non-selective pickup of non-irradiated lithium vapour that deposited on the product plates. This problem was solved after the introduction of a number of shutters and beam slits to prevent direct deposition, as well as back streaming on the product plates. With this in place correlation between in-line spectroscopic enrichment factors (measured with TOF-MS) and enrichment factors of collected product (measured with SIMS) was better than 80%.

Chapter 4

MLIS of UF_6

4.1 Introduction

Molecular Laser Isotope Separation (MLIS) of uranium is based on multi-photon isotope selective excitation of UF_6 vibrational levels by resonant IR lasers, followed by subsequent dissociation by further non-resonant IR irradiation. The dissociated UF_5 product has an extremely low vapour pressure and precipitates from the process gas mixture in the form of solid dust.

The methods of choice for measuring the isotopic abundance of uranium compounds are glow discharge mass spectrometry (GDMS), spark source mass spectrometry (SSMS) and/or thermal ionisation mass spectrometry (TIMS).

An in-line time-of-flight mass spectrometer (TOF-MS) was developed to optimise irradiation parameters with regards to high isotopic selectivity and acceptable cut quantity (Scales, Human and Rohwer, 1991). TOFMS has a high transmission capability and high sensitivity for single event monitoring, ideally suited for pulsed IR radiation of UF_6. Since the

ionisation region is not confined by the presence of electric or magnetic sectors, the instrument can easily be interfaced to a whole range of analytical facilities. From this established technology base, commercial instruments for analysis of solids and biopolymers have now become available. These successes stimulated the investigation of the solid UF_5 product with LD-TOFMS when GDMS and SSMS failed to measure small sample quantities (nanogram quantities deposited in thin films). SIMS analysis, known for mass analysis of surfaces and near-surfaces, were carried out to cross check LD-TOFMS measurements.

This chapter reports on the characterisation of enriched solid uranium fluorides by laser desorption time-of-flight mass spectrometry (LD-TOFMS), secondary ion mass spectrometry (SIMS), and time-of-flight secondary ion mass spectrometry (TOF-SIMS).

4.2. Molecular Laser Isotope Separation

Since the advent of lasers they have been proposed as tools to induce or catalyse chemical reactions. Of all the reactions investigated, laser isotope separation on the one hand has received the most interest, and on the other hand has shown the most promise.

Most elements in nature have more than one isotope. To increase the concentration of a particular isotope, the isotopes have to be sorted according to some difference in their chemical or physical properties. In cases where the electronic and therefore the chemical properties of the isotopes are of close identity, then chemical processing is difficult and inefficient. Conventional methods of separating isotopes of elements rely instead on physical processes that are affected by the small difference in the masses of the different isotopes.

The gaseous diffusion method of passing the element in a gaseous form through a series of chambers separated by porous barriers. The lighter molecules diffuse through the barrier slightly faster. So in each successive chamber the concentration of the lighter isotope relative to that of heavier isotope increases slightly. Several hundreds to thousand of these chambers are needed to increase the concentration of the lighter isotope substantially. Gaseous diffusion thus requires large and expensive facilities that consume large amounts of electricity.

Other separation techniques based on mass differences include the gas centrifuge, multiple distillation, and electromagnetic separation. Of these, the centrifuge has been utilised as an alternative to gaseous diffusion.

More economical is a separation process driven by lasers. Atoms or molecules containing different isotopes have slightly different energy levels, thus having slightly different absorption spectra. Consequently, radiation of a particular frequency can selectively excite an atom or molecule containing one isotope to a higher energy level and leave other isotopic species undisturbed. These selectively excited species can then be separated from the others by conventional physical or chemical methods.

Atomic Vapour Laser Isotope Separation (AVLIS), as seen in the previous chapter uses selective photoionisation to separate isotopes of elements in an atomic beam. Molecular Laser Isotope Separation (MLIS), on the other hand, uses selective photodissociation of molecules into stable fragments.

4.3. MLIS of UF_6

UF_6 plus a carrier gas is flow-cooled via adiabatic expansion through a narrow slit [Thiart et al, (1993)]. At 100 Kelvin approximately 30% of the ground state is populated, where isotope differences in absorption spectra can be used for selective excitation of the ^{235}U isotope containing UF_6 molecules. $^{235}UF_6$ is selectively excited by tunable 16μm laser energy obtained from a Raman shifted CO_2 laser (see Kemp et al, 1990).

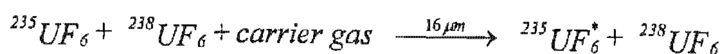

$$^{235}UF_6 + {}^{238}UF_6 + carrier\ gas \xrightarrow{16\mu m} {}^{235}UF_6^* + {}^{238}UF_6$$

The excited species is further excited by a second 16μm laser and finally dissociated by either a 10.6μm CO_2 or a third 16μm laser

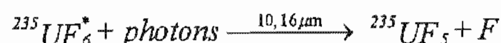

$$^{235}UF_6^* + photons \xrightarrow{10,16\mu m} {}^{235}UF_5 + F$$

The $^{235}UF_5$ molecules coalesce to form particulates that are easily separated from the remaining gas. A suitable scavenger can be used to remove the fluorine radical. The first step in this process, selective excitation by infrared lasers, is the most critical and difficult to achieve. The reasons are twofold. No laser is available at the frequencies of the UF_6 vibrational transitions. The strongest absorption on UF_6 corresponds to the ν_3 transitions around 16μm. The second set of problems arises from the fact that uranium is a heavy element, for which the isotopic shift of the ν_3 vibrational mode of UF_6 is much less than $1cm^{-1}$ compared to $17cm^{-1}$ for the much lighter SF_6 molecules. Power broadening becomes a problem. Furthermore, most of the UF_6 molecules are not in the ground vibrational state, but are distributed among thousands of vibrational states.

The vibrational cooling of the UF_6 molecules is essential for selective photodissociation.

4.3.1. UF_6 Flow Cooling

Expansion supercooling in a nozzle is an efficient and practical means of cooling the UF_6 molecules. Static cooling was impossible because the low

vapour pressure of solid UF_6 would provide too few molecules in the gas phase. The major concern of expansion supercooling is whether the gas emerging from the cooling nozzle remains in the gas phase long enough for the lasers to act on single molecules. After expansion the gas is in a non-equilibrium state of supersaturation and has a strong tendency to condense within the flow. At a given temperature the major factor controlling condensation is the UF_6 number density in the flow-cooled region.

The ratio of final to initial temperature during supersonic expansion is given by:

$$\frac{T_{FINAL}}{T_{INITIAL}} = \left(\frac{P}{P_0}\right)^{\frac{\gamma-1}{\gamma}} \quad (4.1)$$

where P and P_0 are the final and initial pressures; and $\gamma = C_P/C_V$ is the ratio of the specific heats at constant pressure and constant volume. For γ close to unity, as is the case for UF_6, the initial pressure and/or the nozzle area expansion ratios must be very large to achieve substantial cooling. To circumvent this constraint, small amounts of UF_6 are mixed with a carrier gas consisting of atoms or small molecules with larger γ.

Under these conditions substantial gas cooling can be achieved with only modest initial pressure and nozzle area expansion ratios. The carrier gas also provides a collisional environment that ensures continuum fluid flow

and thermal equilibrium among the vibrational, rotational and translational degrees of freedom of the UF_6 before irradiation.

In the present study Laval flow cooling nozzles were used [see Thiart et al, (1993) for detail description].

4.3.2. Selective Photodissociation of UF_6

After expansion cooling through the nozzle, the cooled gas is irradiated by a sequence of infrared laser pulses. The first selective laser frequency is tuned near the resonant frequency of the $^{235}UF_6$ Q branch. The second laser frequency is red-shifted from the first frequency to achieve further excitation of the selected molecules, and still maintaining the selectivity. The third laser frequency is tuned far to the red to achieve maximum excitation/dissociation of the already excited molecules.

4.3.3. The Laser System

In this study a 3xIR selective multiphoton dissociation scheme was used. It consisted of:

λ_1: Lambda 1, a 3bar isotope CO_2 laser, continuously tunable and used for the selective excitation of the ν_3 fundamental mode of

either the $^{235}UF_6$ or the $^{238}UF_6$ molecules. The required output was between the 10R30 and 10R32 lines. This output had to be converted to 16μm by means of Raman conversion.

λ_2: Lambda 2, a TEA CO_2 laser producing a single longitudinal mode through injection mode locking, and amplified by 2-3 CO_2 amplifiers to more than 1.5J/pulse. This line tunable system is red-shifted from the λ_1 wavelength for further vibrational excitation of the λ_1-selected species. The lines used varied from the 10R14 to the 10R26, and again had to be converted to 16μm.

λ_3: Lambda 3, also a TEA CO_2 laser, tuned to the 9R28 line, responsible for the efficient multiphoton dissociation of the (λ_1, λ_2)-selected species. Alternatively, the same line tunable system was used, tuned to the P8 – P20 lines, converted to 16μm for an all 16μm irradiation scheme.

16μm: Raman conversion of the 10μm outputs was done in a Herriot type multipass cell, filled with para-H_2 and cooled to liquid N_2 temperature. The incoming 10μm radiation is converted to 16μm through Stimulated Raman Scattering (SRS).

4.3.3.1. Carbon Dioxide Laser (CO_2)

The carbon dioxide (CO_2) laser is a gas laser, able to operate in either pulsed or continuous mode. The CO_2 laser operates on a set of vibrational-rotational transitions. The CO_2 laser lines are emitted during transitions among three vibrational modes. The laser transitions occur when excited CO_2 molecules drop from the higher-energy asymmetric stretching mode, ν_3 to the lower–energy symmetric stretching or bending modes, ν_1. This transition corresponds to a 10.5μm photon. Relaxation to the bending mode, ν_3, corresponds to a 9.6μm photon. However, the laser does not emit those precise wavelengths because the molecule changes its rotational state when it changes its vibrational state. The rotational energy is smaller than both thermal energy and vibrational transition energy, so the change can be either up or down. Because of this phenomenon, CO_2 lasers can emit a series of closely spaced wavelengths.

Transversely Excited Atmospheric-pressure (TEA) CO_2 lasers operate at atmospheric pressure, with a pulsed electric discharge that is transverse to the laser axis. To select a specific CO_2 wavelength, an optical grating is used to select the oscillation of only that specific line from the entire range of possible transitions. At atmospheric pressures the selection can be made from many discrete lines. However, as the pressure increases, the individual lines broaden. Above 3 atmospheres the separated rotational

lines start blending together to yield some output between the discrete lines. Above 8 atmospheres a continuous spectrum throughout the CO_2 laser's operating range, is obtained.

The frequency range of a CO_2 laser can be extended from 8.9μm to 12.3μm by using isotopic mixtures of ^{12}C, ^{13}C, ^{16}O, and ^{18}O. In this study an isotopic mixture of $^{12}C^{16}O_2$, $^{12}C^{18}O_2$ and $^{12}C^{16}O^{18}O$ is used in the λ_l high-pressure (3-atmosphere) CO_2 laser system (Botha et al, 1991 & 1994).

4.3.3.2. Raman Conversion

The CO_2 laser systems provide 10μm laser pulses, which were converted to 16μm through stimulated Raman scattering (SRS) in a para-H_2 medium. SRS is a process in which a laser beam, called the pump, generates optical gain collinear with the beam. This can be in a down shifted frequency, called the Stokes frequency, or in an up shifted frequency called the anti-Stokes frequency. The frequency shift is equal to an energy level transition frequency of the Raman medium. The Stokes signals are usually generated from amplified blackbody and/or spontaneous Raman emission noise. Since the noise signal is quite small, large gains are required to generate useful signals.

In H_2, two rotational frequency shifts are available, the 354cm^{-1} S(0) transition in para-H_2 and the 586cm^{-1} S(1) transition in ortho-H_2. The first transition converts 10μm radiation to 16μm, whilst the second converts it to 24μm.

4.3.3.3. Integrated Laser System

The integrated laser system used in this study is shown in Fig 4.1. Both options for the 2x16μm + 1x10μm and the 3x16μm-irradiation schemes are shown. L3 refers to the 9R28 wavelength, whilst L3* refers to the third 16μm wavelength.

For stimulated Raman conversion, a certain minimum input energy (referred to as "the Raman threshold") is needed before this non-linear optical process can be observed. The output from the λ_1 laser system was not enough to overcome the Raman threshold on its own. For this reason a Four-Wave-Mixing process (FWM) was used whereby λ_1 and λ_2 or λ_1, λ_2 and λ_3 were combined on a 100 lines/mm grating and after circularly polarising with a Fresnel Rhomb, fed through the Raman cell. The output 16μm pulses were separated with a 90 lines/mm grating (blazed for 16μm) and then transported to the contact cell for irradiation experiments.

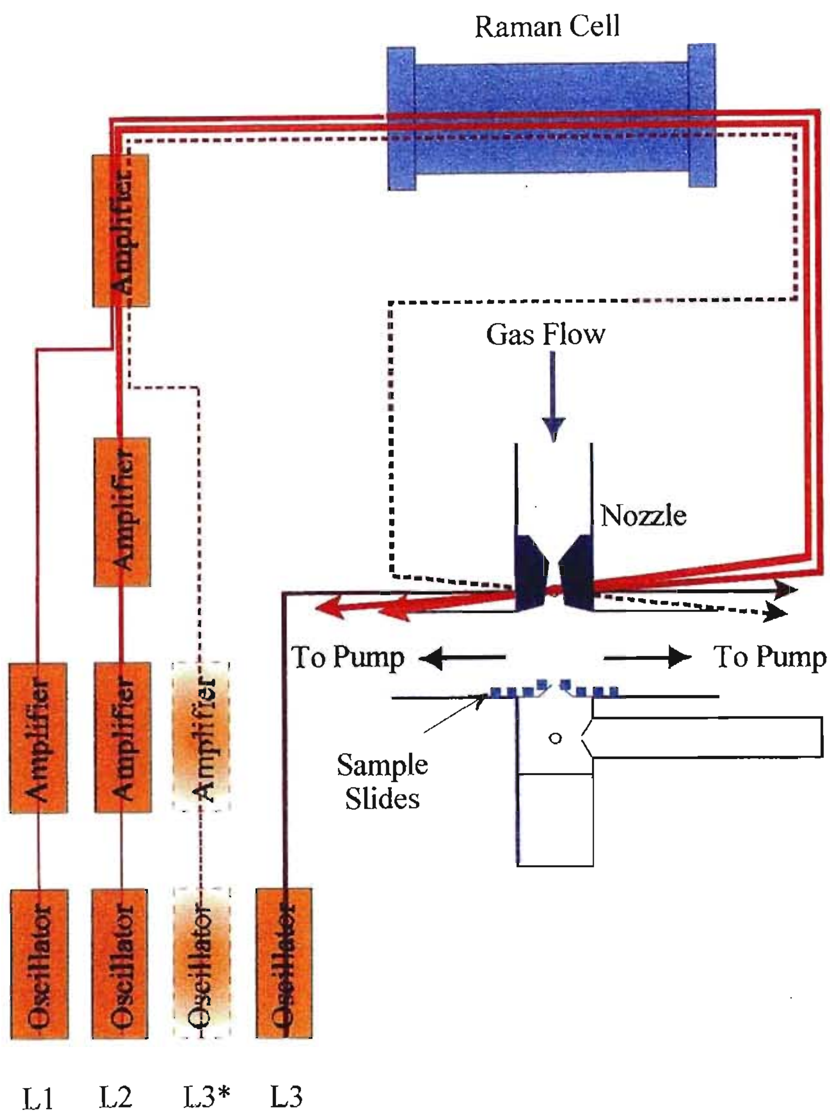

Fig 4.1 Schematic layout of the integrated laser system used. In addition, the flow cooling nozzle and irradiation geometry are shown. L1, 2 and 3 refers to the 1st, 2nd and 3rd wavelengths, respectively. L3 is the 9R28 wavelength and L3 is the 3rd alternative 16μm wavelength.*

4.4. In-line TOFMS

In-line measurement of the enrichment of either ^{235}U or ^{238}U can be done by either direct analysis of uranium containing products, or by indirect analysis in the depleted uranium feed stream. In this study, time-of-flight mass spectrometry was used to measure in-line the enrichment obtained by infrared irradiation of UF_6.

The problem of detecting and analysing UF_5 product formed in the presence of a large excess of UF_6, was solved in the early 80's (M Stuke et al, 1981, and P Dore et al, 1985). From their work, it is known that UF_5 can be selectively ionised by focussed laser irradiation with wavelengths in the region of 450 to 550nm. This is ideal for in-line TOF-MS detection and analysis for isotopic content.

A TOF-MS was developed and integrated with the Laval flow nozzle used for enrichment experiments. Fig. 4.2 is a diagram of the developed system. A gas skimmer with 0.8mm opening (Beam Dynamics Inc., Minneapolis), is situated ~30mm below the outlet of the Laval nozzle. The skimmer, maintaining the molecular beam characteristics of the gas flow, samples a small fraction thereof. The main gas flow is pumped away. The chamber below the skimmer is the front end of the TOF-MS. The flight tube of the TOF-MS is at right angle to the direction of the gas flow. This chamber is

pumped by a 2000 l/s turbo-molecular pump, whilst the flight tube is pumped by a 1000 l/s oil diffusion pump. The TOF utilises a double acceleration plate system of the Wiley-McClaren type.

Molecules are ionised between the first set of plates, on the axis of the TOF-MS, by a laser beam admitted through ports not shown in Fig. 4.1. Two fields through a 1.5mm opening accelerate the ions into the flight tube and towards the detector. The pressure obtained in the main chamber is ~$5x10^{-3}$ mbar, while the pressure in the flight tube is better than 10^{-5} mbar.

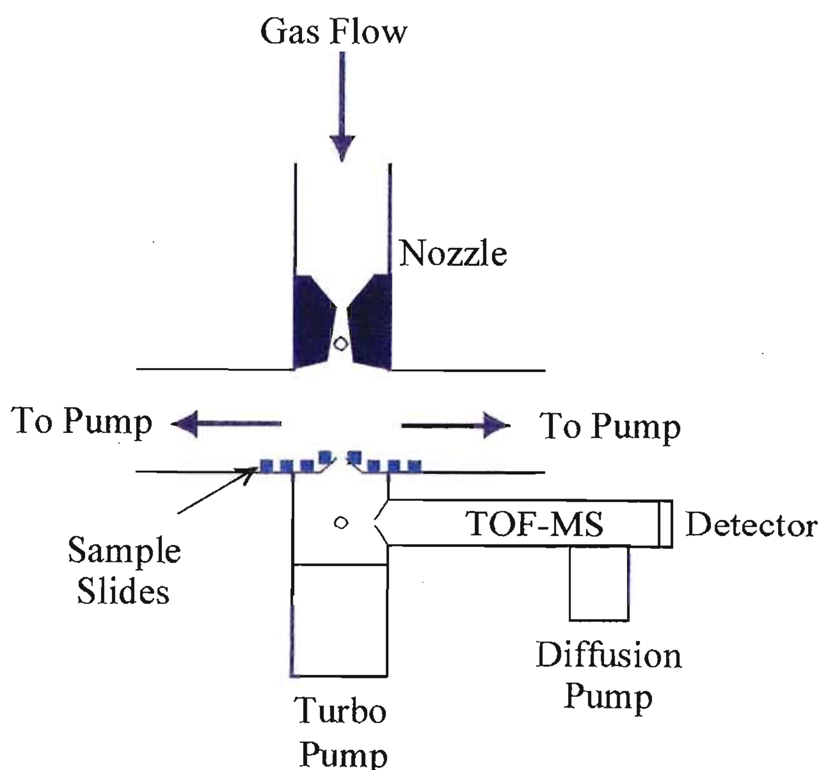

Fig. 4.2 In-line TOF-MS integrated with the Laval nozzle.

The detector consists of a combined microchannel plate, electron multiplier configuration. The microchannel plate (MCP) of 32mm diameter, liberates electrons in response to the incidence of an ion, as well as multiplies such electrons by a factor of ~1000 over its thickness of 0.5mm. Special measures had to be taken to ensure a linear dynamic range large enough to accommodate the 1:140 intensity ratio of the two main uranium isotopes at natural abundance. The double MCP system in a chevron configuration, usually employed for detection of ions in a TOF-MS, does not allow such a dynamic range. Instead of the second MCP, an electron multiplier (Hamamatsu R2362) was used as secondary signal amplifier. The total amplification of this detector configuration is 10^6 at 3500V supply. The electron multiplier was modified to enable the supply of large current pulses in short bursts by connecting capacitors of 220pF over the last four dynodes. These capacitors serve as reservoirs of electrons, making them available during the pulse. The large resistance of the 24-dynode chain (24MΩ) limits the peak current attainable. The signal from the electron multiplier is fed via a feed-through to an external fast amplifier (EG&G Ortec 9305) with 50Ω load resistance and 10x amplification. A fast digital oscilloscope is used to record the pulses.

The 1064 nm fundamental output of a Nd:YAG laser was used to ionise the MLIS product. The laser beam was focussed with a 250mm focal lens between the first two plates of the TOF instrument. The timing of the

ionisation laser was synchronised with the time arrival of the infrared irradiated gas packet at the axis of the TOF-MS. The delay was typically in the order of 460μs. It was found that the irradiated packets spread in time was minimal (Fig 4.3), showing no turbulence in its path from the irradiation position inside the nozzle through the skimmer, to the point of ionisation inside the TOF-MS.

The MLIS experiments used three different colours to selectively excite and dissociate the UF_6. The fluences of these pulsed lasers systems varied from shot to shot – sometimes, rather severely. In order to measure the enrichment factor as a function of the three laser fluences, it was essential to measure the enrichment factor on a shot to shot basis. To get suitable signal amplitude for both isotopes on the oscilloscope, the signal was divided by a 50Ω signal splitter and fed to two channels with different sensitivity settings.

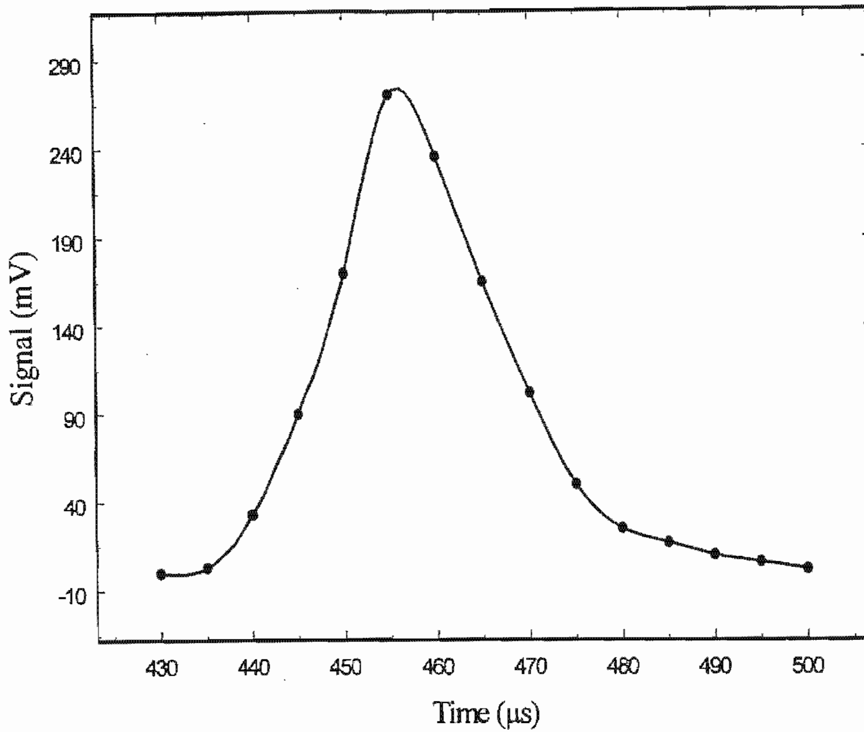

Fig 4.3 Time spread in the laser irradiated packet at the ionisation point in the TOF-MS. The optimum delay to ionise the peak of the irradiated packet in the TOFMS was ~460µs after the upstream laser irradiation.

Originally the idea was to transfer the two spectra captured by the two channels, to a computer for on-line calculation of the isotope ratio on a shot-to-shot basis. However, with the 235 peak intensity barely measurable above the background noise for the natural feed material, careful accumulation/averaging procedures were required. The predominant source of the background noise in the system was found to be due to detector shot noise. This is a purely statistical type of noise originating from the fact that the 235 isotope signal is due to a few or even a single ion only and the

finite (small) probability of detecting such an ion. This noise increases with the square root of the number of the ions being measured – the signal to noise ratio therefore improves with the square root of the signal strength. Increasing the 235-signal strength would obviously alleviate this problem. Increasing the fluence of the ionisation laser, was not an option, as the limited dynamic range of the detector could not cope with the increase in 238-signal strength. Furthermore, increased laser fluence causes increase Coulomb repulsion of ions on each other, deteriorating the resolution between the two peaks.

A procedure was developed for measuring the enrichment factor, α, as a function of the irradiation fluences ϕ_1 and ϕ_2 of the first two wavelengths λ_1 and λ_2, whilst keeping the fluence of the third wavelength as constant as possible. A 4x4 matrix was created on the computer screen with ϕ_1 values classified in 4 intervals on one axis and ϕ_2 values in 4 intervals on the other axis. Each individual value of α calculated from the registered spectra, is stored in one of the 16 matrix elements according to its specific values of ϕ_1 and ϕ_2 for that particular measurement. The α-values in each box can be averaged to improve on the statistical fluctuations.

Measurements with the described in-line TOF mass spectrometer, yielded enrichment α-values significantly different from 1, depending on the different wavelength and fluence combinations for the three wavelengths

used. The exact values cannot be published due to the confidential agreement between the Atomic Energy Corporation and its sponsor, Cogema, of France.

4.5. LD-TOFMS Instrument

The laser desorption time-of-flight mass spectrometer used, was a Wiley-McLaren-type (1955) linear instrument with a 1.2m flight tube. The instrument was designed and build in-house and is described in Chapter 1.

The measurement of the enrichment factor, α, can be done using laser desorption time-of-flight mass spectrometry (LD-TOFMS). The enrichment experiment is carried out and product is collected over a 2-4 hour period. The product is collected on stainless steel plates, placed under the nozzle some 180mm downstream from the irradiation point (see Fig 4.2).

The product plates are removed from the gas loop for external LD-TOFMS analysis. The product plate is mounted on the HV back plate and irradiated with a focussed laser beam (0.5 mm^2). The intensity of the laser beam is attenuated with neutral density filters (to less than 50mJ/cm^2). The laser beam ablates atoms/molecules from the sample surface. Through non-resonant excitation, a portion of this ablated material is ionised. The ions are extracted and accelerated by the static electric field (10-40kV) between

the planar electrodes. The ions then pass through a field-free region and arrive at the front plane of the detector. The detector signal can be viewed directly on an analogue oscilloscope and is stored in a digital oscilloscope. The average of a number of laser shots is used to improve the signal-to-noise ratio and the peak shapes (typically 16 shots).

Fig 4.4 shows a LD-TOFMS spectrum obtained from non-selective UV dissociated UF_6. Uranium oxide and fluoride species can clearly be seen. The oxide species originate from exposure to air. The 235 components of the UO and UO_2 species is indicated with an arrow. The reader will appreciate that the concentration of the 235 components in the natural feed material is only 0.7% vs. the 99.3% of the 238 species. The measurement requires a dynamic range of at least 99.3/0.7 ~ 140. The correct isotopic abundance was obtained using the corresponding uranium dioxide ions $^{235}UO_2^+$ and $^{238}UO_2^+$ at 267 and 270.

To obtain the enrichment factor the ratio of the 235/238 (peak area) in the product is divided by the ratio of the feed material before radiation. In our case the ratio is ~1/140. Therefore, dividing the LD-TOFMS measured 235/238 ratio by 1/140, gives direct measurement of the alpha.

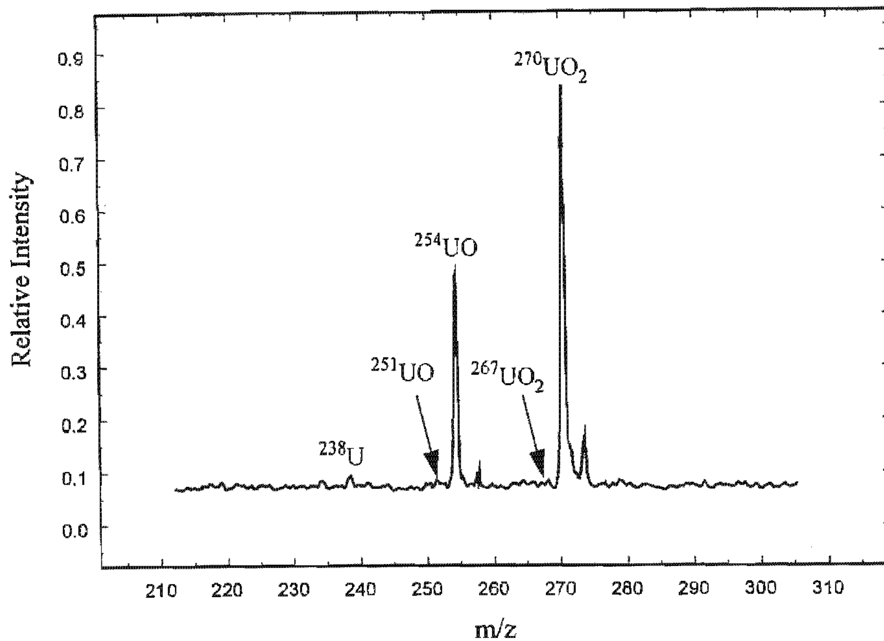

Fig 4.4 *LD-TOFMS spectrum of natural uranium used as feed in the irradiation experiments. The product was collected inside the contact cell on SS collector plates during non-selective UV dissociation of the process gas.*

An alpha depth profile can be obtained by measuring consecutive values on the same position. In Fig 4.5 an example of such a measurement is shown. The variation in alpha from one measurement to the next is in some cases as high as 50%. The variation, however, is believed to be a result of the irregular deposition of the solid uranium product, rather than a variance in attained enrichment. The low duty cycle of radiation (5Hz) combined with the continuous flow of UF_6 gas over the product plates would result in the adsorption of unenriched UF_6 on the porous product layers. An important

feature of this depth profile analysis is the final measurement of the alpha of one, corresponding to natural uranium. The possible reason for this is that unenriched UF_6 gas flows over the product plates for ~15 minutes before laser radiation commences, during which time adsorption takes place. This provides an internal check in each spot analysed.

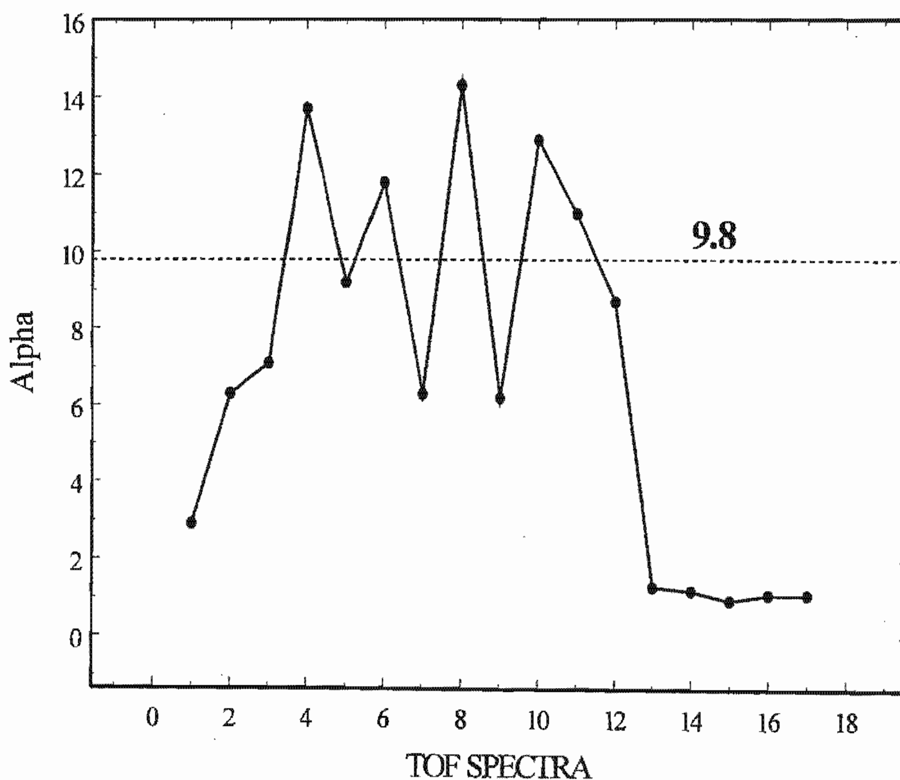

Fig 4.5 *LD-TOFMS measured alpha's from a series of consecutive spectra acquired from the same spot. This is the equivalent of an alpha depth profile extending into the sample.*

4.6. SIMS Instrument

The secondary ion mass spectrometry analysis was conducted at the CSIR, Pretoria, on a commercial Vacuum Generators ESCALAB Mk II, as described in Chapter 2. The option of either the Ga liquid metal ion source or the O/Ar duoplasmatron ion source had to be considered. Using the modified Sigmund's formula, described in Chapter 2, the product of the sputtering yield and surface binding energy is given in Fig 4.6 for Ga, O and Ar primary ions.

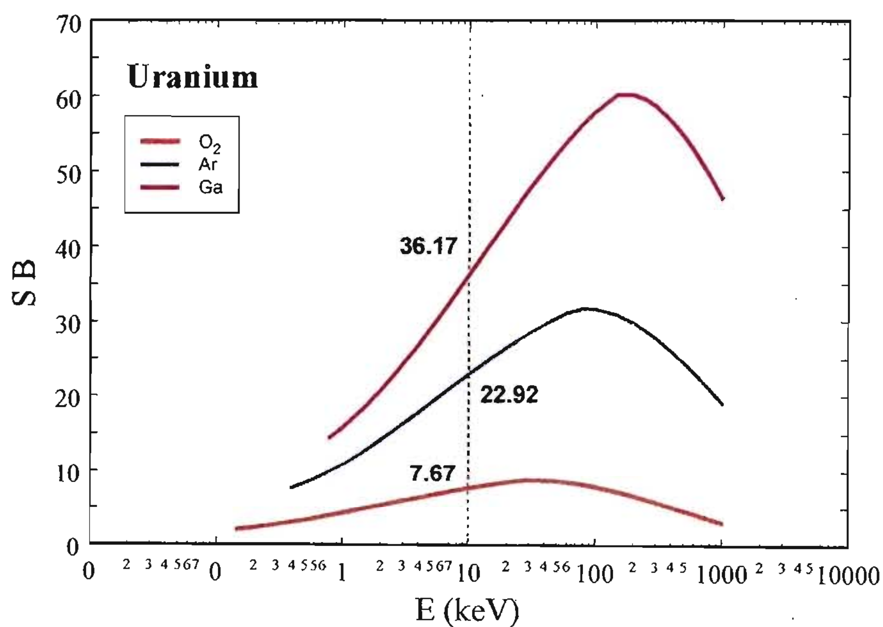

Fig 4.6 *Calculated sputtering yields for U using Ga, Ar or O primary ions. The values at 10keV are 36.17, 22.92 and 7.67 respectively.*

Both ion sources were operated at 10keV, the calculated *SB*-values for Ga, Ar and O are 36.17, 22.92 and 7.67, respectively. However, the angle of incidence with respect to the sample normal was 45^0 and 70^0 for the Ga and Ar and O ion sources, respectively. Using the angle dependence relationship given by equation (2.13) in Chapter II, the calculated SB-values for Ga, Ar and O are 19.0, 14.5 and 4.86, respectively. The enthalpy of sublimation at room temperature for uranium is 5.43eV/atom, resulting in sputtering yields of 3.5, 2.7 and 0.9 atoms/incident ion, respectively. Ga and Ar have the highest sputtering yields. Ga was selected because the source could operate stable at less than a tenth of the beam current of the duoplasmatron source. Furthermore, the superior beam quality of the Ga liquid metal ion source allowed area selection on the samples.

Equation (2.15) was used to estimate the sputtering rate:

$$\dot{z}[\mu m/h] = 3.755 \times 10^{-4} \frac{M[amu]}{\rho[g/cm^3]j[\mu A/cm^2]S}$$

For values of $\rho = 3.28$g/cm^3;

$j = 2\text{x}10^{-3}\mu\text{A}/3\text{x}10^{-4}\text{cm}^2 = 6.67\mu\text{A/cm}^2$; and

$S(45^0)$ 3.5atoms/incident ion,

the sputtering rate is estimated at :

$$\dot{z}[\mu m/h] = 3.755 \times 10^{-4} \frac{238.029}{3.28 \times 6.67 \times 3.5} = 1.167 \times 10^{-3}$$

$$\therefore \dot{z} = 1.95 \times 10^{-5} \mu m / \min = 0.324 \mu / s$$

The estimated sputtering rate is 0.324µm per second. To acquire a SIMS spectrum from mass 230 to 240 the quadrupole is typically scanned in mass steps of 0.05 amu, counting secondary ions for 200ms per step. This implies a total scanned time of 40 seconds per spectrum. The material consumption per single scanned spectrum is therefore ~13µm. Alternatively, there are only ~320 seconds available to acquire ~8 consecutive spectra before 100µm thick uranium material is removed!

The mass resolution of the quadrupole mass spectrometer is typically 300, in other words at mass 300 the mass analyser can resolve mass 300 from mass 301. The enrichment alpha can be determined using either a SIMS mass spectrum or a SIMS depth profile. The Alpha is defined as the 235/238 ratio of the product divided by the ratio in the feed material. Therefore

$$\alpha \approx 140 \times I(235) / I(238),$$

where $I(235)$ and $I(238)$ is the peak (intensity or area) of the measured SIMS peaks.

4.6.1. SIMS Mass Resolution

Secondary Ion Mass Spectrometry (SIMS) is used to analyse the surface and near surface of collected MLIS product. The analysis provides isotopic information. Due to the small amount of product, the analysis (which is a destructive process of ion erosion of sample material) should be done in the shortest possible time. The SIMS instrument is therefore forced to work at the limit of its time, sensitivity and mass resolution. In this section the effect of mass resolution and spectral interference on the measured enrichment alpha is addressed.

The mass resolution of the quadrupole mass spectrometer on the VG ESCALAB II was optimised. Figures 4.7-4.8 show the mass spectra from mass 225 to 245 on enrichment standard (α=9.9) obtained before and after mass resolution optimisation, respectively.

The SIMS spectrum shown in Fig 4.7, is of poor mass resolution. From this spectrum it would appear as if there are peaks at masses 234, 235, 236, 237, 238, 239 and even at 240. The origin of the peaks at 234, 237 and 240 are difficult to explain. However, after optimisation of the mass resolution of the spectrometer only peaks at masses 235, (maybe 236), 238 and 239 were measured, clearly indicating the presence of the UH species.

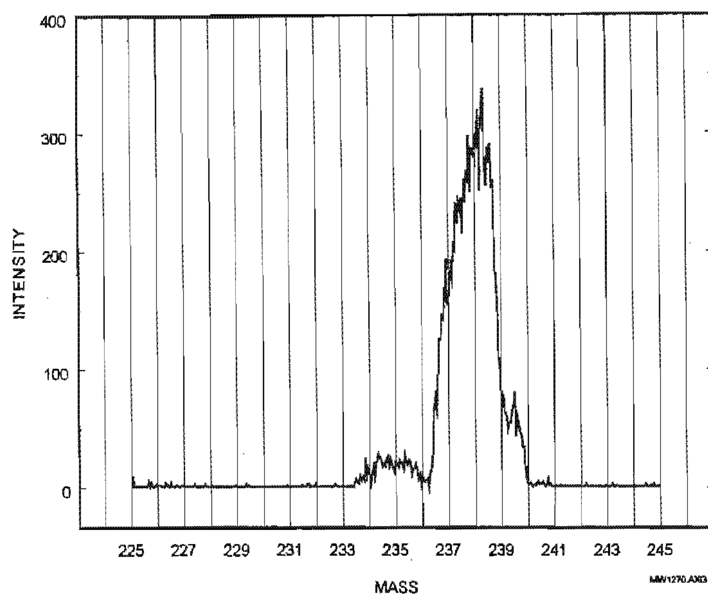

Fig 4.7 SIMS mass spectrum of the ^{235}U and ^{238}U peaks acquire from a ^{235}U-enriched sample before resolution optimisation.

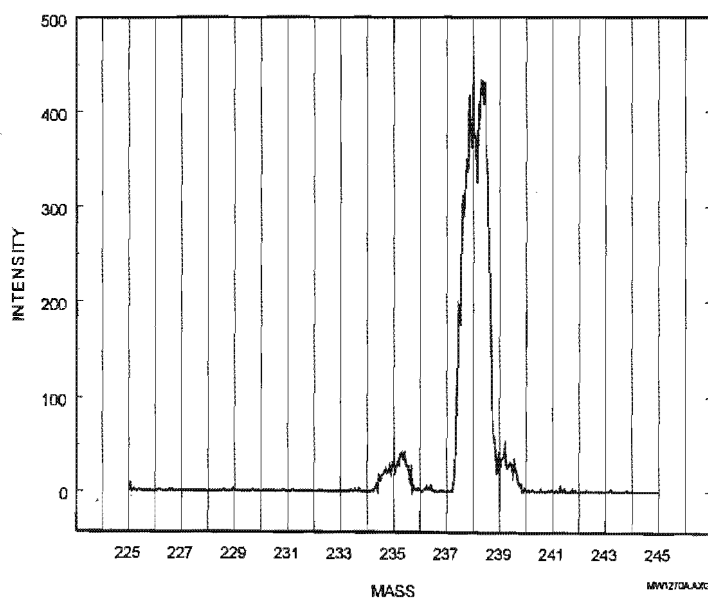

Fig 4.8 SIMS mass spectrum of the ^{235}U and ^{238}U peaks acquire from a ^{235}U-enriched sample before resolution optimisation.

With the mass resolution optimised, a wide mass spectrum from mass 1 up to 300 amu, was recorded. The spectrum is shown in Fig 4.8.

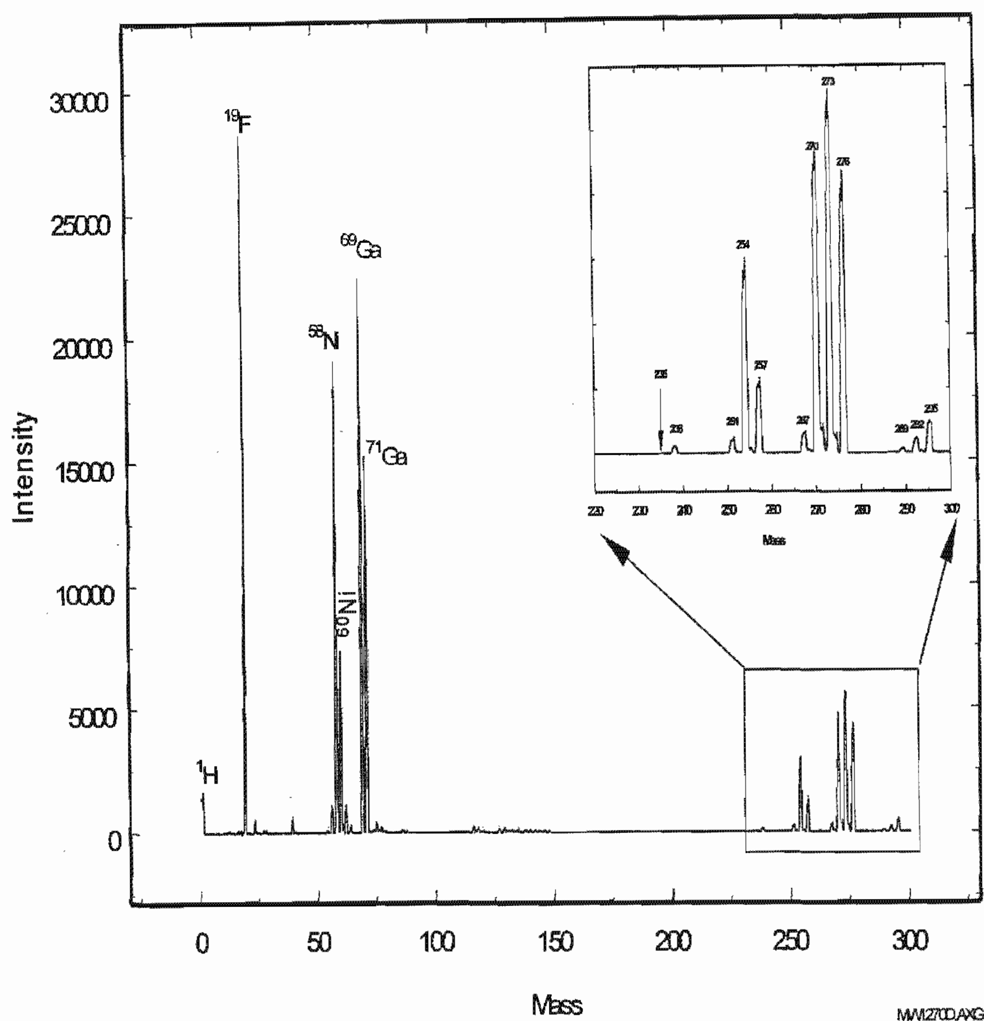

Fig 4.9 A SIMS mass spectrum from mass 1 to 300 amu. The insert shows that unit mass resolution is achieved at mass 300.

The spectrum is fairly clean, with peaks at ^{1}H, ^{19}F, $^{58,60}Ni$, $^{69,71}Ga$, and a series of high mass uranium-oxy-fluoride peaks. The 235 and 238-uranium peaks gives rise to spectral overlap with the different oxide and fluoride species, as given in Table 4.1. For example mass 254 is the combination of

$^{238}U^{16}O$ and $^{235}U^{19}F$, whereas, mass 270 is the combination of $^{238}U^{16}O_2$ and $^{235}U^{16}O^{19}F$.

U	UO	UF	UO_2	UOF	UF_2	UO_3	UO_2F	UOF_2	UF_3
235	251	254	267	270	273	283	286	289	292
238	254	257	270	273	276	286	289	292	295

Table 4.1. Uranium oxide and fluoride masses for the two uranium isotopes.

In the beginning years of this study (SIMS and LD-TOFMS) the enrichment alpha was measured on the 235/238, 251/254 and 267/270 ratios. The above mentioned spectral interference would indicate that the alphas measured on both oxide species would be lower due to the UF and UOF contributions at 254 and 270, respectively. The amount would vary proportional to the alpha, as for high alphas (>10), the 235 components of UF and UOF, becomes significant. Using a standard sample with an alpha of 9.9, the spectral interference can be calculated to be the following:

$$I(251) = {}^{235}U^{16}O \tag{4.1}$$

$$I(254) = {}^{238}U^{16}O + {}^{235}U^{19}F \tag{4.2}$$

$$I(257) = {}^{238}U^{19}F \tag{4.3}$$

The alpha relation:

$$\alpha = 140*{}^{235}U/{}^{238}U \qquad (4.4)$$

$$\Rightarrow {}^{238}U^{16}O = I(254) - [(\alpha/140).I(257)] \qquad (4.5)$$

Similarly $$I(267) = {}^{235}U^{16}O_2 \qquad (4.6)$$

$$I(270) = {}^{238}U^{16}O_2 + {}^{235}U^{16}O^{19}F \qquad (4.7)$$

$$I(273) = {}^{238}U^{16}O^{19}F + {}^{235}U^{19}F_2 \qquad (4.8)$$

$$I(276) = {}^{238}U^{19}F_2 \qquad (4.9)$$

$$\Rightarrow {}^{238}U^{16}O_2 = I(270) - \{\alpha/140)\}.\{I(273) - (\alpha/140).I(276)]\} \qquad (4.10)$$

With these equations the measured alphas obtained from the spectrum shown in Fig 4.9, are as follows:

235	238	251	254	254*	257	267	270	270*	273	276	α_{235}	α_{251}	α_{251}*	α_{267}	α_{267}*
8	108	182	2700	2626	1050	280	4360	4001	5366	4004	10.37	9.437	9.704	8.991	9.799

The values for 235, 238, 251, 254, 257, 267, 270, 273, and 276, are the SIMS peak values. The values for 254* and 270* are the corrected ^{238}UO, and $^{238}UO_2$ peak values, respectively. The three alpha values obtained for 235/238, 251/254*, and 267/270* are 10.37, 9.7, and 9.8. The overestimation of 10.37 of the 235/238 alpha is a result of the low SIMS counts measured for that mass - hence, a higher margin of error. Nevertheless, the average of the three measurements is 9.96 ± 0.36. Without correction of the spectral overlap the average is 9.6 ± 0.70.

A depth analysis of the following masses were made: 234 (background count), ^{235}U, ^{238}U, ^{251}UO, ^{254}UO (including $^{235}U^{19}F$) , $^{267}UO_2$, $^{270}UO_2$ (including $^{235}U^{16}O^{19}F$) . The background counts at mass 234 were found to be less than 10 counts/second, compared to the ~150 counts/second obtained for mass 235. The enrichment alpha for uranium and the two uranium oxide complexes were calculated, and are shown in Fig 4.10.

The spectral overlap of ^{235}UF at mass 254 measured earlier is ~ 2.7%, and that of ^{235}UOF at mass 270 is ~ 8.2%. Using these spectral corrections, the corrected alphas, is shown in Fig 4.11. The average of the U, UO and UO_2 alpha measurements is 10.24 ± 0.93 on the "as is" depth profiles, and 10.58 ± 0.67 on the spectral corrected profiles. Both these measurements are within 10% of one another (even closer for the spectral corrected measurements). For an alpha of 10 the improvement in the measured values

obtained after spectral interference correction, decreased the standard deviation from 9.3% to 6.7%.

At this point in the study it became clear that all SIMS analysis of MLIS accumulated product should:

(i) Provide a spectrum showing ample mass resolution in the region 225-275 amu, and

(ii) Include the U, UO and UO_2 alpha measurements, the average of which (if found to be within 10%) should be considered to be the measured value.

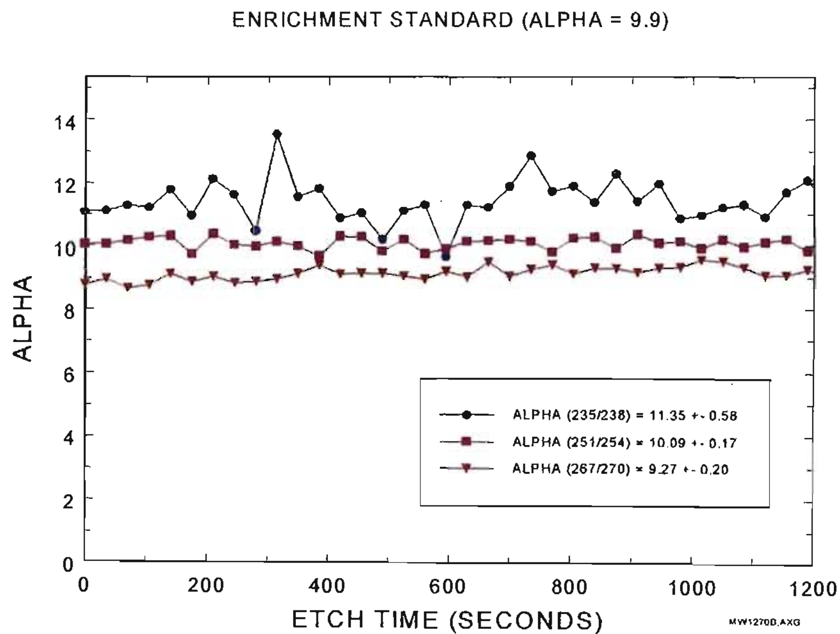

Fig 4.10 SIMS depth profile measure alphas for U, UO and UO_2 on a ^{235}U-enriched sample.

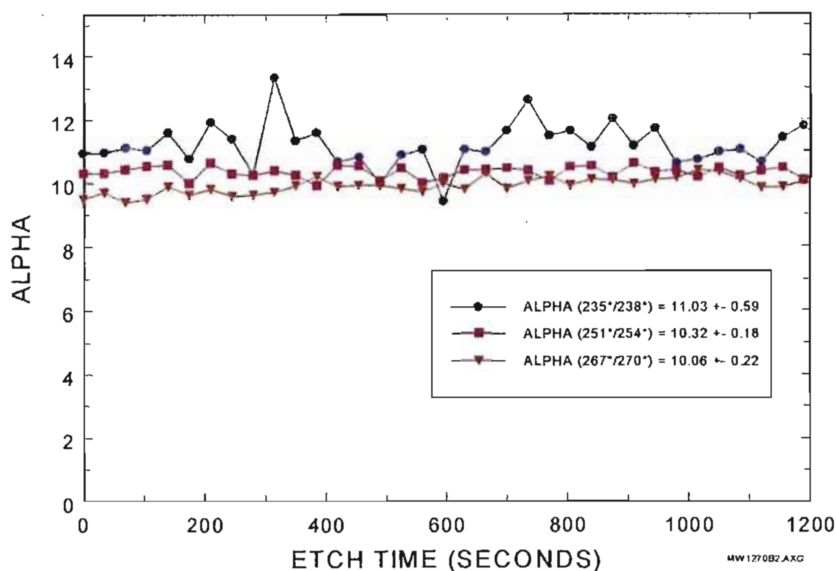

Fig 4.11 SIMS measured alphas on U, UO and UO_2 after a correction for spectral interference. Clearly the correlation in the measured alpha of the enriched standard has improved.

4.6.2. SIMS Analysis of MLIS Produced Product

With SIMS the analyses of a sample is in the form of a spectrum of the sample surface. However, the sputtering process continuously removes sample material form the surface, resulting in the formation of a crater. The SIMS technique can therefore, provide in-depth information on atomic constituents by recording one or more mass peaks as the sputtering process erodes the sample - referred to as SIMS depth profiles.

SIMS depth profiles were made for six different masses:

235 U (235 isotope)

238 U (238 isotope)

267 UO_2 (Uranium oxide of the 235 isotope)

270 UO_2 (Uranium oxide of the 238 isotope)

273 UOF (Uranium oxy fluoride of the 238 isotope)

276 UF_2 (Uranium di fluoride of the 238 isotope)

The instrument setup is such that for each mass the number of secondary ions is counted for a period of 4 seconds.

For correct interpretation of the SIMS depth profiles, the procedure of product collection has to be considered. The chemically cleaned collector plates are placed around the skimmer inside the contact cell, as shown before (Fig 4.2). The process gas is loaded and circulated for a period of up to 15 minutes before the irradiation is started. During this period UF_6 adsorption onto the product plates takes place (layers of natural UF_6 material are deposited on the plates). During laser irradiation of the process gas, quantities of dissociated product as well as UF_6 adsorption accumulate on the collector plates. Once the irradiation is completed, circulation of the process is continued for 5-15 minutes to freeze out process gas sample for MS measurements (during this period further UF_6 adsorption occurs). Hereafter the process gas is pumped away. This procedure was followed for all of the experiments, however, variations in time used for the process gas circulation and pump down were experienced from experiment to

experiment, due to unforeseen instrumental mishaps. This would change the individual layer thickness from one experiment to another.

The collected product should therefore contain three layers as is shown in Fig 4.12 (a). As a result three distinct features are to be seen in the SIMS depth profiles of the uranium product samples, as depicted in Fig 4.12 (b).

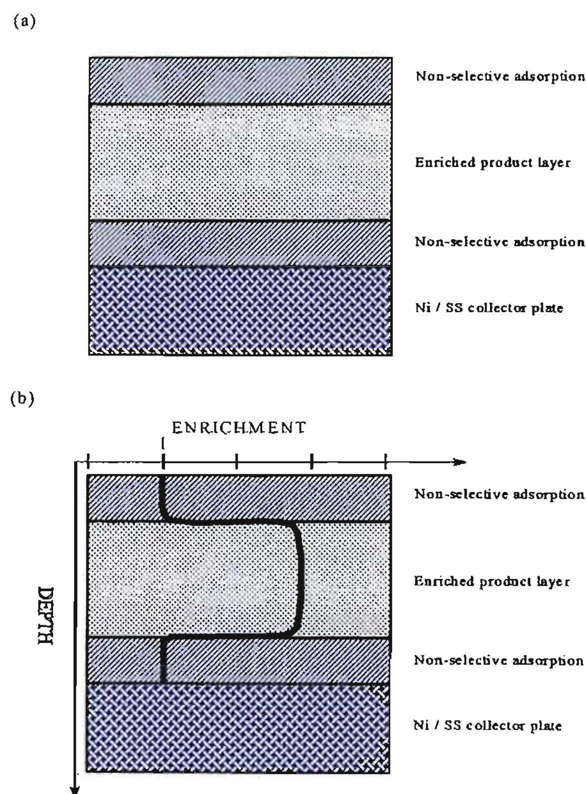

Fig 4.12 (a) Layered structure of product on collector plates.

(b) Expected SIMS depth profile through the product layers.

In Fig 4.13(a) SIMS depth profiles for ^{235}U and ^{238}U through an adsorbed UF_6 layer on a product plate are shown. In order to obtain the enrichment

alpha the ratio of the 235 to 238 isotopes in the product, divided by the ratio in the same ratio in the feed, Fig 4.13(b).

$$\alpha = \frac{\left(\frac{U-235}{U-238}\right)_{Product}}{\left(\frac{U-235}{U-238}\right)_{Feed}} \approx 140 \cdot \left(\frac{U-235}{U-238}\right)_{Product}$$

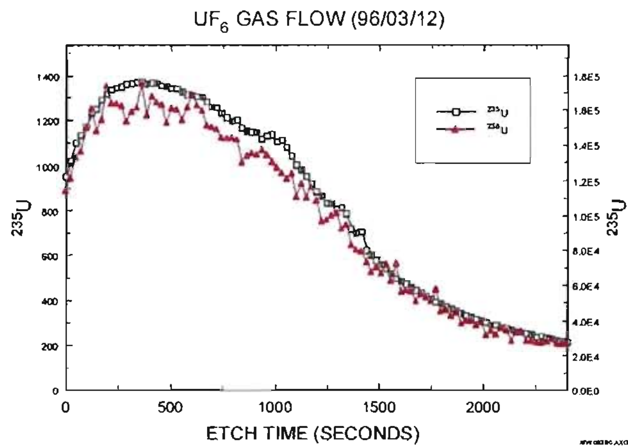

Fig 4.13(a) SIMS depth profiles for masses 235 and 238 through adsorbed UF_6 on a product platelet.

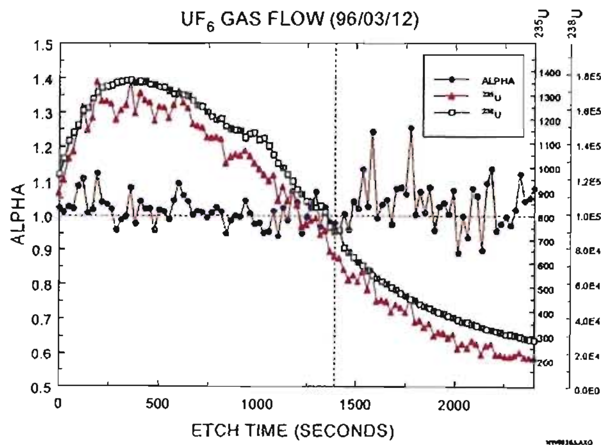

Fig 4.13(b) SIMS depth profiles and calculated alpha curve for adsorbed UF_6 on a product platelet.

The SIMS depth profiles for ^{235}U and ^{238}U, shown in Fig 4.13, do not resemble the "box-like" shape that one might have expected. The profiles can be divided into three distinct regions, the first being a leading edge sputtered through the surface contamination/oxide layer; the second being the actual product layer; and the third being the extended tail.

The fundamental processes of finite sputter segregation, and crater bottom topography often result in a significant discrepancy between the actual elemental distribution and that measured by a SIMS depth profile, but not differences in isotopes of the same element. To be more specific, it is a well known phenomenon that the abruptness of the leading edge is determined by the sputter mixing, whilst the trailing edge is a combination of knock-on broadening and signals originating from collapsing crater walls. Fig 4.14 shows how each of these separate broadening operations affects a box-shaped profile.

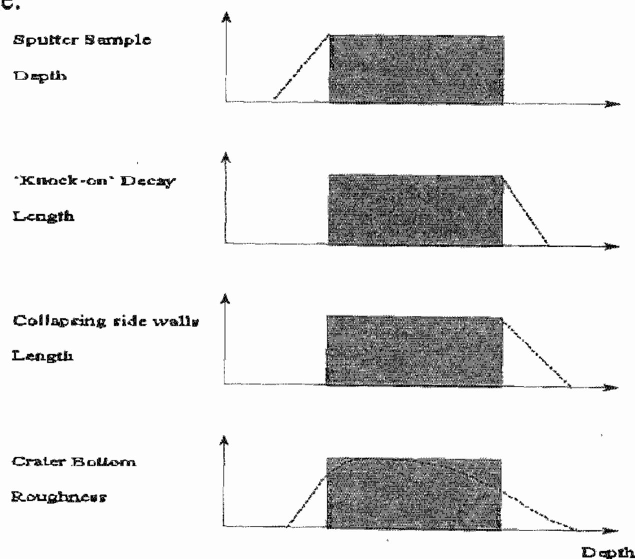

Fig 4.14 SIMS depth profile broadening due to sputter induced defects.

4.6.3. SIMS Analysis of Enriched Standards

A series of product collection experiments were undertaken in an effort to correlate the in line TOFMS measurements of the enrichment factor, alpha, with that obtained from bulk sample measurements, using Secondary Ion Mass Spectrometry (SIMS). The systematic of product collection and analysis has been established however, the absolute values measured for alpha by the SIMS has to be evaluated against standards of known enrichment. The validity of such measurements is dependent on the close resemblance of the standard on the product formation/collection experiments.

Several methods were investigated for the production of enriched uranium standards. However, none of this involved photo-dissociation of UF_6, as well as the collection of dissociated product under the influence of gravity - which is typical experienced in the pilot irradiation setup. Instead UF_6 gas, of known enrichment, was dissociated in a static cell with a UV Mercury lamp. The dissociated product accumulated on product plates under the influence of gravity.

Four different grades of enriched UF_6 gas were prepared and certified by Pelindaba Analytical Laboratories. The enrichment of the four samples constitutes enrichment alphas of 3.9, 6.0, 8.3 and 9.9. A 15-mm static cell

was prepared for the irradiation experiments. Ni collector plates, similar to those used in the pilot irradiation experiments were placed at the bottom of the cell (see Fig 4.15). It was found that the amount of product deposited on the plates decreased as the distance from the entrance window increased. Placing eight Ni plates at regular intervals down the length of the cell produced samples with the same enrichment but of different thickness. Samples resembling more or less the appearance of the pilot irradiation plates could therefore be selected for SIMS analysis.

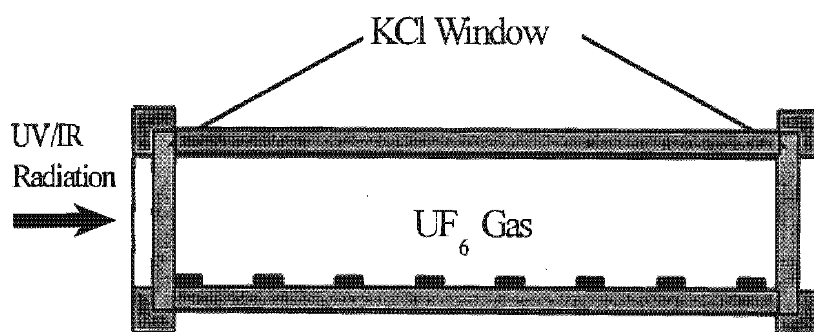

Fig 4.15 Static cell showing the equally spaced Ni product plates used for the non-elective dissociation of known enriched UF_6 gas.

The following experimental procedure was followed for the four different enriched samples:

(1) Load cell with 10kPa natural UF_6 gas, leave for 24 hours to condition;

(2) Evacuate cell and load enriched UF_6 and CH_4 in a 1:5 mixture to an absolute pressure of ~ 48kPa, leave for three hours to stabilise;

(3) Irradiate cell for 30 minutes with a Mercury UV lamp, and evacuate.

A fifth irradiation experiment was done, using enriched UF_6 gas with an alpha of 9.9. In addition to irradiating with the UV Mercury lamp, irradiations with and 16μm laser system, consisting of >50 mJ/cm^2 16R18 and >300 mJ/cm^2 16P20 photons, was carried out.

The SIMS analysis of the standards was done under exactly the same instrumental conditions as those used earlier on the pilot enrichment samples. SIMS depth profiles were made for six different masses:

235 U (235 isotope)

238 U (238 isotope)

267 UO_2 (Uranium oxide of the 235 isotope)

270 UO_2 (Uranium oxide of the 238 isotope)

273 UOF (Uranium oxy fluoride of the 238 isotope)

276 UF_2 (Uranium di fluoride of the 238 isotope)

The instrument setup is such that for each mass the number of secondary ions is counted for a period of 4 seconds. One SIMS depth profile was made for each of the samples. The results are summarised in Table 4.2. Fig 4.16 (a)-(e) shows the SIMS depth profiles and alpha curves.

NO	ALPHA OF STANDARD	SIMS ALPHA
1	3.9 (UV)	4.6 ± 0.33
2	6.0 (UV)	6.7 ± 0.27
3	8.3 (UV)	8.3 ± 0.37
4	9.9 (UV)	10.6 ± 0.20
5	9.9 (IR)	11.2 ± 0.64

Table 4.2 Summary of SIMS measurements.

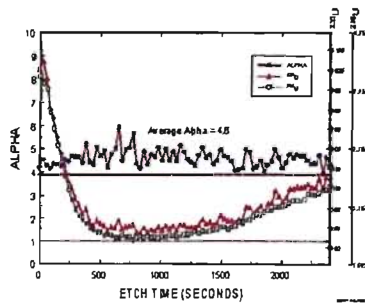

(a) UV dissociation, alpha = 3.9

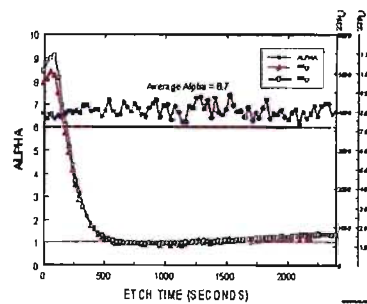

(b) UV dissociation, alpha = 6.0

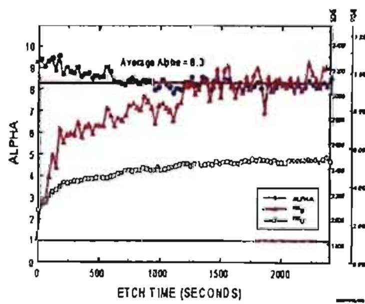

(c) UV dissociation, alpha = 8.3

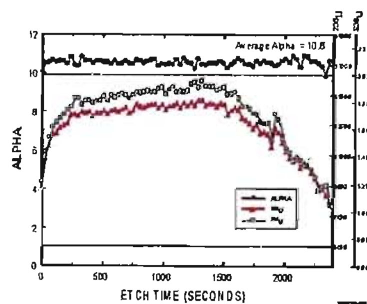

(d) UV dissociation, alpha = 9.9

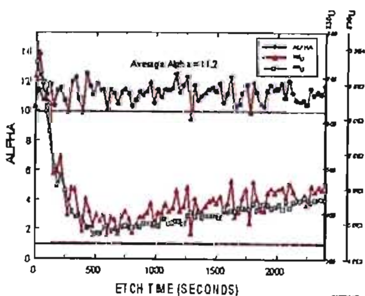

(e) IR dissociation, alpha = 9.9

Fig 4.16 SIMS depth profiles and alpha curves for enriched standards.

The shapes of the 235 and 238 peaks varied from sample to sample, however, the two follow one another with a resulting alpha (ratio of the two) to within 10-15% of the certified standard. Fig 4.17 shows a comparison of the different alpha measurements.

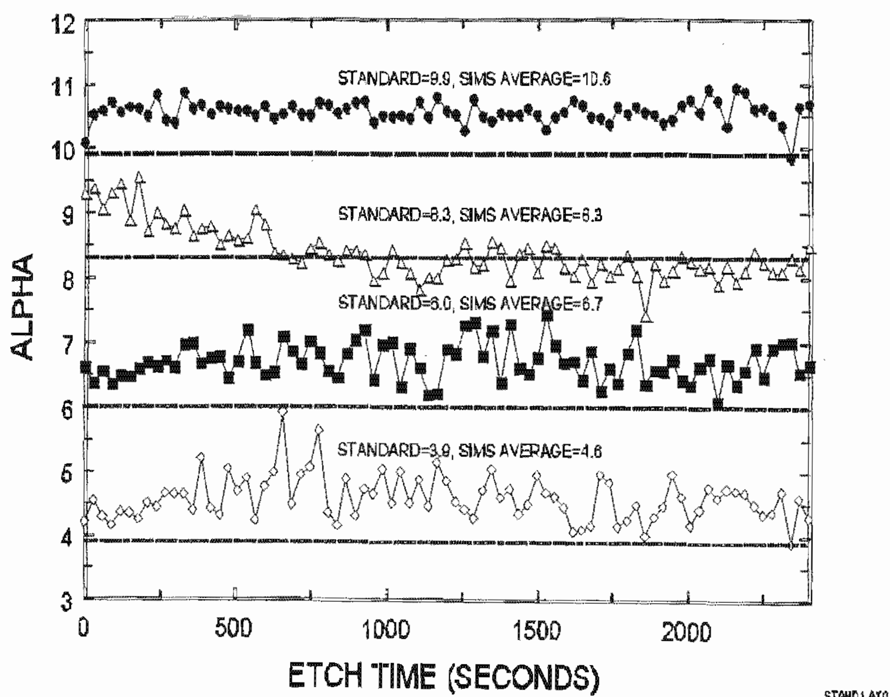

Fig 4.17 SIMS measured alphas on different enriched standard samples.

In addition to the UV dissociation, IR dissociation was done. The resulting alpha measurement is slightly higher than that obtained with UV dissociation - still within 10-15% of the certified standard. Fig 4.18 shows the two different alpha measurements.

No significant difference could be seen in the shapes of the 235 and 238 depth profiles between the two different dissociations, however, for the IR dissociated sample an increase in the standard deviation was observed. The SIMS secondary ion signals for that particular sample was rather low.

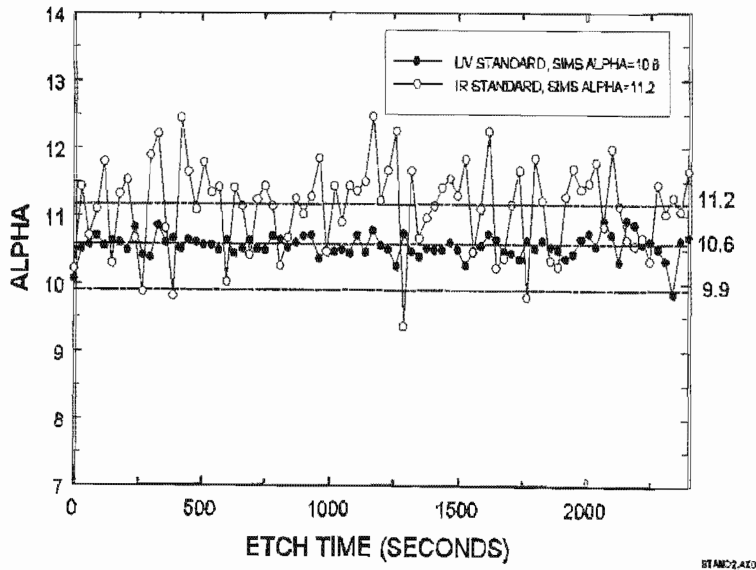

Fig 4.18 SIMS measured alpha on UV vs IR dissociated standard (alpha=9.9).

In conclusion the following remarks can be made:

1) Product collection, followed by SIMS analysis can produce a measure of the average bulk enrichment;

2) The SIMS enrichment measurement is not a single average alpha value, but rather a band of alphas;

3) The validity of the absolute values was checked on standard samples with known enrichment, in collaboration with Pelindaba Analytical Labs, and are within 10-15% of the certified standard.

4.7 LD-TOFMS and SIMS Results

The next part of this Chapter summarises chronologically the LD-TOFMS and SIMS measurements of irradiation experiments over a period of 6 years. The period can be described by 4 distinct experiments, each of which required an enormous amount of design, setup and integration of several systems and sub-systems. The focus is on the MS analysis and interpretation of the measurements.

The *"August `93"* experiment

Table 4.3 summarise the experimental conditions used during the Aug '93 experiment. For the first time the isotope Lambda 1 laser was used to selectively excite on the ^{235}U isotope. The wavelength was tuned to 628.3cm^{-1} which is resonant with the ν_3 ground state of the ^{235}U isotope. The D2T4P5M nozzle was used, with the nozzle swinged open to reduce condensation, the carrier gas was Ar, and the upstream pressure was 15kPa.

Isotope irradiated	U(235)
Duration	2 - 5 hours @ 5Hz
Gas conditions	D2T4P5M
Wavelengths	λ_1 = Resonant, λ_2 = 16R18, λ_3 = 9.3μm
Sample	Product collected on SS impact plates
Analysis	SIMS & LD-TOFMS mass spectra
Accuracy	10-20% accurate
Alpha	6 - 7
Comments	No spectral interference present

Table 4.3 Experimental conditions for the Aug '93 experiment.

Stainless steel impact plates were placed around the base of the skimmer, downstream from the nozzle. The collected product was mass analysed with SIMS and Laser Desorption Time-of-Flight Mass Spectrometry (LD-TOFMS). The LD-TOFMS is an in-house built spectrometer that operates on the same principle as the SIMS, except that a laser beam is used to desorb/ionise the sample. The amount of product collected was small, hence, only a number of spectra from mass 230-240 could be recorded, before the product layer was consumed. From the spectra alpha values were calculated. Both the SIMS and the LD-TOFMS measured alpha values of 6-7. The spectra were somewhat erratic, different alpha values were measured from point to point on the impact plates. The differences were believed to be a result of the thin inhomogeneous deposition of product. Figures 4.19 and 4.20 shows enrichment alpha depth profiles at four different spots of a product platelet, measured with LD-TOFMS and SIMS, respectively.

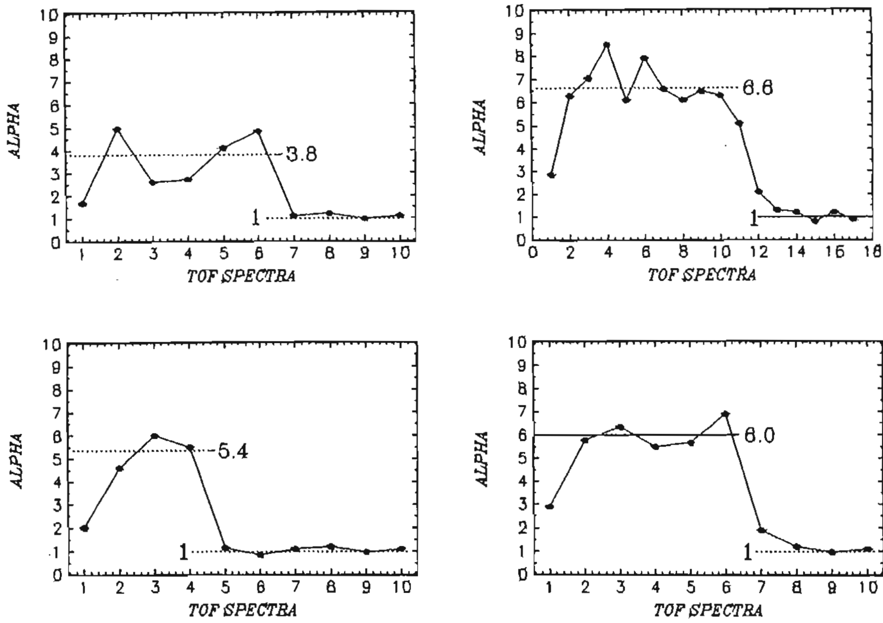

Fig 4.19 Four alpha depth profiles at four different spots of a product platelet, measured with LD-TOFMS.

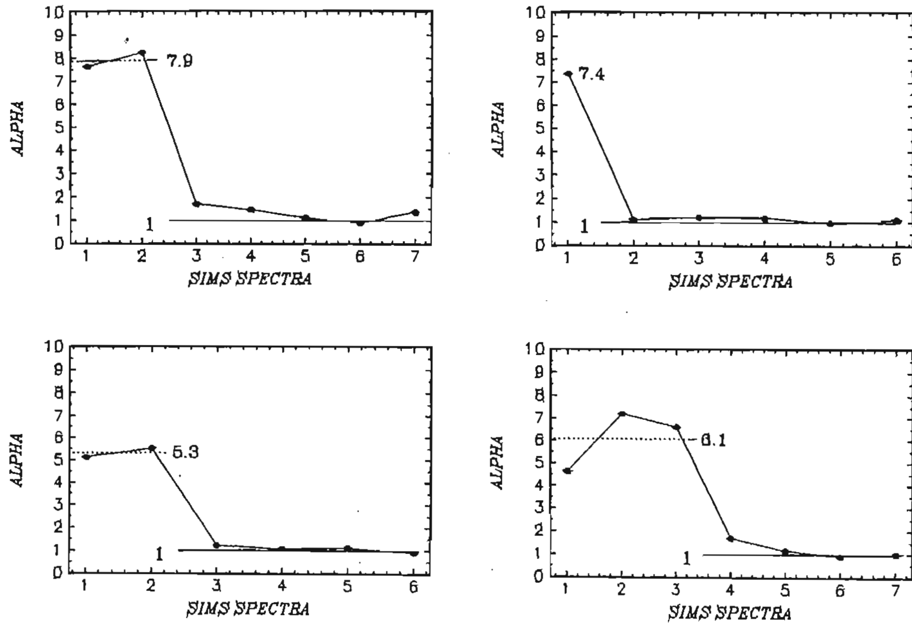

Fig 4.20 Four alpha depth profiles at four different spots of a product platelet, measured with SIMS.

June `96: 3x16μm irradiations

The period after the August '93 experiment saw extensive upgrades in the laboratory. A third 16μm wavelength was added, the sensitivity of the in-line TOFMS was improved to measure at low upstream pressures, HF emission was developed to measure in-line cuts, etc. IR product was collected in a similar fashion as in Aug '93, except that Ni impact plates were used instead of stainless steel (the Cr in the stainless steel plates gave interference during SEM analysis of fluorine). Table 4.4 summarise the experimental conditions used during the June `96 experiment.

Isotope irradiated	U(235)
Duration	3 hours @ 2Hz
Gas conditions	D2T4P5M 3.5 kPa Ar
Wavelengths	λ_1 = varied, λ_2 = 16R16, λ_3 = 16P20
Sample	Product collected on Ni impact plates
Analysis	SIMS depth profiles
Accuracy	10-20% accurate
Alpha	1 - 14
Comments	Significant more product. Report on 235/238 ratio. No spectral interference suspected

Table 4.4 Experimental conditions for the June `96 experiments.

The June '96 experiment was a series of product collection experiments for which the SIMS alpha was measured for UV dissociation, gas flow without

any laser irradiation, and different Lambda 1 wavelengths. Table 4.5 summarises these experiments.

GAS	$P_{Upstream}$ (kPa)	Irradiation	TOF α	SIMS α
$UF_6 + CH_4 + Ar$	3.5	No irradiation	None	1.0 - 1.1
$UF_6 + CH_4 + Ar$	3.5	Only L2 & L3	None	1.0 - 1.1
$UF_6 + CH_4 + Ar$	3.5	UV dissociation	1.0 - 1.1	1.1 - 1.2
$UF_6 + CH_4 + Ar$	3.5	L1 = Resonant	1.6 - 1.8	2.4 - 13.9
$UF_6 + CH_4 + Ar$	3.5	L1 = R24*	1.7	7.0 - 9.4
$UF_6 + CH_4 + Ar$	3.5	L1 = R30	1.3	1.1
$UF_6 + CH_4 + Ar$	3.5	R28 < L1 < R30	0.9	1.5 - 2.8
$UF_6 + CH_4 + Ar$	3.5	L1 = R28	None	1.6 - 1.8
$UF_6 + CH_4 + Ar$	15	L1 = Resonant	1.1	1.1
$UF_6 + CH_4 + N_2$	15	L1 = Resonant	1.5	4.8 - 8.3
$UF_6 + CH_4 + N_2$	10	L1 = Resonant	1.2 - 2.0	1.1 - 8.6

Table 4.5 Summary of June '96 product collection experiments. (R24 refers to the R24 line of the dual labelled $C^{16}O^{18}O$ isotope).*

The amount of product accumulated on the impact plates were substantially more than that of Aug '93. Consequently, the SIMS measurements could be improved by acquiring concentration depth profiles of the 235 and 238 isotopes, instead of acquiring consecutive spectra. A number of SIMS depth profiles were recorded per impact plate. From these profiles peak and average alpha values were calculated. Similar to Aug '93 it was found that the alpha would vary from position to position on an impact plate - indicating once again inhomogeneous layer deposition. The product

collections for UV dissociation, IR irradiation with only Lambda's 2 and 3 (no selective excitation), and gas flow without any laser irradiation were seen as control samples. Since no selective excitation/dissociation of the ^{235}U isotope was done, the measured SIMS alpha should be one. This was clearly the case, as can be seen in the Table 4.5.

Fig 4.21 shows a comparison between the SIMS alpha, the in-line TOFMS alpha and the two-level model prediction as a function of λ_1 wavelength. This model takes into consideration the excitation of two molecular vibration levels.

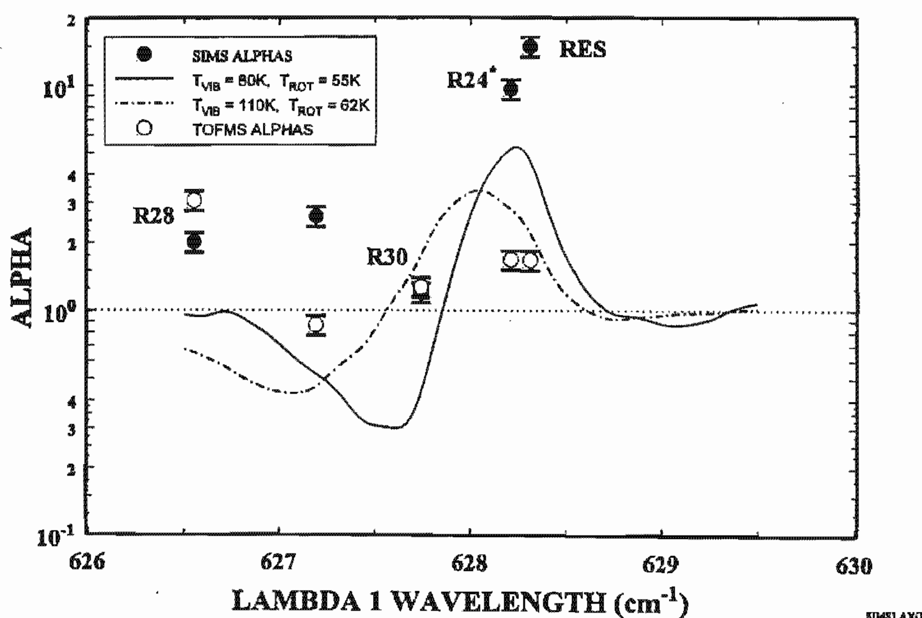

Fig 4.21 A Comparison between SIMS alphas, in line TOFMS alphas and model prediction as a function of λ_1 wavelength.

The SIMS alphas and in line TOFMS alphas have more or less the same trend, except between the R28 and R30 lines (627.2 cm^{-1}) where the SIMS alpha is greater than one. Further comparison with the two-level model prediction, indicates over estimation by the SIMS measurements.

October - December `96: MLIS Plant Specification

During this period, MLIS product was collected under the MLIS Plant specification conditions, given in Table 4.6. This was done for the original D2T4P5O nozzle, as well as the modified D2T4P5M nozzle. Enrichment alphas of 6-8 were measured only for the modified D2T4P5M nozzle.

Isotope irradiated	U(235)
Duration	3 hours @ 2Hz
Gas conditions	D2T4P5M & D2T4P5O, 10 kPa N_2
Wavelengths	λ_1 = 16R24*, λ_2 = 16R16, λ_3 = 16P20
Sample	Product collected on Ni impact plates
Analysis	SIMS depth profile
Accuracy	10-20% accurate
Alpha	6 – 8
Comments	Report on 235/238 ratio. No spectral interference suspected

Table 4.6 Selective irradiation experiments simulating the irradiation parameters specified for a typical MLIS plant.

September 1996 – July 1997: Operation Bulk Analysis I-III

This period saw an expansive investigation into the difference between the bulk analysed sample, and the in-line TOF mass spectrometer. Some dilution of the enriched sample occurs whilst in contact with the natural content of the non-irradiated process gas. The smaller the sample, the more pronounced the effect. Another effect that still needed investigation is the changed ionisation cross-section of the vibrationally hot UF_6 that have not dissociated in the process and the influence this has on the selectivity to ionise the uranium bearing product only.

Operation Bulk Analyses (OBA) was initiated to investigate numerous bulk techniques to measure selectivity and cut (the amount of product formed per irradiation pulse) and to explain the difference between the SIMS and the in-line TOFMS.

Techniques employed were:

SIMS	Secondary ion mass spectrometry of uranium bearing product;
TIMS	Thermal ionisation mass spectrometry;
LD-TOFMS	Laser desorption time-of-flight mass spectrometry;
ZYGO	Optical spectrometry for thickness measurement of product layers;

EDX Energy dispersive X-rays to measure uranium content and layer thickness; and

U-mass Chemical spectrophotometry to determine U-concentration.

Three experiments were planned and performed:

OBA1 Product was accumulated for 20,000 laser shots for a series of different laser irradiation parameters;

OBA2 Product was accumulated for 100,000 laser shots for the same series of laser irradiation parameters as in OBA1; and

OBA2 Repeat of OBA2 but with different sample platelets that showed little UF_6 absorption and less spectral interference.

The operation was extremely extensive. A few important conclusions were put forward originating from the results, of which the following is perhaps the most important. It was established that mass spectral interference from large carbo-hydrate molecules, later work on TOF-SIMS confirms this, can be found on the surface of some of the samples. Although this can be sputtered away in the SIMS depth profiling, care must be exercised when interpreting the depth profiles of uranium samples. The interference can cause apparent selectivity even for non-selective dissociations. Furthermore, the high enrichment factors that were previously measured with SIMS could not be repeated during the OBA experiments.

4.8 TOF-SIMS analysis of Collected MLIS Product

Time-of-Flight Secondary Ion Mass Spectrometry (TOF-SIMS) uses a pulsed primary ion beam to desorb and ionise species from a sample surface. The resulting secondary ions are accelerated into a mass spectrometer, where they are mass analysed by measuring their time-of-flight from the sample surface to the detector. The stigmatic imaging mass spectrometer of the raster primary ion beam encodes the location of the species on the surface. The mass spectrum and the secondary ion images are then used to determine the composition and distribution of the sample surface constituents.

The secondary ions generated during sputtering process do not leave the sample surface with the same kinetic energies. This leads to a broadening in the velocity distributions of species with the same mass. To compensate, TOF mass spectrometers using either retarding fields or reflectrons or hemispherical electrostatic analysers have been developed. The result is spectra with high mass resolution, capable of distinguishing species with mass differences of less than 0.03 amu at mass 235.

The combined high surface sensitivity (can analyse thin monolayers), low sample consumption (can analyse small amounts of product for hours on

end), and high mass resolution, makes TOF-SIMS ideally suited for the characterisation of collected MLIS products.

Analysis was performed on a PHI TRIFT II Time-of-Flight SIMS system, equipped with a triple sector mass analyser. A major strength of the TRIFT II analyser is its ability to provide energy compensation over a 200eV wide energy window. This is important for analysing elemental species, which have broad kinetic energy distributions, because the THRIFT II provides high mass resolution and the rejection of low energy metastable ions without any significant loss in signal levels (sensitivity). Alternative analyser technologies (reflectron analyser) can only provide accurate energy compensation over a narrow energy window of approximately 10eV.

Analysis of MLIS samples

The objective of the analysis was twofold:

(i) Characterisation of the MLIS product; and

(ii) Measure isotope ratio (measurement of enrichment alpha).

The analysis were performed in two phases, at first the double sided tape and samples B30, F7 and F22 were analysed to assess the nature of the

results, after which the rest of the samples were done. Table 4.7 gives a listing of the samples submitted for analysis:

NO	SAMPLE	DESCRIPTION
1	TAPE	Double-sided conductive tape, for sample adhesion
2	B30	IR irradiation, L1 resonant with 235 (12/4/96)
3	F7	Gas flow, no laser irradiation
4	F22	UV (266nm) irradiation, 6-7% cut
5	F81	IR irradiation, Old
6	EH7	UV irradiation, 2% cut, 2 000 laser shots
7	EH8	UV irradiation, 2% cut, 50 000 laser shots
8	RH2	Enrichment standard α=7
9	A88	IR irradiation, Operation Bulk Analysis III
10	B99	$UF_6 + H_2$, IR irradiation (experiment without CH_4)

Table 4.7. Summary of MLIS product samples submitted for analysis.

Experimental

1. Mass Spectral Analysis: a primary Ga^+ beam with energy of 15kV was used to scan the surface. This beam was electrodynamically compressed ("bunched") to provide sub-nanosecond primary beam pulses at the sample surfaces. In combination with the TRIFT spectrometer, this permitted high mass resolution spectra to be acquired.

2. Depth Profiling: depth profiling was achieved using the same 15kV Ga^+ beam. After analysis in a 30µm x 30µm area, the beam raster size was increased to concentrically to a 120µm x 120µm, and then 'unblanked' to produce a continuous Ga^+ beam which was used to sputter remove sample material. The sequence of analysis/sputtering proceeded, producing the depth profile. A higher depth resolution is achievable by changing the sputter beam to lower energies, but for the purpose of this preliminary investigation, the 15kV beam was sufficient

3. Pulse Mode Depth Profiling: the problem using the sequential analysis/sputtering procedure is that the sensitivity of TOF-SIMS is reduced significantly, since during the separate sputter phase, sputtered material is <u>not</u> analysed by the mass spectrometer. For this purpose a 'Pulse Mode' approach was used. At a high enough primary current and repetition rate (20nA, 20kHz) and into a small enough area (40µm x 40µm), the beam erode the near surface of the sample, producing near surface profiles at maximum sensitivity.

Results Phase 1:

<u>Conductive Double Sided Tape:</u>

Fig 4.22 shows a mass spectrum acquired from the conductive double-sided tape used to mount and transport the metal substrate disks. All the major peaks in the mass spectrum are assigned to polydimethyl siloxane PDMS. This compound is widely used as a release agent in the manufacturing of industrial polymer products. The PDMS contamination that has been observed on nearly all the MLIS samples is believed to have come from this tape material.

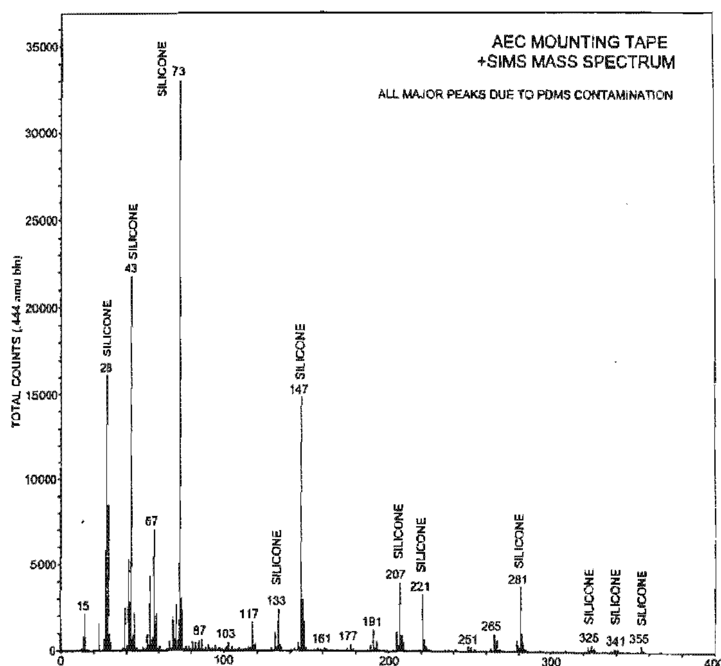

Fig 4.22 Positive TOF-SIMS spectra from the double sided tape.

Samples B30, F7 and F22:

For all three samples, a survey analysis was taken near the centre of the sample, in both +SIMS and -SIMS modes. Then following a light sputter etch with the primary ion beam to remove surface contamination, the analyses were repeated.

Fig 4.23 shows positive TOF-SIMS survey scans of the as-received samples. The rich ensemble of elemental and molecular peaks is typical of SIMS being operated in a static mode. Under these very low sputtering conditions, the sample surface stays virtually intact, and several spectra can be recorded without too much material consumption.

In +SIMS mode, logarithmic mass spectrum is shown for the three samples, and demonstrates the incredible amount of information that is available in a TOF-SIMS mass spectrum.

Fig 4.24 shows a narrow scan, 200 to 300 amu of the same samples. The same scan is repeated after a 30s surface cleaning etch shown in Fig 4.25. The UO_2 peaks are now much more prominent.

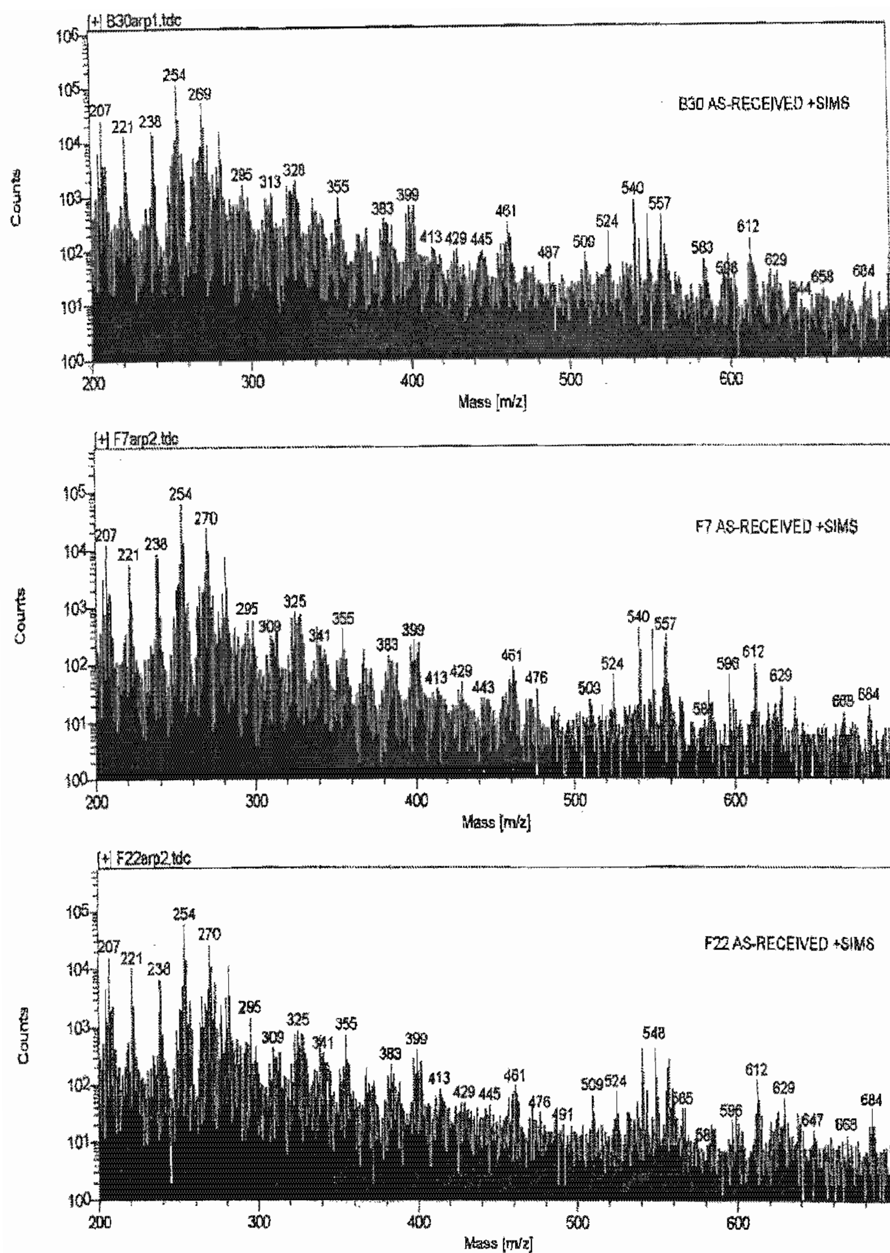

Fig 4.23 Positive TOF-SIMS spectra for as-received samples B30, F7 and F22 (200-800 m/z).

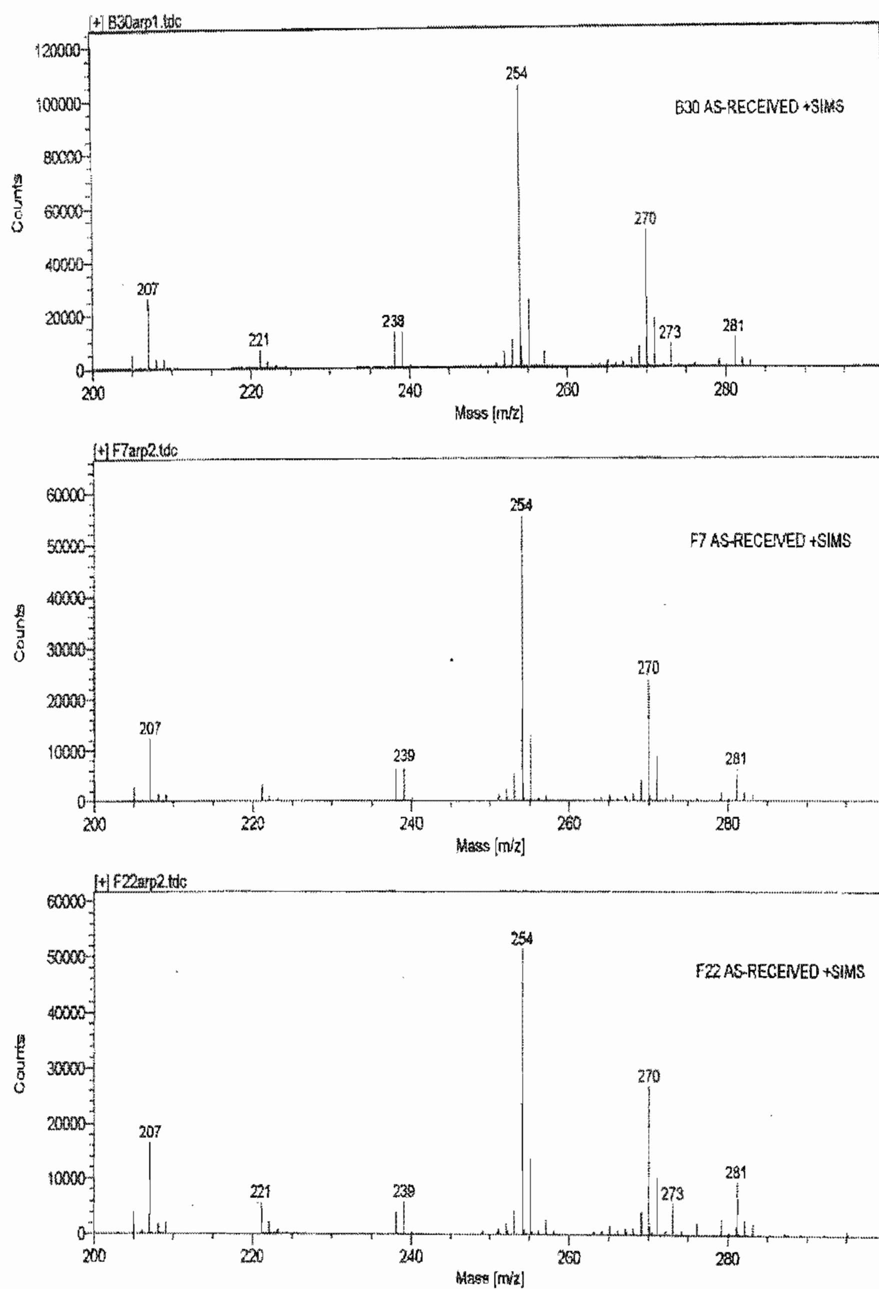

Fig 4.24 Positive TOF-SIMS spectra for as-received samples B30, F7 and F22 (200-300 m/z).

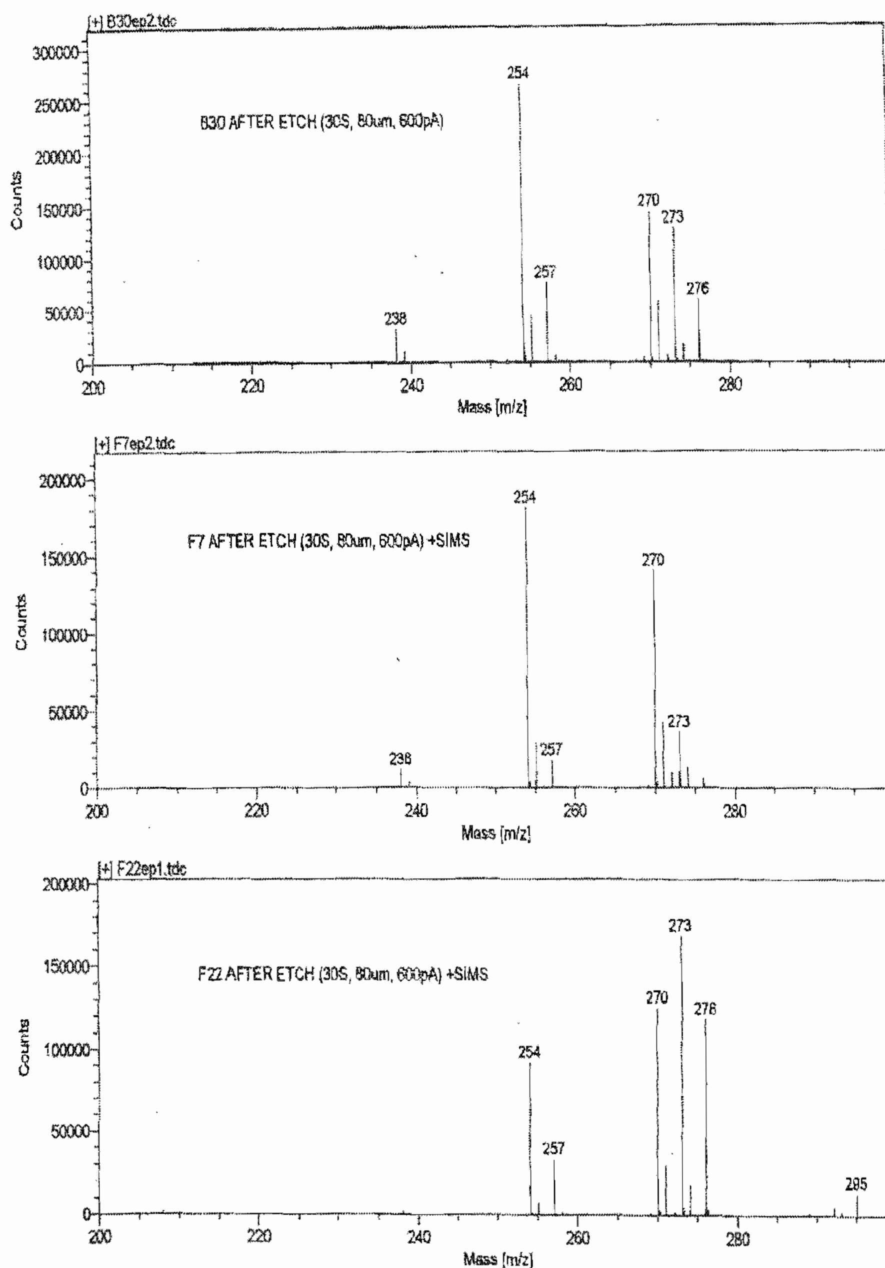

Fig 4.25 Positive TOF-SIMS spectra for 30s etched samples B30, F7 and F22 (200-300 m/z).

Positive TOF-SIMS depth profiles were done for sample B30. Species monitored included ^{235}U, ^{238}U, ^{235}UO, ^{238}UO, ^{238}UF, $^{235}UO_2$, ^{238}UOF, $^{238}UF_2$, $^{238}UF_3$, $^{238}UF_4$, Fe and $Si_3O_2C_7H_{21}$ (representing surface silicone contamination). Even though the TRIFT has a good mass resolution of more than 7000 amu, it was insufficient to separate the following interference: ^{238}UO (mass 254.0456) and ^{235}UF (mass 254.0423); and $^{238}UO_2$ (mass 270.0406) and ^{235}UOF (mass 270.0372). To resolve these interference a mass resolution of $R=M/\Delta M$ = 254/0/0033 = 76970 for the first interference and 79442 for the second one. The only spectrometer capable of resolving this kind of interference is Fourier Transform Magnetic Sector analysers. Unfortunately, the ionisation process associated with these analysers is laser desorption, which need large amounts of sample product to produce repeatable results.

Therefore, the TOF-SIMS depth profiles obtained for mass 254 and 270 would represent the concentration of the dominant species (^{238}UO and ^{238}UOF). Because TOF-SIMS is a parallel detection technique, all species are monitored simultaneously. Three profiles were taken under the same conditions:

(a) Very near surface, Fig 4.26

(b) Near surface, Fig 4.27

(c) Deeper into near surface Fig 4.28, with expansions in Figs 4.29-4.33.

Only those for sample B30 are shown.

The data is plotted as intensity vs. sputter time. The time axis can be converted to depth when a suitable standard is profiled under the same conditions and its crater depth subsequently measured (or if a sputter rate is known for the material being profiled). Unfortunately, no standard was available at the time that these analyses were performed. Furthermore, it is anticipated that the making of such a representative standard would be extremely difficult, as so many different U-containing species are observed. In addition the surface flatness of the metal substrates were larger than the order of thickness of the collected product layer. The resulting SIMS crater would therefore follow the surface roughness contour of the substrate, hence, complicating the already complex TOF-SIMS depth profiles. A better sample collector platelet would be smooth CaF_2 substrates.

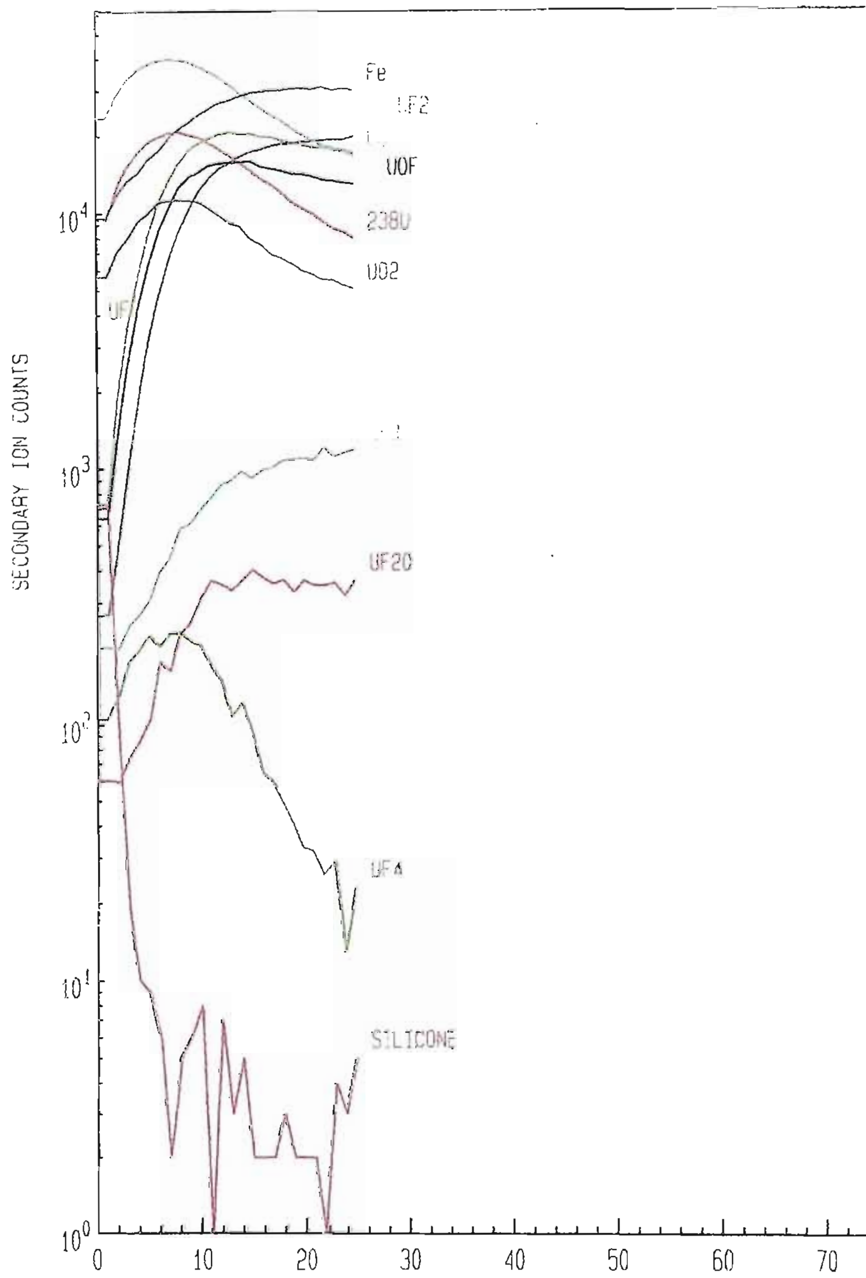

Fig 4.26 Positive TOF-SIMS depth profiles in the very near surface.

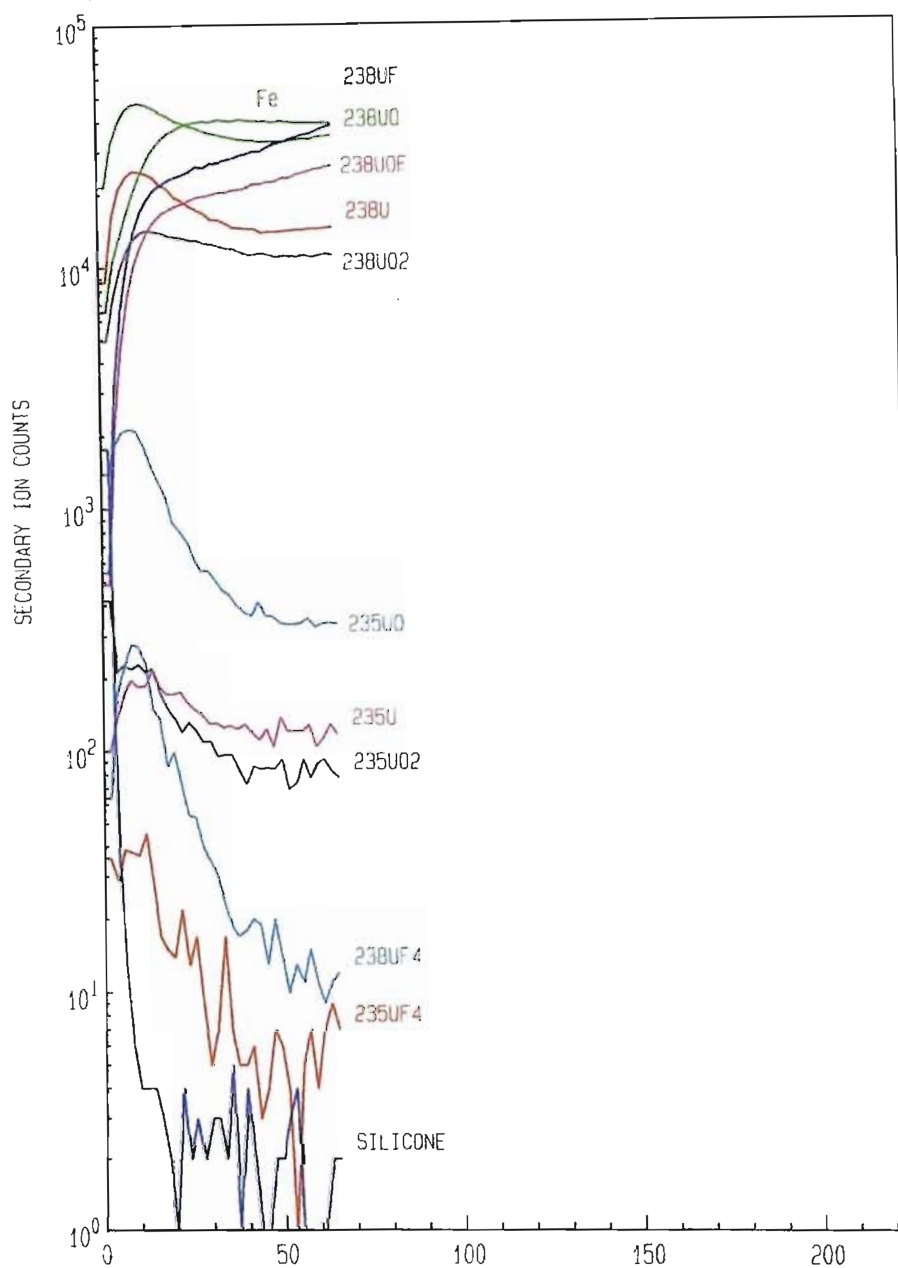

Fig 4.27 Positive TOF-SIMS depth profiles in the near surface.

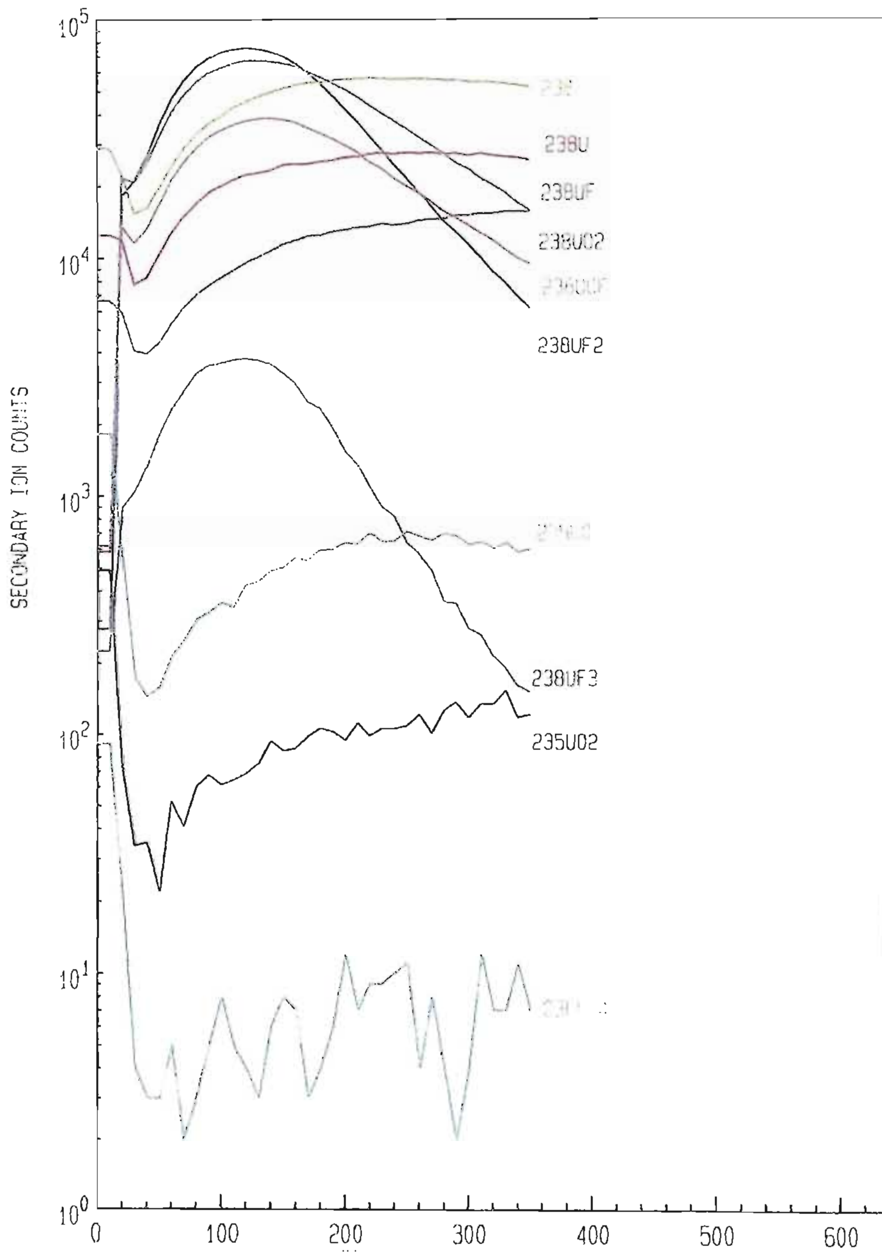

Fig 4.28a Positive TOF-SIMS depth profiles deeper into the near surface.

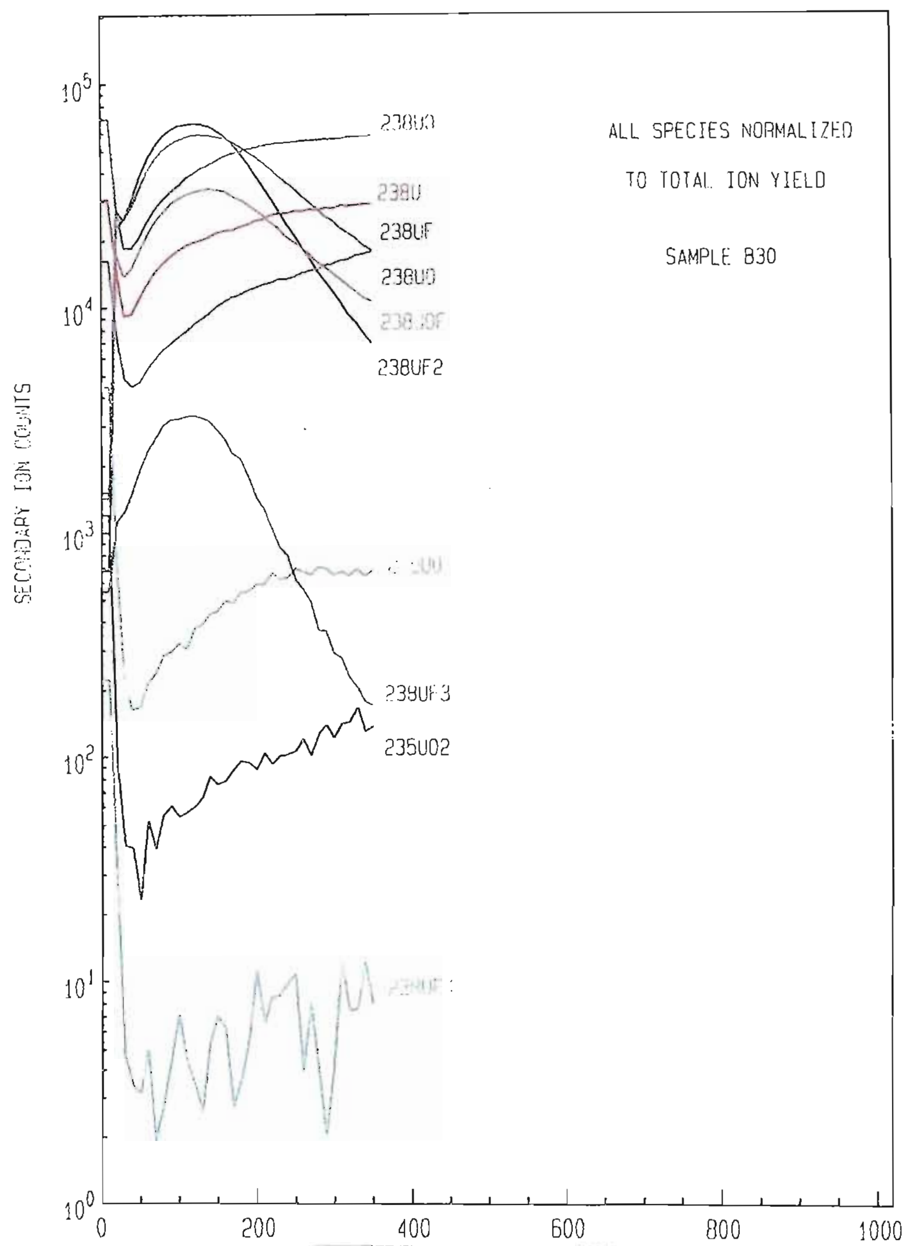

Fig 4.28b Positive TOF-SIMS depth profiles deeper into the near surface.

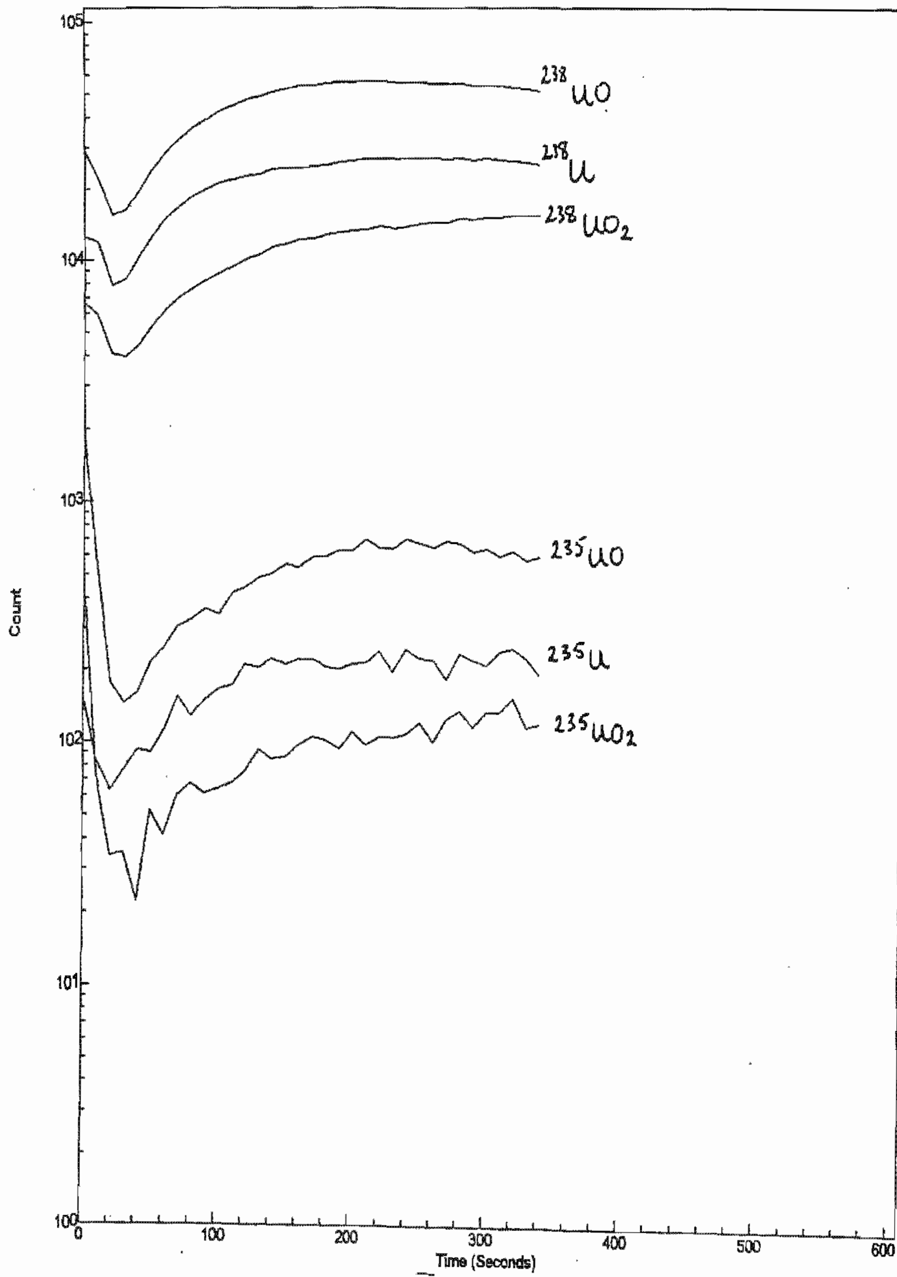

Fig 4.29 TOF-SIMS depth profiles deeper into the near surface for U, UO and UO_2.

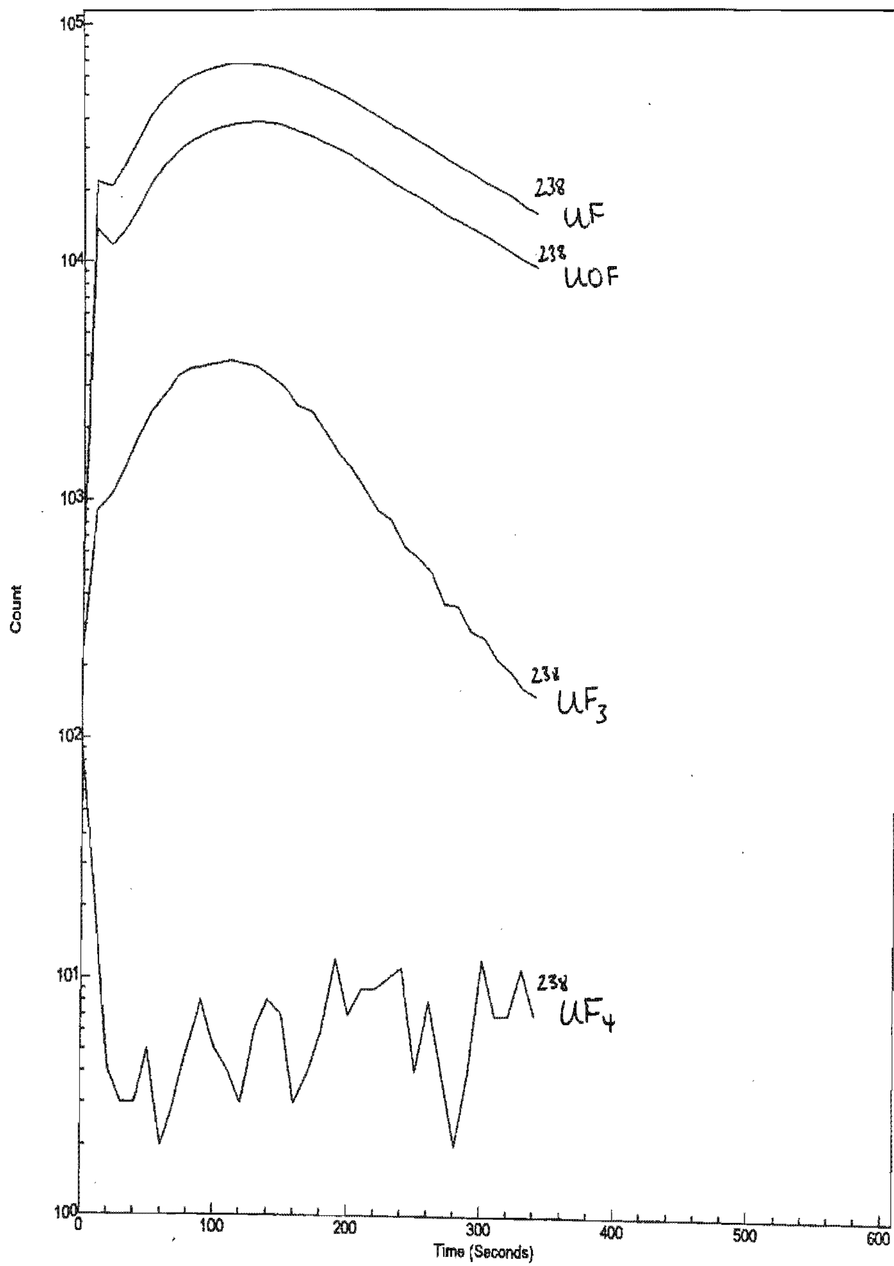

Fig 4.30 TOF-SIMS depth profiles deeper into the near surface for UOF and UF_X.

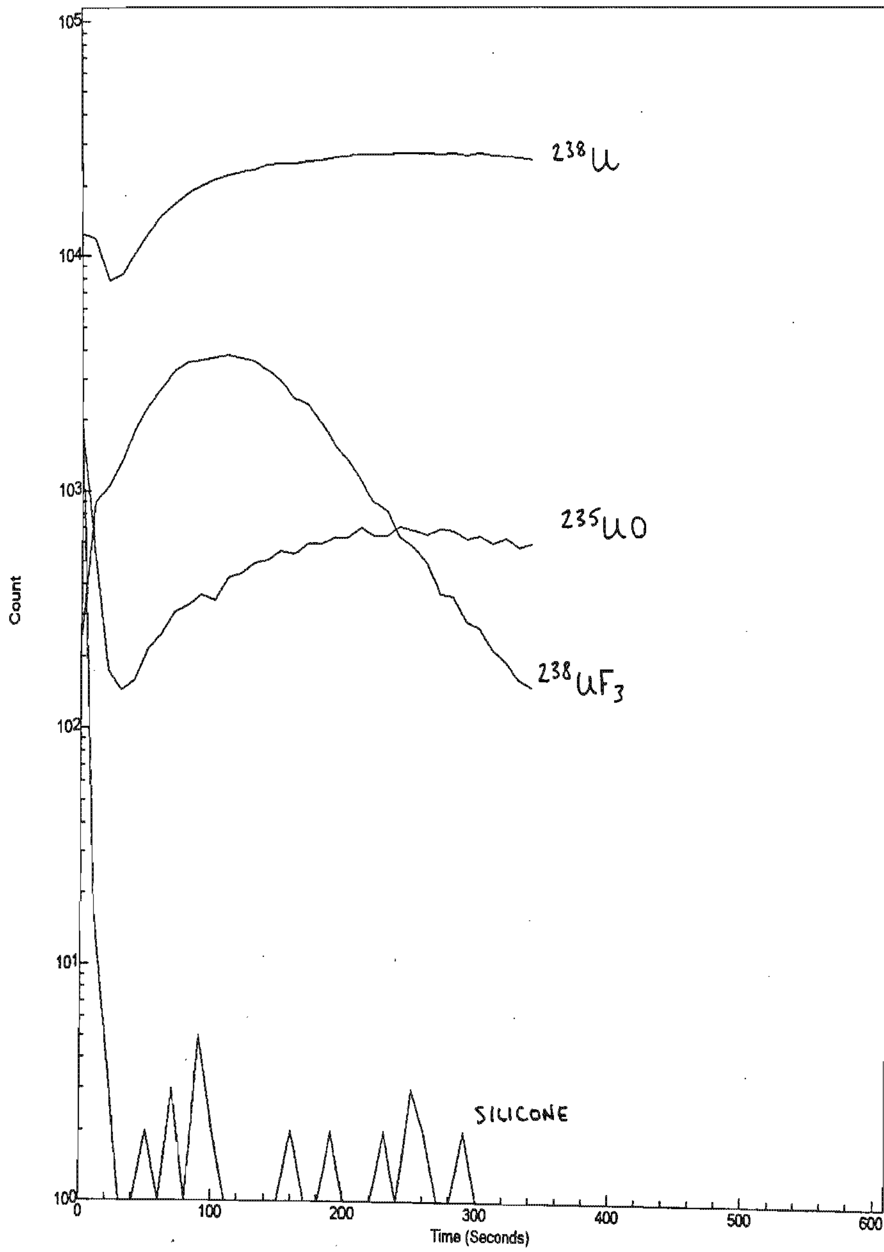

Fig 4.31 TOF-SIMS depth profiles deeper into the near surface for U, UO and UF_3.

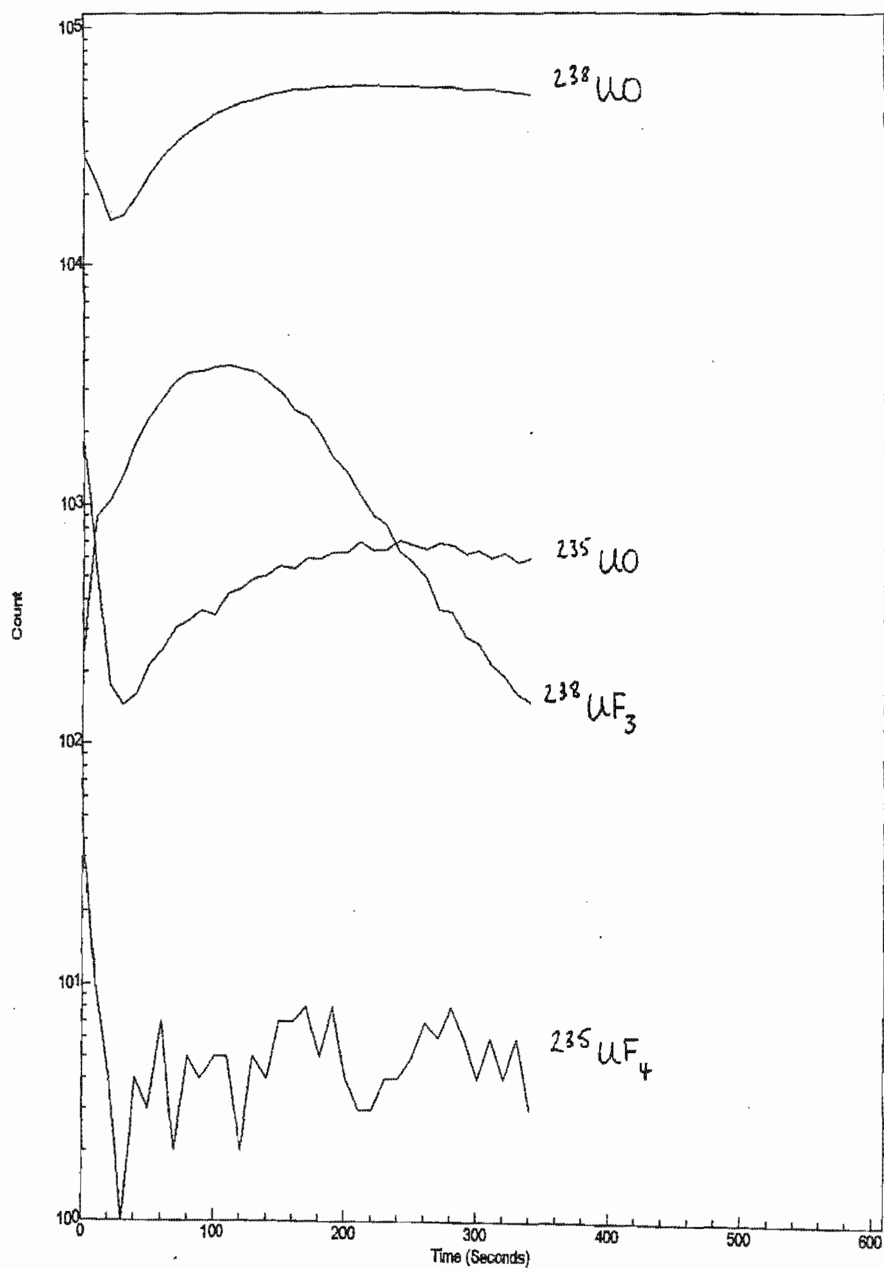

Fig 4.32 TOF-SIMS depth profiles deeper into the near surface for UO, UF_3 and UF_4.

Measurement of the ^{235}U isotopic signal at the outer surface of the sample is complicated by organic interference at mass 235. In order to make a measurement of the ^{235}U signal, a very narrow mass window must be used around the centroid of ^{235}U to minimise the contribution from organics. The data are shown in Table 4.8. Similar organic interference complicates the measurement at UO. For instance, ^{238}UCH interferes with ^{235}UO.

After sputter cleaning (etching) with the primary ion beam, the organic contributions are removed at mass 235, and indeed at the higher masses. Also, after sputter cleaning, the intensity of the UO and UO_2 signals increases. The ratio measurements for 235/238, are thus made after some surface cleaning of organic material. The data is shown in Table 4.9. Because of the intensity of the oxide peaks, these have been used to make the ratio measurements.

SAMPLE	CONDITION	^{235}U	^{238}U	TOTAL	%235
F7	Surface	1135	140745	141880	0.80
F22	Surface	1415	170478	170745	0.82
B30	Surface	1243	143909	145152	0.85

Table 4.8 TOF-SIMS isotopic measured values for U on as-received surfaces.

SAMPLE	CONDITION	^{235}UO	^{238}UO	$^{235}UO_2$	$^{238}UO_2$	TOTAL	%235
F7	Cleaned	1654	182032	1168	141200	326054	0.86
F22	Cleaned	828	102032	1017	129252	233129	0.79
B30	Cleaned	2926	275846	1421	146183	426376	1.01

Table 4.9 TOF-SIMS measured isotopic values for UO and UO_2 after sputter cleaning.

Conclusion Phase 1

(a) Siloxane contamination: all samples were contaminated by the compound polydimethyl siloxane (PDMS). This compound is widely used as a release agent in the manufacturing of industrial polymer products. Since all three samples were stuck to double-sided tape, which has shown the presence of large amounts of PDMS, it is likely that the PDMS had "crawled" up and over the samples (PDMS is very surface active). Consequently, all the

intense secondary ions detected in the low mass region (0-200 m/z) of the positive spectrum are assigned to various fragments from PDMS. For instance, the peaks at 28, 43, 73, 147, 207, 221 and 228 are due to Si, $SiCH_3$, $Si(CH_3)_3$, $Si_2OC_5H_{15}$, $Si_3O_3C_5H_{15}$, $Si_3O_2C_7H_{21}$ and $Si_4O_4C_7H_{21}$ respectively. In the negative SIMS data, peaks at 60 and 75 are due to SiO_2 and $SiOC_2H_5$ (not shown here). These and other surface organics tend to complicate the measurement of the 235/238 isotope ratios.

(b) The major U-related peaks above 200 m/z in the positive SIMS spectra of the as-received samples are U(238), UO(254), UO_2(270), UOF(273), UF_4(314), U_2O_3(524), U_2O_4(540), U_2O_3F(543) and U_2O_5(556). Peaks that are not yet assigned, but are surely U containing are 313, 323, 328, 339, 355, 368, 402, 423 and 461. Mass 325 is another siloxane peak.

(c) After sputter etching, the low mass organic material observed in the positive SIMS is removed, and Na, Al, K, Cr, Fe and Ga (implanted from the primary beam) are seen as intense peaks. Due to the high intensity of Na and K on sample B30, they were deliberately blanked from the spectra in order to measure the other less intense peaks (by setting a time delay before starting the detector). After sputter etching, the U oxides are increased in intensity, and now the

U oxyfluorides are much more evident. The intensity of the UF_4 (mass 314) is considerably lower after this sputter etching.

(d) In the negative SIMS spectra from the as-received samples, oxygen is the most intense peak, although the fluorine level is significant too. The reader should be reminded that in SIMS there are different relative sensitivities for different species - any direct comparison on the amounts of each species present is purely qualitative. Quantitative measurements are indeed possibly if applicable standards are provided. In the higher mass region above 200 m/z, U-related peaks such as UO_2(270), UO_3(286), UO_2F(289), U_2O_5(556), U_2O_6(572) and U_2O_5F(575), are clearly observed. A host of low intensity peaks are also observed which are not yet assigned.

(e) After sputter etching, the negative SIMS spectra also show an increased yield of oxide and oxyfluoride peaks. In addition, intense signals from CN(26), Cl(35) and phosphates (PO_2, PO_3), were observed. Mass 85 is due to GaO (primary beam artefact).

(f) In the depth profiling data for the very near surface region on sample B30, the silicone contaminant falls away at the very outer few monolayers, as expected. The intensities of all the F-containing

peaks increase with depth, except UF_4. The uranium and uranium oxide peaks (UO and UO_2) all appear to reach a peak at the near surface and then begin to fall in intensity. The depth profile for the near surface shows similar trends. However, in the depth profile for the deeper region, the uranium and uranium oxide peaks fall immediately from the outer surface, but rise up later and effectively level out in the sample. The F-containing peaks rise sharply form the outer surface (with the exception of UF_4 which fall from the outer surface), and then peak and fall away. The UF_3 signal demonstrates this most dramatically. Clearly these profiles need to be depth calibrated with suitable standards. The different shapes of the ^{235}UO and ^{238}UO signals seems to indicate a change in the 235/238 ratio as a function of depth, however, this is not shown in the atomic ^{235}U and ^{238}U signals, nor in the $^{235}UO_2$ and $^{238}UO_2$ signals. This is likely due to the organic interference of ^{238}UCH at the same mass as ^{235}UO. As the organic is removed by sputtering, the peak at mass 251 represents the true ^{235}UO signal.

(g) Uranium isotope ratios: These are expressed purely by making a simple calculation of the (235 signal) / (235 + 238 signal), expressed as a percentage. In SIMS measurements of isotope ratios, there are various effects which can shift an isotope ratio to a higher value than the published abundance, namely dead time correction of

the detector for intense masses, mass-dependant quantum efficiency of the detector, other possible mass interference (^{234}UH), and so on. Ideally, a known standard would be measured at the same time. Unfortunately none was available at the time of the analysis.

(h) In conclusion of Phase 1, the following remarks:

- Origin of PDMS surface contamination is the double-sided tape;
- Additional surface organics complicate the already complex depth profiles;
- Different shapes of the depth profiles of the uranium, uranium oxides and uranium fluorides, were observed;
- 235/238 ratio measurements are strongly influenced by mass interference;
- No significant differences in the presence of the different U-containing species could be seen between the three different samples.

PHASE 2:

In Phase 2 clarity on the following two issues were sought after:

- At high mass resolution, what is the extent of mass interference effecting 235/238 ratio measurements; and
- Extend depth profiles to include 235/238 ratio calculations on U, UO, UO_2, UF_3, and UF_4.

Mass Spectral Data

Mass spectral data over the mass range 200-350 m/z were acquired for samples F81, EH7, EH8, RH2, A88 and B99. Fig 4.33 shows a typical spectrum acquired from sample F81. These spectra are cumulative spectra acquired during the near surface profiles. These are not top surface spectra. Because of this, the major peaks in this mass range include F-containing masses, which are not so prominent at the outer surface (as were seen in Phase 1). Also, the PDMS peaks (which are annotated in the spectra) have a relatively low intensity, because once removed from the outer surface, they no longer dominate.

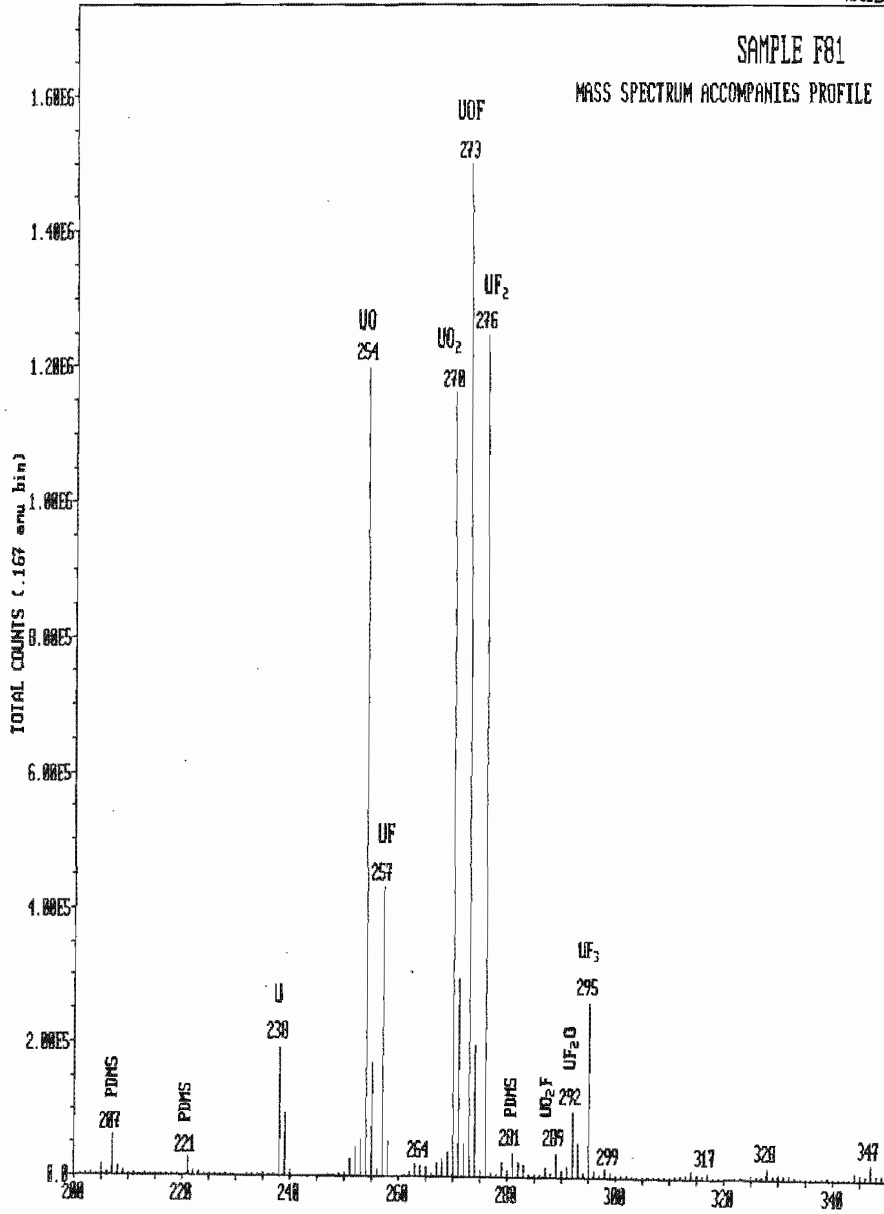

Fig 4.33 Positive TOF-SIMS spectrum for sample F81 (200-350 m/z).

To evaluate the mass interference at the important U-containing mass peaks, narrow mass ranges around the peaks of interest were recorded. The maximum mass resolution performance is achieved with 600pA to 2nA primary Ga beams (the 20nA beam suffers a 10-20% loss of mass resolution). A mass spectrum at mass 235 taken with a 2nA beam from sample F81 is shown in Fig 4.34. There are three distinctive mass peaks, only one of which is the ^{235}U peak. For the equivalent data acquired on sample F81 with a 20nA beam (Fig 4.35), the slight reduction in mass resolution means that the middle (organic) peak is not distinguishable from the ^{235}U peak. Analysis with lesser mass resolution capability would therefore measure a higher ^{235}U content than what is actually present in the sample. A minimisation of organic interference would greatly assist in the accurate determination of this particular ratio.

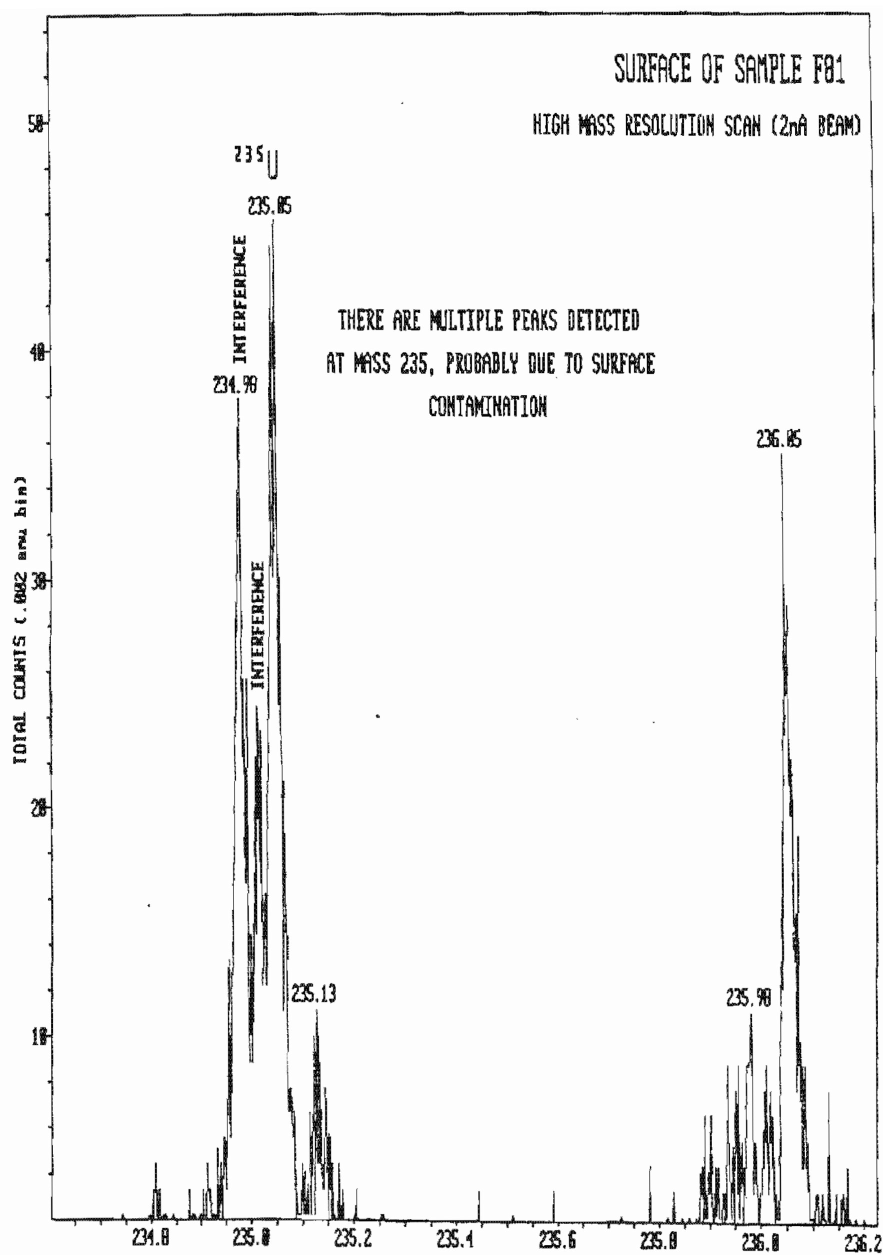

Fig 4.34 High mass resolution TOF-SIMS spectrum (2nA beam) for sample F81 at mass 235.

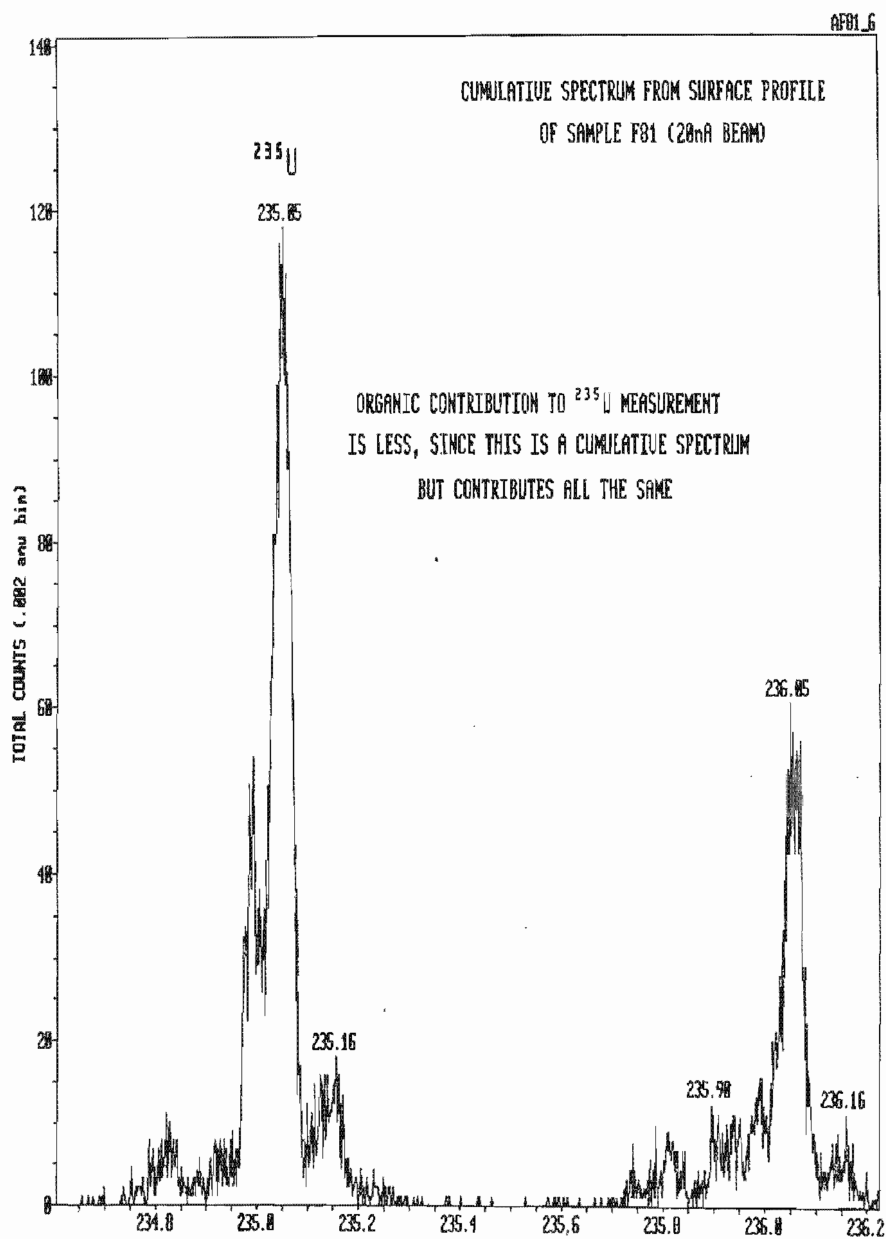

Fig 4.35 Medium mass resolution spectrum (20nA beam) for sample F81 at mass 235.

For surface contaminated samples, the measurement of ^{235}UO and $^{238}UO_2$ is complicated by the interference due to ^{238}UCH and $^{238}UOCH$. Even at the highest mass resolution available in TOF-SIMS, it is unlikely that these interference will be fully resolved. In Fig 4.36 a high mass resolution (2nA beam), narrow mass (265.7 - 267.6 m/z) surface scan for UO_2 from sample F81, is shown. There is a possible interference from $^{238}UOCH$ (267.0535).

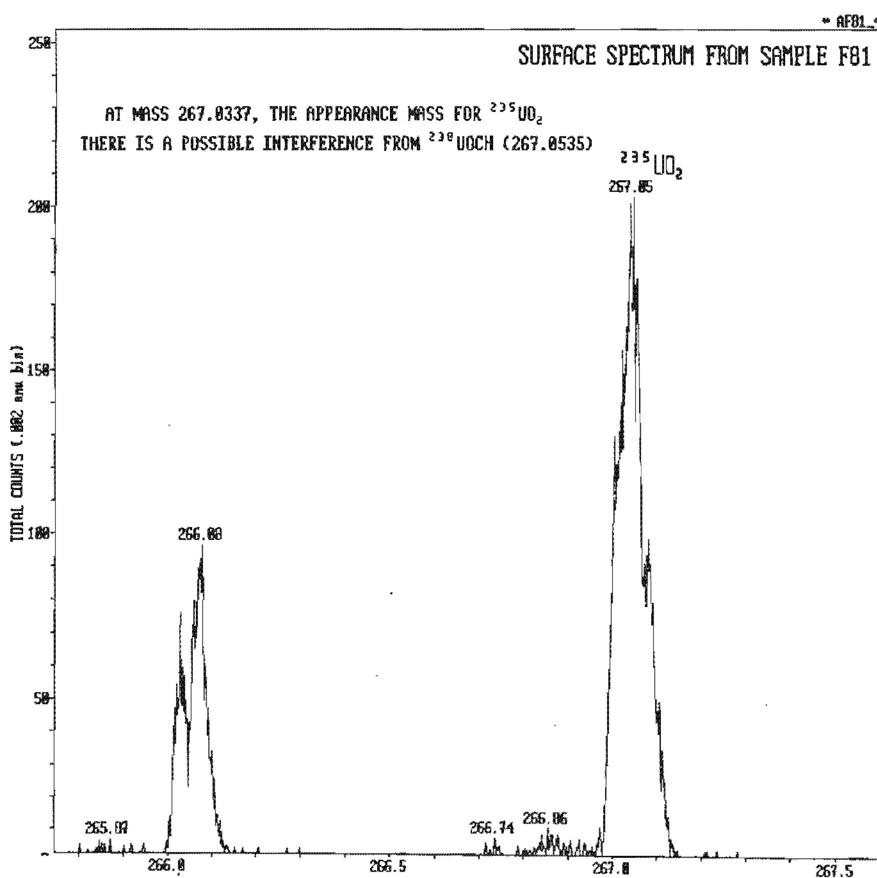

Fig 4.36 High mass resolution TOF-SIMS spectrum (2nA beam) for sample F81 at mass 267.

Fig 4.37 shows even narrower mass scans around mass 267 on sample F81. The appearance windows for both ^{235}U and $^{238}UOCH$ are indicated, showing clearly the overlap that cannot be resolved at the highest possible TOF-SIMS resolution.

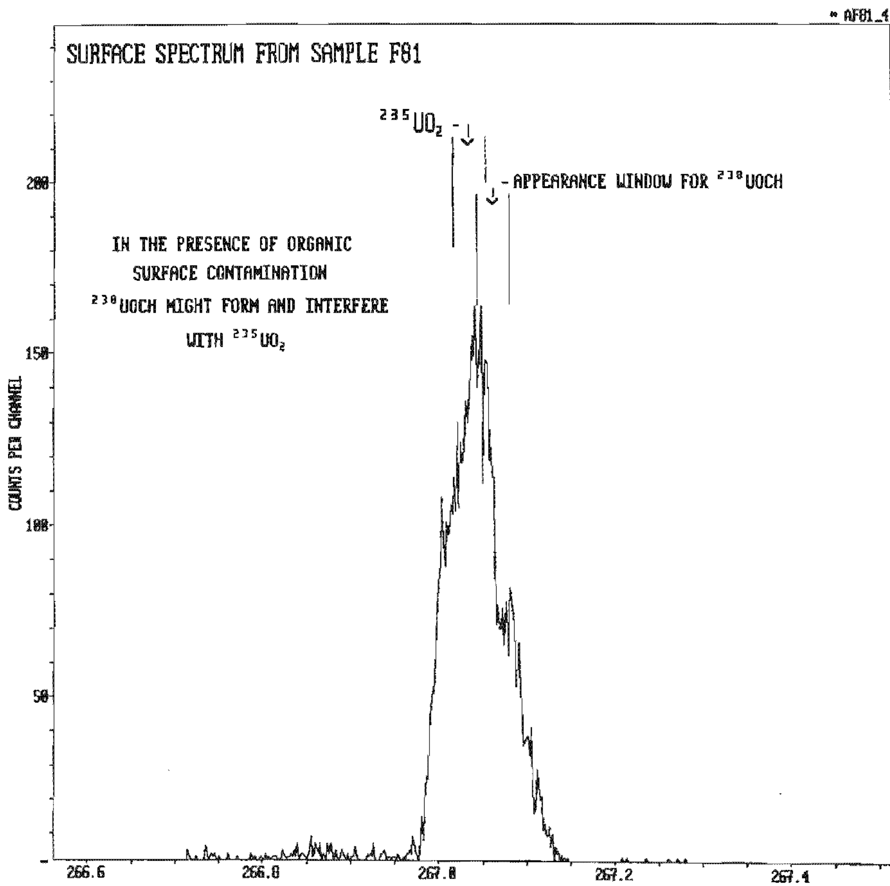

Fig 4.37 High mass resolution TOF-SIMS spectrum (2nA beam) for sample F81 at mass 267, indicating the appearance windows for $^{235}UO_2$ and $^{238}UOCH$.

Fortunately, the intensities of the $^{235}UO_X$ species increase dramatically away from the outer surface, where the organic contribution is reduced. Consequently the measured alpha values are nearer to the truth. It would appear therefore, that the UO and UO_2 ratios will be the most useful for monitoring the uranium enrichment in positive TOF-SIMS., provided:

- samples can be created which are contamination-free, and
- the mass biases for ionization efficiency and detection efficiency between ^{235}U-containing species and ^{238}U-containing species can be accurately quantified for TOF-SIMS.

In Fig 4.38, the $^{238}UF_3$ peak is identified unambiguously by software at mass 294.04. There is very low intensity organic interference at a slightly higher mass that appears as a "shoulder" on the $^{238}UF_3$ peak. However, at mass 292, where the $^{235}UF_3$ mass would appear, there is a significantly larger peak due to the $^{238}UF_2O$ peak (see Fig 4.39). After sputter etching deeper into the surface, the problem becomes even worse. Now, the F-containing peaks are more intense, and the $^{238}UF_2O$ peak completely swamps the low intensity $^{235}UF_3$ peak (see Fig 4.40). The same situation occurs at mass 311, where $^{235}UF_4$ would be found, since there is more intense $^{238}UF_3O$ (see Figs 4.41-4.42).

Thus, although $^{238}UF_3$ and $^{238}UF_4$ can be identified quite clearly in the mass spectra, there will be little chance to determine $^{235}UF_X$ / $^{238}UF_X$ ratios because of the interference at $^{238}UF_{(1-X)}O$.

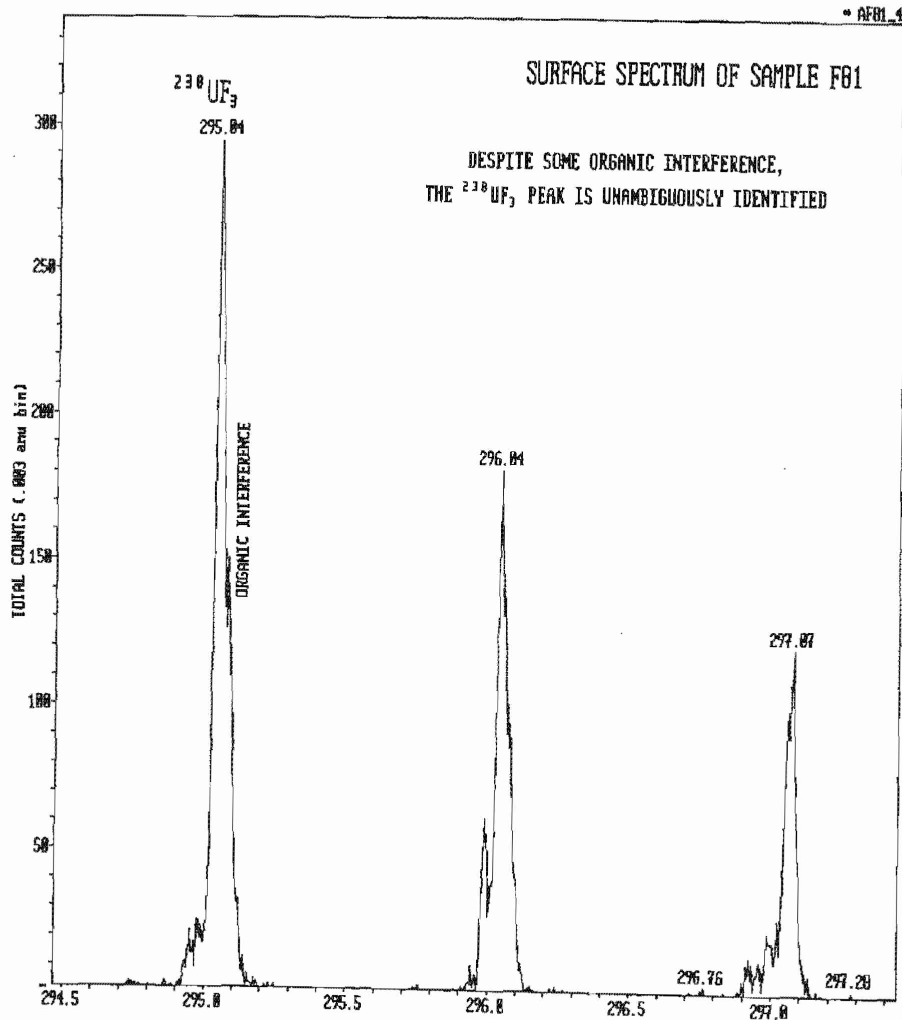

Fig 4.38 TOF-SIMS spectrum (294.5 - 297.4 m/z) showing $^{238}UF_3$ present on sample F81.

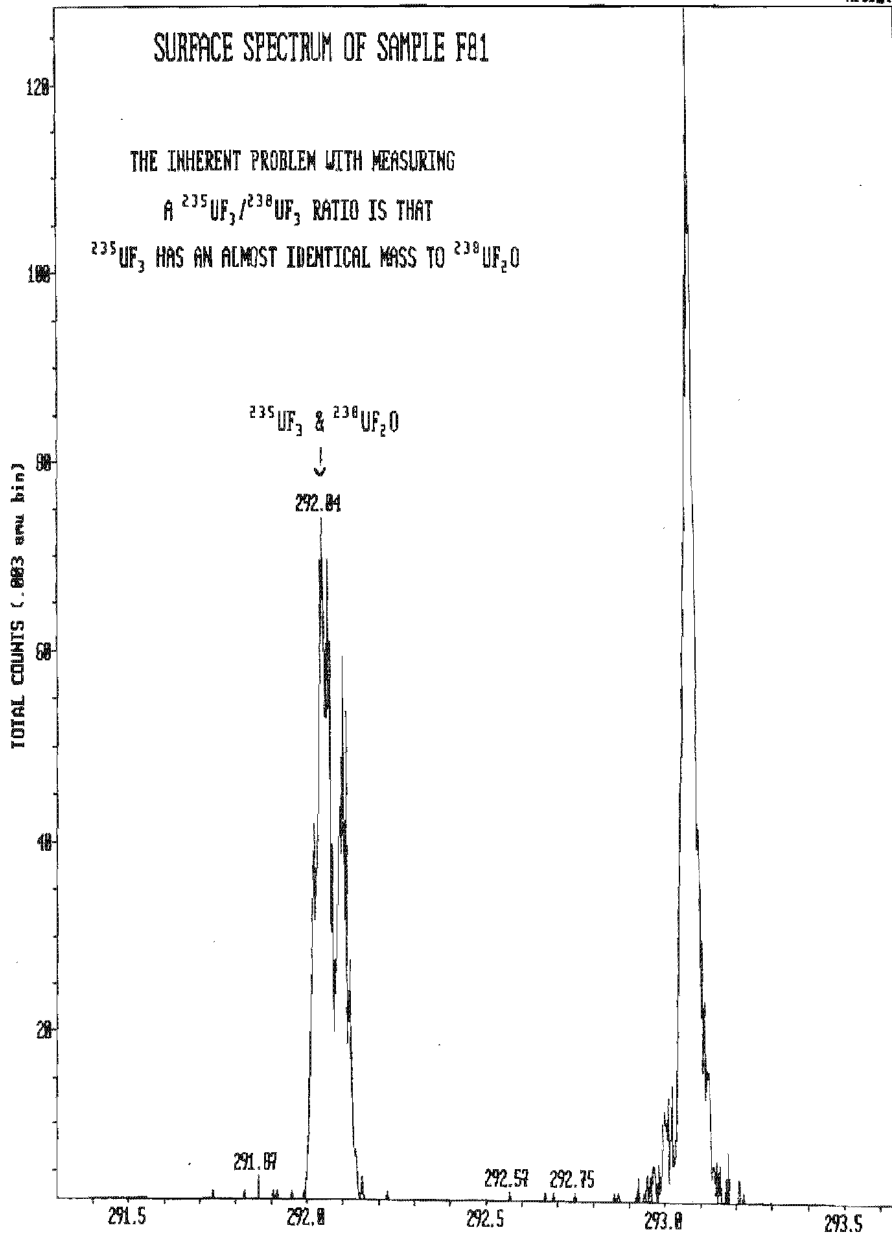

Fig 4.39 TOF-SIMS spectrum (291.3 - 293.7 m/z) showing interference at $^{235}UF_3$.

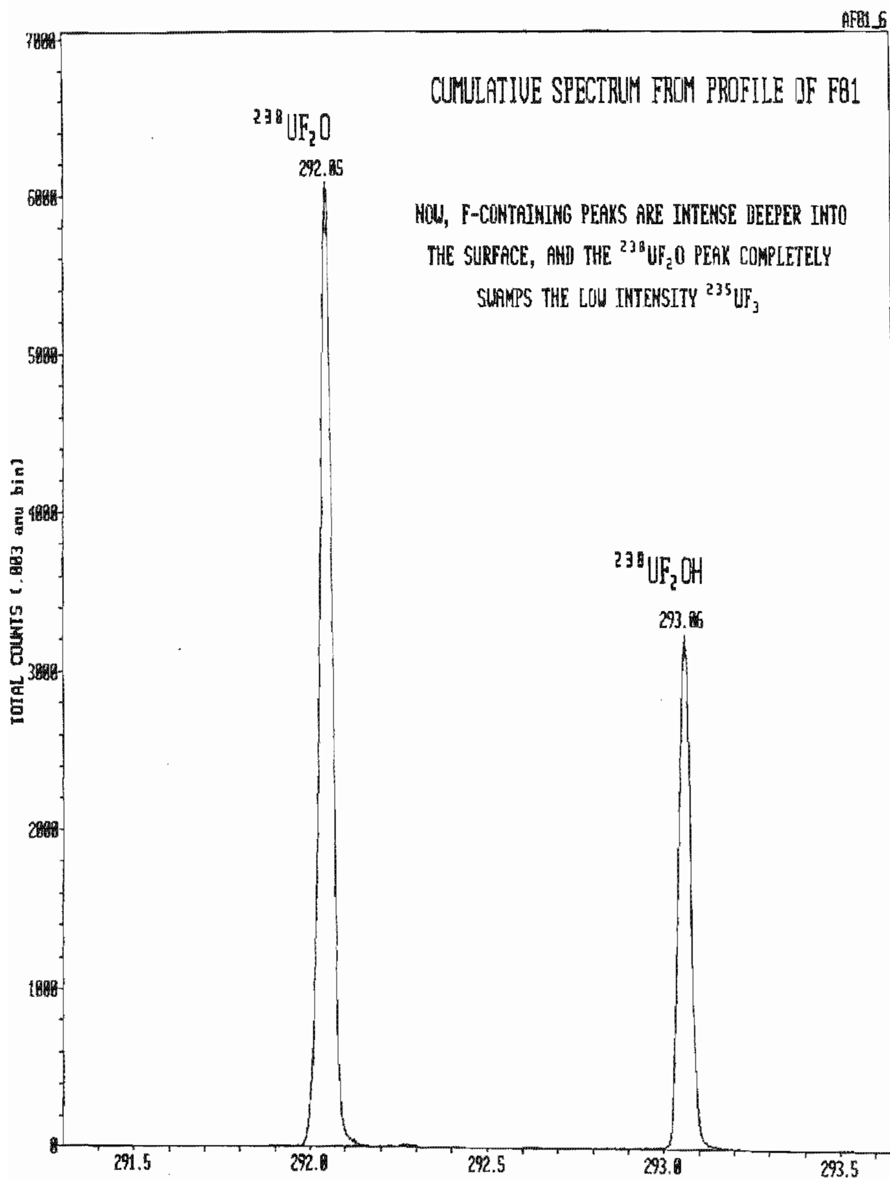

Fig 4.40 TOF-SIMS spectrum (291.3 - 293.7 m/z) showing the overwhelming of $^{235}UF_3$ by $^{238}UF_2O$ after sputter etching.

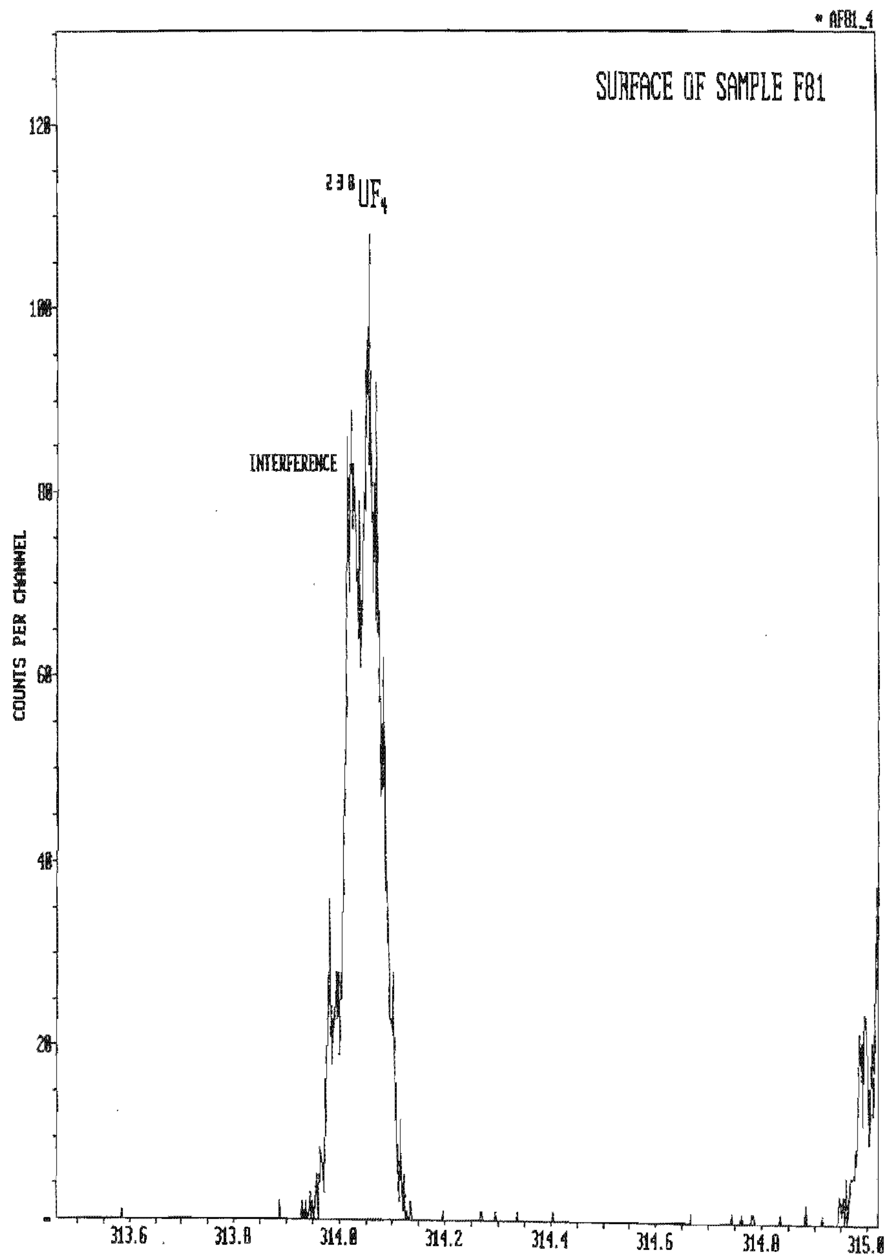

Fig 4.41 *TOF-SIMS spectrum (313.3 - 315 m/z) showing $^{238}UF_4$ present on sample F81.*

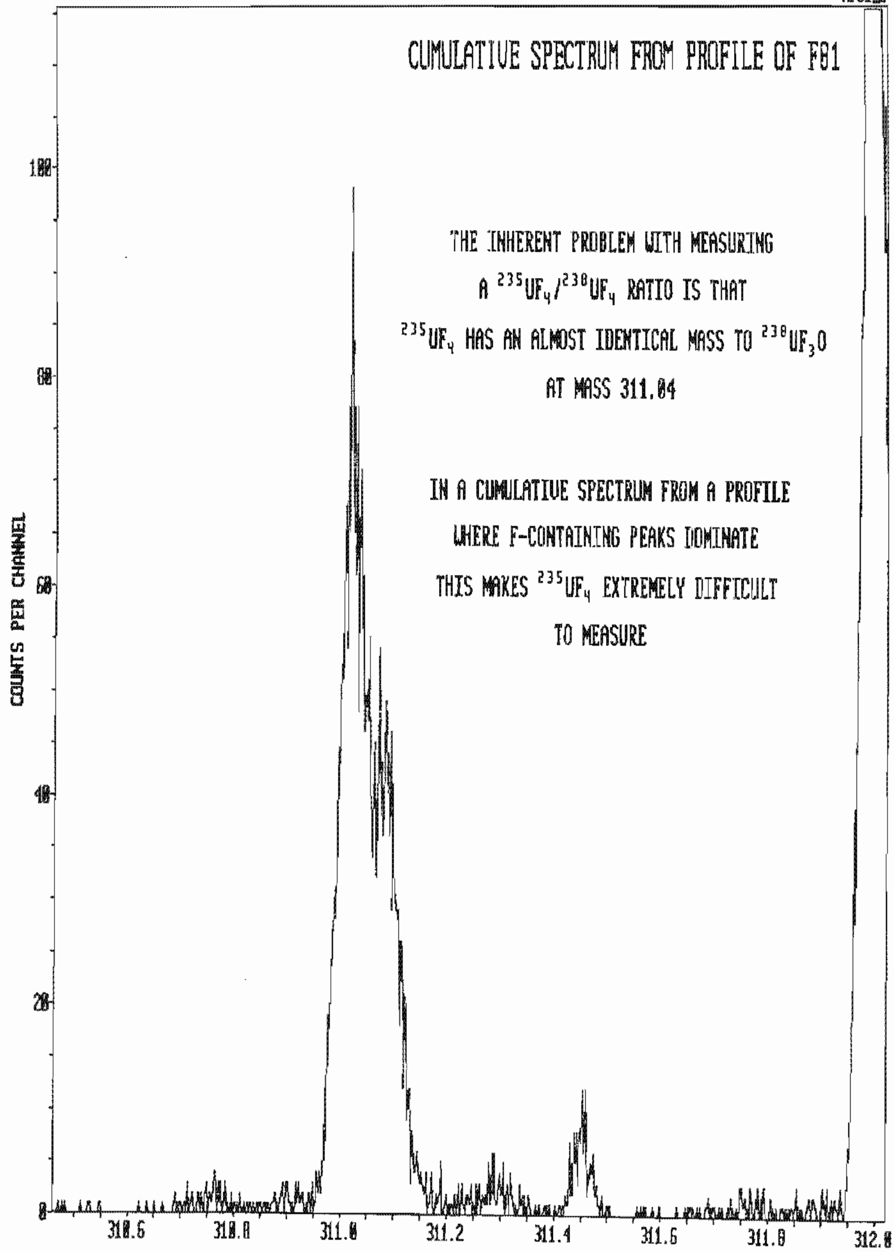

Fig 4.42 TOF-SIMS spectrum (310.3 - 312 m/z) showing interference at $^{235}UF_4$.

Near Surface Profiles

The depth profile data for the various samples were acquired. Figs 4.43 – 4.49 show these depth profiles for sample F81. The data is organised as follows:

- Fig 4.43 showing ^{238}U-containing species as counts vs. depth;
- Fig 4.44 showing ^{235}U-containing species as counts vs. depth (although the mass 292 peak, for reasons given above, is due to $^{238}UF_2O$, not $^{235}UF_3$);
- Fig 4.45 the ^{235}U / $^{238}U \times 140$ ratio vs. depth;
- Fig 4.46 the ^{235}UO / $^{238}UO \times 140$ ratio vs. depth;
- Fig 4.47 the $^{235}UO_2$ / $^{238}UO_2 \times 140$ ratio vs. depth;
- Fig 4.48 the $^{235}UF_3$ / $^{238}UF_3 \times 140$ ratio vs. depth; and
- Fig 4.49 the $^{235}UF_4$ / $^{238}UF_4 \times 140$ ratio vs. depth.

The depth axes on all the plots are in arbitrary units

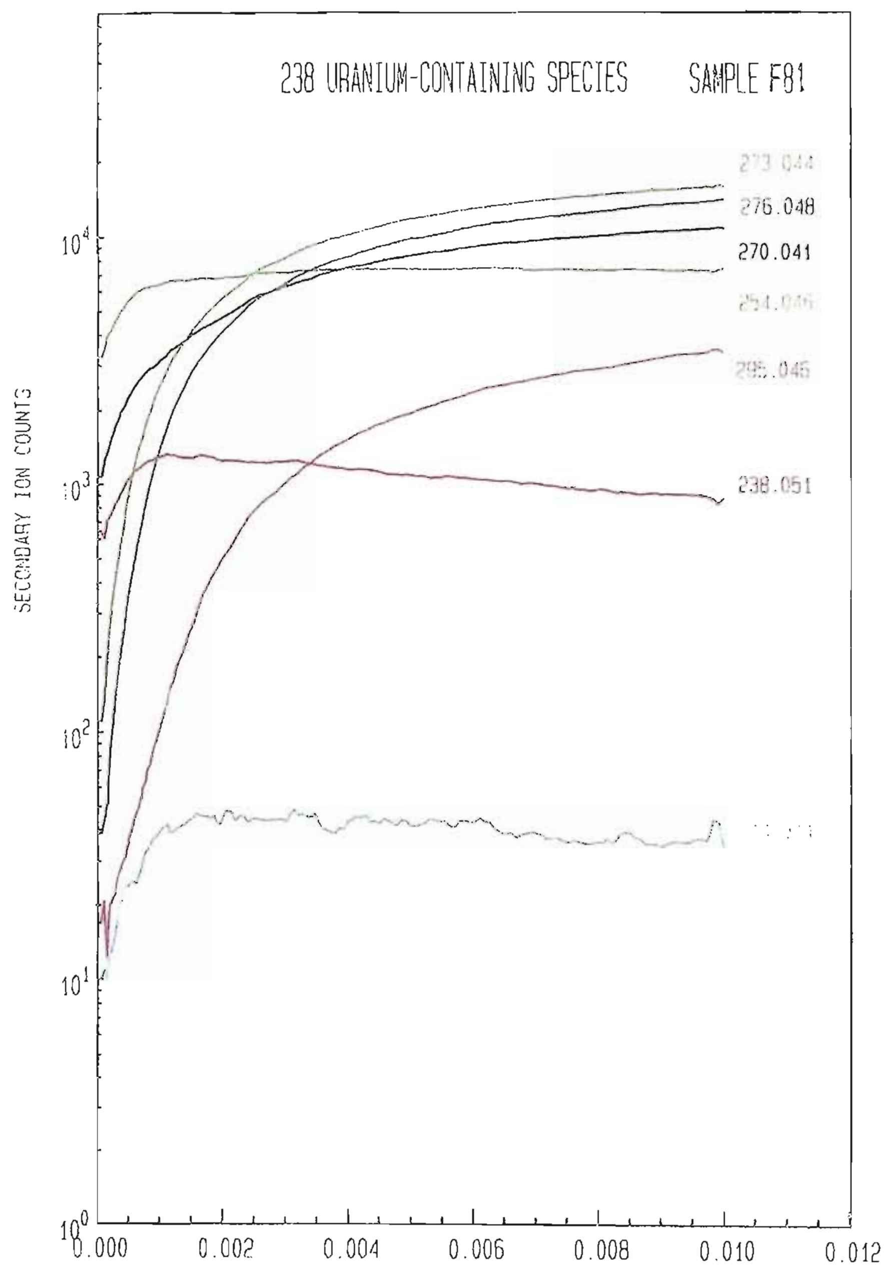

Fig 4.43 TOF-SIMS near surface depth profiles for ^{238}U-containing species on Sample F81.

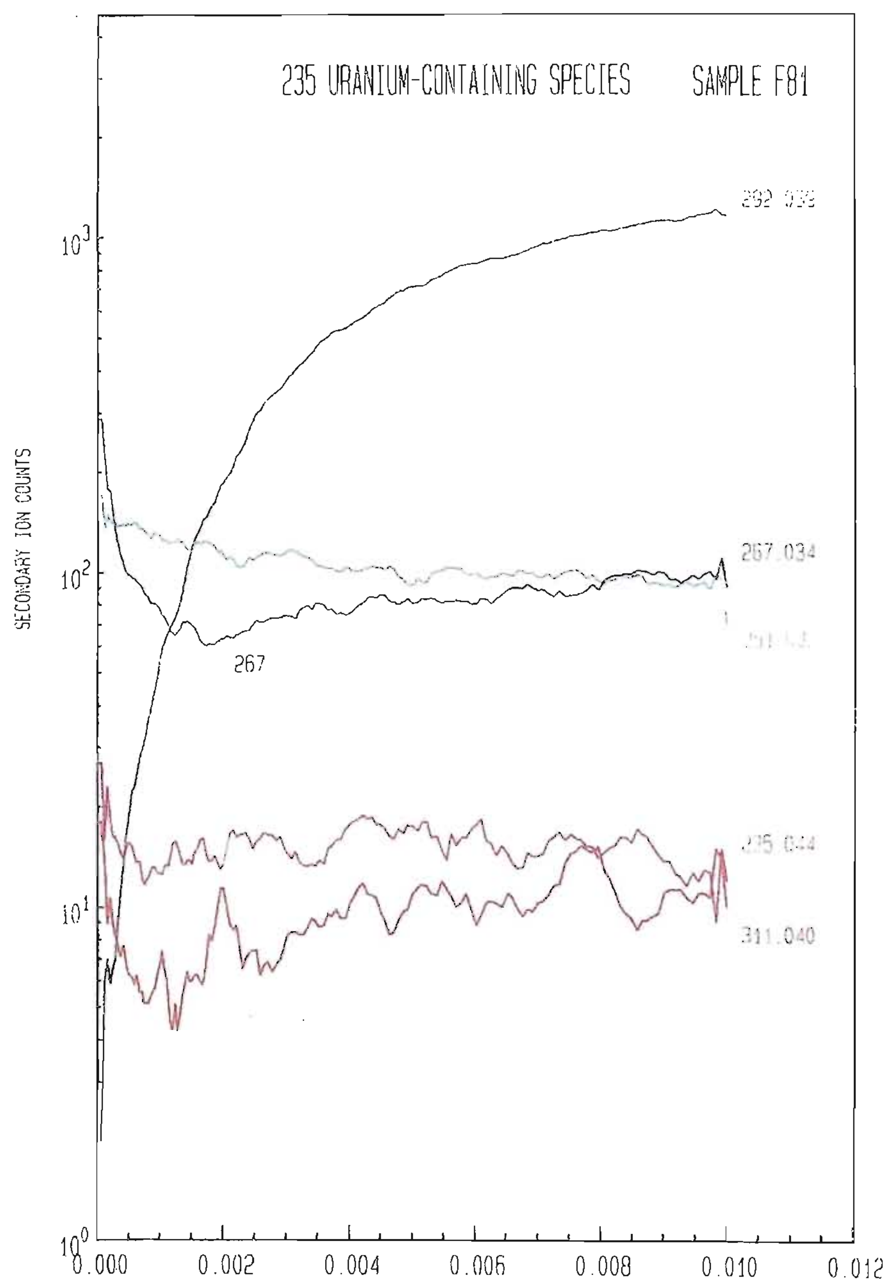

Fig 4.44 TOF-SIMS near surface depth profiles for ^{235}U-containing species on Sample F81.

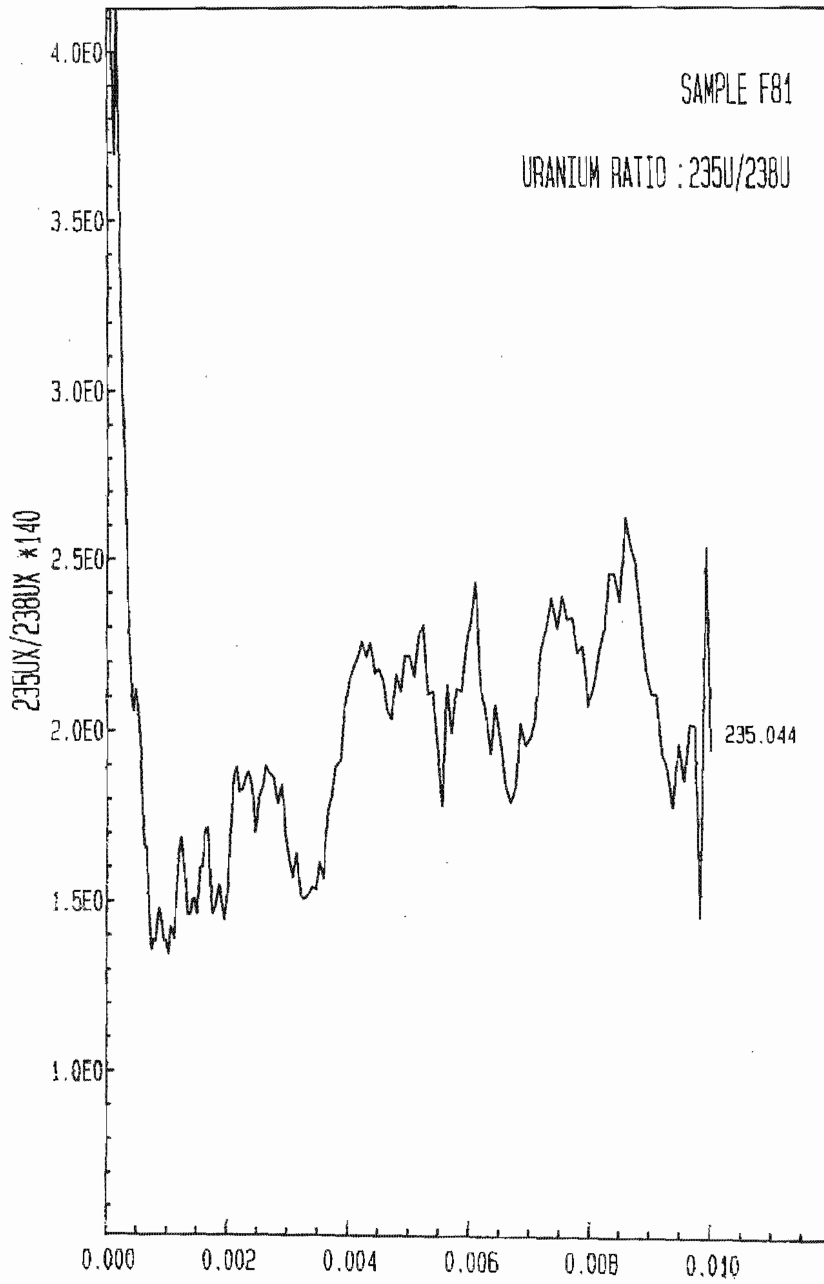

Fig 4.45 TOF-SIMS near surface depth profile ratio for ^{235}U / ^{238}U on Sample F81.

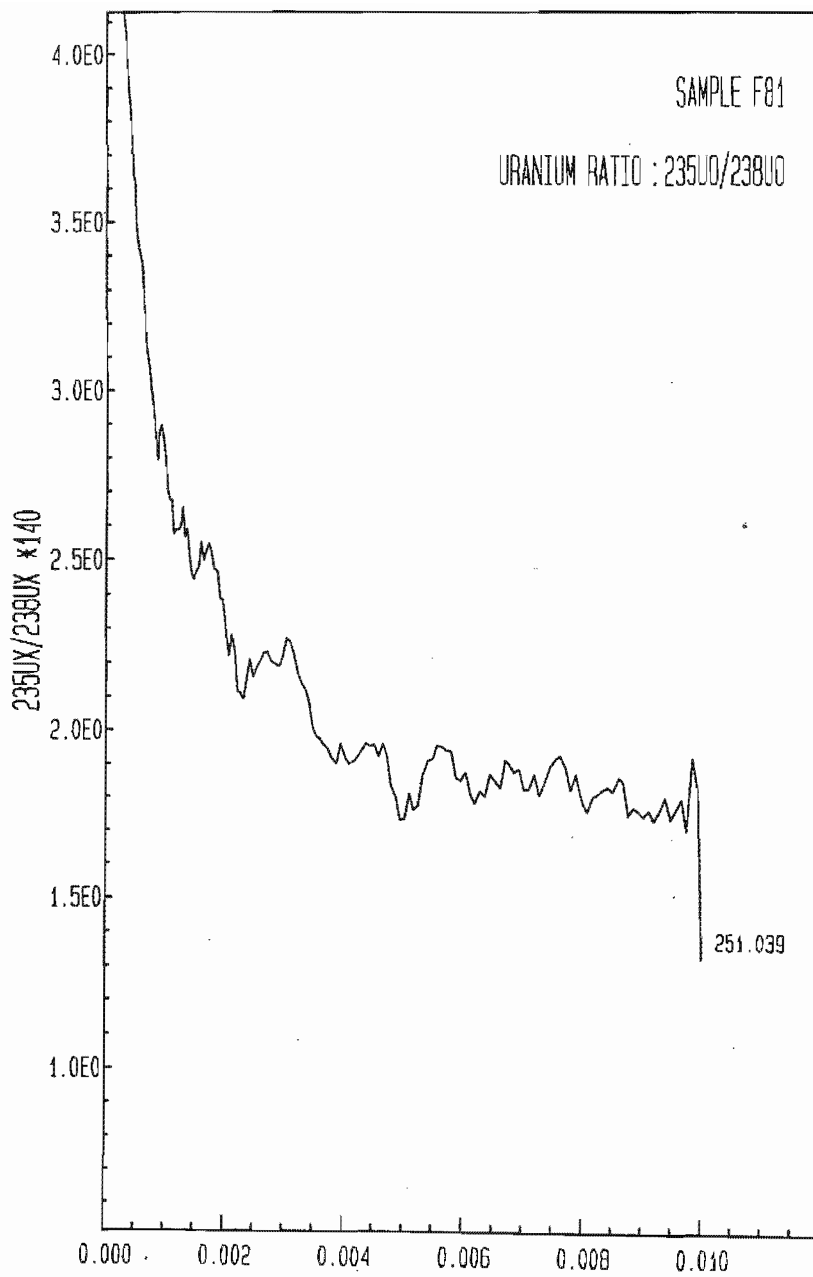

Fig 4.46 TOF-SIMS near surface depth profile ratio for ^{235}UO / ^{238}UO on Sample F81.

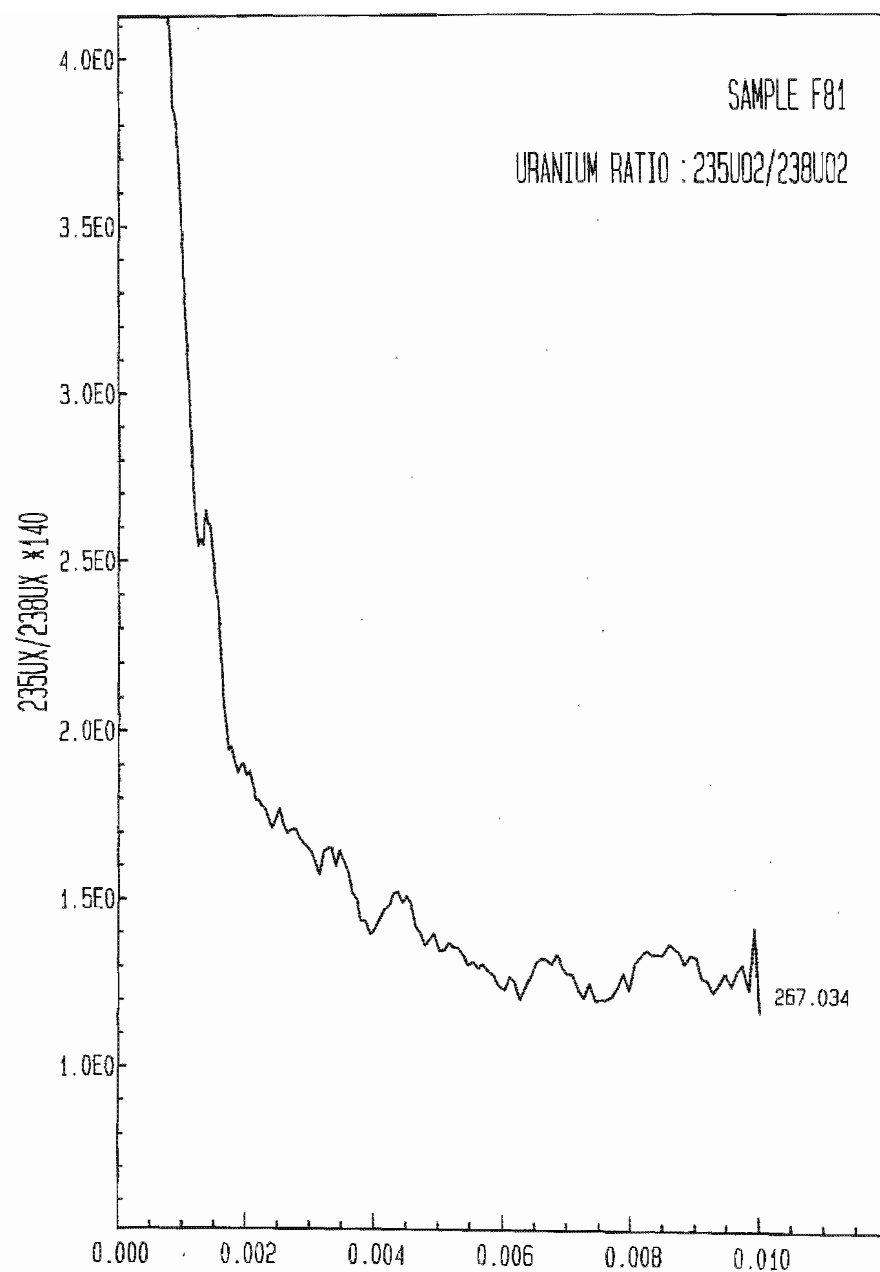

Fig 4.47 TOF-SIMS near surface depth profile ratio for $^{235}UO_2$ / $^{238}UO_2$ on Sample F81.

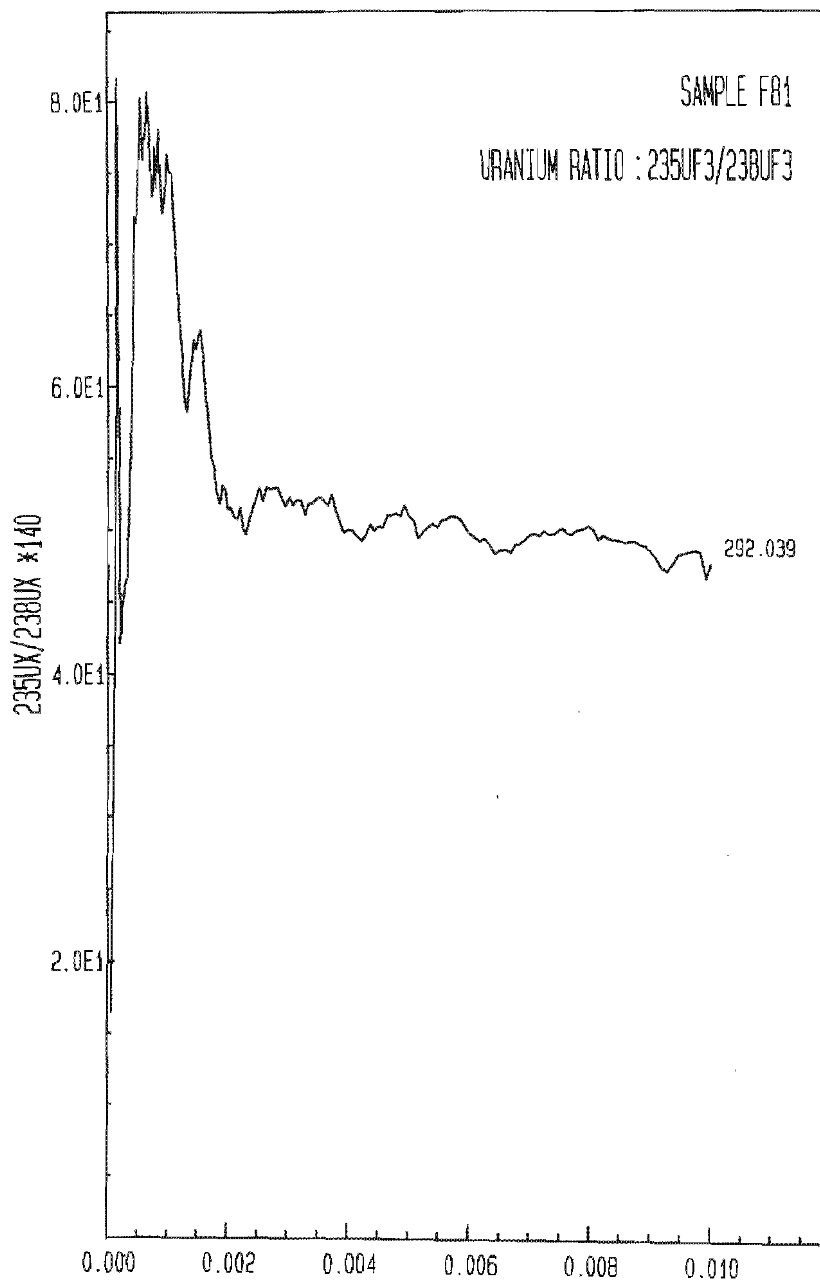

Fig 4.48 TOF-SIMS near surface depth profile ratio for $^{235}UF_3$ / $^{238}UF_3$ *on Sample F81.*

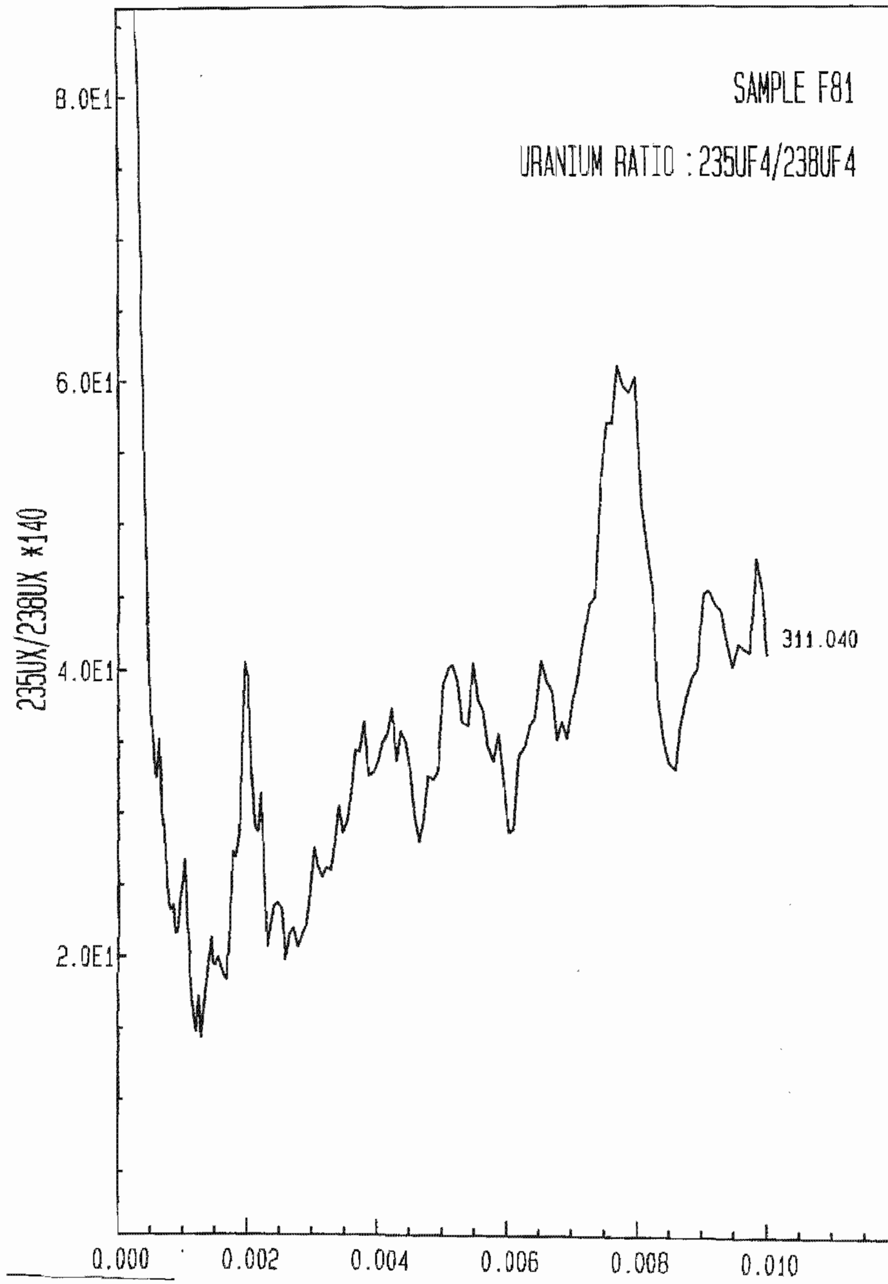

Fig 4.49 TOF-SIMS near surface depth profile ratio for $^{235}UF_4$ / $^{238}UF_4$ on Sample F81.

Conclusion Phase 2

It is clear from the series of analysis from Phase 2, that there is some work yet to be done. This is necessary to understand how best to make measurements not only of the surface chemistry, but also of the ^{235}UX / ^{238}UX ratios that will eventually permit meaningful statements to be made about whether a sample is enriched or not. It is evident that a good protocol needs to be created for sample preparation, to prevent future surface contamination. After clean samples can be generated, work will need to be done to understand the mass bias effects on ionisation and detection efficiency of ^{235}U- and ^{238}U-containing species. The simple, measured ratio of peak integrals (^{235}UX / ^{238}UX) will need to be determined several times with good statistics for normal abundance material. After this, there is some hope to be able to monitor samples with varying enrichment ratios at their outer surface.

The meaning of all the various $U_xF_yO_z$ species and their intensities in the mass spectra are not yet understood. Much work will be required to correlate the appearance and disappearance of various peaks at the surface with process variables.

5.9 Conclusion

The application of mass spectrometry to the analyses of isotopic abundance of gas phase and or solid samples is a well-visited subject. The stringent conditions required by molecular laser isotope separation to be able to measure very small quantities (extreme sensitivity required) in a very short time and in a confined space have been challenged. The additional complexity of working with highly reactive uranium has put time-of-flight, laser desorption time-of-flight, secondary ion, and time-of-flight secondary ion mass spectrometry to the test of their limits.

This study has evolved over a period of more than six years. At the termination of the program at the AEC, a tremendous amount of information has been gathered around the selective excitation and dissociation of UF_6. The parameter space, in which experiments were done, is enormous. At the outset the use of a couple of diagnostics to measure the enrichment and the amount enriched, were considered. At the end an ensemble of diagnostics were developed and evaluated. No one diagnostic was found to be able to measure the enrichment outright. Instead, a couple was needed to support one another under different operating conditions.

The low duty cycle (5/18000) at which MLIS uranium product was harvested, just did not yield enough product from which repeatable bulk

enrichment measurements could be obtained. Pushing the in-line TOFMS, the LD-TOFMS and the Quadrupole-based SIMS to its sensitivity limits unfortunately introduced shot noise and spectral interference constraints that hampered the measurement of absolute enrichment values.

The use of the TOF-SIMS with its excellent resolution and sensitivity on the one hand exposed this spectral interference. On the other hand it proved to be a vital tool in the characterisation of harvested product. Unfortunately, this was towards the end of the program, and the opportunity to fully characterise the MLIS product was lost.

5 References

1. Adams, J., and Manley, B.W., *IEEE Trans. Nucl. Sci.,* **NS-13**, 88, (1966).
2. Almén O., and Bruce, G., *Nucl. Instr. and Meth.,* **11**, 257, (1961).
3. Andrews, A.E., Hasseltine, E.H., Olson, N.T., and Smith, H.P., *J. Appl. Phys.,* **37**, 3344, (1966).
4. Barnard, W.O., Strydom, H.J., Kruger, M.M., Schildhauer, C., and Lacquet, B.M., *Nucl. Instr. and Methods in Phys. Res.*, **B35**, 238, (1988).
5. Bay, H.L., Andersen, H.H., Hofer, W.O., and Nielsen, O., *Nucl. Instr. and Methods in Phys. Res.*, **132**, 301, (1976).
6. Bay, H.L., Roth, J., and Bodansky, J., *J. Appl. Phys.,* **48**, 1, (1977).
7. Bay, H.L., and Bodansky, J., *Rad. Eff.,* **4**, 77, (1979).
8. Behrisch, R., Maderlechner, G., and Scherzer, B.M.U., *Appl. Phys.,* **18**, 391, (1979).
9. Blank, P., and Wittmaack, K., *J. Appl. Phys.,* **50**, 1519, (1979).
10. Bohdansky, J., *Proc. Symp. Surface Science, Obertraun (Austria),* 127, (1983).
11. Botha, A.P., Strydom, H.J., and Marais, M.A., *Nucl. Instr. and Methods in Phys. Res.*, **B35**, 420, (1988).
12. Botha, L.R., *High repetition rate continuously tunable CO_2 laser system investigation,* PhD thesis, Univ. of Natal, (1991).

13. Botha, L.R., Liebenberg, C.J., Von Bergman, H., Prinsloo, F.J., Ronander, E., and Strydom, H.J., *Optical Engineering*, **33**, 2861, (1994).

14. Boutot, J.P., Delmotte, J.C., Mieke, J.A,, and Sipp, B., *Rev. Sci. Instr.,* **48**, 1405, (1977).

15. Browder, J.A., Miller, R.L., Thomas, W.A., and Sanzone, G., *Int. J. Mass Spectrom. Ion Processes,* **37**, 99, (1981).

16. Carter, G., and Grant, W.A., *Ion implantation in semiconductors.,* Edward Arnold Publishers Ltd, London (1976).

17. Coburn, J.W., Winters, H.F., and Chuang, T.J., *J. Appl. Phys.,* **48**, 3535, (1977).

18. Demanet, C.M. and Strydom, H.J., *Phys. Stat. Sol.* (a) **90**, K131, (1985).

19. Demanet, C.M., Strydom, H.J., Basson, J.H., Botha, A.P., and Stander, C.M., *Appl. Surf. Sci.*, **25**, 279, (1986).

20. Dolan, K.W. and Chang, J., *X-ray imaging, Proc. SPIE,* **106**, 178, (1977).

21. Dore, P., et al, *Chem. Phys. Lett.,* **116**, 521, (1985).

22. Eckstein, W., Scherzer, B.M.U., and Verbeek, H., *Rad. Eff.*, **18**, 135, (1973).

23. Eschard, G., and Manley, B.W., *Acta Electronica,* **14**, 19, (1971).

24. Fontell, A., and Arminen, E., *Can. J. Appl. Phys.*, **47**, 2405, (1969).

25. Furr, A.K., and Finfgeld, C.R., *J. Appl. Phys.,* **41**, 1739, (1970).

26. Girard, J. and Bolore, M., *Nucl. Instr. and Meth.,* **140**, 279, (1977).

27. Green, M.I., Kenealy, P.F., and Beard, G.B., *Nucl. Instr. and Meth.,* **126**, 175, (1975).

28. Gregg, R., and Tombrello, T.A., *Rad. Eff.,* **35**, 243, (1977).

29. Gries, W.H. and Strydom, H.J., Fresenius *Z. Anal. Chem.*, **319**, 727, (1984a).

30. Gries, W.H. and Strydom, H.J., *Report SMAT 3*, NIMR/CSIR, P. O. Box 395, Pretoria, 0001, South Africa, (1984b).

31. Grix, R., Kutscher, R., Li, G., Gruner, U., and Wollnik, H., *Rapid Commun. Mass Spectrom.*, **2**, 83-85, (1988).

32. Hecht, J., *The Laser Guidebook, McGraw-Hill Company*, (1986).

33. Hechtl, E., Bay, H.L., and Bohdansky, J., *Appl. Phys.,* **16**, 148, (1978).

34. Hertzog, R.F.K. and Vieböck, F.P., *Phys. Rev.,* **76**, 855, (1949).

35. Hill, G.E., *Proc. 6th Symp. On Photo-electronic image devices, (London), Advan. Electron. Electronic. Phys.,* **40A**, 153, (1976).

36. Hultgren, R., Desai, P.D., Hawkins, D.T., Gleiser, M., Kelly, K.K., and Wagman, D.D., *Selected values of thermodynamic properties of the elements.*, American Society of Metals, (1973).

37. Johar, S.S., and Thompson, D.A., *Surf. Sci.*, **90**, 319, (1979).

38. Kellogg, E., Henry, P., Murray, S., and Van Speybroeck, *Rev. Sci. Instr.,* **47**, 282, (1976).

39. Kemp, D.M., Bredell, P.J., Ponelis, A., and Ronander, E., in *Proceedings of the International Symposium on Isotope Separation and Chemical Exchange Uranium Enrichment*, Tokyo, Japan, Eds. Fujii, Y., Ishida, T., and Takeuchi, K., pp. 115, (1990).

40. Krutenat, R.C., and Panzera, C., *J. Appl. Phys.,* **41**, 4953, (1970).

41. Lampton, M., Cash, W., Malina, R.F., and Bowyer, S., *X-ray imaging, Proc. SPIE,* **106**, 93, (1977).

42. Letokhov, V.S., *Laser Photoionisation Spectroscopy*, Academic Press Inc., (1987).

43. Lindhard, J., Scharff, M., and Schiφtt, H.E., *Dan. Vid. Selsk. Mat. Fys. Medd.*, **33**, (14), (1963).

44. Loty, C., *Acta Electronica,* **14**, 107, (1971).

45. Marais, M.A., Strydom, H.J., Basson, J.H., Rogers, D.E.C., and Booyens, H., *J. of Crystal Growth*, **88**, 391, (1988).

46. Macfarlane, R.D., Skowronski, R.P., and Torgerson, D.F., *Biochem. Biophys. Res. Commun.*, **60**, 616, (1974).

47. Mamyrin, B.A., Karatajev, V.J., Shmikk, D.V., and Zagulin, V.A., *Sov. Phys. JETP* **37**, 45, (1973).

48. Medved, D.B., and Poppa, H., *J. Appl. Phys.,* **33**, 1759, (1962).

49. Miyagawa, S., Ato, Y., and Moriya, Y., *J. Appl. Phys.,* **49**, 6194, (1978).

50. Möller, K. and Holmid, L., *Int. J. Mass Spectrom. Ion Processes,* **61**, 323, (1984).

51. Oechsner, H., *Appl. Phys.*, **8**, 185, (1975).

52. Robinson, M.T., and Southern, A.L., *J. Appl. Phys.*, **38**, 2969, (1967).

53. Roth, J., *Proc. Sympos. on Sputtering 1980*, eds Varga, P., Betz, G., and Viehböck, F.P., Institut F. Allgemeine Physik, TU, Vienna, Austria, (1980).

54. Scales, R.C., Human, H.G.C., and Rohwer, E.R., in *Proceedings of the 12th Int. Mass Spectrometry Conf. Amsterdam*, (1991).

55. Schagen, P., *Advances in image pick-up and display (Academic Press, New York)*, **vol. 1, 1**, (1974).

56. Schiϕtt, H.E., *Dan. Vid. Selsk. Mat. Fys. Medd.*, **35**, (9), (1966).

57. Sigmund, P., *Phys. Rev.*, **184**, 383, (1969).

58. Sigmund, P., *Dan. Vid. Selsk. Mat. Fys. Medd.*, **43**, 255 (1993).

59. Strydom, H.J. and Gries, W.H., *Rad. Eff. Lett.* **86**, 145, (1984).

60. Strydom, H.J., *Quantification of secondary ion mass spectrometry on semiconductor materials*, MSc Thesis, University of Port Elizabeth, (1989).

61. Strydom, H.J., Botha, A.P., and Barnard, W.O., *S. Afr. J. Phys.* **12**, 7c, (1989).

62. Strydom, H.J., Botha, A.P., Strydom, C.A., and Vermaak, J.S., *Proceedings of the 7th Int. Conf. on SIMS (SIMS VII)*, Monterey, California, 163, (1989).

63. Strydom, H.J., Botha, A.P., and Barnard, W.O., *S. Afr. J. Phys.* **12**, 7, (1989).

64. Strydom, H.J., Botha, A.P., and Vermaak, J.S., *S. Afr. J. Sci.* **87**, 138, (1991).

65. Strydom, H.J., Human, H.G.C., Green, C.R., and Rohwer, E.R., in *Proceedings of 2nd International Workshop on Physics and Modern Application of Lasers*, Harare, Zimbabwe, 260, (1993).

66. Strydom, H.J., Human, H.G.C., Green, C.R., Ronander, E., Rohwer, E.R., and Michaelis, M.M., *Proceedings of 13th International Mass Spectrometry Conference*, Budapest, Hungary, 597, (1993).

67. Stuke, M., et al, *Appl. Phys. Lett.*, **39**, 201, (1980).

68. Summer, A.J., Freeman, N.J., and Daly, N.R., *J. Appl. Phys.*, **42**, 4774, (1971).

69. Thiart, C.J.H., Van Zyl, G.P., Ronander, E., and Mathews, E.H., *N&O Joernaal*, **9**, 31, (1993).

70. Thomson, J.J., *Rays of Positive Electricity,* Longmans Greens, London, (1913).

71. Timothy, J.G., and Bybee, R.L., *Rev. Sci. Instr.*, **48**, 202, (1977).

72. Tullmin, M.A.A., Witcomb, M.J., Cortie, M.B., Strydom, H.J., and Robinson, F.P.A., *Proceedings of the Electron Microscopy Society of Southern Africa,* **19**, 167, (1989).

73. Tullmin, M.A.A., Strydom, H.J., Cortie, M.B., and Robinson, F.P.A., *S. Afr. J. Sci.* **86**, 205, (1990).

74. Turner,J.E., et.al. *Proceedings of the 7th Int. Conf. on SIMS (SIMS VII)*, Monterey, California, 95, (1989).

75. Wehner, G.K., and Rosenberg, D., *J. Appl. Phys.,* **32**, 887, (1961).

76. Weinkauf, R., Walter, K., Weickhardt, C., Boesl, U., and Schlag, E.W., *Z. Naturforsch., Teil A,* **44**, 1219, (1989).

77. Werner, H.W. and De Grefte, H.A.M., *Vakuum-Technik,* 17, 37, (1968).

78. Wiley, W.C., and Hendee, C.F., *IRE Trans. Nucl. Sci.,* **NS-9**, 103, (1962).

79. Wiley, W.C., and McLaren, I.H., *Rev. Sci. Instrum.* **26**, 1150, (1955).

80. Yamamura, Y., Matsunami, N., and Itoh, N., *Rad. Eff. Lett.,* **68**, 83, (1982).

81. Yants, O.C., Normand, C.E., and Harrison, D.E., Jr., *J. Appl. Phys.,* **31**, 447, (1960).

A. Ion Implantation Theory

A.1. Introduction

Ion implantation is the introduction of atoms into the surface layer of a solid substrate by bombardment of the solid with ions in the keV to MeV energy range.

A.2. Basic Concepts

In order to describe the ion implantation process it is necessary to consider the separate concepts and events that contribute to the overall picture. Amongst these are the following:

- *Binary Collisions*

  Although ion implantation involves a beam of many ions interacting with a solid containing many atoms, the collision between one ion and one target atom is of basic importance. In many circumstances the problem of an ion entering a solid can be treated as a succession of binary collisions in which the ion interacts or collides with only one target atom at a time.

- *Interatomic Potential*

  The collision between two atoms depends intrinsically on the interatomic potential *V(r)*. The forces acting on both particles and hence their trajectories are derived from *V(r)* so that knowledge of the interatomic potential is of fundamental importance.

- *Energy Loss*

  As an ion penetrates a solid it looses its energy in a series of collisions with the target atoms until it eventually comes to rest. The amount of energy lost in each collision will decide the total path length or range of the ion. Energy loss is considered to occur by either elastic or inelastic processes.

- *Ion Range*

  The range of an ion is determined by the rate at which it loses energy. Having described and evaluated energy loss processes one can calculate the ranges and predict the spatial distribution of implanted impurities within surface layers and targets.

- *Channelling*

  In a single crystal the lattice atoms are arranged periodically in space and in certain directions the structure has open channels bound by densely packed walls. Ions entering in these directions often do not

make a random sequence of collisions, as in an amorphous material, but rather are steered by a succession of correlated interactions with atoms in the channel walls. This has a profound effect on many aspects of ion implantation.

- *Damage*

  Energy is transferred from the projectiles to the target atoms as they slow down. An atom receiving sufficient kinetic energy will be displaced from its lattice site and the target will suffer radiation damage. Since the energy required displacing an atom is typically 26eV, heavy ions of a few keV energies cause considerable damage. A recoiling target atom may itself be sufficient energetic to act as a secondary projectile which in turn displace further atoms and produces a cascade of displacement collisions.

A.3. Energy Loss

It is usual to consider that the implanted ion loses energy to the target atom by two independent processes, namely nuclear and electronic collisions (or, as they are also called, elastic and inelastic collisions). Electronic collisions involve energy transfer from the moving ion to the electrons of the target atoms and usually result in negligible deflection. In nuclear collisions kinetic energy is transferred to the struck atoms as a whole and this results

in the projectile suffering relatively large angle deflections. At high energy the electronic losses dominates the slowing down process.

The rate of energy loss with distance –dE/dx is consequently composed of two terms which can be written as

$$-\frac{dE}{dx} = N\left(S_n(E) + S_e(E)\right) \tag{A.1}$$

where N is the number of target atoms per unit volume and $S_n(E)$ and $S_e(E)$ are the nuclear and electronic stopping powers, respectively.

A.4. Ion Range

R represents the total path length of an incident ion coming to rest inside a target. The projected path length, R_P, is the distance perpendicular from the outer surface to the rest position inside the target. Each ion that strikes the target will not follow the same path even though its initial energy is fixed. Not only will the number of collisions suffered by an individual ion vary but also its path length. This will naturally result in a distribution of stopping positions, which usually are assumed to have Gaussian (or normal distribution) shape. There will, of course, also be a statistical spread in the total range. In calculating ion ranges one will consequently be concerned with averages of many events and must consider such properties as the

average projected range and its standard deviation. Differential equations for computing the projected range and related quantities have been given by Linhard, Scharff, and Schiϕtt, (1963) – usually referred to as the LSS).

A.5. Summary of LSS Theory

A Thomas-Fermi statistical model of the interaction between heavy ions is used to derive a universal nuclear stopping power, S_n, and an electronic stopping power S_e, proportional the velocity of the projectile, v. The potential has the form:

$$V(r) = \frac{Z_1 Z_2 e^2}{4\pi\varepsilon_0 r}\Phi\left(\frac{r}{a}\right) \tag{A.2}$$

where

$$a = a_0\left(Z_1^{2/3} + Z_2^{2/3}\right)^{-1/2} \tag{A.3}$$

and Φ is the Thomas-Fermi screening function and has been tabulated numerically, Z_1 and Z_2 is the atomic mass number of the incident ion and target, respectively. r is the distance from the centre of the atom and Z_1e and Z_2e is the charge of the ion and target atom, respectively.

Using approximation methods, the LSS theory predicts a nuclear stopping power S_n of the form shown in Fig A.1. Energies and distances are expressed in terms of dimensionless parameters ε and ρ where

$$\varepsilon = E\frac{aM_2}{Z_1Z_2e^2(M_1+M_2)} \tag{A.4}$$

and

$$\rho = rN4\pi a^2\frac{M_1M_2}{(M_1+M_2)^2} \tag{A.5}$$

where N is Avogadro's number.

Using these 'reduced' energy and distance parameters, the nuclear stopping power S_n, i.e. $\{d\varepsilon/d\rho\}_n$, is a function of ε only and is dependent on incoming particle or stopping substance, so that the curve in Fig A.1 is a universal nuclear stopping power. Using the same units, the electronic stopping power S_e is given by

$$\left\{\frac{d\varepsilon}{d\rho}\right\}_e = k\varepsilon^{1/2} \tag{A.6}$$

where

$$k = \xi_e\frac{0.0793Z_1^{1/2}Z_2^{1/2}(M_1+M_2)^{3/2}}{\left(Z_1^{2/3}+Z_2^{2/3}\right)^{3/4}M_1^{3/2}M_2^{1/2}} \tag{A.7}$$

and

$$\xi_e = Z_1^{1/6} \tag{A.8}$$

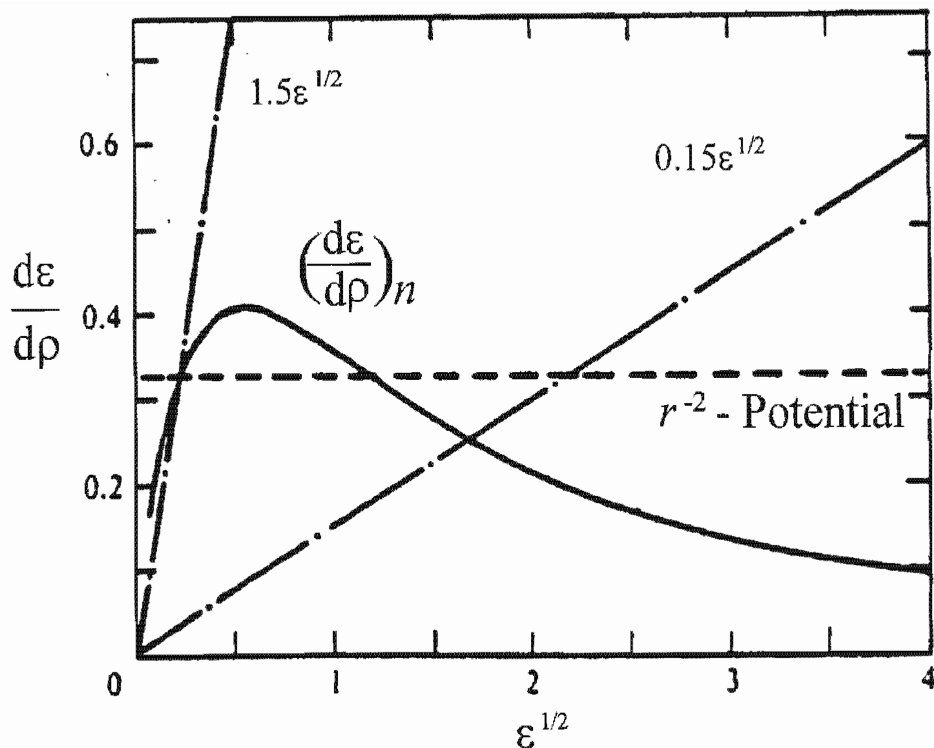

Fig A.1. Nuclear and electronic stopping powers in reduced units. Full drawn curve represent the Thomas-Fermi nuclear stopping power, dot and dash lines the electronic stopping for k=0.5. Dashed line gives the nuclear stopping power for the r^{-2} potential. (see Carter and Grant, (1976)).

In practice the most interesting range quantity is the average projected range R_P, since this is the property usually measured in experiments. At very high energies where the stopping is predominantly electronic, the projectile tends to move in a straight line in the direction of the incidence at the target surface. Under these circumstances the average total path length

R and the average projected range R_P are to a good approximation equal. Naturally, for low energy particles, where nuclear stopping is important, large angle scattering occur throughout the whole slowing down process and under these circumstances R_P can be considerably less than R, the more so the larger the mass ratio M_2/M_1. As a general approximation one has

$$\frac{R}{R_p} \approx 1 + \frac{M_2}{3M_1} \qquad \text{(A.9)}$$

which has been calculated using an inverse square power law potential and for situations where nuclear stopping dominates.

B. Table of Measured Sputtering Yields (S) for Polycrystalline Targets

The table is arranged in order of ascending M_2/M_1 ratio (where M_1 and M_2 are the mass numbers of the incident ion and the target element, respectively), and for given M_2/M_1 ratio in the order of ascending ion energy E.

The values of S were taken from tabulations or from the text where possible. Where this was not possible, the values were read from graphs by means of an X-Y digitizer instrument.

The sublimation enthalpies of solid chemical elements were compiled from data in Hultgren et al, (1973).

No.	Z1	M1	Z2	M2	B(eV)	E(keV)	S	Log(M2/M1)	Alpha_eff	Reference
1	55	133	13	26	3.42	1.00	0.744	-0.709	0.049	Andrews et al (1966)
2	55	133	13	26	3.42	2.49	1.700	-0.709	0.079	
3	55	133	13	26	3.42	4.00	1.880	-0.709	0.073	
4	55	133	13	26	3.42	5.00	1.970	-0.709	0.071	
5	55	133	13	26	3.42	7.00	2.250	-0.709	0.073	
6	55	133	13	26	3.42	7.40	1.890	-0.709	0.060	
7	55	133	13	26	3.42	8.00	2.340	-0.709	0.072	
8	55	133	13	26	3.42	9.50	2.370	-0.709	0.070	
9	55	133	13	26	3.42	10.00	2.310	-0.709	0.067	
10	54	131	14	28	4.73	10.00	2.720	-0.670	0.104	Blank et al (1979)
11	54	131	14	28	4.73	20.00	3.080	-0.670	0.099	
12	54	131	14	28	4.73	40.00	3.430	-0.670	0.095	
13	54	131	14	28	4.73	80.00	3.720	-0.670	0.093	
14	54	131	14	28	4.73	140.00	3.880	-0.670	0.091	
15	54	131	14	28	4.73	270.00	4.030	-0.670	0.096	
16	54	131	14	28	4.73	540.00	3.660	-0.670	0.096	
17	80	201	22	48	4.87	4.00	1.830	-0.622	0.068	Wehner et al, (1961)
18	80	201	22	48	4.87	6.00	2.200	-0.622	0.070	
19	80	201	22	48	4.87	8.00	2.430	-0.622	0.069	
20	80	201	22	48	4.87	10.00	2.990	-0.622	0.079	
21	80	201	22	48	4.87	13.00	2.880	-0.622	0.071	
22	80	201	22	48	4.87	14.00	3.020	-0.622	0.071	
23	80	201	23	51	4.87	4.00	2.050	-0.596	0.074	Wehner et al, (1961)
24	80	201	23	51	4.87	6.00	2.650	-0.596	0.090	
25	80	201	23	51	4.87	8.00	3.080	-0.596	0.094	
26	80	201	23	51	4.87	10.00	3.400	-0.596	0.095	
27	80	201	23	51	4.87	12.00	3.580	-0.596	0.094	
28	80	201	23	51	4.87	14.00	3.400	-0.596	0.085	
29	80	201	23	51	4.87	15.00	3.560	-0.596	0.088	
30	80	201	26	56	4.31	4.00	3.080	-0.555	0.092	Wehner et al, (1961)
31	80	201	26	56	4.31	6.00	3.770	-0.555	0.097	
32	80	201	26	56	4.31	8.00	3.600	-0.555	0.083	
33	80	201	26	56	4.31	10.00	3.790	-0.555	0.080	
34	80	201	26	56	4.31	12.00	5.260	-0.555	0.105	
35	80	201	26	56	4.31	14.00	5.260	-0.555	0.099	
36	80	201	26	56	4.31	15.00	5.780	-0.555	0.107	

No.	Z1	M1	Z2	M2	B(eV)	E(keV)	S	Log(M2/M1)	Alpha_eff	Reference
37	80	201	27	59	4.44	4.00	3.690	-0.532	0.112	Wehner et al, (1961)
38	80	201	27	59	4.44	6.00	4.660	-0.532	0.130	
39	80	201	27	59	4.44	7.00	5.240	-0.532	0.128	
40	80	201	27	59	4.44	8.00	5.240	-0.532	0.121	
41	80	201	27	59	4.44	10.00	5.880	-0.532	0.125	
42	80	201	27	59	4.44	11.00	5.600	-0.532	0.116	
43	80	201	27	59	4.44	12.00	6.380	-0.532	0.128	
44	80	201	27	59	4.44	14.00	6.420	-0.532	0.122	
45	80	201	27	59	4.44	15.00	6.720	-0.532	0.125	
46	80	201	28	59	4.46	4.00	4.930	-0.532	0.147	Wehner et al, (1961)
47	80	201	28	59	4.46	5.00	5.600	-0.532	0.153	
48	80	201	28	59	4.46	6.00	6.010	-0.532	0.153	
49	80	201	28	59	4.46	8.00	7.090	-0.532	0.162	
50	80	201	28	59	4.46	10.00	6.810	-0.532	0.143	
51	80	201	28	59	4.46	12.00	8.210	-0.532	0.162	
52	80	201	28	59	4.46	15.00	7.910	-0.532	0.145	
53	80	201	29	64	3.49	4.00	8.260	-0.497	0.189	Wehner et al, (1961)
54	80	201	29	64	3.49	5.00	7.370	-0.497	0.155	
55	80	201	29	64	3.49	5.00	10.400	-0.497	0.218	
56	80	201	29	64	3.49	6.00	9.720	-0.497	0.190	
57	80	201	29	64	3.49	7.00	9.770	-0.497	0.180	
58	80	201	29	64	3.49	8.00	10.300	-0.497	0.180	
59	80	201	29	64	3.49	8.00	10.800	-0.497	0.189	
60	80	201	29	64	3.49	8.00	11.600	-0.497	0.203	
61	80	201	29	64	3.49	9.00	11.100	-0.497	0.187	
62	80	201	29	64	3.49	10.00	11.300	-0.497	0.182	
63	80	201	29	64	3.49	10.00	11.800	-0.497	0.190	
64	80	201	29	64	3.49	10.00	12.100	-0.497	0.196	
65	80	201	29	64	3.49	10.00	12.500	-0.497	0.202	
66	80	201	29	64	3.49	11.00	13.100	-0.497	0.204	
67	80	201	29	64	3.49	12.00	12.300	-0.497	0.187	
68	80	201	29	64	3.49	13.00	12.500	-0.497	0.184	
69	80	201	29	64	3.49	14.00	14.400	-0.497	0.203	
70	80	201	29	64	3.49	15.00	13.000	-0.497	0.183	
71	80	201	29	64	3.49	15.00	13.200	-0.497	0.185	
72	80	201	29	64	3.49	15.00	13.400	-0.497	0.189	

No.	Z1	M1	Z2	M2	B(eV)	E(keV)	S	Log(M2/M1)	Alpha_eff	Reference
73	54	131	29	64	3.49	5.00	6.280	-0.311	0.151	Sigmund, (1969)
74	54	131	29	64	3.49	10.00	9.070	-0.311	0.174	
75	54	131	29	64	3.49	10.00	10.500	-0.311	0.201	
76	54	131	29	64	3.49	15.00	10.100	-0.311	0.173	
77	54	131	29	64	3.49	18.00	10.500	-0.311	0.171	
78	54	131	29	64	3.49	20.00	14.500	-0.311	0.230	
79	54	131	29	64	3.49	30.00	15.900	-0.311	0.230	
80	54	131	29	64	3.49	30.00	16.400	-0.311	0.237	
81	54	131	29	64	3.49	40.00	17.800	-0.311	0.243	
82	54	131	29	64	3.49	50.00	19.900	-0.311	0.260	
83	54	131	29	64	3.49	75.00	23.000	-0.311	0.282	
84	54	131	29	64	3.49	95.00	25.000	-0.311	0.296	
85	54	131	29	64	3.49	125.00	25.900	-0.311	0.296	
86	54	131	29	64	3.49	150.00	25.000	-0.311	0.280	
87	54	131	29	64	3.49	200.00	23.400	-0.311	0.259	
88	54	131	29	64	3.49	240.00	20.200	-0.311	0.225	
89	54	131	29	64	3.49	300.00	19.000	-0.311	0.214	
90	54	131	29	64	3.49	400.00	18.100	-0.311	0.209	
91	54	131	29	64	3.49	500.00	14.500	-0.311	0.173	
92	54	131	29	64	3.49	600.00	12.900	-0.311	0.159	
93	54	131	29	64	3.49	700.00	13.300	-0.311	0.168	
94	54	131	29	64	3.49	800.00	11.200	-0.311	0.147	
95	54	131	29	64	3.49	900.00	11.900	-0.311	0.160	
96	54	131	29	64	3.49	1000.00	10.500	-0.311	0.145	
97	80	201	45	103	5.74	4.00	4.080	-0.290	0.128	Wehner et al, (1961)
98	80	201	45	103	5.74	5.00	4.250	-0.290	0.122	
99	80	201	45	103	5.74	6.00	5.560	-0.290	0.148	
100	80	201	45	103	5.74	7.00	6.680	-0.290	0.168	
101	80	201	45	103	5.74	8.00	4.360	-0.290	0.104	
102	80	201	45	103	5.74	10.00	6.600	-0.290	0.145	
103	80	201	45	103	5.74	12.00	7.560	-0.290	0.155	
104	80	201	45	103	5.74	13.00	7.010	-0.290	0.140	
105	80	201	45	103	5.74	14.00	7.460	-0.290	0.145	
106	80	201	45	103	5.74	15.00	6.750	-0.290	0.128	

No.	Z1	M1	Z2	M2	B(eV)	E(keV)	S	Log(M2/M1)	Alpha_eff	Reference
107	80	201	46	106	3.91	4.00	5.140	-0.278	0.109	Wehner et al, (1961)
108	80	201	46	106	3.91	5.00	6.680	-0.278	0.129	
109	80	201	46	106	3.91	6.00	7.130	-0.278	0.129	
110	80	201	46	106	3.91	7.00	7.750	-0.278	0.132	
111	80	201	46	106	3.91	8.00	8.230	-0.278	0.133	
112	80	201	46	106	3.91	10.00	9.270	-0.278	0.138	
113	80	201	46	106	3.91	10.00	9.680	-0.278	0.144	
114	80	201	46	106	3.91	12.00	9.010	-0.278	0.125	
115	80	201	46	106	3.91	14.00	9.680	-0.278	0.127	
116	80	201	46	106	3.91	15.00	9.920	-0.278	0.128	
117	80	201	47	108	2.95	4.00	11.900	-0.270	0.188	Wehner et al, (1961)
118	80	201	47	108	2.95	5.00	14.100	-0.270	0.205	
119	80	201	47	108	2.95	6.00	17.500	-0.270	0.237	
120	80	201	47	108	2.95	8.00	19.800	-0.270	0.240	
121	80	201	47	108	2.95	10.00	20.900	-0.270	0.232	
122	80	201	47	108	2.95	10.00	24.200	-0.270	0.268	
123	80	201	47	108	2.95	12.00	25.600	-0.270	0.266	
124	80	201	47	108	2.95	14.00	26.100	-0.270	0.257	
125	18	40	14	28	4.73	0.5	0.441	-0.155	0.073	Coburn et al, (1977)
126	18	40	14	28	4.73	0.50	0.473	-0.155	0.078	
127	18	40	14	28	4.73	0.50	0.494	-0.155	0.082	
128	18	40	14	28	4.73	0.75	0.499	-0.155	0.072	
129	18	40	14	28	4.73	1.00	0.653	-0.155	0.087	
130	18	40	14	28	4.73	1.00	0.702	-0.155	0.093	
131	18	40	14	28	4.73	1.50	0.697	-0.155	0.083	
132	18	40	14	28	4.73	2.00	0.849	-0.155	0.093	
133	18	40	14	28	4.73	2.00	0.882	-0.155	0.097	
134	18	40	14	28	4.73	3.00	0.932	-0.155	0.094	
135	18	40	14	28	4.73	3.00	0.978	-0.155	0.098	
136	54	131	42	96	6.83	30.00	3.550	-0.135	0.089	Almén et al, (1961)
137	54	131	42	96	6.83	65.00	4.430	-0.135	0.095	

No.	Z1	M1	Z2	M2	B(eV)	E(keV)	S	Log(M2/M1)	Alpha_eff	Reference
138	36	84	29	64	3.49	1.00	2.600	-0.118	0.142	Sigmund, (1969)
139	36	84	29	64	3.49	2.50	4.720	-0.118	0.183	
140	36	84	29	64	3.49	4.00	5.760	-0.118	0.191	
141	36	84	29	64	3.49	5.00	6.250	-0.118	0.194	
142	36	84	29	64	3.49	5.00	6.940	-0.118	0.215	
143	36	84	29	64	3.49	8.00	7.990	-0.118	0.217	
144	36	84	29	64	3.49	10.00	7.710	-0.118	0.198	
145	36	84	29	64	3.49	10.00	8.400	-0.118	0.216	
146	36	84	29	64	3.49	15.00	8.920	-0.118	0.210	
147	36	84	29	64	3.49	20.00	8.920	-0.118	0.198	
148	36	84	29	64	3.49	20.00	9.930	-0.118	0.220	
149	36	84	29	64	3.49	25.00	8.960	-0.118	0.191	
150	36	84	29	64	3.49	30.00	11.400	-0.118	0.235	
151	36	84	29	64	3.49	40.00	11.500	-0.118	0.226	
152	36	84	29	64	3.49	50.00	11.900	-0.118	0.228	
153	36	84	29	64	3.49	65.00	13.300	-0.118	0.246	
154	36	84	29	64	3.49	75.00	13.100	-0.118	0.240	
155	36	84	29	64	3.49	100.00	13.600	-0.118	0.248	
156	36	84	29	64	3.49	150.00	13.100	-0.118	0.244	
157	36	84	29	64	3.49	200.00	12.500	-0.118	0.240	
158	36	84	29	64	3.49	250.00	11.800	-0.118	0.234	
159	36	84	29	64	3.49	300.00	11.400	-0.118	0.233	
160	36	84	29	64	3.49	400.00	10.400	-0.118	0.227	
161	36	84	29	64	3.49	500.00	9.240	-0.118	0.214	
162	36	84	29	64	3.49	600.00	8.130	-0.118	0.198	
163	36	84	29	64	3.49	700.00	7.710	-0.118	0.198	
164	36	84	29	64	3.49	800.00	7.810	-0.118	0.210	
165	36	84	29	64	3.49	900.00	6.940	-0.118	0.195	
166	36	84	29	64	3.49	1000.00	7.710	-0.118	0.226	
167	54	131	46	106	3.91	10.00	8.000	-0.092	0.151	Almén et al, (1961)
168	54	131	46	106	3.91	20.00	11.400	-0.092	0.176	
169	54	131	46	106	3.91	30.00	12.000	-0.092	0.167	
170	54	131	46	106	3.91	30.00	12.700	-0.092	0.177	
171	54	131	46	106	3.91	40.00	13.600	-0.092	0.178	
172	54	131	46	106	3.91	40.00	14.000	-0.092	0.183	
173	54	131	46	106	3.91	50.00	16.300	-0.092	0.204	
174	54	131	46	106	3.91	55.00	15.400	-0.092	0.189	
175	54	131	46	106	3.91	65.00	15.600	-0.092	0.186	

No.	Z1	M1	Z2	M2	B(eV)	E(keV)	S	Log(M2/M1)	Alpha_eff	Reference
176	54	131	47	108	2.95	9.00	15.900	-0.084	0.232	Almén et al, (1961)
177	54	131	47	108	2.95	10.00	17.100	-0.084	0.243	
178	54	131	47	108	2.95	20.00	25.200	-0.084	0.292	
179	54	131	47	108	2.95	30.00	31.500	-0.084	0.330	
180	54	131	47	108	2.95	30.00	32.700	-0.084	0.343	
181	54	131	47	108	2.95	40.00	33.700	-0.084	0.331	
182	54	131	47	108	2.95	40.00	35.200	-0.084	0.345	
183	54	131	47	108	2.95	50.00	37.700	-0.084	0.353	
184	51	122	47	108	2.95	10.00	15.000	-0.053	0.223	Johar et al, (1979)
185	51	122	47	108	2.95	15.00	18.000	-0.053	0.237	
186	51	122	47	108	2.95	30.00	25.000	-0.053	0.277	
187	51	122	47	108	2.95	47.00	32.000	-0.053	0.325	
188	51	122	47	108	2.95	70.00	37.000	-0.053	0.347	
189	80	201	73	181	8.11	4.00	2.190	-0.046	0.088	Wehner et al, (1961)
190	80	201	73	181	8.11	5.00	2.620	-0.046	0.096	
191	80	201	73	181	8.11	6.00	2.780	-0.046	0.095	
192	80	201	73	181	8.11	7.00	2.750	-0.046	0.088	
193	80	201	73	181	8.11	8.00	3.200	-0.046	0.098	
194	80	201	73	181	8.11	9.00	3.340	-0.046	0.095	
195	80	201	73	181	8.11	10.00	3.360	-0.046	0.094	
196	80	201	73	181	8.11	11.00	2.990	-0.046	0.081	
197	80	201	73	181	8.11	12.00	3.330	-0.046	0.087	
198	80	201	73	181	8.11	13.00	3.360	-0.046	0.085	
199	80	201	73	181	8.11	14.00	3.350	-0.046	0.083	
200	80	201	73	181	8.11	15.00	3.790	-0.046	0.092	
201	54	131	50	119	3.13	10.00	8.160	-0.042	0.122	Almén et al, (1961)
202	54	131	50	119	3.13	20.00	10.700	-0.042	0.131	
203	54	131	50	119	3.13	20.00	11.200	-0.042	0.137	
204	54	131	50	119	3.13	25.00	11.000	-0.042	0.127	
205	54	131	50	119	3.13	35.00	12.200	-0.042	0.131	
206	54	131	50	119	3.13	40.00	11.500	-0.042	0.119	
207	54	131	50	119	3.13	50.00	11.500	-0.042	0.114	
208	54	131	50	119	3.13	50.00	12.100	-0.042	0.130	

No.	Z1	M1	Z2	M2	B(eV)	E(keV)	S	Log(M2/M1)	Alpha_eff	Reference
209	80	201	74	184	8.81	4.00	2.190	-0.038	0.095	Wehner et al, (1961)
210	80	201	74	184	8.81	6.00	2.430	-0.038	0.090	
211	80	201	74	184	8.81	8.00	2.560	-0.038	0.085	
212	80	201	74	184	8.81	10.00	2.620	-0.038	0.080	
213	80	201	74	184	8.81	12.00	2.840	-0.038	0.081	
214	80	201	74	184	8.81	14.00	2.800	-0.038	0.075	
215	80	201	74	184	8.81	15.00	2.360	-0.038	0.088	
216	80	201	78	195	5.86	4.00	6.340	-0.013	0.182	Wehner et al, (1961)
217	80	201	78	195	5.86	5.00	8.650	-0.013	0.229	
218	80	201	78	195	5.86	6.00	8.650	-0.013	0.213	
219	80	201	78	195	5.86	8.00	9.380	-0.013	0.206	
220	80	201	78	195	5.86	10.00	9.530	-0.013	0.192	
221	80	201	78	195	5.86	12.00	12.400	-0.013	0.233	
222	80	201	78	195	5.86	13.00	11.600	-0.013	0.211	
223	80	201	78	195	5.86	14.00	10.800	-0.013	0.192	
224	80	201	78	195	5.86	15.00	10.100	-0.013	0.176	
225	80	201	79	197	3.82	4.00	12.300	-0.009	0.231	Wehner et al, (1961)
226	80	201	79	197	3.82	5.00	12.300	-0.009	0.212	
227	80	201	79	197	3.82	6.00	15.700	-0.009	0.251	
228	80	201	79	197	3.82	7.00	16.000	-0.009	0.241	
229	80	201	79	197	3.82	8.00	18.900	-0.009	0.270	
230	80	201	79	197	3.82	10.00	21.900	-0.009	0.284	
231	80	201	79	197	3.82	12.00	22.500	-0.009	0.275	
232	80	201	79	197	3.82	13.00	25.000	-0.009	0.297	
233	80	201	79	197	3.82	15.00	24.300	-0.009	0.274	
234	30	65	30	65	1.35	0.31	0.802	0.000	0.030	Fontell et al, (1969)
235	28	59	28	59	4.46	0.30	0.827	0.000	0.110	Hechtl et al, (1978)
236	28	59	28	59	4.46	0.30	0.863	0.000	0.115	
237	28	59	28	59	4.46	0.35	0.870	0.000	0.109	
238	28	59	28	59	4.46	0.40	0.919	0.000	0.110	
239	28	59	28	59	4.46	0.45	1.000	0.000	0.114	
240	28	59	28	59	4.46	0.50	1.020	0.000	0.111	
241	28	59	28	59	4.46	0.50	1.040	0.000	0.114	
242	28	59	28	59	4.46	0.60	1.110	0.000	0.113	
243	28	59	28	59	4.46	1.00	1.320	0.000	0.110	
244	28	59	28	59	4.46	3.00	1.730	0.000	0.100	

No.	Z1	M1	Z2	M2	B(eV)	E(keV)	S	Log(M2/M1)	Alpha_eff	Reference
245	41	93	41	93	7.48	10.00	2.510	0.000	0.117	Bay et al, (1979)
246	41	93	41	93	7.48	20.00	2.450	0.000	0.096	
247	41	93	41	93	7.48	30.00	3.040	0.000	0.110	
248	41	93	41	93	7.48	40.00	3.220	0.000	0.111	
249	41	93	41	93	7.48	60.00	3.810	0.000	0.123	
250	41	93	41	93	7.48	80.00	4.100	0.000	0.127	
251	79	197	79	197	3.82	60.00	56.900	0.000	0.425	Bay et al, (1976)
252	79	197	79	197	3.82	90.00	107.000	0.000	0.728	
253	79	197	79	197	3.82	120.00	101.000	0.000	0.646	
254	79	197	79	197	3.82	180.00	122.000	0.000	0.723	
255	79	197	79	197	3.82	260.00	109.000	0.000	0.609	
256	79	197	79	197	3.82	400.00	103.000	0.000	0.542	
257	79	197	79	197	3.82	500.00	107.000	0.000	0.550	
258	79	197	79	197	3.82	700.00	93.300	0.000	0.476	
259	79	197	79	197	3.82	1000.00	78.300	0.000	0.406	
260	79	197	79	197	3.82	2500.00	65.600	0.000	0.391	
261	79	197	79	197	3.82	4000.00	50.400	0.000	0.339	
262	79	197	79	197	3.82	7000.00	35.200	0.000	0.289	
263	79	197	79	197	3.82	11500.00	41.500	0.000	0.430	
264	79	197	79	197	3.82	18000.00	26.500	0.000	0.357	
265	36	84	42	96	6.83	30.00	2.580	0.058	0.096	Almén et al, (1961)
266	36	84	42	96	6.83	45.00	2.880	0.058	0.101	
267	36	84	42	96	6.83	50.00	3.600	0.058	0.124	
268	36	84	42	96	6.83	65.00	2.700	0.058	0.090	
269	36	84	46	106	3.91	5.00	4.510	0.101	0.149	Sigmund, (1969)
270	36	84	46	106	3.91	7.00	6.760	0.101	0.202	
271	36	84	46	106	3.91	10.00	6.380	0.101	0.173	
272	36	84	46	106	3.91	20.00	9.160	0.101	0.211	
273	36	84	46	106	3.91	30.00	9.460	0.101	0.201	
274	36	84	46	106	3.91	40.00	10.100	0.101	0.203	
275	36	84	46	106	3.91	50.00	10.900	0.101	0.212	
276	36	84	46	106	3.91	70.00	12.500	0.101	0.232	

No.	Z1	M1	Z2	M2	B(eV)	E(keV)	S	Log(M2/M1)	Alpha_eff	Reference
277	36	84	47	108	2.95	1.00	5.560	0.109	0.251	Sigmund, (1969)
278	36	84	47	108	2.95	1.50	6.810	0.109	0.261	
279	36	84	47	108	2.95	2.00	7.430	0.109	0.255	
280	36	84	47	108	2.95	2.50	7.990	0.109	0.253	
281	36	84	47	108	2.95	3.00	10.400	0.109	0.308	
282	36	84	47	108	2.95	3.50	9.900	0.109	0.278	
283	36	84	47	108	2.95	4.50	10.900	0.109	0.282	
284	36	84	47	108	2.95	4.70	10.200	0.109	0.261	
285	36	84	47	108	2.95	5.00	11.400	0.109	0.283	
286	36	84	47	108	2.95	5.00	12.200	0.109	0.305	
287	36	84	47	108	2.95	10.50	14.800	0.109	0.298	
288	36	84	47	108	2.95	10.50	16.700	0.109	0.335	
289	36	84	47	108	2.95	15.50	16.000	0.109	0.292	
290	36	84	47	108	2.95	20.00	16.700	0.109	0.288	
291	36	84	47	108	2.95	20.00	18.100	0.109	0.312	
292	36	84	47	108	2.95	20.00	18.200	0.109	0.314	
293	36	84	47	108	2.95	26.00	18.800	0.109	0.307	
294	36	84	47	108	2.95	26.00	19.600	0.109	0.321	
295	36	84	47	108	2.95	30.00	20.100	0.109	0.321	
296	36	84	47	108	2.95	36.00	22.200	0.109	0.343	
297	36	84	47	108	2.95	45.00	22.900	0.109	0.341	
298	36	84	47	108	2.95	50.00	24.900	0.109	0.364	
299	36	84	47	108	2.95	65.00	26.400	0.109	0.373	

No.	Z1	M1	Z2	M2	B(eV)	E(keV)	S	Log(M2/M1)	Alpha_eff	Reference
300	18	40	29	64	3.49	0.70	2.390	0.204	0.255	Oeschsner, (1975)
301	18	40	29	64	3.49	1.00	2.880	0.204	0.272	
302	18	40	29	64	3.49	1.30	3.170	0.204	0.275	
303	18	40	29	64	3.49	1.50	3.530	0.204	0.293	
304	18	40	29	64	3.49	2.00	3.820	0.204	0.292	
305	18	40	29	64	3.49	2.50	4.540	0.204	0.327	
306	18	40	29	64	3.49	3.00	5.050	0.204	0.347	
307	18	40	29	64	3.49	4.00	5.260	0.204	0.339	
308	18	40	29	64	3.49	5.00	4.040	0.204	0.260	
309	18	40	29	64	3.49	5.00	6.130	0.204	0.376	
310	18	40	29	64	3.49	7.50	7.210	0.204	0.409	
311	18	40	29	64	3.49	10.00	4.900	0.204	0.265	
312	18	40	29	64	3.49	10.00	5.840	0.204	0.315	
313	18	40	29	64	3.49	10.00	7.930	0.204	0.428	
314	18	40	29	64	3.49	15.00	5.260	0.204	0.268	
315	18	40	29	64	3.49	15.00	8.440	0.204	0.430	
316	18	40	29	64	3.49	20.00	5.700	0.204	0.280	
317	18	40	29	64	3.49	20.00	6.780	0.204	0.333	
318	18	40	29	64	3.49	20.00	8.580	0.204	0.422	
319	18	40	29	64	3.49	25.00	5.340	0.204	0.258	
320	18	40	29	64	3.49	25.00	9.190	0.204	0.444	
321	18	40	29	64	3.49	30.00	6.560	0.204	0.316	
322	18	40	29	64	3.49	30.00	8.940	0.204	0.431	
323	18	40	29	64	3.49	35.00	8.940	0.204	0.432	
324	18	40	29	64	3.49	40.00	6.490	0.204	0.315	
325	18	40	29	64	3.49	40.00	6.540	0.204	0.366	
326	18	40	29	64	3.49	40.00	9.270	0.204	0.451	
327	18	40	29	64	3.49	50.00	7.030	0.204	0.347	
328	18	40	29	64	3.49	65.00	7.070	0.204	0.360	
329	18	40	29	64	3.49	75.00	6.310	0.204	0.328	
330	18	40	29	64	3.49	100.00	5.770	0.204	0.316	
331	18	40	29	64	3.49	150.00	5.260	0.204	0.318	
332	18	40	29	64	3.49	200.00	5.260	0.204	0.346	
333	18	40	29	64	3.49	300.00	4.490	0.204	0.342	
334	18	40	29	64	3.49	400.00	3.710	0.204	0.320	
335	18	40	29	64	3.49	500.00	2.920	0.204	0.280	
336	18	40	29	64	3.49	600.00	2.670	0.204	0.282	
337	18	40	29	64	3.49	700.00	2.670	0.204	0.309	
338	18	40	29	64	3.49	800.00	2.270	0.204	0.286	
339	18	40	29	64	3.49	900.00	2.270	0.204	0.309	
340	18	40	29	64	3.49	1000.00	2.270	0.204	0.333	

No.	Z1	M1	Z2	M2	B(eV)	E(keV)	S	Log(M2/M1)	Alpha_eff	Reference
341	18	40	46	106	3.91	5.00	3.530	0.423	0.257	Sigmund, (1969)
342	18	40	46	106	3.91	10.00	5.560	0.423	0.350	
343	18	40	46	106	3.91	20.00	5.630	0.423	0.317	
344	18	40	46	106	3.91	30.00	4.730	0.423	0.253	
345	18	40	46	106	3.91	40.00	5.480	0.423	0.288	
346	18	40	46	106	3.91	50.00	4.500	0.423	0.237	
347	18	40	46	106	3.91	50.00	5.710	0.423	0.300	
348	18	40	46	106	3.91	65.00	5.710	0.423	0.304	
349	18	40	47	108	2.95	0.23	1.320	0.431	0.208	Medved et al, (1962)
350	18	40	47	108	2.95	0.25	1.330	0.431	0.204	
351	18	40	47	108	2.95	0.25	1.450	0.431	0.221	
352	18	40	47	108	2.95	10.00	10.200	0.431	0.485	
353	18	40	47	108	2.95	40.00	11.200	0.431	0.443	
354	18	40	47	108	2.95	120.00	10.600	0.431	0.456	
355	2	4	5	11	5.92	30.00	0.016	0.439	0.366	Miyagawa et al, (1978)
356	2	4	5	11	5.92	50.00	0.010	0.439	0.347	
357	2	4	5	11	5.92	100.00	0.006	0.439	0.349	
358	2	4	5	11	5.92	150.00	0.005	0.439	0.436	
359	18	40	48	112	1.16	20.00	23.900	0.447	0.403	Sigmund, (1969)
360	18	40	48	112	1.16	30.00	24.800	0.447	0.399	
361	18	40	48	112	1.16	40.00	25.500	0.447	0.401	
362	18	40	48	112	1.16	50.00	25.000	0.447	0.393	
363	18	40	48	112	1.16	60.00	24.900	0.447	0.394	
364	18	40	48	112	1.16	70.00	24.800	0.447	0.396	
365	18	40	48	112	1.16	80.00	26.200	0.447	0.423	
366	18	40	48	112	1.16	90.00	23.800	0.447	0.389	
367	18	40	48	112	1.16	100.00	24.900	0.447	0.412	

No.	Z1	M1	Z2	M2	B(eV)	E(keV)	S	Log(M2/M1)	Alpha_eff	Reference
368	18	40	50	119	3.13	0.20	0.790	0.473	0.143	Krutenat et al, (1970)
369	18	40	50	119	3.13	0.24	0.823	0.473	0.140	
370	18	40	50	119	3.13	0.34	1.030	0.473	0.153	
371	18	40	50	119	3.13	0.35	1.040	0.473	0.153	
372	18	40	50	119	3.13	0.40	1.420	0.473	0.199	
373	18	40	50	119	3.13	0.45	1.180	0.473	0.157	
374	18	40	50	119	3.13	0.60	1.190	0.473	0.141	
375	18	40	50	119	3.13	0.80	1.260	0.473	0.134	
376	18	40	50	119	3.13	4.00	3.330	0.473	0.213	
377	18	40	50	119	3.13	20.00	4.920	0.473	0.228	
378	18	40	50	119	3.13	30.00	4.360	0.473	0.191	
379	18	40	50	119	3.13	40.00	4.360	0.473	0.187	
380	18	40	50	119	3.13	50.00	4.230	0.473	0.181	
381	18	40	50	119	3.13	65.00	4.210	0.473	0.182	
382	10	20	29	64	3.49	5.00	2.610	0.505	0.371	Sigmund, (1969)
383	10	20	29	64	3.49	11.00	2.860	0.505	0.374	
384	10	20	29	64	3.49	11.00	3.630	0.505	0.474	
385	10	20	29	64	3.49	15.00	3.420	0.505	0.447	
386	10	20	29	64	3.49	20.00	2.790	0.505	0.371	
387	10	20	29	64	3.49	20.00	3.420	0.505	0.455	
388	10	20	29	64	3.49	25.00	2.860	0.505	0.389	
389	10	20	29	64	3.49	30.00	3.350	0.505	0.467	
390	10	20	29	64	3.49	5.00	2.760	0.505	0.392	
391	10	20	29	64	3.49	10.00	2.910	0.505	0.381	
392	10	20	29	64	3.49	15.00	2.990	0.505	0.390	
393	10	20	29	64	3.49	20.00	3.160	0.505	0.421	
394	10	20	29	64	3.49	25.00	3.010	0.505	0.410	
395	10	20	29	64	3.49	30.00	3.110	0.505	0.434	
396	10	20	29	64	3.49	40.00	3.490	0.505	0.512	
397	10	20	29	64	3.49	50.00	3.000	0.505	0.462	
398	10	20	29	64	3.49	80.00	2.370	0.505	0.416	
399	10	20	29	64	3.49	100.00	2.790	0.505	0.527	
400	10	20	29	64	3.49	150.00	2.440	0.505	0.541	
401	10	20	29	64	3.49	200.00	2.090	0.505	0.531	
402	10	20	29	64	3.49	300.00	1.920	0.505	0.610	
403	10	20	29	64	3.49	400.00	1.120	0.505	0.429	
404	10	20	29	64	3.49	500.00	1.120	0.505	0.503	
405	10	20	29	64	3.49	600.00	1.050	0.505	0.530	
406	10	20	29	64	3.49	700.00	1.050	0.505	0.587	
407	10	20	29	64	3.49	800.00	0.698	0.505	0.428	
408	10	20	29	64	3.49	900.00	0.698	0.505	0.465	
409	10	20	29	64	3.49	1000.00	0.698	0.505	0.500	

No.	Z1	M1	Z2	M2	B(eV)	E(keV)	S	Log(M2/M1)	Alpha_eff	Reference
410	7	14	29	64	3.49	5.00	1.630	0.660	0.397	Almén et al, (1961)
411	7	14	29	64	3.49	10.00	1.750	0.660	0.419	
412	7	14	29	64	3.49	15.00	2.000	0.660	0.495	
413	7	14	29	64	3.49	18.00	1.750	0.660	0.444	
414	7	14	29	64	3.49	20.00	1.250	0.660	0.322	
415	7	14	29	64	3.49	22.50	1.630	0.660	0.427	
416	7	14	29	64	3.49	30.00	1.330	0.660	0.369	
417	7	14	29	64	3.49	40.00	1.550	0.660	0.464	
418	7	14	29	64	3.49	50.00	1.150	0.660	0.368	
419	18	40	79	197	3.82	1.00	3.580	0.692	0.536	Robinson et al, (1967)
420	18	40	79	197	3.82	1.50	4.750	0.692	0.611	
421	18	40	79	197	3.82	2.00	5.640	0.692	0.655	
422	18	40	79	197	3.82	2.50	6.310	0.692	0.680	
423	18	40	79	197	3.82	3.00	6.790	0.692	0.690	
424	18	40	79	197	3.82	3.50	7.180	0.692	0.695	
425	18	40	79	197	3.82	4.00	7.380	0.692	0.687	
426	18	40	79	197	3.82	4.50	7.620	0.692	0.685	
427	18	40	79	197	3.82	5.00	7.900	0.692	0.690	
428	10	20	46	106	3.91	10.00	2.110	0.724	0.342	Sigmund, (1969)
429	10	20	46	106	3.91	20.00	2.560	0.724	0.393	
430	10	20	46	106	3.91	30.00	2.630	0.724	0.411	
431	10	20	46	106	3.91	40.00	2.560	0.724	0.411	
432	10	20	46	106	3.91	50.00	2.260	0.724	0.374	

No.	Z1	M1	Z2	M2	B(eV)	E(keV)	S	Log(M2/M1)	Alpha_eff	Reference
433	10	20	47	108	2.95	0.15	0.607	0.732	0.242	Medved et al, (1962)
434	10	20	47	108	2.95	0.17	0.619	0.732	0.236	
435	10	20	47	108	2.95	0.19	0.675	0.732	0.246	
436	10	20	47	108	2.95	0.19	0.708	0.732	0.258	
437	10	20	47	108	2.95	0.20	0.703	0.732	0.252	
438	10	20	47	108	2.95	0.22	0.742	0.732	0.255	
439	10	20	47	108	2.95	0.22	0.760	0.732	0.261	
440	10	20	47	108	2.95	0.24	0.813	0.732	0.270	
441	10	20	47	108	2.95	0.24	0.830	0.732	0.275	
442	10	20	47	108	2.95	0.25	0.868	0.732	0.286	
443	10	20	47	108	2.95	0.25	0.826	0.732	0.270	
444	10	20	47	108	2.95	0.25	0.900	0.732	0.294	
445	10	20	47	108	2.95	0.20	1.030	0.732	0.369	
446	10	20	47	108	2.95	0.30	1.380	0.732	0.420	
447	10	20	47	108	2.95	0.40	1.720	0.732	0.471	
448	10	20	47	108	2.95	0.50	1.970	0.732	0.496	
449	10	20	47	108	2.95	0.60	1.280	0.732	0.302	
450	10	20	47	108	2.95	0.60	2.070	0.732	0.490	
451	10	20	47	108	2.95	1.80	3.450	0.732	0.590	
452	10	20	47	108	2.95	2.50	4.550	0.732	0.719	
453	10	20	47	108	2.95	4.00	4.550	0.732	0.650	
454	10	20	47	108	2.95	5.20	5.720	0.732	0.778	
455	10	20	47	108	2.95	10.00	4.480	0.732	0.551	
456	10	20	47	108	2.95	20.00	4.310	0.732	0.500	
457	10	20	47	108	2.95	20.00	5.000	0.732	0.580	
458	10	20	47	108	2.95	30.00	4.310	0.732	0.507	
459	10	20	47	108	2.95	30.00	5.000	0.732	0.588	
460	10	20	47	108	2.95	40.00	4.650	0.732	0.563	
461	10	20	47	108	2.95	50.00	5.000	0.732	0.623	
462	10	20	50	119	3.13	10.00	2.150	0.775	0.293	Sigmund, (1969)
463	10	20	50	119	3.13	20.00	1.920	0.775	0.244	
464	10	20	50	119	3.13	30.00	1.850	0.775	0.237	
465	10	20	50	119	3.13	40.00	1.720	0.775	0.226	
466	10	20	50	119	3.13	50.00	1.720	0.775	0.232	
467	7	14	47	108	2.95	20.00	2.640	0.887	0.589	Almén et al, (1961)
468	7	14	47	108	2.95	30.00	2.570	0.887	0.598	
469	7	14	47	108	2.95	40.00	2.420	0.887	0.590	
470	7	14	47	108	2.95	50.00	2.570	0.887	0.657	

No.	Z1	M1	Z2	M2	B(eV)	E(keV)	S	Log(M2/M1)	Alpha_eff	Reference
471	1	1	5	11	5.92	13.00	0.001	1.041	0.227	Miyagawa et al, (1978)
472	1	1	5	11	5.92	15.00	0.002	1.041	0.377	
473	2	4	26	59	4.31	0.15	0.083	1.169	0.345	Behrisch et al, (1979)
474	2	4	26	59	4.31	0.25	0.107	1.169	0.396	
475	2	4	26	59	4.31	0.40	0.136	1.169	0.461	
476	2	4	26	59	4.31	0.80	0.170	1.169	0.517	
477	2	4	26	59	4.31	2.00	0.190	1.169	0.552	
478	2	4	26	59	4.31	4.00	0.161	1.169	0.503	
479	2	4	26	59	4.31	6.00	0.141	1.169	0.476	
480	2	4	26	59	4.31	8.00	0.122	1.169	0.443	
481	2	4	28	59	4.46	0.15	0.075	1.169	0.314	Roth, (1980)
482	2	4	28	59	4.46	0.25	0.114	1.169	0.421	
483	2	4	28	59	4.46	0.50	0.106	1.169	0.344	
484	2	4	28	59	4.46	0.50	0.159	1.169	0.514	
485	2	4	28	59	4.46	1.00	0.100	1.169	0.294	
486	2	4	28	59	4.46	1.00	0.130	1.169	0.382	
487	2	4	28	59	4.46	1.00	0.155	1.169	0.455	
488	2	4	28	59	4.46	1.00	0.188	1.169	0.553	
489	2	4	28	59	4.46	2.00	0.188	1.169	0.535	
490	2	4	28	59	4.46	4.00	0.146	1.169	0.442	
491	2	4	28	59	4.46	4.00	0.188	1.169	0.569	
492	2	4	28	59	4.46	4.70	0.168	1.169	0.520	
493	2	4	28	59	4.46	7.50	0.159	1.169	0.542	
494	2	4	29	64	3.49	0.20	0.127	1.204	0.412	Roth, (1980)
495	2	4	29	64	3.49	0.30	0.180	1.204	0.535	
496	2	4	29	64	3.49	0.40	0.213	1.204	0.596	
497	2	4	29	64	3.49	0.50	0.250	1.204	0.673	
498	2	4	29	64	3.49	0.60	0.228	1.204	0.596	
499	2	4	29	64	3.49	4.00	0.280	1.204	0.681	
500	2	4	29	64	3.49	2.00	0.329	1.204	0.769	
501	2	4	29	64	3.49	4.00	0.284	1.204	0.702	
502	2	4	29	64	3.49	8.00	0.247	1.204	0.701	
503	2	4	29	64	3.49	15.00	0.206	1.204	0.707	
504	2	4	29	64	3.49	20.00	0.200	1.204	0.770	
505	2	4	29	64	3.49	23.00	0.204	1.204	0.832	
506	2	4	29	64	3.49	30.00	0.151	1.204	0.703	
507	2	4	29	64	3.49	38.50	0.089	1.204	0.476	

No.	Z1	M1	Z2	M2	B(eV)	E(keV)	S	Log(M2/M1)	Alpha_eff	Reference
508	2	4	42	96	6.83	0.20	0.020	1.380	0.161	Roth, (1980)
509	2	4	42	96	6.83	0.30	0.022	1.380	0.162	
510	2	4	42	96	6.83	0.50	0.032	1.380	0.205	
511	2	4	42	96	6.83	1.00	0.014	1.380	0.080	
512	2	4	42	96	6.83	2.00	0.011	1.380	0.059	
513	2	4	42	96	6.83	2.00	0.050	1.380	0.262	
514	2	4	42	96	6.83	4.00	0.045	1.380	0.233	
515	2	4	42	96	6.83	4.00	0.053	1.380	0.274	
516	2	4	42	96	6.83	6.00	0.040	1.380	0.217	
517	2	4	42	96	6.83	6.00	0.048	1.380	0.260	
518	2	4	42	96	6.83	7.50	0.040	1.380	0.224	
519	2	4	42	96	6.83	8.00	0.039	1.380	0.221	
520	2	4	42	96	6.83	100.00	0.016	1.380	0.256	
521	1	2	28	59	4.46	0.80	0.050	1.470	0.534	Roth, (1980)
522	1	2	28	59	4.46	1.00	0.040	1.470	0.431	
523	1	2	28	59	4.46	2.00	0.039	1.470	0.447	
524	1	2	28	59	4.46	4.00	0.029	1.470	0.381	
525	1	2	28	59	4.46	7.50	0.021	1.470	0.345	
526	1	2	29	64	3.49	0.50	0.071	1.505	0.645	Roth, (1980)
527	1	2	29	64	3.49	1.00	0.080	1.505	0.702	
528	1	2	29	64	3.49	2.00	0.075	1.505	0.707	
529	1	2	29	64	3.49	8.00	0.045	1.505	0.607	
530	1	2	29	64	3.49	10.00	0.049	1.505	0.730	
531	1	2	29	64	3.49	12.00	0.047	1.505	0.766	
532	1	2	29	64	3.49	20.00	0.032	1.505	0.675	
533	1	2	29	64	3.49	30.00	0.028	1.505	0.798	
534	1	2	29	64	3.49	30.00	0.035	1.505	0.993	
535	1	2	29	64	3.49	40.00	0.021	1.505	0.717	
536	1	2	29	64	3.49	10.00	0.051	1.505	0.763	Yants et al, (1960)
537	1	2	29	64	3.49	11.00	0.046	1.505	0.711	
538	1	2	29	64	3.49	20.00	0.032	1.505	0.684	
539	1	2	29	64	3.49	30.00	0.029	1.505	0.808	
540	1	2	29	64	3.49	31.00	0.035	1.505	1.010	
541	1	2	29	64	3.49	45.00	0.023	1.505	0.825	

No.	Z1	M1	Z2	M2	B(eV)	E(keV)	S	Log(M2/M1)	Alpha_eff	Reference
542	2	4	74	184	8.81	1.00	0.021	1.663	0.225	Roth, (1980)
543	2	4	74	184	8.81	2.00	0.028	1.663	0.258	
544	2	4	74	184	8.81	4.00	0.030	1.663	0.260	
545	2	4	74	184	8.81	8.00	0.044	1.663	0.376	
546	2	4	74	184	8.81	20.00	0.037	1.663	0.354	
547	1	2	41	93	7.48	3.00	0.004	1.667	0.097	Eckstein et al, (1973)
548	1	2	41	93	7.48	4.00	0.005	1.667	0.109	
549	1	2	41	93	7.48	5.00	0.005	1.667	0.114	
550	1	2	41	93	7.48	6.50	0.005	1.667	0.130	
551	1	2	41	93	7.48	8.00	0.003	1.667	0.274	
552	1	2	41	93	7.48	12.00	0.008	1.667	0.274	Summer et al, (1971)
553	1	2	41	93	7.48	18.00	0.005	1.667	0.207	
554	1	2	41	93	7.48	28.00	0.005	1.667	0.229	
555	1	2	41	93	7.48	36.00	0.003	1.667	0.151	
556	1	2	41	93	7.48	56.50	0.002	1.667	0.122	
557	1	2	42	96	6.83	0.50	0.004	1.681	0.077	Roth, (1980)
558	1	2	42	96	6.83	1.00	0.006	1.681	0.119	
559	1	2	42	96	6.83	2.00	0.008	1.681	0.160	
560	1	2	42	96	6.83	2.00	0.009	1.681	0.190	
561	1	2	42	96	6.83	4.00	0.008	1.681	0.174	
562	1	2	42	96	6.83	8.00	0.005	1.681	0.133	
563	1	2	42	96	6.83	40.00	0.001	1.681	0.058	
564	1	2	42	96	6.83	60.00	0.001	1.681	0.052	
565	1	2	42	96	6.83	115.00	0.001	1.681	0.057	
566	2	4	92	235	5.43	40.00	0.013	1.769	0.093	Gregg et al, (1977)
567	2	4	92	235	5.43	60.00	0.014	1.769	0.115	
568	2	4	92	235	5.43	80.00	0.012	1.769	0.111	
569	2	4	92	235	5.43	100.00	0.009	1.769	0.094	
570	2	4	92	235	5.43	120.00	0.010	1.769	0.109	
571	1	1	28	59	4.46	0.50	0.011	1.771	0.242	Roth, (1980)
572	1	1	28	59	4.46	1.00	0.013	1.771	0.266	
573	1	1	28	59	4.46	2.00	0.013	1.771	0.302	
574	1	1	28	59	4.46	4.00	0.011	1.771	0.295	
575	1	1	28	59	4.46	7.50	0.008	1.771	0.266	

No.	Z1	M1	Z2	M2	B(eV)	E(keV)	S	Log(M2/M1)	Alpha_eff	Reference
576	1	1	29	64	3.49	0.25	0.014	1.806	0.279	Roth, (1980)
577	1	1	29	64	3.49	0.50	0.025	1.806	0.450	
578	1	1	29	64	3.49	1.00	0.036	1.806	0.618	
579	1	1	29	64	3.49	2.00	0.032	1.806	0.588	
580	1	1	29	64	3.49	7.50	0.017	1.806	0.441	
581	1	1	29	64	3.49	30.00	0.005	1.806	0.299	
582	1	1	29	64	3.49	50.00	0.004	1.806	0.278	
583	1	1	29	64	3.49	70.00	0.002	1.806	0.221	
584	1	1	29	64	3.49	100.00	0.002	1.806	0.228	
585	1	1	29	64	3.49	120.00	0.001	1.806	0.207	
586	1	1	29	64	3.49	150.00	0.001	1.806	0.184	
587	1	2	74	184	8.81	2.00	0.006	1.964	0.153	Roth, (1980)
588	1	2	74	184	8.81	4.00	0.007	1.964	0.210	
589	1	2	74	184	8.81	8.00	0.007	1.964	0.259	
590	1	2	74	184	8.81	15.00	0.005	1.964	0.198	
591	1	2	74	184	8.81	30.00	0.004	1.964	0.224	
592	1	2	74	184	8.81	50.00	0.003	1.964	0.169	
593	1	1	47	108	2.95	2.00	0.034	2.033	0.602	Furr et al, (1970)
594	1	1	47	108	2.95	3.00	0.033	2.033	0.595	
595	1	1	47	108	2.95	3.00	0.037	2.033	0.678	
596	1	1	47	108	2.95	4.00	0.035	2.033	0.667	
597	1	1	47	108	2.95	5.00	0.033	2.033	0.655	
598	1	1	47	108	2.95	6.00	0.034	2.033	0.702	
599	1	1	47	108	2.95	7.00	0.033	2.033	0.696	
600	1	1	47	108	2.95	7.00	0.036	2.033	0.771	
601	1	1	47	108	2.95	8.00	0.032	2.033	0.710	
602	1	1	47	108	2.95	8.00	0.033	2.033	0.732	
603	1	1	47	108	2.95	9.00	0.034	2.033	0.780	
604	1	1	47	108	2.95	10.00	0.032	2.033	0.759	
605	1	1	47	108	2.95	11.00	0.033	2.033	0.807	
606	1	1	47	108	2.95	12.00	0.025	2.033	0.630	

No.	Z1	M1	Z2	M2	B(eV)	E(keV)	S	Log(M2/M1)	Alpha_eff	Reference
607	1	1	74	184	8.81	4.00	0.002	2.265	0.140	Roth, (1980)
608	1	1	74	184	8.81	4.00	0.002	2.265	0.125	
609	1	1	74	184	8.81	8.00	0.002	2.265	0.152	
610	1	1	79	197	3.82	2.00	0.011	2.294	0.326	Bay et al, (1977)
611	1	1	79	197	3.82	4.00	0.016	2.294	0.467	
612	1	1	79	197	3.82	8.00	0.014	2.294	0.441	
613	1	1	79	197	3.82	20.00	0.009	2.294	0.337	
614	1	1	79	197	3.82	2.00	0.018	2.294	0.518	Furr et al, (1970)
615	1	1	79	197	3.82	3.00	0.021	2.294	0.599	
616	1	1	79	197	3.82	4.00	0.022	2.294	0.642	
617	1	1	79	197	3.82	5.00	0.022	2.294	0.643	
618	1	1	79	197	3.82	6.00	0.024	2.294	0.716	
619	1	1	79	197	3.82	7.00	0.022	2.294	0.669	
620	1	1	79	197	3.82	8.00	0.021	2.294	0.673	

C. Predicted Normalised Sputtering Yields for Mono-elemental Polycrystalline Targets

The table contains values of SB as calculated from equations 2.7 and 2.9 for LSS energies within the range $0.001 < \varepsilon < 100$.

Z_1	=	Atomic number of the incident ion
M_1	=	Mass number of the incident ion
Z_2	=	Atomic number of the target
M_2	=	Mass number of the target
E	=	Ion energy in keV
SB	=	Product of sputtering yield S and surface binding energy B

The SB values are tabulated for Z_1 and Z_2 ranging from 1 to 90 in intervals of 2 or 5, and for E values ranging from 0.1 to 1,000 keV, provided these fall within the $0.001 < \varepsilon < 100$ (the defined range for equation 2.7).

M_1 and M_2 values corresponding to the Z_1 and Z_2 values used are:

Z_1 or Z_2	1	3	5	10	15	20	25	30	35	40	45	50	55	60	65	70	75	80	85	90
M_1 or M_2	1	6	10	21	32	43	54	66	79	92	105	118	131	145	159	172	186	200	216	230

Z1	1																		
M1	1																		
Z2	3	5	10	15	20	25	30	35	40	45	50	55	60	65	70	75	80	85	90
M2	6	10	21	32	43	54	66	79	92	105	118	131	145	159	172	186	200	216	230

E	SB	SB	SB	SB	SB	SB	SB	SB	SB	SB	SB	SB	SB	SB	SB	SB	SB	SB	SB
0.1	0.17	0.20	0.18	0.15	0.12	0.10													
0.15	0.16	0.19	0.18	0.15	0.11	0.09													
0.2	0.15	0.19	0.19	0.15	0.12	0.09													
0.25	0.14	0.18	0.19	0.16	0.12	0.10													
0.3	0.13	0.18	0.19	0.16	0.13	0.10													
0.4	0.12	0.17	0.18	0.16	0.13	0.10													
0.5	0.11	0.16	0.18	0.16	0.13	0.11													
0.6	0.10	0.15	0.17	0.15	0.13	0.11													
0.8	0.09	0.13	0.16	0.15	0.13	0.11													
1	0.08	0.12	0.15	0.14	0.13	0.11													
1.5	0.06	0.10	0.14	0.13	0.12	0.10													
2	0.05	0.09	0.12	0.12	0.11	0.10													
2.5	0.04	0.08	0.11	0.11	0.11	0.09													
3	0.04	0.07	0.10	0.11	0.10	0.09													
4	0.03	0.06	0.09	0.10	0.09	0.08													
5	0.02	0.05	0.08	0.09	0.08	0.08													
6	0.02	0.04	0.07	0.08	0.08	0.07													
8	0.01	0.03	0.06	0.07	0.07	0.06													
10	0.01	0.03	0.05	0.06	0.06	0.06													
15	0.01	0.02	0.04	0.04	0.05	0.05													
20		0.02	0.03	0.04	0.04	0.04													
25		0.01	0.03	0.03	0.03	0.03													
30		0.01	0.02	0.03	0.03	0.03													
40			0.02	0.02	0.02	0.02													
50			0.02	0.02	0.02	0.02													
60			0.01	0.02	0.02	0.02													
80				0.01	0.01	0.01													
100				0.01	0.01	0.01													
150					0.01	0.01													
200						0.01													
250																			
300																			
400																			
500																			
600																			
800																			
1000																			

Z1	3
M1	6

Z2	3	5	10	15	20	25	30	35	40	45	50	55	60	65	70	75	80	85	90
M2	6	10	21	32	43	54	66	79	92	105	118	131	145	159	172	186	200	216	230

E	SB	SB	SB	SB	SB	SB	SB	SB	SB	SB	SB	SB	SB	SB	SB	SB	SB	SB	SB
0.10	0.55	0.79	1.25	1.07	1.08	1.06	1.00	0.93	0.87	0.80	0.74	0.69	0.63	0.58	0.54	0.50	0.47	0.43	0.40
0.15	0.55	0.75	1.06	1.18	1.21	1.19	1.14	1.06	0.99	0.92	0.86	0.80	0.74	0.68	0.64	0.59	0.55	0.50	0.47
0.20	0.57	0.78	1.12	1.26	1.30	1.29	1.23	1.16	1.09	1.01	0.94	0.88	0.82	0.76	0.71	0.65	0.61	0.56	0.52
0.25	0.58	0.81	1.16	1.32	1.37	1.36	1.31	1.24	1.16	1.08	1.01	0.95	0.88	0.81	0.76	0.71	0.66	0.61	0.57
0.30	0.59	0.82	1.20	1.37	1.42	1.42	1.37	1.30	1.22	1.14	1.07	1.00	0.93	0.86	0.81	0.75	0.70	0.65	0.60
0.40	0.58	0.84	1.25	1.44	1.51	1.51	1.47	1.39	1.31	1.24	1.16	1.09	1.01	0.94	0.88	0.82	0.77	0.71	0.66
0.50	0.58	0.84	1.29	1.49	1.57	1.58	1.54	1.46	1.39	1.31	1.23	1.15	1.08	1.00	0.94	0.88	0.82	0.76	0.71
0.60	0.57	0.84	1.32	1.53	1.62	1.63	1.59	1.52	1.44	1.36	1.29	1.21	1.13	1.06	0.99	0.93	0.87	0.80	0.75
0.80	0.55	0.82	1.34	1.59	1.69	1.71	1.68	1.61	1.53	1.45	1.37	1.29	1.21	1.14	1.07	1.00	0.94	0.87	0.82
1.0	0.52	0.80	1.34	1.63	1.74	1.77	1.74	1.68	1.60	1.52	1.44	1.36	1.27	1.20	1.13	1.06	0.99	0.92	0.87
1.5	0.48	0.75	1.30	1.64	1.81	1.87	1.85	1.79	1.71	1.63	1.55	1.47	1.38	1.30	1.23	1.16	1.09	1.01	0.96
2.0	0.44	0.70	1.26	1.62	1.82	1.91	1.91	1.86	1.78	1.71	1.63	1.55	1.46	1.37	1.30	1.23	1.16	1.08	1.02
2.5	0.41	0.66	1.21	1.58	1.80	1.92	1.94	1.91	1.83	1.76	1.68	1.60	1.51	1.43	1.35	1.28	1.21	1.12	1.06
3.0	0.38	0.63	1.17	1.55	1.78	1.91	1.95	1.93	1.88	1.80	1.72	1.64	1.55	1.47	1.39	1.32	1.24	1.16	1.10
4.0	0.34	0.57	1.09	1.48	1.72	1.87	1.93	1.93	1.89	1.84	1.78	1.70	1.61	1.52	1.45	1.38	1.30	1.22	1.15
5.0	0.31	0.52	1.03	1.41	1.66	1.82	1.90	1.91	1.89	1.85	1.79	1.73	1.65	1.57	1.49	1.42	1.34	1.26	1.19
6.0	0.28	0.48	0.97	1.35	1.61	1.78	1.86	1.88	1.87	1.84	1.79	1.74	1.67	1.59	1.53	1.45	1.37	1.29	1.22
8.0	0.23	0.42	0.88	1.25	1.51	1.68	1.78	1.82	1.82	1.80	1.77	1.73	1.66	1.60	1.54	1.48	1.41	1.33	1.26
10	0.20	0.37	0.80	1.16	1.42	1.60	1.71	1.75	1.77	1.76	1.73	1.70	1.64	1.59	1.54	1.48	1.41	1.34	1.28
15	0.15	0.29	0.66	0.99	1.25	1.43	1.55	1.61	1.64	1.65	1.64	1.62	1.58	1.53	1.49	1.44	1.39	1.32	1.27
20	0.13	0.23	0.56	0.87	1.11	1.30	1.42	1.49	1.53	1.55	1.55	1.54	1.51	1.47	1.44	1.40	1.35	1.29	1.24
25	0.11	0.20	0.49	0.78	1.01	1.19	1.31	1.39	1.43	1.46	1.47	1.46	1.44	1.41	1.38	1.35	1.31	1.25	1.21
30	0.10	0.18	0.43	0.70	0.92	1.10	1.23	1.30	1.35	1.38	1.40	1.40	1.38	1.35	1.33	1.30	1.27	1.21	1.18
40	0.08	0.15	0.36	0.58	0.79	0.96	1.08	1.16	1.22	1.25	1.28	1.28	1.27	1.26	1.24	1.22	1.19	1.15	1.11
50	0.07	0.13	0.31	0.49	0.69	0.85	0.97	1.05	1.11	1.15	1.18	1.19	1.19	1.18	1.17	1.15	1.12	1.09	1.06
60	0.06	0.11	0.27	0.44	0.61	0.76	0.88	0.96	1.02	1.06	1.09	1.11	1.11	1.11	1.10	1.09	1.07	1.03	1.01
80	0.05	0.09	0.22	0.36	0.50	0.63	0.74	0.82	0.88	0.93	0.96	0.98	0.99	0.99	0.99	0.98	0.97	0.94	0.92
100	0.04	0.07	0.19	0.31	0.43	0.54	0.63	0.71	0.77	0.82	0.86	0.88	0.89	0.90	0.90	0.90	0.89	0.87	0.85
150		0.05	0.14	0.23	0.33	0.41	0.48	0.54	0.58	0.63	0.67	0.70	0.72	0.73	0.74	0.74	0.74	0.73	0.72
200			0.11	0.19	0.27	0.34	0.40	0.44	0.49	0.52	0.55	0.58	0.60	0.62	0.63	0.64	0.64	0.63	0.63
250			0.09	0.16	0.23	0.29	0.34	0.38	0.42	0.45	0.48	0.50	0.51	0.53	0.54	0.55	0.56	0.55	0.55
300			0.08	0.14	0.20	0.25	0.30	0.34	0.37	0.40	0.42	0.44	0.45	0.46	0.47	0.49	0.49	0.49	0.49
400				0.11	0.16	0.20	0.24	0.27	0.30	0.33	0.35	0.36	0.38	0.39	0.40	0.40	0.40	0.40	0.41
500					0.13	0.17	0.20	0.23	0.26	0.28	0.30	0.31	0.32	0.33	0.34	0.35	0.35	0.35	0.35
600					0.11	0.15	0.18	0.20	0.22	0.24	0.26	0.27	0.28	0.29	0.30	0.31	0.31	0.31	0.31
800						0.12	0.14	0.16	0.18	0.20	0.21	0.22	0.23	0.24	0.25	0.25	0.25	0.25	0.26
1000							0.12	0.14	0.15	0.17	0.18	0.19	0.20	0.20	0.21	0.21	0.22	0.22	0.22

Z1	5
M1	10

Z2	3	5	10	15	20	25	30	35	40	45	50	55	60	65	70	75	80	85	90
M2	6	10	21	32	43	54	66	79	92	105	118	131	145	159	172	186	200	216	230

E	SB	SB	SB	SB	SB	SB	SB	SB	SB	SB	SB	SB	SB	SB	SB	SB	SB	SB	SB
0.10	0.70	0.95	1.35	1.57	1.68	1.72	1.70	1.65	1.59	1.52	1.45	1.38	1.31	1.24	1.18	1.12	1.07	1.01	0.96
0.15	0.76	1.05	1.50	1.78	1.92	1.97	1.97	1.92	1.85	1.78	1.70	1.62	1.54	1.46	1.39	1.32	1.25	1.18	1.12
0.20	0.80	1.11	1.62	1.92	2.09	2.16	2.16	2.12	2.05	1.97	1.89	1.81	1.72	1.63	1.56	1.48	1.40	1.32	1.26
0.25	0.83	1.16	1.70	2.04	2.22	2.31	2.32	2.27	2.21	2.13	2.05	1.96	1.86	1.77	1.69	1.61	1.53	1.44	1.37
0.30	0.85	1.20	1.77	2.13	2.33	2.43	2.45	2.41	2.34	2.26	2.18	2.09	1.99	1.89	1.81	1.72	1.64	1.55	1.47
0.40	0.89	1.25	1.87	2.27	2.50	2.62	2.65	2.62	2.56	2.48	2.39	2.30	2.19	2.09	2.00	1.91	1.82	1.72	1.64
0.50	0.91	1.29	1.95	2.38	2.63	2.77	2.81	2.78	2.72	2.65	2.56	2.46	2.36	2.25	2.16	2.06	1.97	1.86	1.78
0.60	0.93	1.32	2.01	2.46	2.74	2.89	2.94	2.92	2.86	2.78	2.70	2.60	2.49	2.38	2.29	2.19	2.09	1.98	1.89
0.80	0.94	1.37	2.09	2.59	2.89	3.07	3.13	3.12	3.07	3.00	2.91	2.82	2.71	2.59	2.50	2.39	2.29	2.17	2.08
1.0	0.93	1.38	2.15	2.68	3.01	3.20	3.28	3.28	3.24	3.17	3.08	2.99	2.87	2.76	2.66	2.55	2.44	2.32	2.22
1.5	0.90	1.36	2.24	2.83	3.21	3.43	3.54	3.55	3.52	3.46	3.38	3.29	3.17	3.05	2.95	2.84	2.73	2.59	2.49
2.0	0.87	1.33	2.24	2.92	3.33	3.58	3.71	3.74	3.71	3.66	3.58	3.49	3.38	3.26	3.16	3.04	2.92	2.79	2.68
2.5	0.83	1.29	2.22	2.94	3.42	3.69	3.83	3.87	3.85	3.80	3.73	3.65	3.53	3.41	3.31	3.19	3.08	2.94	2.83
3.0	0.80	1.25	2.18	2.93	3.45	3.77	3.92	3.97	3.96	3.92	3.85	3.77	3.65	3.54	3.43	3.31	3.20	3.05	2.94
4.0	0.74	1.18	2.11	2.88	3.45	3.83	4.05	4.11	4.12	4.09	4.02	3.95	3.83	3.72	3.62	3.50	3.38	3.23	3.12
5.0	0.70	1.12	2.04	2.82	3.41	3.83	4.08	4.21	4.23	4.20	4.15	4.07	3.97	3.85	3.75	3.63	3.51	3.37	3.25
6.0	0.66	1.06	1.97	2.75	3.36	3.80	4.08	4.23	4.29	4.30	4.24	4.17	4.07	3.95	3.86	3.74	3.62	3.47	3.36
8.0	0.59	0.97	1.84	2.62	3.24	3.71	4.02	4.20	4.31	4.35	4.35	4.32	4.21	4.10	4.01	3.89	3.77	3.62	3.51
10	0.54	0.89	1.73	2.50	3.12	3.60	3.94	4.14	4.27	4.34	4.36	4.35	4.29	4.20	4.11	4.00	3.88	3.73	3.62
15	0.44	0.75	1.52	2.25	2.86	3.36	3.71	3.95	4.12	4.22	4.28	4.30	4.27	4.22	4.18	4.10	4.02	3.89	3.79
20	0.37	0.65	1.35	2.05	2.65	3.14	3.51	3.76	3.95	4.07	4.15	4.20	4.19	4.16	4.14	4.08	4.01	3.90	3.82
25	0.32	0.57	1.22	1.88	2.47	2.95	3.32	3.59	3.78	3.92	4.02	4.08	4.09	4.07	4.06	4.02	3.96	3.86	3.79
30	0.28	0.51	1.12	1.75	2.31	2.79	3.16	3.43	3.63	3.78	3.89	3.96	3.98	3.98	3.98	3.95	3.90	3.81	3.75
40	0.23	0.41	0.95	1.53	2.06	2.52	2.88	3.16	3.37	3.53	3.65	3.74	3.78	3.79	3.81	3.79	3.76	3.69	3.64
50	0.20	0.36	0.83	1.36	1.86	2.30	2.66	2.93	3.15	3.32	3.45	3.55	3.60	3.62	3.65	3.64	3.63	3.56	3.53
60	0.18	0.32	0.73	1.22	1.70	2.12	2.47	2.74	2.96	3.13	3.27	3.37	3.43	3.47	3.50	3.51	3.50	3.45	3.42
80	0.14	0.26	0.60	1.02	1.44	1.84	2.17	2.43	2.65	2.83	2.97	3.08	3.15	3.20	3.25	3.26	3.27	3.23	3.21
100	0.12	0.22	0.52	0.87	1.25	1.62	1.93	2.19	2.40	2.58	2.72	2.84	2.92	2.97	3.03	3.06	3.07	3.04	3.04
150	0.09	0.17	0.39	0.67	0.95	1.24	1.51	1.75	1.95	2.12	2.27	2.39	2.48	2.54	2.61	2.65	2.68	2.67	2.68
200	0.07	0.13	0.32	0.55	0.78	1.02	1.23	1.45	1.64	1.80	1.94	2.07	2.16	2.23	2.30	2.35	2.38	2.39	2.40
250	0.06	0.11	0.27	0.47	0.67	0.88	1.07	1.24	1.41	1.56	1.70	1.82	1.91	1.99	2.06	2.11	2.15	2.16	2.19
300		0.10	0.24	0.41	0.59	0.78	0.95	1.10	1.24	1.36	1.50	1.62	1.71	1.79	1.86	1.92	1.96	1.98	2.01
400			0.19	0.33	0.48	0.63	0.78	0.91	1.03	1.13	1.23	1.32	1.41	1.49	1.56	1.62	1.67	1.69	1.72
500			0.16	0.28	0.41	0.54	0.66	0.78	0.88	0.98	1.07	1.14	1.21	1.27	1.34	1.39	1.44	1.47	1.51
600			0.14	0.24	0.36	0.47	0.58	0.68	0.78	0.86	0.94	1.01	1.07	1.13	1.18	1.22	1.26	1.30	1.34
800				0.19	0.29	0.38	0.47	0.55	0.63	0.70	0.77	0.83	0.89	0.93	0.98	1.02	1.05	1.07	1.09
1000					0.24	0.32	0.40	0.47	0.54	0.60	0.66	0.71	0.76	0.80	0.84	0.87	0.90	0.92	0.95

Z1	10																	
M1	21																	
Z2	3	5	10	15	20	25	30	35	40	45	50	55	60	65	70	75	80	85	90
M2	6	10	21	32	43	54	66	79	92	105	118	131	145	159	172	186	200	216	230

E	SB	SB	SB	SB	SB	SB	SB	SB	SB	SB	SB	SB	SB	SB	SB	SB	SB	SB	SB
0.10	0.86	1.22	1.82	2.18	2.43	2.62	2.75	2.83	2.88	2.90	2.90	2.90	2.88						
0.15	0.98	1.40	2.11	2.53	2.85	3.07	3.23	3.32	3.37	3.39	3.38	3.36	3.32	3.27	3.22	3.17	3.11	3.04	
0.20	1.06	1.53	2.32	2.80	3.17	3.43	3.61	3.72	3.78	3.80	3.79	3.76	3.71	3.65	3.59	3.52	3.45	3.36	3.29
0.25	1.13	1.63	2.49	3.02	3.42	3.72	3.93	4.05	4.12	4.15	4.14	4.11	4.05	3.98	3.92	3.84	3.76	3.65	3.57
0.30	1.18	1.71	2.62	3.20	3.64	3.97	4.20	4.34	4.42	4.45	4.44	4.41	4.35	4.28	4.21	4.13	4.04	3.92	3.83
0.40	1.26	1.84	2.84	3.49	3.99	4.37	4.63	4.81	4.91	4.95	4.96	4.93	4.87	4.79	4.72	4.62	4.52	4.40	4.30
0.50	1.33	1.93	3.01	3.72	4.26	4.68	4.99	5.18	5.30	5.36	5.38	5.36	5.30	5.22	5.14	5.04	4.94	4.80	4.69
0.60	1.38	2.01	3.15	3.90	4.49	4.95	5.28	5.50	5.64	5.71	5.73	5.72	5.66	5.58	5.50	5.40	5.29	5.15	5.04
0.80	1.45	2.13	3.36	4.19	4.85	5.36	5.74	6.00	6.17	6.27	6.31	6.31	6.26	6.18	6.11	6.00	5.89	5.74	5.62
1.0	1.51	2.22	3.52	4.41	5.12	5.68	6.11	6.40	6.59	6.71	6.77	6.78	6.73	6.66	6.59	6.49	6.37	6.21	6.09
1.5	1.60	2.37	3.79	4.79	5.60	6.26	6.76	7.12	7.36	7.52	7.61	7.65	7.62	7.56	7.50	7.40	7.28	7.12	6.99
2.0	1.66	2.46	3.97	5.05	5.93	6.65	7.21	7.62	7.90	8.09	8.21	8.27	8.26	8.21	8.16	8.06	7.95	7.78	7.65
2.5	1.69	2.53	4.10	5.23	6.18	6.95	7.55	7.99	8.31	8.53	8.67	8.75	8.75	8.71	8.67	8.58	8.47	8.30	8.17
3.0	1.70	2.57	4.20	5.38	6.37	7.18	7.82	8.29	8.64	8.88	9.04	9.13	9.15	9.12	9.08	9.00	8.89	8.73	8.60
4.0	1.68	2.58	4.34	5.59	6.64	7.52	8.22	8.75	9.14	9.42	9.61	9.73	9.76	9.75	9.73	9.66	9.56	9.40	9.27
5.0	1.66	2.56	4.37	5.73	6.84	7.77	8.52	9.08	9.51	9.82	10.0	10.2	10.2	10.2	10.2	10.2	10.1	9.91	9.78
6.0	1.63	2.52	4.37	5.80	6.99	7.96	8.74	9.34	9.79	10.1	10.4	10.5	10.6	10.6	10.6	10.6	10.5	10.3	10.2
8.0	1.56	2.44	4.30	5.81	7.13	8.24	9.07	9.72	10.2	10.6	10.9	11.1	11.1	11.2	11.2	11.2	11.1	10.9	10.8
10	1.50	2.36	4.21	5.75	7.13	8.32	9.29	9.98	10.5	10.9	11.2	11.4	11.6	11.6	11.6	11.6	11.6	11.4	11.3
15	1.36	2.18	3.97	5.53	6.96	8.24	9.32	10.2	10.9	11.4	11.8	12.1	12.2	12.3	12.4	12.4	12.3	12.2	12.1
20	1.25	2.02	3.75	5.29	6.73	8.05	9.18	10.1	10.9	11.5	12.0	12.4	12.6	12.7	12.8	12.8	12.8	12.7	12.6
25	1.16	1.89	3.55	5.06	6.50	7.83	8.99	9.96	10.8	11.4	12.0	12.4	12.7	12.9	13.1	13.2	13.2	13.1	13.0
30	1.08	1.77	3.38	4.85	6.28	7.61	8.77	9.77	10.6	11.3	11.9	12.4	12.7	13.0	13.2	13.3	13.4	13.3	13.3
40	0.96	1.59	3.08	4.50	5.88	7.19	8.36	9.37	10.2	11.0	11.6	12.1	12.5	12.8	13.1	13.3	13.4	13.4	13.5
50	0.86	1.44	2.84	4.19	5.54	6.82	7.98	8.99	9.88	10.6	11.3	11.8	12.3	12.6	12.9	13.1	13.3	13.3	13.4
60	0.78	1.32	2.64	3.94	5.24	6.49	7.64	8.64	9.53	10.3	11.0	11.5	12.0	12.4	12.7	12.9	13.1	13.2	13.3
80	0.66	1.13	2.31	3.51	4.74	5.94	7.04	8.03	8.91	9.69	10.4	11.0	11.4	11.8	12.2	12.5	12.7	12.8	13.0
100	0.57	0.98	2.06	3.18	4.34	5.48	6.55	7.51	8.38	9.15	9.84	10.4	10.9	11.4	11.7	12.0	12.3	12.4	12.6
150	0.43	0.74	1.62	2.57	3.59	4.62	5.60	6.49	7.32	8.07	8.74	9.35	9.85	10.3	10.7	11.0	11.3	11.5	11.7
200	0.35	0.62	1.31	2.15	3.06	4.00	4.90	5.74	6.53	7.24	7.90	8.49	8.99	9.44	9.86	10.2	10.5	10.7	10.9
250	0.30	0.53	1.14	1.84	2.66	3.52	4.36	5.15	5.90	6.59	7.22	7.80	8.29	8.74	9.16	9.51	9.83	10.0	10.3
300	0.27	0.47	1.01	1.63	2.35	3.14	3.93	4.67	5.38	6.04	6.65	7.22	7.70	8.14	8.57	8.92	9.24	9.46	9.71
400	0.22	0.38	0.83	1.35	1.93	2.56	3.26	3.93	4.58	5.19	5.76	6.29	6.76	7.19	7.60	7.95	8.27	8.50	8.76
500	0.18	0.32	0.71	1.16	1.67	2.22	2.78	3.38	3.97	4.54	5.08	5.58	6.03	6.44	6.84	7.18	7.50	7.73	7.99
600	0.16	0.28	0.62	1.02	1.47	1.97	2.47	2.97	3.49	4.02	4.53	5.00	5.43	5.83	6.22	6.55	6.86	7.10	7.36
800	0.13	0.23	0.50	0.83	1.21	1.62	2.04	2.47	2.88	3.29	3.68	4.13	4.52	4.89	5.25	5.57	5.87	6.10	6.36
1000	0.11	0.19	0.42	0.70	1.03	1.38	1.75	2.12	2.49	2.85	3.20	3.53	3.84	4.19	4.53	4.83	5.12	5.35	5.59

Z1	15
M1	32

Z2	3	5	10	15	20	25	30	35	40	45	50	55	60	65	70	75	80	85	90
M2	6	10	21	32	43	54	66	79	92	105	118	131	145	159	172	186	200	216	230

E	SB	SB	SB	SB	SB	SB	SB	SB	SB	SB	SB	SB	SB	SB	SB	SB	SB	SB	SB
0.10	0.89	1.29	2.02	2.48	2.81	3.09	3.33	3.54											
0.15	1.03	1.50	2.37	2.92	3.30	3.61	3.87	4.08	4.25	4.39	4.51	4.60							
0.20	1.14	1.67	2.64	3.26	3.69	4.04	4.33	4.56	4.75	4.89	4.99	5.07	5.12	5.16	5.19	5.20			
0.25	1.23	1.80	2.87	3.55	4.03	4.41	4.73	4.99	5.18	5.33	5.44	5.51	5.56	5.58	5.60	5.59	5.58	5.54	5.51
0.30	1.31	1.91	3.06	3.79	4.31	4.73	5.08	5.36	5.57	5.73	5.84	5.92	5.96	5.98	5.99	5.97	5.95	5.90	5.86
0.40	1.42	2.09	3.36	4.19	4.79	5.27	5.67	5.99	6.24	6.42	6.55	6.64	6.68	6.70	6.70	6.67	6.63	6.56	6.51
0.50	1.52	2.23	3.61	4.51	5.17	5.71	6.16	6.52	6.79	7.00	7.15	7.25	7.30	7.32	7.32	7.29	7.24	7.16	7.09
0.60	1.59	2.35	3.81	4.78	5.49	6.08	6.57	6.96	7.27	7.50	7.66	7.78	7.84	7.86	7.86	7.83	7.79	7.70	7.62
0.80	1.71	2.53	4.13	5.21	6.01	6.68	7.24	7.69	8.05	8.32	8.52	8.66	8.74	8.78	8.79	8.77	8.72	8.62	8.54
1.0	1.80	2.67	4.37	5.54	6.42	7.15	7.77	8.28	8.68	8.99	9.22	9.39	9.48	9.53	9.56	9.54	9.50	9.40	9.32
1.5	1.95	2.91	4.81	6.14	7.16	8.02	8.75	9.36	9.85	10.2	10.5	10.8	10.9	11.0	11.0	11.0	11.0	10.9	10.8
2.0	2.06	3.08	5.11	6.56	7.68	8.63	9.45	10.1	10.7	11.2	11.5	11.8	11.9	12.1	12.1	12.2	12.1	12.1	12.0
2.5	2.14	3.20	5.34	6.88	8.07	9.10	9.99	10.7	11.4	11.9	12.3	12.6	12.8	12.9	13.0	13.0	13.0	13.0	12.9
3.0	2.19	3.29	5.52	7.13	8.39	9.48	10.4	11.2	11.9	12.4	12.9	13.2	13.4	13.6	13.7	13.8	13.8	13.7	13.7
4.0	2.28	3.43	5.78	7.50	8.86	10.1	11.1	12.0	12.7	13.3	13.8	14.2	14.5	14.7	14.9	14.9	15.0	14.9	14.9
5.0	2.34	3.53	5.97	7.78	9.22	10.5	11.6	12.5	13.4	14.0	14.6	15.0	15.3	15.5	15.7	15.8	15.9	15.9	15.8
6.0	2.37	3.61	6.11	7.99	9.49	10.8	12.0	13.0	13.9	14.6	15.1	15.6	16.0	16.2	16.5	16.6	16.7	16.6	16.6
8.0	2.37	3.64	6.32	8.29	9.89	11.3	12.6	13.7	14.6	15.4	16.0	16.6	17.0	17.3	17.6	17.7	17.8	17.8	17.8
10	2.35	3.63	6.37	8.52	10.2	11.7	13.0	14.2	15.2	16.0	16.7	17.3	17.7	18.1	18.4	18.6	18.7	18.7	18.8
15	2.26	3.52	6.31	8.59	10.5	12.2	13.7	15.0	16.1	17.0	17.8	18.5	19.0	19.4	19.8	20.1	20.2	20.3	20.4
20	2.16	3.39	6.15	8.48	10.5	12.3	14.0	15.5	16.6	17.7	18.5	19.3	19.8	20.3	20.7	21.0	21.3	21.3	21.4
25	2.07	3.27	5.98	8.31	10.4	12.3	14.0	15.6	16.9	18.1	19.0	19.8	20.4	20.9	21.4	21.7	22.0	22.1	22.2
30	1.98	3.15	5.81	8.13	10.2	12.1	13.9	15.5	17.0	18.2	19.3	20.2	20.9	21.4	21.9	22.3	22.5	22.7	22.8
40	1.83	2.93	5.49	7.76	9.82	11.8	13.6	15.3	16.8	18.2	19.4	20.4	21.3	22.0	22.6	23.1	23.3	23.5	23.7
50	1.71	2.75	5.20	7.42	9.46	11.4	13.3	15.0	16.5	18.0	19.2	20.3	21.2	22.0	22.7	23.3	23.8	24.1	24.4
60	1.61	2.60	4.95	7.11	9.12	11.1	12.9	14.6	16.2	17.7	19.0	20.1	21.1	21.9	22.7	23.3	23.8	24.2	24.5
80	1.43	2.34	4.52	6.57	8.51	10.4	12.2	14.0	15.5	17.0	18.4	19.6	20.6	21.5	22.4	23.0	23.7	24.1	24.5
100	1.30	2.13	4.17	6.12	7.99	9.85	11.6	13.3	14.9	16.4	17.7	19.0	20.0	21.0	21.9	22.6	23.3	23.7	24.2
150	1.05	1.75	3.51	5.25	6.97	8.69	10.4	12.0	13.5	15.0	16.3	17.6	18.7	19.7	20.6	21.4	22.1	22.7	23.2
200	0.88	1.48	3.03	4.62	6.20	7.81	9.40	10.9	12.4	13.8	15.1	16.4	17.5	18.5	19.4	20.3	21.0	21.6	22.2
250	0.75	1.28	2.67	4.12	5.59	7.11	8.62	10.1	11.5	12.9	14.2	15.4	16.4	17.4	18.4	19.2	20.0	20.6	21.2
300	0.66	1.12	2.38	3.72	5.09	6.53	7.96	9.36	10.7	12.0	13.3	14.5	15.5	16.5	17.5	18.3	19.1	19.7	20.3
400	0.55	0.93	1.94	3.10	4.32	5.61	6.92	8.20	9.48	10.7	11.9	13.0	14.0	15.0	15.9	16.8	17.5	18.2	18.8
500	0.47	0.80	1.68	2.63	3.74	4.91	6.11	7.31	8.50	9.66	10.8	11.9	12.8	13.8	14.7	15.5	16.2	16.9	17.5
600	0.42	0.71	1.49	2.35	3.26	4.36	5.47	6.58	7.70	8.80	9.87	10.9	11.8	12.7	13.6	14.4	15.2	15.8	16.4
800	0.34	0.58	1.23	1.94	2.72	3.56	4.49	5.47	6.47	7.46	8.43	9.38	10.3	11.1	11.9	12.7	13.4	14.0	14.6
1000	0.29	0.49	1.05	1.67	2.34	3.08	3.86	4.65	5.55	6.46	7.35	8.22	9.05	9.84	10.6	11.3	12.0	12.6	13.2

Z1	20																		
M1	43																		
Z2	3	5	10	15	20	25	30	35	40	45	50	55	60	65	70	75	80	85	90
M2	6	10	21	32	43	54	66	79	92	105	118	131	145	159	172	186	200	216	230

E	SB	SB	SB	SB	SB	SB	SB	SB	SB	SB	SB	SB	SB	SB	SB	SB	SB	SB	SB
0.10	0.88	1.30	2.11	2.71	3.14														
0.15	1.04	1.52	2.46	3.15	3.62	4.00	4.34	4.65											
0.20	1.16	1.70	2.76	3.53	4.04	4.45	4.81	5.13	5.42	5.67	5.90								
0.25	1.26	1.85	3.01	3.86	4.42	4.86	5.25	5.58	5.88	6.13	6.35	6.54	6.71	6.84					
0.30	1.35	1.98	3.23	4.14	4.75	5.23	5.64	6.00	6.31	6.57	6.79	6.98	7.14	7.26	7.38	7.47			
0.40	1.49	2.20	3.59	4.62	5.31	5.85	6.32	6.72	7.06	7.35	7.59	7.79	7.94	8.07	8.17	8.24	8.30	8.32	8.34
0.50	1.60	2.37	3.89	5.02	5.78	6.38	6.89	7.34	7.72	8.03	8.29	8.50	8.67	8.79	8.89	8.96	9.01	9.01	9.03
0.60	1.70	2.51	4.14	5.35	6.17	6.83	7.39	7.87	8.29	8.63	8.91	9.14	9.32	9.45	9.56	9.62	9.67	9.67	9.67
0.80	1.85	2.74	4.53	5.89	6.82	7.57	8.21	8.77	9.25	9.64	9.97	10.2	10.4	10.6	10.7	10.8	10.8	10.8	10.8
1.0	1.96	2.92	4.85	6.32	7.34	8.17	8.88	9.50	10.0	10.5	10.8	11.1	11.4	11.6	11.7	11.8	11.8	11.8	11.8
1.5	2.17	3.25	5.43	7.12	8.31	9.29	10.1	10.9	11.5	12.1	12.5	12.9	13.2	13.4	13.6	13.7	13.8	13.8	13.8
2.0	2.32	3.47	5.83	7.68	9.01	10.1	11.1	11.9	12.6	13.3	13.8	14.2	14.6	14.9	15.1	15.2	15.4	15.4	15.4
2.5	2.43	3.64	6.14	8.12	9.54	10.7	11.8	12.7	13.5	14.2	14.8	15.3	15.7	16.0	16.3	16.5	16.6	16.6	16.7
3.0	2.52	3.78	6.39	8.47	9.98	11.2	12.4	13.3	14.2	15.0	15.6	16.2	16.6	17.0	17.3	17.5	17.6	17.7	17.8
4.0	2.65	3.98	6.76	9.00	10.6	12.0	13.3	14.4	15.3	16.2	16.9	17.6	18.1	18.5	18.8	19.1	19.3	19.4	19.5
5.0	2.74	4.14	7.04	9.41	11.2	12.6	14.0	15.2	16.2	17.1	17.9	18.6	19.2	19.7	20.1	20.4	20.6	20.8	20.9
6.0	2.82	4.25	7.26	9.72	11.6	13.1	14.5	15.8	16.9	17.9	18.8	19.5	20.1	20.7	21.1	21.4	21.7	21.9	22.0
8.0	2.92	4.42	7.58	10.2	12.2	13.9	15.4	16.7	18.0	19.1	20.0	20.9	21.6	22.2	22.7	23.1	23.4	23.6	23.8
10	2.99	4.54	7.81	10.5	12.6	14.4	16.0	17.5	18.8	20.0	21.0	21.9	22.7	23.3	23.9	24.3	24.7	25.0	25.2
15	3.01	4.63	8.14	11.1	13.3	15.3	17.0	18.7	20.1	21.5	22.7	23.7	24.6	25.3	26.0	26.6	27.0	27.3	27.6
20	2.96	4.59	8.17	11.3	13.8	15.8	17.7	19.4	21.0	22.5	23.7	24.9	25.8	26.7	27.4	28.1	28.6	28.9	29.3
25	2.90	4.51	8.10	11.3	13.9	16.2	18.2	20.0	21.7	23.2	24.5	25.7	26.8	27.7	28.5	29.2	29.7	30.1	30.5
30	2.83	4.42	7.99	11.2	13.9	16.2	18.4	20.4	22.2	23.7	25.1	26.4	27.5	28.4	29.3	30.0	30.6	31.1	31.5
40	2.70	4.24	7.74	11.0	13.7	16.1	18.4	20.6	22.5	24.4	26.0	27.3	28.5	29.5	30.5	31.3	31.9	32.5	32.9
50	2.58	4.06	7.48	10.7	13.4	15.9	18.2	20.5	22.5	24.5	26.2	27.8	29.2	30.4	31.3	32.1	32.9	33.4	34.0
60	2.47	3.90	7.23	10.4	13.1	15.6	18.0	20.2	22.4	24.4	26.2	27.9	29.3	30.6	31.8	32.8	33.6	34.2	34.7
80	2.27	3.62	6.78	9.82	12.5	15.0	17.4	19.7	21.9	23.9	25.8	27.6	29.2	30.6	31.9	33.1	34.1	34.9	35.7
100	2.12	3.39	6.39	9.33	11.9	14.4	16.8	19.1	21.3	23.4	25.3	27.2	28.8	30.3	31.7	32.9	34.0	34.9	35.8
150	1.81	2.92	5.61	8.30	10.7	13.1	15.4	17.7	19.8	21.9	23.9	25.8	27.5	29.1	30.6	31.9	33.2	34.2	35.2
200	1.59	2.58	5.02	7.51	9.81	12.1	14.3	16.4	18.6	20.6	22.6	24.5	26.2	27.8	29.4	30.7	32.0	33.1	34.2
250	1.41	2.31	4.55	6.87	9.05	11.2	13.3	15.4	17.5	19.5	21.4	23.3	25.0	26.6	28.2	29.6	30.9	32.0	33.1
300	1.27	2.10	4.16	6.34	8.41	10.5	12.5	14.5	16.5	18.5	20.4	22.2	23.9	25.5	27.1	28.5	29.8	30.9	32.0
400	1.06	1.76	3.56	5.50	7.38	9.28	11.2	13.1	15.0	16.8	18.6	20.4	22.0	23.6	25.1	26.5	27.8	29.0	30.1
500	0.90	1.51	3.10	4.85	6.58	8.34	10.1	11.9	13.7	15.5	17.2	18.9	20.5	22.0	23.5	24.9	26.2	27.3	28.4
600	0.80	1.33	2.74	4.34	5.93	7.57	9.24	10.9	12.6	14.3	16.0	17.6	19.2	20.6	22.1	23.4	24.7	25.8	27.0
800	0.66	1.10	2.25	3.52	4.94	6.39	7.87	9.39	10.9	12.5	14.0	15.6	17.0	18.4	19.8	21.1	22.3	23.4	24.5
1000	0.57	0.95	1.94	3.06	4.19	5.50	6.85	8.22	9.65	11.1	12.5	14.0	15.3	16.6	18.0	19.2	20.4	21.4	22.5

Z1	25
M1	54

Z2	3	5	10	15	20	25	30	35	40	45	50	55	60	65	70	75	80	85	90
M2	6	10	21	32	43	54	66	79	92	105	118	131	145	159	172	186	200	216	230

E	SB	SB	SB	SB	SB	SB	SB	SB	SB	SB	SB	SB	SB	SB	SB	SB	SB	SB	SB
0.10	0.89	1.31	2.20																
0.15	1.03	1.52	2.53	3.29	3.92														
0.20	1.16	1.70	2.82	3.66	4.33	4.82	5.25	5.66											
0.25	1.26	1.86	3.08	3.99	4.71	5.23	5.68	6.09	6.46	6.81									
0.30	1.36	2.00	3.31	4.29	5.06	5.61	6.08	6.50	6.89	7.24	7.56	7.86							
0.40	1.51	2.23	3.71	4.81	5.67	6.28	6.80	7.26	7.67	8.04	8.37	8.67	8.93	9.16	9.37	9.55			
0.50	1.64	2.42	4.03	5.24	6.19	6.86	7.43	7.93	8.38	8.77	9.12	9.42	9.69	9.92	10.1	10.3	10.4	10.6	10.7
0.60	1.75	2.59	4.31	5.61	6.64	7.37	7.98	8.53	9.00	9.43	9.80	10.1	10.4	10.6	10.8	11.0	11.1	11.3	11.3
0.80	1.92	2.85	4.77	6.23	7.39	8.22	8.92	9.54	10.1	10.6	11.0	11.3	11.6	11.9	12.1	12.3	12.4	12.5	12.6
1.0	2.06	3.06	5.14	6.73	8.00	8.92	9.70	10.4	11.0	11.5	12.0	12.4	12.7	13.0	13.2	13.4	13.6	13.7	13.8
1.5	2.31	3.45	5.83	7.68	9.16	10.3	11.2	12.0	12.7	13.4	14.0	14.5	14.9	15.2	15.5	15.8	15.9	16.1	16.2
2.0	2.50	3.73	6.32	8.36	10.0	11.2	12.3	13.2	14.1	14.8	15.5	16.0	16.5	16.9	17.3	17.6	17.8	18.0	18.1
2.5	2.63	3.95	6.71	8.89	10.7	12.0	13.2	14.2	15.1	15.9	16.7	17.3	17.9	18.3	18.7	19.1	19.3	19.5	19.7
3.0	2.75	4.12	7.02	9.32	11.2	12.7	13.9	15.0	16.0	16.9	17.7	18.4	19.0	19.5	19.9	20.3	20.6	20.8	21.0
4.0	2.92	4.38	7.50	10.0	12.1	13.7	15.0	16.3	17.4	18.4	19.3	20.1	20.8	21.4	21.9	22.4	22.7	23.0	23.2
5.0	3.04	4.58	7.86	10.5	12.7	14.4	15.9	17.3	18.5	19.6	20.6	21.5	22.2	22.9	23.5	24.0	24.4	24.7	25.0
6.0	3.14	4.74	8.15	10.9	13.3	15.1	16.6	18.1	19.4	20.5	21.6	22.6	23.4	24.1	24.8	25.3	25.8	26.1	26.4
8.0	3.29	4.98	8.59	11.6	14.1	16.0	17.7	19.3	20.7	22.0	23.2	24.3	25.2	26.1	26.8	27.4	28.0	28.4	28.7
10	3.40	5.15	8.90	12.0	14.7	16.7	18.6	20.2	21.8	23.2	24.5	25.6	26.7	27.6	28.4	29.1	29.7	30.1	30.6
15	3.57	5.42	9.43	12.8	15.7	18.0	20.0	21.8	23.6	25.2	26.6	28.0	29.2	30.2	31.2	32.0	32.7	33.3	33.8
20	3.62	5.55	9.78	13.3	16.3	18.7	20.9	22.9	24.8	26.5	28.1	29.5	30.8	32.0	33.1	34.0	34.8	35.5	36.1
25	3.62	5.56	9.88	13.6	16.8	19.3	21.6	23.7	25.6	27.5	29.2	30.7	32.1	33.3	34.5	35.5	36.4	37.1	37.8
30	3.58	5.53	9.89	13.7	17.1	19.7	22.1	24.2	26.3	28.2	30.0	31.6	33.1	34.4	35.6	36.7	37.6	38.4	39.1
40	3.50	5.42	9.78	13.7	17.2	20.1	22.7	25.2	27.2	29.3	31.2	32.9	34.5	35.9	37.3	38.4	39.5	40.3	41.1
50	3.40	5.29	9.60	13.5	17.1	20.1	22.8	25.4	27.8	30.1	32.0	33.8	35.5	37.0	38.4	39.7	40.8	41.7	42.6
60	3.30	5.15	9.39	13.3	16.9	20.0	22.8	25.4	27.9	30.3	32.5	34.6	36.3	37.9	39.3	40.6	41.8	42.8	43.7
80	3.11	4.88	8.98	12.8	16.4	19.5	22.4	25.1	27.8	30.3	32.6	34.9	36.9	38.8	40.5	42.0	43.3	44.3	45.3
100	2.95	4.64	8.60	12.3	15.9	19.0	21.9	24.7	27.3	29.9	32.4	34.7	36.9	38.8	40.7	42.4	43.9	45.2	46.4
150	2.62	4.15	7.78	11.3	14.7	17.7	20.6	23.3	26.1	28.7	31.2	33.7	35.9	38.1	40.1	42.0	43.7	45.1	46.6
200	2.36	3.76	7.12	10.4	13.7	16.6	19.4	22.1	24.8	27.4	30.0	32.4	34.7	36.9	39.0	40.9	42.7	44.3	45.9
250	2.15	3.45	6.58	9.71	12.8	15.6	18.3	21.0	23.6	26.2	28.7	31.2	33.5	35.7	37.8	39.8	41.6	43.3	44.9
300	1.98	3.19	6.13	9.10	12.1	14.8	17.4	20.0	22.6	25.1	27.6	30.0	32.3	34.5	36.7	38.6	40.5	42.2	43.8
400	1.71	2.78	5.40	8.10	10.8	13.4	15.9	18.3	20.8	23.2	25.6	28.0	30.2	32.4	34.5	36.5	38.4	40.1	41.7
500	1.51	2.46	4.82	7.31	9.84	12.2	14.6	16.9	19.3	21.6	24.0	26.3	28.4	30.6	32.7	34.6	36.5	38.2	39.8
600	1.34	2.20	4.36	6.66	9.03	11.3	13.5	15.7	18.0	20.3	22.5	24.7	26.9	29.0	31.0	32.9	34.8	36.4	38.1
800	1.09	1.81	3.65	5.65	7.76	9.80	11.8	13.8	15.9	18.0	20.2	22.3	24.3	26.3	28.2	30.1	31.9	33.5	35.1
1000	0.95	1.55	3.09	4.89	6.79	8.65	10.5	12.4	14.3	16.3	18.3	20.3	22.2	24.1	26.0	27.8	29.5	31.1	32.7

Z1	30
M1	66

Z2	3	5	10	15	20	25	30	35	40	45	50	55	60	65	70	75	80	85	90
M2	6	10	21	32	43	54	66	79	92	105	118	131	145	159	172	186	200	216	230

E	SB	SB	SB	SB	SB	SB	SB	SB	SB	SB	SB	SB	SB	SB	SB	SB	SB	SB	SB
0.10																			
0.15	1.03	1.53	2.59																
0.20	1.14	1.70	2.86	3.77	4.55														
0.25	1.25	1.85	3.11	4.09	4.90	5.57	6.11												
0.30	1.34	1.99	3.34	4.38	5.23	5.93	6.49	6.98	7.44										
0.40	1.50	2.23	3.74	4.90	5.85	6.61	7.21	7.73	8.20	8.64	9.06	9.44							
0.50	1.64	2.43	4.09	5.36	6.39	7.22	7.86	8.41	8.91	9.37	9.80	10.2	10.5	10.9	11.2	11.5			
0.60	1.75	2.61	4.39	5.76	6.87	7.76	8.45	9.04	9.57	10.1	10.5	10.9	11.3	11.6	11.9	12.2	12.4	12.6	12.8
0.80	1.95	2.90	4.89	6.43	7.68	8.69	9.46	10.1	10.7	11.3	11.7	12.2	12.6	12.9	13.2	13.5	13.8	14.0	14.2
1.0	2.10	3.13	5.29	6.98	8.36	9.47	10.3	11.1	11.7	12.3	12.8	13.3	13.7	14.1	14.4	14.7	15.0	15.2	15.4
1.5	2.39	3.57	6.07	8.04	9.66	11.0	12.0	12.9	13.7	14.4	15.0	15.6	16.1	16.6	17.0	17.3	17.6	17.8	18.0
2.0	2.60	3.89	6.64	8.82	10.6	12.1	13.3	14.3	15.2	16.0	16.7	17.4	18.0	18.5	19.0	19.4	19.7	20.0	20.2
2.5	2.77	4.15	7.09	9.44	11.4	13.0	14.3	15.4	16.4	17.3	18.1	18.9	19.5	20.1	20.6	21.1	21.5	21.8	22.0
3.0	2.90	4.35	7.45	9.95	12.0	13.8	15.1	16.3	17.4	18.4	19.3	20.1	20.8	21.5	22.0	22.5	23.0	23.3	23.6
4.0	3.11	4.67	8.03	10.8	13.1	15.0	16.5	17.8	19.1	20.2	21.2	22.1	22.9	23.7	24.3	24.9	25.4	25.8	26.2
5.0	3.26	4.92	8.47	11.4	13.8	15.9	17.6	19.0	20.3	21.6	22.7	23.7	24.6	25.4	26.2	26.8	27.4	27.9	28.3
6.0	3.39	5.11	8.82	11.9	14.5	16.7	18.4	20.0	21.4	22.7	23.9	25.0	26.0	26.9	27.7	28.4	29.1	29.6	30.1
8.0	3.58	5.41	9.36	12.6	15.5	17.9	19.8	21.5	23.1	24.5	25.9	27.1	28.2	29.2	30.2	31.0	31.7	32.3	32.9
10	3.72	5.63	9.77	13.2	16.2	18.7	20.8	22.6	24.3	25.9	27.4	28.7	29.9	31.0	32.1	33.0	33.8	34.5	35.1
15	3.95	6.00	10.5	14.2	17.5	20.3	22.6	24.6	26.6	28.4	30.0	31.6	33.0	34.3	35.5	36.6	37.5	38.4	39.1
20	4.10	6.23	10.9	14.8	18.3	21.3	23.8	26.0	28.1	30.0	31.8	33.5	35.1	36.5	37.9	39.1	40.2	41.1	42.0
25	4.20	6.41	11.2	15.3	18.9	22.1	24.7	27.0	29.2	31.3	33.2	35.0	36.7	38.2	39.7	41.0	42.1	43.2	44.1
30	4.22	6.47	11.4	15.6	19.4	22.6	25.3	27.8	30.1	32.2	34.2	36.2	37.9	39.6	41.1	42.4	43.7	44.8	45.8
40	4.20	6.47	11.5	16.0	20.1	23.5	26.3	28.9	31.3	33.6	35.8	37.9	39.8	41.5	43.2	44.7	46.1	47.3	48.4
50	4.14	6.40	11.5	16.1	20.2	23.9	27.0	29.7	32.2	34.6	36.9	39.1	41.1	43.0	44.7	46.3	47.8	49.1	50.3
60	4.07	6.31	11.4	16.0	20.2	24.0	27.2	30.2	32.9	35.4	37.8	40.0	42.1	44.1	45.9	47.6	49.2	50.5	51.8
80	3.92	6.10	11.1	15.7	20.0	23.9	27.2	30.3	33.3	36.1	38.8	41.4	43.6	45.7	47.6	49.4	51.1	52.6	54.0
100	3.77	5.88	10.7	15.3	19.6	23.5	26.9	30.1	33.2	36.1	39.0	41.7	44.2	46.6	48.8	50.8	52.5	54.0	55.5
150	3.44	5.40	9.97	14.3	18.5	22.4	25.8	29.0	32.2	35.3	38.3	41.2	43.9	46.5	49.0	51.3	53.5	55.4	57.3
200	3.17	5.00	9.29	13.4	17.5	21.3	24.7	27.9	31.0	34.1	37.2	40.1	43.0	45.7	48.3	50.7	53.0	55.1	57.1
250	2.95	4.66	8.72	12.7	16.6	20.3	23.6	26.7	29.9	33.0	36.0	39.0	41.8	44.6	47.2	49.7	52.1	54.3	56.4
300	2.76	4.37	8.22	12.0	15.8	19.4	22.6	25.7	28.8	31.9	34.9	37.9	40.7	43.5	46.1	48.7	51.1	53.3	55.5
400	2.45	3.90	7.40	10.9	14.4	17.8	20.9	23.9	26.9	29.8	32.8	35.7	38.5	41.3	44.0	46.5	49.0	51.2	53.4
500	2.20	3.53	6.74	10.0	13.3	16.5	19.5	22.3	25.2	28.1	31.0	33.9	36.6	39.3	42.0	44.5	46.9	49.2	51.4
600	2.00	3.22	6.20	9.25	12.4	15.5	18.3	21.0	23.8	26.6	29.4	32.2	34.9	37.5	40.2	42.7	45.1	47.3	49.6
800	1.69	2.75	5.34	8.06	10.9	13.7	16.3	18.8	21.4	24.1	26.7	29.4	32.0	34.5	37.0	39.5	41.8	44.0	46.2
1000	1.46	2.39	4.68	7.13	9.70	12.3	14.7	17.1	19.5	22.0	24.5	27.1	29.6	32.0	34.4	36.8	39.1	41.2	43.4

Z1	35																		
M1	79																		
Z2	3	5	10	15	20	25	30	35	40	45	50	55	60	65	70	75	80	85	90
M2	6	10	21	32	43	54	66	79	92	105	118	131	145	159	172	186	200	216	230

E	SB	SB	SB	SB	SB	SB	SB	SB	SB	SB	SB	SB	SB	SB	SB	SB	SB	SB	SB
0.10																			
0.15																			
0.20	1.14	1.70																	
0.25	1.23	1.84	3.14	4.19															
0.30	1.32	1.97	3.35	4.46	5.39	6.21													
0.40	1.48	2.21	3.74	4.96	5.97	6.85	7.58	8.19	8.73										
0.50	1.62	2.41	4.09	5.41	6.50	7.44	8.22	8.85	9.42	9.94	10.4	10.9							
0.60	1.73	2.59	4.39	5.82	6.99	7.99	8.82	9.48	10.1	10.6	11.1	11.6	12.0	12.5	12.9				
0.80	1.94	2.90	4.92	6.52	7.83	8.95	9.88	10.6	11.3	11.8	12.4	12.9	13.3	13.8	14.2	14.6	14.9	15.2	15.5
1.0	2.10	3.15	5.35	7.11	8.55	9.78	10.8	11.6	12.3	12.9	13.5	14.0	14.5	15.0	15.4	15.8	16.1	16.5	16.7
1.5	2.42	3.63	6.19	8.25	9.95	11.4	12.6	13.6	14.4	15.2	15.9	16.5	17.1	17.6	18.1	18.5	18.9	19.2	19.5
2.0	2.65	3.99	6.82	9.12	11.0	12.7	14.0	15.1	16.1	16.9	17.7	18.4	19.1	19.7	20.3	20.7	21.2	21.6	21.9
2.5	2.84	4.27	7.32	9.81	11.9	13.7	15.2	16.4	17.4	18.4	19.3	20.1	20.8	21.5	22.1	22.6	23.1	23.5	23.9
3.0	2.99	4.50	7.74	10.4	12.6	14.5	16.1	17.4	18.6	19.6	20.6	21.4	22.2	23.0	23.6	24.2	24.8	25.3	25.7
4.0	3.23	4.87	8.39	11.3	13.7	15.9	17.7	19.1	20.4	21.6	22.7	23.7	24.6	25.5	26.2	26.9	27.6	28.1	28.6
5.0	3.41	5.16	8.90	12.0	14.6	17.0	18.9	20.5	21.9	23.2	24.4	25.5	26.5	27.5	28.3	29.1	29.8	30.4	31.0
6.0	3.56	5.39	9.32	12.6	15.4	17.8	19.9	21.6	23.1	24.5	25.8	27.0	28.1	29.2	30.1	30.9	31.7	32.4	33.0
8.0	3.79	5.74	9.96	13.5	16.5	19.2	21.5	23.4	25.1	26.6	28.1	29.4	30.7	31.8	32.9	33.9	34.8	35.6	36.3
10	3.96	6.01	10.4	14.2	17.4	20.3	22.7	24.7	26.6	28.3	29.8	31.3	32.7	34.0	35.1	36.2	37.2	38.1	38.9
15	4.25	6.47	11.3	15.4	18.9	22.1	24.9	27.2	29.2	31.2	33.0	34.7	36.3	37.8	39.2	40.4	41.6	42.7	43.6
20	4.44	6.77	11.8	16.2	20.0	23.4	26.3	28.8	31.1	33.2	35.2	37.0	38.8	40.4	42.0	43.4	44.7	45.9	47.0
25	4.58	6.98	12.2	16.7	20.7	24.3	27.4	30.0	32.4	34.7	36.8	38.8	40.7	42.5	44.1	45.7	47.1	48.4	49.6
30	4.68	7.14	12.5	17.2	21.3	25.0	28.3	31.0	33.5	35.8	38.1	40.2	42.2	44.1	45.8	47.5	49.0	50.4	51.6
40	4.78	7.35	13.0	17.8	22.1	26.1	29.5	32.4	35.1	37.6	40.0	42.3	44.5	46.5	48.4	50.2	51.9	53.4	54.8
50	4.79	7.38	13.1	18.3	22.7	26.8	30.4	33.4	36.2	38.9	41.4	43.8	46.1	48.3	50.3	52.2	54.0	55.6	57.2
60	4.76	7.36	13.1	18.4	23.1	27.4	31.1	34.2	37.1	39.9	42.5	45.0	47.4	49.7	51.8	53.8	55.7	57.4	59.0
80	4.66	7.23	13.0	18.3	23.1	27.7	31.7	35.1	38.4	41.2	44.0	46.7	49.3	51.7	54.0	56.1	58.2	60.0	61.8
100	4.54	7.06	12.8	18.0	22.9	27.6	31.7	35.3	38.7	41.9	45.0	48.0	50.6	53.1	55.5	57.8	59.9	61.9	63.7
150	4.24	6.64	12.1	17.2	22.1	26.8	31.0	34.7	38.2	41.7	45.0	48.3	51.4	54.4	57.2	59.9	62.5	64.8	67.0
200	3.98	6.25	11.5	16.4	21.2	25.8	30.0	33.7	37.3	40.8	44.3	47.6	50.9	54.0	57.0	59.9	62.6	65.2	67.6
250	3.75	5.90	10.9	15.7	20.3	24.8	29.0	32.7	36.2	39.8	43.3	46.7	50.0	53.2	56.3	59.3	62.1	64.7	67.3
300	3.55	5.60	10.4	15.0	19.5	23.9	28.0	31.6	35.2	38.7	42.2	45.6	48.9	52.2	55.3	58.4	61.3	64.0	66.7
400	3.22	5.10	9.49	13.8	18.1	22.3	26.2	29.8	33.2	36.7	40.1	43.5	46.9	50.1	53.3	56.4	59.3	62.1	64.9
500	2.95	4.69	8.78	12.9	16.9	20.9	24.7	28.1	31.5	34.9	38.3	41.6	44.9	48.1	51.3	54.4	57.3	60.1	62.9
600	2.72	4.34	8.17	12.0	15.9	19.8	23.4	26.7	30.0	33.3	36.6	39.9	43.1	46.3	49.4	52.5	55.4	58.2	61.0
800	2.37	3.80	7.20	10.7	14.2	17.8	21.1	24.2	27.4	30.5	33.7	36.8	39.9	43.0	46.1	49.1	52.0	54.7	57.5
1000	2.09	3.37	6.44	9.62	12.9	16.2	19.4	22.3	25.2	28.2	31.2	34.3	37.3	40.2	43.2	46.1	49.0	51.7	54.4

Z1	40
M1	92

Z2	3	5	10	15	20	25	30	35	40	45	50	55	60	65	70	75	80	85	90
M2	6	10	21	32	43	54	66	79	92	105	118	131	145	159	172	186	200	216	230

E	SB	SB	SB	SB	SB	SB	SB	SB	SB	SB	SB	SB	SB	SB	SB	SB	SB	SB	SB
0.10																			
0.15																			
0.20																			
0.25	1.22	1.86																	
0.30	1.30	1.97	3.39																
0.40	1.45	2.19	3.75	5.02	6.11	7.06													
0.50	1.58	2.39	4.08	5.46	6.61	7.61	8.55	9.29	9.94										
0.60	1.70	2.57	4.38	5.86	7.08	8.14	9.13	9.90	10.6	11.2	11.7	12.3							
0.80	1.91	2.88	4.91	6.56	7.93	9.10	10.2	11.0	11.7	12.4	13.0	13.5	14.1	14.6	15.0	15.5	15.9		
1.0	2.08	3.14	5.36	7.17	8.66	9.94	11.1	12.0	12.8	13.5	14.1	14.7	15.3	15.8	16.3	16.7	17.2	17.6	18.0
1.5	2.41	3.65	6.25	8.38	10.1	11.7	13.1	14.1	15.0	15.8	16.6	17.2	17.9	18.5	19.0	19.5	20.0	20.4	20.8
2.0	2.66	4.04	6.93	9.30	11.3	13.0	14.6	15.8	16.8	17.7	18.5	19.3	20.0	20.7	21.3	21.9	22.4	22.8	23.3
2.5	2.86	4.35	7.47	10.1	12.2	14.1	15.8	17.2	18.3	19.3	20.2	21.1	21.8	22.6	23.2	23.9	24.4	25.0	25.4
3.0	3.03	4.61	7.93	10.7	13.0	15.0	16.9	18.3	19.5	20.6	21.6	22.6	23.4	24.2	24.9	25.6	26.2	26.8	27.3
4.0	3.30	5.02	8.65	11.7	14.3	16.5	18.6	20.2	21.6	22.8	24.0	25.0	26.0	26.9	27.8	28.6	29.3	29.9	30.5
5.0	3.50	5.34	9.22	12.5	15.3	17.7	20.0	21.7	23.3	24.6	25.9	27.0	28.1	29.2	30.1	31.0	31.8	32.5	33.2
6.0	3.67	5.60	9.69	13.1	16.1	18.7	21.1	23.0	24.6	26.1	27.5	28.7	29.9	31.0	32.0	33.0	33.9	34.7	35.4
8.0	3.93	6.01	10.4	14.2	17.4	20.2	22.9	25.0	26.8	28.5	30.0	31.4	32.8	34.0	35.2	36.3	37.3	38.2	39.1
10	4.13	6.32	11.0	15.0	18.4	21.4	24.3	26.6	28.5	30.3	32.0	33.6	35.0	36.4	37.7	38.9	40.0	41.1	42.0
15	4.48	6.86	12.0	16.3	20.2	23.6	26.8	29.4	31.6	33.7	35.6	37.4	39.2	40.8	42.3	43.7	45.1	46.3	47.4
20	4.71	7.22	12.6	17.3	21.4	25.1	28.5	31.3	33.8	36.0	38.1	40.1	42.0	43.8	45.5	47.1	48.6	50.0	51.3
25	4.87	7.48	13.1	18.0	22.3	26.2	29.8	32.7	35.4	37.8	40.1	42.2	44.2	46.2	48.0	49.7	51.4	52.9	54.3
30	5.00	7.68	13.5	18.5	23.0	27.0	30.8	33.9	36.6	39.2	41.6	43.9	46.0	48.1	50.0	51.8	53.6	55.2	56.7
40	5.18	7.98	14.0	19.3	24.0	28.3	32.3	35.6	38.6	41.3	43.9	46.3	48.7	50.9	53.1	55.1	57.0	58.7	60.4
50	5.30	8.19	14.4	19.9	24.8	29.2	33.4	36.9	40.0	42.8	45.6	48.2	50.7	53.1	55.3	57.5	59.5	61.4	63.2
60	5.32	8.25	14.6	20.3	25.3	29.9	34.3	37.8	41.0	44.0	46.9	49.6	52.2	54.7	57.1	59.4	61.5	63.5	65.4
80	5.29	8.24	14.7	20.6	26.0	30.9	35.5	39.2	42.6	45.8	48.8	51.7	54.5	57.2	59.7	62.2	64.5	66.7	68.7
100	5.22	8.14	14.6	20.5	26.0	31.1	36.0	40.0	43.7	47.0	50.1	53.2	56.1	58.9	61.6	64.2	66.6	68.9	71.1
150	4.98	7.80	14.1	20.0	25.5	30.8	35.8	40.1	44.0	47.8	51.4	54.9	58.3	61.5	64.7	67.6	70.1	72.6	75.0
200	4.74	7.45	13.5	19.3	24.8	30.0	35.1	39.4	43.4	47.3	51.1	54.8	58.4	61.8	65.2	68.4	71.5	74.3	77.1
250	4.52	7.12	13.0	18.6	24.0	29.1	34.2	38.5	42.5	46.5	50.4	54.1	57.8	61.3	64.9	68.2	71.4	74.5	77.4
300	4.32	6.82	12.5	17.9	23.2	28.3	33.2	37.5	41.6	45.5	49.4	53.3	57.0	60.6	64.2	67.6	70.9	74.1	77.2
400	3.98	6.31	11.6	16.8	21.8	26.7	31.5	35.7	39.7	43.6	47.5	51.3	55.1	58.7	62.4	65.9	69.3	72.6	75.8
500	3.69	5.87	10.8	15.7	20.5	25.3	29.9	34.0	37.9	41.8	45.6	49.4	53.1	56.8	60.5	64.0	67.5	70.8	74.0
600	3.45	5.50	10.2	14.9	19.5	24.0	28.5	32.5	36.3	40.1	43.9	47.6	51.3	55.0	58.6	62.1	65.6	68.9	72.2
800	3.06	4.90	9.14	13.4	17.7	21.9	26.2	29.9	33.6	37.2	40.8	44.5	48.0	51.6	55.2	58.6	62.1	65.3	68.6
1000	2.75	4.42	8.29	12.2	16.2	20.2	24.2	27.8	31.2	34.7	38.2	41.7	45.2	48.7	52.2	55.6	58.9	62.1	65.4

Z1	45																	
M1	105																	
Z2	3	5	10	15	20	25	30	35	40	45	50	55	60	65	70	75	80	85	90
M2	6	10	21	32	43	54	66	79	92	105	118	131	145	159	172	186	200	216	230

E	SB	SB	SB	SB	SB	SB	SB	SB	SB	SB	SB	SB	SB	SB	SB	SB	SB	SB	SB
0.10																			
0.15																			
0.20																			
0.25																			
0.30	1.30																		
0.40	1.43	2.19	3.78	5.12															
0.50	1.55	2.38	4.09	5.51	6.73	7.81													
0.60	1.67	2.55	4.38	5.89	7.18	8.31	9.34	10.3	11.1										
0.80	1.87	2.86	4.90	6.59	8.01	9.24	10.4	11.4	12.2	12.9	13.6	14.2	14.8						
1.0	2.04	3.12	5.35	7.19	8.74	10.1	11.3	12.4	13.3	14.0	14.7	15.3	15.9	16.5	17.1	17.6	18.1	18.6	
1.5	2.38	3.65	6.27	8.44	10.3	11.8	13.3	14.6	15.5	16.4	17.2	17.9	18.6	19.2	19.8	20.4	20.9	21.4	21.9
2.0	2.65	4.06	6.98	9.41	11.5	13.2	14.8	16.3	17.4	18.4	19.3	20.1	20.8	21.5	22.2	22.8	23.4	23.9	24.4
2.5	2.86	4.39	7.56	10.2	12.4	14.4	16.1	17.8	19.0	20.1	21.0	21.9	22.7	23.5	24.2	24.9	25.5	26.1	26.7
3.0	3.04	4.67	8.05	10.9	13.3	15.4	17.3	19.0	20.3	21.5	22.5	23.5	24.4	25.3	26.0	26.8	27.4	28.1	28.7
4.0	3.32	5.11	8.84	12.0	14.7	17.0	19.1	21.1	22.6	23.9	25.1	26.2	27.2	28.2	29.1	29.9	30.7	31.4	32.1
5.0	3.55	5.47	9.46	12.8	15.7	18.3	20.6	22.7	24.4	25.8	27.2	28.4	29.5	30.6	31.6	32.5	33.4	34.2	35.0
6.0	3.73	5.75	9.97	13.6	16.6	19.4	21.8	24.1	25.9	27.5	28.9	30.2	31.5	32.6	33.7	34.7	35.7	36.6	37.4
8.0	4.02	6.21	10.8	14.7	18.1	21.1	23.8	26.3	28.3	30.1	31.7	33.2	34.6	35.9	37.2	38.3	39.4	40.5	41.4
10	4.24	6.56	11.4	15.6	19.2	22.4	25.4	28.1	30.2	32.2	33.9	35.6	37.1	38.6	39.9	41.2	42.4	43.6	44.6
15	4.63	7.18	12.5	17.1	21.2	24.8	28.2	31.2	33.7	35.9	38.0	39.9	41.7	43.4	45.0	46.6	48.0	49.4	50.7
20	4.90	7.60	13.3	18.2	22.6	26.5	30.1	33.5	36.2	38.6	40.8	43.0	45.0	46.9	48.7	50.4	52.0	53.6	55.0
25	5.09	7.91	13.8	19.0	23.6	27.8	31.6	35.1	38.0	40.6	43.0	45.3	47.5	49.5	51.5	53.4	55.1	56.8	58.4
30	5.24	8.15	14.3	19.7	24.4	28.7	32.7	36.5	39.5	42.2	44.8	47.2	49.5	51.7	53.8	55.8	57.7	59.4	61.1
40	5.47	8.50	14.9	20.6	25.7	30.2	34.5	38.5	41.7	44.7	47.5	50.1	52.6	55.0	57.3	59.5	61.5	63.5	65.4
50	5.62	8.76	15.4	21.3	26.6	31.3	35.8	40.0	43.4	46.5	49.4	52.2	54.9	57.4	59.9	62.2	64.5	66.6	68.6
60	5.75	8.94	15.7	21.8	27.2	32.2	36.8	41.1	44.7	47.9	51.0	53.9	56.7	59.4	62.0	64.4	66.8	69.0	71.1
80	5.81	9.11	16.2	22.6	28.2	33.4	38.2	42.8	46.6	50.0	53.3	56.4	59.4	62.3	65.1	67.7	70.3	72.7	75.0
100	5.79	9.11	16.2	22.7	28.7	34.2	39.2	43.9	47.9	51.5	54.9	58.2	61.3	64.4	67.3	70.1	72.8	75.4	77.8
150	5.63	8.89	16.0	22.5	28.7	34.4	39.9	45.0	49.4	53.5	57.4	61.1	64.4	67.7	70.9	74.0	77.0	79.8	82.5
200	5.43	8.59	15.5	22.0	28.1	33.9	39.5	44.7	49.3	53.5	57.7	61.6	65.4	69.1	72.8	76.2	79.6	82.7	85.4
250	5.23	8.29	15.0	21.4	27.5	33.2	38.8	44.0	48.6	53.0	57.2	61.3	65.3	69.2	73.0	76.6	80.2	83.5	86.8
300	5.04	8.01	14.5	20.8	26.7	32.5	38.0	43.2	47.9	52.3	56.5	60.7	64.7	68.7	72.6	76.4	80.1	83.6	87.0
400	4.70	7.50	13.7	19.6	25.4	31.0	36.3	41.5	46.1	50.5	54.8	59.1	63.2	67.2	71.2	75.1	78.9	82.6	86.2
500	4.41	7.06	12.9	18.6	24.2	29.6	34.8	39.9	44.4	48.8	53.0	57.3	61.4	65.4	69.5	73.5	77.3	81.0	84.7
600	4.17	6.67	12.2	17.7	23.1	28.3	33.4	38.3	42.8	47.1	51.3	55.5	59.6	63.6	67.7	71.7	75.6	79.3	83.0
800	3.75	6.03	11.1	16.2	21.2	26.1	30.9	35.7	39.9	44.1	48.2	52.3	56.3	60.3	64.3	68.2	72.1	75.8	79.6
1000	3.42	5.52	10.2	14.9	19.6	24.3	28.9	33.4	37.5	41.5	45.5	49.4	53.3	57.2	61.2	65.0	68.9	72.5	76.3

Z1	50																		
M1	118																		
Z2	3	5	10	15	20	25	30	35	40	45	50	55	60	65	70	75	80	85	90
M2	6	10	21	32	43	54	66	79	92	105	118	131	145	159	172	186	200	216	230

E	SB	SB	SB	SB	SB	SB	SB	SB	SB	SB	SB	SB	SB	SB	SB	SB	SB	SB	SB
0.10																			
0.15																			
0.20																			
0.25																			
0.30																			
0.40	1.43	2.21																	
0.50	1.54	2.38	4.12	5.60															
0.60	1.64	2.54	4.39	5.94	7.30	8.50													
0.80	1.84	2.84	4.89	6.61	8.08	9.37	10.6	11.7	12.6	13.5									
1.0	2.01	3.10	5.34	7.20	8.80	10.2	11.5	12.6	13.7	14.5	15.3	16.0	16.6	17.3					
1.5	2.35	3.63	6.27	8.46	10.3	12.0	13.4	14.8	16.0	16.9	17.7	18.5	19.2	19.9	20.6	21.2	21.8	22.4	22.9
2.0	2.62	4.06	7.00	9.46	11.6	13.4	15.0	16.6	17.9	18.9	19.9	20.7	21.5	22.3	23.0	23.6	24.3	24.9	25.5
2.5	2.85	4.40	7.61	10.3	12.6	14.6	16.4	18.1	19.5	20.7	21.7	22.7	23.5	24.3	25.1	25.8	26.5	27.2	27.8
3.0	3.03	4.69	8.12	11.0	13.5	15.6	17.6	19.4	21.0	22.2	23.3	24.3	25.3	26.2	27.0	27.8	28.5	29.2	29.8
4.0	3.34	5.17	8.96	12.2	14.9	17.3	19.5	21.6	23.4	24.8	26.0	27.2	28.3	29.3	30.2	31.1	31.9	32.7	33.4
5.0	3.58	5.55	9.63	13.1	16.1	18.7	21.1	23.4	25.3	26.9	28.2	29.5	30.7	31.8	32.9	33.8	34.8	35.7	36.5
6.0	3.78	5.86	10.2	13.9	17.1	19.9	22.5	24.8	26.9	28.6	30.1	31.5	32.8	34.0	35.1	36.2	37.2	38.2	39.1
8.0	4.09	6.36	11.1	15.1	18.6	21.8	24.6	27.3	29.6	31.5	33.2	34.7	36.2	37.6	38.9	40.1	41.3	42.4	43.4
10	4.34	6.75	11.8	16.1	19.9	23.2	26.3	29.2	31.7	33.8	35.6	37.3	38.9	40.5	41.9	43.3	44.5	45.8	46.9
15	4.77	7.43	13.0	17.8	22.1	25.9	29.4	32.6	35.5	37.9	40.1	42.1	44.0	45.8	47.5	49.1	50.7	52.1	53.5
20	5.07	7.91	13.8	19.0	23.6	27.7	31.5	35.1	38.3	40.9	43.3	45.5	47.6	49.6	51.5	53.4	55.1	56.7	58.3
25	5.29	8.26	14.5	19.9	24.8	29.2	33.2	37.0	40.3	43.2	45.8	48.2	50.4	52.6	54.7	56.6	58.5	60.3	62.0
30	5.46	8.54	15.0	20.6	25.7	30.3	34.5	38.4	42.0	45.0	47.7	50.3	52.7	55.0	57.2	59.3	61.3	63.3	65.1
40	5.72	8.96	15.7	21.7	27.1	32.0	36.5	40.7	44.6	47.8	50.8	53.6	56.2	58.7	61.1	63.5	65.7	67.8	69.8
50	5.91	9.26	16.3	22.5	28.1	33.2	38.0	42.4	46.5	49.9	53.0	56.0	58.8	61.5	64.1	66.6	69.0	71.3	73.5
60	6.05	9.48	16.7	23.1	28.9	34.2	39.1	43.8	48.0	51.5	54.8	57.9	60.9	63.7	66.5	69.1	71.6	74.0	76.3
80	6.26	9.84	17.3	24.0	30.1	35.7	40.8	45.7	50.2	54.0	57.5	60.8	64.0	67.1	70.0	72.9	75.6	78.2	80.8
100	6.30	9.94	17.7	24.7	30.9	36.7	42.0	47.1	51.8	55.7	59.4	62.9	66.3	69.5	72.6	75.6	78.5	81.3	84.0
150	6.23	9.88	17.7	24.8	31.5	37.8	43.6	49.2	54.3	58.6	62.5	66.3	70.0	73.5	76.9	80.2	83.4	86.5	89.4
200	6.08	9.66	17.3	24.5	31.3	37.6	43.6	49.4	54.7	59.4	63.8	68.1	72.1	76.0	79.6	83.1	86.4	89.7	92.9
250	5.91	9.40	16.9	24.0	30.8	37.1	43.2	49.0	54.4	59.3	63.9	68.3	72.5	76.6	80.6	84.5	88.3	91.9	95.4
300	5.73	9.14	16.5	23.5	30.2	36.5	42.5	48.4	53.9	58.8	63.4	67.9	72.3	76.5	80.7	84.8	88.7	92.5	96.2
400	5.41	8.66	15.7	22.4	28.9	35.2	41.1	46.9	52.4	57.3	62.0	66.7	71.1	75.5	79.8	84.1	88.2	92.2	96.1
500	5.13	8.22	14.9	21.4	27.7	33.8	39.7	45.3	50.8	55.7	60.4	65.0	69.5	73.9	78.4	82.7	86.9	91.0	95.1
600	4.88	7.83	14.3	20.5	26.6	32.6	38.3	43.8	49.2	54.0	58.8	63.4	67.8	72.3	76.7	81.1	85.4	89.5	93.6
800	4.45	7.17	13.1	19.0	24.7	30.4	35.8	41.1	46.3	51.0	55.6	60.2	64.6	69.0	73.4	77.8	82.0	86.2	90.3
1000	4.11	6.63	12.2	17.7	23.1	28.5	33.7	38.8	43.8	48.3	52.8	57.3	61.6	65.9	70.3	74.6	78.8	82.9	87.1

Z1	55																		
M1	131																		
Z2	3	5	10	15	20	25	30	35	40	45	50	55	60	65	70	75	80	85	90
M2	6	10	21	32	43	54	66	79	92	105	118	131	145	159	172	186	200	216	230

E	SB	SB	SB	SB	SB	SB	SB	SB	SB	SB	SB	SB	SB	SB	SB	SB	SB	SB	SB
0.10																			
0.15																			
0.20																			
0.25																			
0.30																			
0.40																			
0.50	1.49	2.39																	
0.60	1.59	2.54	4.42	6.03															
0.80	1.77	2.82	4.89	6.64	8.17	9.53	10.8	12.0											
1.0	1.93	3.07	5.32	7.22	8.86	10.3	11.6	12.9	14.0	15.0	15.9								
1.5	2.26	3.61	6.25	8.46	10.4	12.0	13.6	15.0	16.3	17.4	18.3	19.1	19.9	20.6	21.3	22.0	22.7	23.3	23.9
2.0	2.53	4.04	7.00	9.48	11.6	13.5	15.2	16.8	18.2	19.4	20.4	21.3	22.2	23.0	23.7	24.4	25.1	25.8	26.4
2.5	2.75	4.39	7.62	10.3	12.7	14.7	16.6	18.3	19.9	21.2	22.3	23.3	24.2	25.1	25.9	26.7	27.4	28.1	28.7
3.0	2.94	4.70	8.16	11.1	13.6	15.8	17.8	19.7	21.4	22.8	24.0	25.1	26.0	27.0	27.8	28.6	29.4	30.2	30.9
4.0	3.25	5.20	9.04	12.3	15.1	17.6	19.9	22.0	23.9	25.5	26.8	28.0	29.2	30.2	31.2	32.1	33.0	33.8	34.6
5.0	3.50	5.60	9.75	13.3	16.4	19.1	21.5	23.8	25.9	27.7	29.2	30.5	31.8	32.9	34.0	35.0	36.0	36.9	37.8
6.0	3.70	5.93	10.3	14.1	17.4	20.3	23.0	25.4	27.7	29.6	31.2	32.6	34.0	35.2	36.4	37.5	38.6	39.6	40.5
8.0	4.03	6.46	11.3	15.4	19.1	22.3	25.2	28.0	30.5	32.7	34.5	36.1	37.6	39.1	40.4	41.7	42.9	44.1	45.1
10	4.29	6.88	12.0	16.5	20.4	23.9	27.1	30.0	32.8	35.1	37.1	38.9	40.6	42.2	43.6	45.1	46.4	47.7	48.9
15	4.75	7.64	13.4	18.4	22.8	26.8	30.4	33.8	37.0	39.7	42.0	44.1	46.1	48.0	49.7	51.4	53.0	54.6	56.0
20	5.07	8.16	14.3	19.7	24.5	28.8	32.8	36.5	39.9	42.9	45.5	47.9	50.1	52.2	54.1	56.0	57.8	59.6	61.2
25	5.31	8.56	15.0	20.7	25.8	30.4	34.6	38.5	42.2	45.5	48.2	50.8	53.2	55.4	57.6	59.6	61.6	63.5	65.3
30	5.50	8.87	15.6	21.5	26.8	31.6	36.0	40.2	44.1	47.5	50.4	53.1	55.7	58.1	60.4	62.6	64.7	66.7	68.7
40	5.79	9.34	16.5	22.7	28.4	33.5	38.3	42.7	46.9	50.6	53.8	56.8	59.5	62.2	64.7	67.2	69.5	71.8	73.9
50	6.00	9.69	17.1	23.6	29.6	35.0	40.0	44.6	49.1	53.0	56.4	59.5	62.5	65.3	68.0	70.7	73.2	75.6	77.9
60	6.16	9.95	17.6	24.3	30.5	36.1	41.3	46.1	50.8	54.8	58.4	61.7	64.8	67.8	70.7	73.5	76.1	78.7	81.1
80	6.39	10.3	18.3	25.4	31.8	37.7	43.2	48.4	53.3	57.6	61.4	65.0	68.4	71.6	74.7	77.7	80.6	83.4	86.1
100	6.56	10.6	18.8	26.1	32.8	38.9	44.6	50.0	55.1	59.7	63.7	67.4	71.0	74.4	77.7	80.8	83.9	86.9	89.8
150	6.60	10.8	19.2	26.9	34.1	40.8	47.0	52.6	58.1	63.0	67.3	71.4	75.3	79.0	82.6	86.1	89.5	92.8	96.0
200	6.50	10.6	19.0	26.8	34.2	41.0	47.5	53.6	59.5	64.8	69.6	73.8	77.9	81.9	85.7	89.4	93.0	96.5	99.9
250	6.37	10.4	18.7	26.5	33.9	40.8	47.3	53.6	59.6	65.2	70.1	74.8	79.3	83.6	87.9	92.0	95.5	99.1	103
300	6.23	10.2	18.4	26.1	33.4	40.3	46.9	53.2	59.3	65.0	70.0	74.9	79.5	84.0	88.4	92.7	96.9	101	105
400	5.94	9.76	17.6	25.1	32.3	39.2	45.7	52.0	58.2	63.9	69.1	74.1	78.8	83.5	88.2	92.7	97.1	101	106
500	5.67	9.35	16.9	24.2	31.2	38.0	44.4	50.6	56.7	62.4	67.7	72.7	77.6	82.3	87.1	91.7	96.3	101	105
600	5.43	8.96	16.3	23.3	30.2	36.8	43.1	49.2	55.2	60.9	66.1	71.2	76.0	80.8	85.7	90.3	95.0	99	104
800	5.02	8.30	15.1	21.8	28.2	34.6	40.7	46.5	52.4	57.9	63.1	68.1	72.9	77.7	82.5	87.2	91.9	96	101
1000	4.67	7.74	14.1	20.4	26.6	32.7	38.5	44.2	49.9	55.2	60.3	65.2	69.9	74.7	79.5	84.1	88.8	93.3	97.8

Z1	60
M1	145

Z2	3	5	10	15	20	25	30	35	40	45	50	55	60	65	70	75	80	85	90
M2	6	10	21	32	43	54	66	79	92	105	118	131	145	159	172	186	200	216	230

E	SB	SB	SB	SB	SB	SB	SB	SB	SB	SB	SB	SB	SB	SB	SB	SB	SB	SB	SB
0.10																			
0.15																			
0.20																			
0.25																			
0.30																			
0.40																			
0.50																			
0.60	1.62																		
0.80	1.79	2.80	4.90	6.69	8.28														
1.0	1.95	3.04	5.31	7.23	8.92	10.4	11.8	13.1	14.3										
1.5	2.28	3.56	6.22	8.44	10.4	12.1	13.7	15.2	16.5	17.8	18.8	19.7	20.5	21.3	22.1	22.8	23.6		
2.0	2.56	3.99	6.97	9.46	11.6	13.6	15.3	16.9	18.4	19.8	20.9	21.9	22.8	23.7	24.5	25.2	26.0	26.7	27.4
2.5	2.79	4.35	7.61	10.3	12.7	14.8	16.7	18.5	20.1	21.6	22.8	23.9	24.9	25.8	26.6	27.4	28.2	29.0	29.7
3.0	2.98	4.67	8.16	11.1	13.7	15.9	18.0	19.9	21.6	23.3	24.5	25.7	26.7	27.7	28.6	29.5	30.3	31.1	31.8
4.0	3.31	5.18	9.07	12.4	15.2	17.8	20.1	22.2	24.2	26.1	27.5	28.8	30.0	31.0	32.0	33.0	33.9	34.8	35.6
5.0	3.58	5.60	9.81	13.4	16.5	19.3	21.8	24.2	26.3	28.4	30.0	31.4	32.7	33.9	35.0	36.0	37.0	38.0	38.9
6.0	3.80	5.95	10.4	14.2	17.6	20.6	23.3	25.8	28.2	30.4	32.1	33.6	35.0	36.3	37.5	38.7	39.8	40.8	41.8
8.0	4.15	6.52	11.4	15.7	19.4	22.7	25.7	28.6	31.2	33.6	35.6	37.3	38.9	40.4	41.8	43.1	44.3	45.5	46.7
10	4.43	6.96	12.2	16.8	20.8	24.4	27.7	30.7	33.6	36.2	38.4	40.3	42.0	43.7	45.2	46.7	48.0	49.4	50.6
15	4.94	7.78	13.7	18.8	23.4	27.5	31.3	34.8	38.0	41.1	43.6	45.9	48.0	49.9	51.7	53.5	55.1	56.7	58.2
20	5.30	8.35	14.7	20.2	25.2	29.7	33.8	37.7	41.3	44.7	47.5	50.0	52.3	54.4	56.5	58.5	60.3	62.1	63.9
25	5.57	8.78	15.5	21.3	26.6	31.4	35.8	39.9	43.7	47.4	50.4	53.1	55.6	58.0	60.2	62.4	64.4	66.4	68.3
30	5.79	9.13	16.1	22.2	27.8	32.8	37.4	41.7	45.8	49.7	52.8	55.7	58.4	60.9	63.3	65.6	67.8	69.9	71.9
40	6.12	9.65	17.1	23.6	29.5	34.9	39.9	44.5	48.9	53.1	56.6	59.7	62.7	65.4	68.1	70.6	73.0	75.4	77.7
50	6.36	10.0	17.8	24.6	30.8	36.5	41.7	46.6	51.3	55.7	59.4	62.8	65.9	68.9	71.7	74.5	77.1	79.6	82.1
60	6.55	10.3	18.3	25.4	31.8	37.7	43.2	48.3	53.1	57.8	61.7	65.2	68.5	71.7	74.7	77.5	80.3	83.0	85.6
80	6.82	10.8	19.2	26.6	33.3	39.6	45.4	50.8	56.0	61.0	65.1	68.9	72.5	75.9	79.1	82.3	85.3	88.2	91.1
100	7.01	11.1	19.7	27.4	34.4	40.9	47.0	52.6	58.0	63.3	67.6	71.6	75.4	79.0	82.5	85.8	89.0	92.1	95.2
150	7.23	11.5	20.6	28.8	36.2	43.1	49.6	55.6	61.4	67.1	71.8	76.2	80.3	84.2	88.1	91.8	95.3	98.8	102
200	7.21	11.5	20.6	29.0	36.8	44.1	51.0	57.5	63.7	69.4	74.4	79.1	83.4	87.6	91.6	95.6	99.4	103	107
250	7.12	11.4	20.5	28.8	36.8	44.2	51.2	57.9	64.3	70.6	76.0	81.0	85.8	89.9	94.1	98.2	102	106	110
300	7.00	11.2	20.2	28.5	36.5	44.0	51.1	57.8	64.3	70.8	76.4	81.6	86.5	91.2	95.8	100	105	108	112
400	6.74	10.8	19.6	27.7	35.6	43.1	50.2	57.0	63.6	70.2	75.9	81.3	86.4	91.4	96.3	101	106	110	115
500	6.49	10.4	18.9	26.9	34.6	42.0	49.0	55.8	62.4	69.0	74.8	80.3	85.5	90.6	95.7	101	105	110	115
600	6.25	10.1	18.3	26.1	33.6	40.9	47.8	54.5	61.1	67.6	73.4	79.0	84.2	89.4	94.5	99.5	104	109	114
800	5.83	9.41	17.1	24.5	31.8	38.8	45.5	52.0	58.4	64.8	70.6	76.1	81.3	86.5	91.7	96.8	102	107	111
1000	5.47	8.85	16.2	23.2	30.1	36.9	43.4	49.6	55.9	62.2	67.8	73.2	78.4	83.6	88.8	93.8	98.8	104	109

Z1	65																		
M1	159																		
Z2	3	5	10	15	20	25	30	35	40	45	50	55	60	65	70	75	80	85	90
M2	6	10	21	32	43	54	66	79	92	105	118	131	145	159	172	186	200	216	230

E	SB	SB	SB	SB	SB	SB	SB	SB	SB	SB	SB	SB	SB	SB	SB	SB	SB	SB	SB
0.10																			
0.15																			
0.20																			
0.25																			
0.30																			
0.40																			
0.50																			
0.60																			
0.80	1.78	2.78	4.94																
1.0	1.92	3.01	5.32	7.27	9.01	10.6													
1.5	2.24	3.51	6.19	8.43	10.4	12.2	13.8	15.3	16.7	18.0	19.3	20.3	21.2	22.1					
2.0	2.52	3.93	6.94	9.44	11.6	13.6	15.4	17.1	18.6	20.0	21.4	22.4	23.4	24.3	25.2	26.0	26.8	27.6	28.3
2.5	2.75	4.29	7.58	10.3	12.7	14.9	16.8	18.7	20.3	21.8	23.3	24.4	25.5	26.4	27.3	28.2	29.0	29.8	30.6
3.0	2.95	4.61	8.14	11.1	13.7	16.0	18.1	20.1	21.8	23.5	25.0	26.2	27.3	28.4	29.3	30.2	31.1	31.9	32.7
4.0	3.28	5.13	9.08	12.4	15.3	17.9	20.3	22.5	24.5	26.3	28.0	29.4	30.7	31.8	32.8	33.8	34.8	35.7	36.6
5.0	3.56	5.56	9.85	13.4	16.6	19.4	22.1	24.5	26.7	28.7	30.6	32.1	33.5	34.7	35.9	37.0	38.0	39.0	40.0
6.0	3.79	5.93	10.5	14.3	17.8	20.8	23.6	26.2	28.6	30.7	32.8	34.4	35.9	37.3	38.5	39.7	40.8	41.9	42.9
8.0	4.16	6.52	11.6	15.8	19.6	23.0	26.1	29.0	31.7	34.2	36.5	38.3	40.0	41.5	43.0	44.3	45.6	46.8	48.0
10	4.45	6.99	12.4	17.0	21.1	24.8	28.2	31.3	34.2	36.9	39.4	41.5	43.3	45.0	46.6	48.1	49.5	50.9	52.2
15	4.99	7.85	14.0	19.2	23.8	28.1	32.0	35.6	39.0	42.1	45.0	47.4	49.6	51.7	53.5	55.3	57.1	58.7	60.3
20	5.38	8.45	15.1	20.7	25.8	30.4	34.7	38.7	42.4	45.9	49.1	51.8	54.3	56.5	58.7	60.7	62.6	64.5	66.3
25	5.67	8.92	15.9	21.9	27.3	32.3	36.8	41.1	45.1	48.8	52.3	55.2	57.9	60.4	62.7	64.9	67.0	69.1	71.0
30	5.90	9.30	16.6	22.9	28.6	33.8	38.6	43.1	47.3	51.2	54.9	58.0	60.9	63.5	66.0	68.4	70.6	72.8	74.9
40	6.26	9.87	17.6	24.3	30.5	36.1	41.3	46.1	50.7	55.0	59.0	62.4	65.5	68.4	71.2	73.8	76.3	78.8	81.1
50	6.53	10.3	18.4	25.5	31.9	37.8	43.3	48.4	53.2	57.8	62.1	65.8	69.1	72.2	75.2	78.0	80.7	83.4	85.9
60	6.74	10.6	19.0	26.3	33.0	39.2	44.9	50.3	55.3	60.1	64.6	68.4	72.0	75.2	78.4	81.4	84.3	87.1	89.8
80	7.05	11.1	20.0	27.7	34.7	41.3	47.3	53.0	58.4	63.5	68.4	72.5	76.3	79.9	83.3	86.6	89.8	92.8	95.8
100	7.27	11.5	20.6	28.6	36.0	42.8	49.1	55.1	60.7	66.1	71.2	75.6	79.6	83.4	87.0	90.5	93.9	97.1	100
150	7.63	12.1	21.7	30.1	38.0	45.3	52.1	58.5	64.6	70.4	76.0	80.7	85.1	89.3	93.3	97.2	101	104	108
200	7.69	12.2	22.1	30.9	39.2	46.9	53.9	60.6	67.0	73.1	79.0	84.0	88.6	93.1	97.3	101	105	109	113
250	7.65	12.2	22.1	31.0	39.4	47.3	54.8	61.8	68.6	75.1	81.0	86.3	91.1	95.7	100	105	109	113	117
300	7.56	12.1	21.9	30.8	39.3	47.3	54.9	62.1	69.0	75.7	82.2	87.8	93.0	98.0	102	107	111	115	119
400	7.35	11.8	21.4	30.2	38.7	46.8	54.4	61.7	68.7	75.6	82.4	88.2	93.7	99.0	104	109	114	119	123
500	7.13	11.4	20.8	29.5	37.8	45.9	53.5	60.8	67.8	74.8	81.6	87.6	93.2	98.7	104	109	114	119	124
600	6.90	11.1	20.2	28.7	37.0	44.9	52.4	59.6	66.7	73.6	80.5	86.6	92.2	97.8	103	109	114	119	124
800	6.50	10.4	19.1	27.3	35.2	42.9	50.2	57.3	64.2	71.1	77.9	83.9	89.7	95.2	101	106	112	117	122
1000	6.14	9.89	18.1	25.9	33.6	41.0	48.2	55.0	61.8	68.5	75.2	81.2	86.9	92.5	98.0	103	109	114	119

Z1	70
M1	172

Z2	3	5	10	15	20	25	30	35	40	45	50	55	60	65	70	75	80	85	90
M2	6	10	21	32	43	54	66	79	92	105	118	131	145	159	172	186	200	216	230
E	**SB**	**SB**	**SB**	**SB**	**SB**	**SB**	**SB**	**SB**	**SB**	**SB**	**SB**	**SB**	**SB**	**SB**	**SB**	**SB**	**SB**	**SB**	**SB**
0.10																			
0.15																			
0.20																			
0.25																			
0.30																			
0.40																			
0.50																			
0.60																			
0.80																			
1.0	1.91	3.00	5.36	7.35															
1.5	2.22	3.48	6.19	8.45	10.5	12.3	14.0	15.6	17.0	18.4	19.7								
2.0	2.48	3.89	6.92	9.43	11.7	13.7	15.5	17.3	18.8	20.3	21.7	23.0	24.0	25.0	25.9	26.8	27.7	28.5	
2.5	2.71	4.25	7.56	10.3	12.7	14.9	16.9	18.8	20.5	22.1	23.6	24.9	26.0	27.1	28.0	28.9	29.8	30.7	31.5
3.0	2.91	4.57	8.13	11.1	13.7	16.0	18.2	20.2	22.0	23.7	25.3	26.7	27.9	29.0	30.0	31.0	31.9	32.8	33.6
4.0	3.25	5.10	9.09	12.4	15.3	18.0	20.4	22.6	24.7	26.6	28.4	30.0	31.3	32.5	33.6	34.6	35.6	36.6	37.5
5.0	3.53	5.55	9.88	13.5	16.7	19.6	22.2	24.7	27.0	29.0	31.0	32.7	34.2	35.5	36.7	37.8	38.9	40.0	40.9
6.0	3.77	5.92	10.6	14.4	17.9	21.0	23.8	26.5	28.9	31.1	33.2	35.1	36.7	38.1	39.4	40.7	41.8	43.0	44.0
8.0	4.16	6.53	11.7	16.0	19.8	23.3	26.5	29.4	32.2	34.7	37.0	39.2	41.0	42.6	44.1	45.5	46.8	48.1	49.3
10	4.46	7.02	12.5	17.2	21.3	25.1	28.6	31.8	34.8	37.6	40.1	42.5	44.4	46.2	47.9	49.4	50.9	52.3	53.6
15	5.03	7.93	14.2	19.5	24.2	28.6	32.6	36.4	39.8	43.0	46.0	48.8	51.1	53.2	55.2	57.1	58.8	60.5	62.1
20	5.44	8.58	15.4	21.1	26.3	31.1	35.5	39.6	43.4	47.0	50.4	53.5	56.0	58.4	60.6	62.7	64.7	66.6	68.5
25	5.75	9.08	16.3	22.4	28.0	33.1	37.8	42.2	46.3	50.1	53.8	57.1	59.9	62.5	64.9	67.2	69.4	71.5	73.5
30	6.00	9.48	17.0	23.4	29.3	34.6	39.6	44.3	48.6	52.7	56.6	60.1	63.1	65.9	68.5	70.9	73.3	75.5	77.7
40	6.39	10.1	18.1	25.0	31.3	37.1	42.5	47.6	52.3	56.7	60.9	64.8	68.1	71.2	74.1	76.8	79.4	81.9	84.4
50	6.68	10.6	19.0	26.2	32.9	39.0	44.7	50.1	55.1	59.8	64.3	68.5	72.0	75.3	78.4	81.3	84.2	86.9	89.5
60	6.91	10.9	19.7	27.2	34.1	40.5	46.5	52.1	57.3	62.3	67.0	71.4	75.1	78.6	81.9	85.0	88.0	90.9	93.7
80	7.26	11.5	20.7	28.7	36.0	42.8	49.1	55.1	60.7	66.0	71.1	75.9	79.9	83.7	87.3	90.7	94.0	97.1	100
100	7.50	11.9	21.4	29.7	37.4	44.5	51.1	57.4	63.2	68.8	74.2	79.2	83.5	87.5	91.3	95.0	98.5	102	105
150	7.91	12.5	22.6	31.5	39.6	47.3	54.4	61.1	67.5	73.6	79.4	84.9	89.6	94.0	98.3	102	106	110	114
200	8.10	12.9	23.4	32.6	41.0	49.0	56.5	63.5	70.2	76.6	82.8	88.6	93.6	98.3	103	107	111	115	119
250	8.12	13.0	23.5	32.9	41.8	50.2	58.0	65.2	72.1	78.7	85.1	91.2	96.4	101	106	111	115	119	123
300	8.07	12.9	23.5	32.9	41.9	50.4	58.4	66.0	73.3	80.3	87.1	93.1	98.5	104	108	113	118	122	126
400	7.91	12.7	23.1	32.6	41.6	50.2	58.4	66.1	73.6	80.8	87.9	94.6	101	106	112	117	122	127	131
500	7.72	12.4	22.6	31.9	40.9	49.5	57.7	65.5	73.0	80.4	87.6	94.5	101	106	112	117	123	128	133
600	7.52	12.1	22.1	31.3	40.1	48.7	56.8	64.5	72.1	79.5	86.8	93.7	99.9	106	112	117	123	128	133
800	7.13	11.5	21.0	29.9	38.5	46.8	54.8	62.4	69.9	77.2	84.5	91.5	97.7	104	110	115	121	126	132
1000	6.78	10.9	20.1	28.6	36.9	45.1	52.8	60.2	67.6	74.8	82.0	88.9	95.1	101	107	113	119	124	130

Z1	75
M1	186

Z2	3	5	10	15	20	25	30	35	40	45	50	55	60	65	70	75	80	85	90
M2	6	10	21	32	43	54	66	79	92	105	118	131	145	159	172	186	200	216	230

E	SB	SB	SB	SB	SB	SB	SB	SB	SB	SB	SB	SB	SB	SB	SB	SB	SB	SB	SB
0.10																			
0.15																			
0.20																			
0.25																			
0.30																			
0.40																			
0.50																			
0.60																			
0.80																			
1.0	1.91																		
1.5	2.19	3.45	6.19	8.47	10.5	12.4	14.1	15.8											
2.0	2.45	3.85	6.90	9.42	11.7	13.7	15.6	17.4	19.0	20.6	22.0	23.4	24.6	25.7	26.7				
2.5	2.67	4.20	7.53	10.3	12.7	14.9	17.0	18.9	20.7	22.3	23.8	25.3	26.6	27.7	28.7	29.7	30.6	31.5	32.4
3.0	2.87	4.52	8.10	11.0	13.7	16.1	18.3	20.3	22.2	23.9	25.5	27.1	28.4	29.6	30.7	31.7	32.6	33.6	34.5
4.0	3.21	5.06	9.07	12.4	15.3	18.0	20.5	22.8	24.9	26.8	28.6	30.3	31.8	33.1	34.3	35.4	36.4	37.4	38.3
5.0	3.50	5.51	9.88	13.5	16.7	19.6	22.3	24.9	27.2	29.3	31.3	33.1	34.8	36.2	37.4	38.6	39.7	40.8	41.8
6.0	3.74	5.89	10.6	14.4	17.9	21.1	24.0	26.7	29.2	31.4	33.6	35.6	37.4	38.9	40.2	41.5	42.7	43.9	45.0
8.0	4.14	6.52	11.7	16.0	19.9	23.4	26.7	29.7	32.5	35.1	37.5	39.7	41.8	43.5	45.0	46.5	47.8	49.2	50.4
10	4.46	7.03	12.6	17.3	21.5	25.3	28.9	32.2	35.3	38.1	40.7	43.2	45.4	47.3	49.0	50.6	52.1	53.6	54.9
15	5.05	7.98	14.4	19.7	24.6	29.0	33.1	36.9	40.5	43.8	46.9	49.8	52.4	54.6	56.7	58.6	60.4	62.2	63.8
20	5.48	8.66	15.6	21.5	26.8	31.6	36.2	40.4	44.3	48.0	51.4	54.7	57.6	60.1	62.4	64.6	66.6	68.6	70.5
25	5.81	9.19	16.6	22.8	28.5	33.7	38.6	43.1	47.3	51.3	55.0	58.5	61.7	64.5	67.0	69.4	71.6	73.8	75.8
30	6.08	9.62	17.4	23.9	29.9	35.4	40.5	45.4	49.8	54.0	58.0	61.7	65.1	68.1	70.8	73.3	75.7	78.1	80.3
40	6.49	10.3	18.6	25.6	32.1	38.0	43.6	48.9	53.7	58.3	62.6	66.8	70.5	73.7	76.7	79.6	82.3	84.9	87.4
50	6.81	10.8	19.5	26.9	33.8	40.1	46.0	51.5	56.7	61.6	66.2	70.7	74.7	78.1	81.4	84.5	87.4	90.2	92.9
60	7.06	11.2	20.2	28.0	35.1	41.7	47.9	53.7	59.1	64.2	69.1	73.8	78.0	81.7	85.1	88.4	91.5	94.5	97.4
80	7.43	11.8	21.3	29.6	37.1	44.2	50.8	57.0	62.8	68.3	73.6	78.6	83.2	87.2	91.0	94.5	98.0	101	104
100	7.70	12.2	22.2	30.7	38.6	46.0	52.9	59.4	65.6	71.4	76.9	82.3	87.1	91.4	95.4	99.2	103	106	110
150	8.16	13.0	23.5	32.7	41.2	49.1	56.6	63.6	70.3	76.6	82.6	88.5	93.8	98.5	103	107	111	115	119
200	8.46	13.4	24.4	33.9	42.7	51.1	58.9	66.3	73.3	79.9	86.3	92.5	98.2	103	108	113	117	121	125
250	8.54	13.6	24.8	34.7	44.0	52.4	60.5	68.1	75.4	82.3	89.0	95.4	101	107	112	116	121	125	130
300	8.54	13.7	24.9	34.9	44.3	53.3	61.7	69.7	77.0	84.1	91.0	97.6	104	109	114	119	124	129	133
400	8.44	13.5	24.7	34.8	44.3	53.5	62.1	70.3	78.2	85.8	93.2	100	107	113	119	123	128	133	138
500	8.28	13.3	24.4	34.3	43.9	53.0	61.7	70.0	78.0	85.7	93.3	101	108	114	120	125	131	136	141
600	8.10	13.0	23.9	33.7	43.2	52.4	61.0	69.3	77.3	85.2	92.8	100	107	114	120	126	131	137	142
800	7.75	12.5	22.9	32.5	41.7	50.7	59.3	67.4	75.4	83.2	90.9	99	106	112	118	124	130	136	142
1000	7.41	12.0	22.0	31.3	40.3	49.0	57.4	65.4	73.3	81.0	88.7	96	103	110	116	122	128	134	140

Z1	80
M1	200

Z2	3	5	10	15	20	25	30	35	40	45	50	55	60	65	70	75	80	85	90
M2	6	10	21	32	43	54	66	79	92	105	118	131	145	159	172	186	200	216	230

E	SB	SB	SB	SB	SB	SB	SB	SB	SB	SB	SB	SB	SB	SB	SB	SB	SB	SB	SB
0.10																			
0.15																			
0.20																			
0.25																			
0.30																			
0.40																			
0.50																			
0.60																			
0.80																			
1.0																			
1.5	2.17	3.43	6.20	8.51	10.6														
2.0	2.42	3.81	6.88	9.42	11.7	13.8	15.7	17.6	19.3	20.9	22.4	23.8							
2.5	2.64	4.16	7.50	10.3	12.7	15.0	17.1	19.0	20.9	22.5	24.1	25.6	27.1	28.3	29.4	30.5	31.5	32.4	
3.0	2.83	4.47	8.07	11.0	13.7	16.1	18.3	20.4	22.3	24.1	25.8	27.4	28.9	30.2	31.3	32.4	33.4	34.4	35.4
4.0	3.18	5.01	9.04	12.4	15.3	18.0	20.5	22.9	25.0	27.0	28.8	30.6	32.3	33.7	34.9	36.1	37.2	38.2	39.2
5.0	3.46	5.46	9.86	13.5	16.7	19.7	22.4	25.0	27.3	29.5	31.5	33.4	35.3	36.8	38.1	39.3	40.5	41.6	42.7
6.0	3.71	5.85	10.6	14.5	17.9	21.1	24.1	26.8	29.4	31.7	33.9	35.9	37.9	39.5	41.0	42.3	43.5	44.8	45.9
8.0	4.11	6.50	11.7	16.1	20.0	23.5	26.9	30.0	32.8	35.4	37.9	40.2	42.4	44.2	45.9	47.4	48.8	50.2	51.4
10	4.44	7.02	12.7	17.4	21.7	25.5	29.1	32.5	35.6	38.5	41.2	43.7	46.2	48.2	50.0	51.7	53.2	54.7	56.1
15	5.06	8.01	14.5	19.9	24.8	29.3	33.5	37.4	41.1	44.4	47.6	50.6	53.5	55.9	58.0	60.0	61.9	63.7	65.4
20	5.50	8.72	15.8	21.7	27.1	32.1	36.7	41.1	45.1	48.8	52.3	55.7	59.0	61.6	64.0	66.3	68.4	70.4	72.4
25	5.85	9.28	16.8	23.2	28.9	34.3	39.2	43.9	48.3	52.3	56.1	59.7	63.3	66.2	68.8	71.3	73.6	75.9	78.0
30	6.13	9.73	17.7	24.3	30.4	36.0	41.3	46.3	50.9	55.2	59.2	63.1	66.9	70.0	72.8	75.5	78.0	80.4	82.7
40	6.58	10.4	19.0	26.2	32.8	38.9	44.6	50.0	55.0	59.7	64.2	68.4	72.6	76.0	79.2	82.2	85.0	87.6	90.2
50	6.91	11.0	19.9	27.6	34.5	41.0	47.1	52.8	58.2	63.2	68.0	72.5	77.0	80.7	84.2	87.4	90.4	93.3	96.1
60	7.18	11.4	20.7	28.7	36.0	42.8	49.1	55.1	60.8	66.1	71.1	75.9	80.6	84.6	88.2	91.6	94.8	97.9	101
80	7.58	12.1	22.0	30.4	38.2	45.4	52.3	58.7	64.7	70.4	75.9	81.1	86.2	90.5	94.4	98.2	102	105	108
100	7.88	12.5	22.8	31.7	39.8	47.4	54.6	61.4	67.7	73.7	79.5	85.0	90.4	95.0	99.2	103	107	111	114
150	8.38	13.4	24.3	33.8	42.6	50.8	58.6	65.9	72.8	79.4	85.7	91.7	97.7	103	107	112	116	120	124
200	8.69	13.9	25.3	35.1	44.3	53.0	61.1	68.8	76.1	83.1	89.7	96.1	103	108	113	118	122	127	131
250	8.90	14.2	26.0	36.1	45.6	54.5	62.9	70.9	78.5	85.7	92.6	99.3	106	112	117	122	127	131	136
300	8.95	14.3	26.3	36.7	46.5	55.6	64.3	72.5	80.3	87.7	94.8	102	109	114	120	125	130	135	140
400	8.92	14.3	26.3	36.9	46.9	56.5	65.5	74.2	82.4	90.4	98.0	105	112	119	124	130	135	140	145
500	8.80	14.2	26.0	36.6	46.7	56.3	65.5	74.3	82.7	90.8	98.7	106	114	121	127	133	139	144	149
600	8.66	13.9	25.6	36.1	46.2	55.8	65.1	73.8	82.3	90.6	98.6	106	114	121	128	134	140	145	151
800	8.33	13.4	24.8	35.0	44.9	54.5	63.6	72.3	80.8	89.1	97.2	105	113	120	127	133	140	145	151
1000	8.02	12.9	23.9	33.9	43.5	52.9	61.9	70.5	78.9	87.1	95.2	103	111	118	125	132	138	144	150

Z1	85
M1	216

Z2	3	5	10	15	20	25	30	35	40	45	50	55	60	65	70	75	80	85	90
M2	6	10	21	32	43	54	66	79	92	105	118	131	145	159	172	186	200	216	230

E	SB	SB	SB	SB	SB	SB	SB	SB	SB	SB	SB	SB	SB	SB	SB	SB	SB	SB	SB
0.10																			
0.15																			
0.20																			
0.25																			
0.30																			
0.40																			
0.50																			
0.60																			
0.80																			
1.0																			
1.5	2.15	3.42	6.23																
2.0	2.38	3.78	6.87	9.4	11.7	13.8	15.9	17.8	19.5										
2.5	2.60	4.11	7.47	10.2	12.7	15.0	17.1	19.2	21.0	22.8	24.4	25.9	27.5	28.9	30.1				
3.0	2.79	4.41	8.01	11.0	13.6	16.0	18.3	20.5	22.5	24.3	26.0	27.6	29.2	30.7	32.0	33.1	34.2	35.3	36.3
4.0	3.13	4.95	8.98	12.3	15.3	18.0	20.5	22.9	25.1	27.1	29.0	30.8	32.5	34.2	35.5	36.7	37.9	39.0	40.0
5.0	3.41	5.40	9.81	13.4	16.7	19.6	22.4	25.0	27.4	29.6	31.7	33.6	35.5	37.3	38.7	40.0	41.2	42.4	43.5
6.0	3.66	5.79	10.5	14.4	17.9	21.1	24.1	26.9	29.5	31.8	34.0	36.1	38.1	40.0	41.6	43.0	44.3	45.6	46.7
8.0	4.07	6.45	11.7	16.1	20.0	23.6	26.9	30.1	33.0	35.6	38.1	40.4	42.7	44.9	46.6	48.2	49.6	51.1	52.4
10	4.41	6.98	12.7	17.4	21.7	25.6	29.3	32.7	35.9	38.8	41.5	44.1	46.5	48.9	50.8	52.6	54.2	55.7	57.2
15	5.04	8.00	14.6	20.0	25.0	29.5	33.8	37.8	41.5	44.9	48.1	51.1	54.1	56.9	59.1	61.2	63.2	65.0	66.7
20	5.51	8.74	15.9	21.9	27.4	32.4	37.1	41.6	45.7	49.5	53.1	56.5	59.7	62.9	65.4	67.8	70.0	72.1	74.1
25	5.87	9.33	17.0	23.4	29.3	34.7	39.8	44.5	49.0	53.1	57.0	60.7	64.3	67.7	70.5	73.1	75.5	77.8	80.0
30	6.17	9.80	17.9	24.7	30.8	36.5	41.9	47.0	51.7	56.1	60.3	64.2	68.0	71.7	74.7	77.5	80.1	82.6	84.9
40	6.63	10.6	19.3	26.6	33.3	39.5	45.4	50.9	56.1	60.9	65.5	69.8	74.0	78.1	81.4	84.5	87.4	90.2	92.8
50	6.99	11.1	20.3	28.1	35.2	41.8	48.1	54.0	59.5	64.6	69.5	74.2	78.7	83.1	86.7	90.0	93.2	96.2	99.1
60	7.27	11.6	21.2	29.3	36.7	43.7	50.2	56.4	62.2	67.7	72.8	77.7	82.5	87.1	90.9	94.5	97.9	101	104
80	7.71	12.3	22.5	31.1	39.1	46.5	53.5	60.2	66.4	72.3	77.9	83.2	88.4	93.5	97.6	102	105	109	112
100	8.03	12.8	23.4	32.5	40.8	48.7	56.1	63.1	69.6	75.9	81.8	87.4	92.9	98.3	103	107	111	115	118
150	8.57	13.7	25.1	34.8	43.9	52.3	60.4	68.0	75.2	82.0	88.5	94.7	101	107	112	116	121	125	129
200	8.92	14.3	26.1	36.3	45.8	54.7	63.2	71.2	78.8	86.0	92.9	99.5	106	112	118	123	127	132	136
250	9.16	14.6	26.9	37.4	47.2	56.4	65.2	73.5	81.4	88.9	96.1	103	110	116	122	127	132	137	142
300	9.32	14.9	27.5	38.2	48.2	57.7	66.7	75.2	83.4	91.1	98.5	106	113	119	125	131	136	141	146
400	9.36	15.0	27.7	38.8	49.3	59.3	68.7	77.8	86.4	94.3	102	110	117	124	130	136	142	147	152
500	9.30	15.0	27.6	38.7	49.3	59.5	69.1	78.3	87.1	95.7	104	112	120	127	134	140	145	151	156
600	9.18	14.8	27.3	38.4	49.0	59.2	68.9	78.2	87.1	95.8	104	112	120	128	135	142	148	154	160
800	8.91	14.4	26.6	37.5	48.0	58.1	67.8	77.1	86.1	94.8	103	112	120	128	135	142	149	155	161
1000	8.62	13.9	25.8	36.5	46.7	56.7	66.3	75.5	84.4	93.1	102	110	118	127	134	141	148	154	160

Z1	90																		
M1	230																		
Z2	3	5	10	15	20	25	30	35	40	45	50	55	60	65	70	75	80	85	90
M2	6	10	21	32	43	54	66	79	92	105	118	131	145	159	172	186	200	216	230

E	SB	SB	SB	SB	SB	SB	SB	SB	SB	SB	SB	SB	SB	SB	SB	SB	SB	SB	SB
0.10																			
0.15																			
0.20																			
0.25																			
0.30																			
0.40																			
0.50																			
0.60																			
0.80																			
1.0																			
1.5																			
2.0	2.4	3.8	6.9	9.5	11.8	14.0													
2.5	2.6	4.1	7.5	10.2	12.7	15.0	17.2	19.3	21.2	23.0	24.7	26.3							
3.0	2.8	4.4	8.0	11.0	13.6	16.1	18.4	20.6	22.6	24.5	26.3	28.0	29.6	31.2	32.6	33.9	35.0		
4.0	3.1	4.9	8.9	12.3	15.2	18.0	20.5	23.0	25.2	27.3	29.2	31.0	32.8	34.5	36.1	37.4	38.6	39.8	40.9
5.0	3.4	5.3	9.8	13.4	16.7	19.6	22.4	25.1	27.5	29.8	31.9	33.8	35.7	37.6	39.3	40.6	41.9	43.2	44.3
6.0	3.6	5.7	10.5	14.4	17.9	21.1	24.1	27.0	29.6	32.0	34.3	36.4	38.4	40.4	42.2	43.6	45.0	46.3	47.5
8.0	4.0	6.4	11.7	16.1	20.0	23.6	27.0	30.2	33.1	35.9	38.4	40.8	43.1	45.2	47.3	48.9	50.4	51.9	53.3
10	4.4	7.0	12.7	17.5	21.8	25.7	29.4	32.9	36.1	39.1	41.9	44.5	47.0	49.4	51.6	53.4	55.1	56.7	58.2
15	5.0	8.0	14.6	20.1	25.1	29.7	34.0	38.1	41.9	45.4	48.7	51.7	54.7	57.5	60.2	62.3	64.3	66.3	68.1
20	5.5	8.8	16.1	22.1	27.6	32.7	37.5	42.0	46.2	50.1	53.8	57.2	60.6	63.7	66.7	69.1	71.4	73.6	75.6
25	5.9	9.4	17.2	23.7	29.6	35.1	40.2	45.1	49.7	53.9	57.9	61.6	65.3	68.7	72.0	74.6	77.2	79.6	81.8
30	6.2	9.9	18.1	25.0	31.2	37.0	42.5	47.7	52.5	57.1	61.3	65.3	69.2	72.9	76.4	79.3	82.0	84.5	87.0
40	6.7	10.7	19.6	27.0	33.8	40.1	46.1	51.8	57.1	62.1	66.7	71.2	75.5	79.6	83.5	86.7	89.7	92.6	95.3
50	7.1	11.3	20.7	28.6	35.8	42.6	49.0	55.0	60.7	66.0	71.0	75.8	80.4	84.8	89.0	92.5	95.8	98.9	102
60	7.4	11.7	21.6	29.9	37.4	44.5	51.2	57.6	63.6	69.2	74.5	79.5	84.4	89.1	93.6	97.2	101	104	107
80	7.8	12.5	23.0	31.8	39.9	47.6	54.8	61.6	68.1	74.1	79.9	85.3	90.6	95.8	101	105	109	112	116
100	8.2	13.0	24.0	33.3	41.8	49.8	57.4	64.7	71.5	77.9	84.0	89.8	95.4	101	106	110	115	119	122
150	8.8	14.0	25.8	35.8	45.1	53.8	62.1	69.9	77.4	84.4	91.1	97.6	104	110	116	121	125	130	134
200	9.1	14.6	26.9	37.4	47.2	56.4	65.1	73.4	81.3	88.8	95.9	103	109	116	122	127	132	137	142
250	9.4	15.1	27.7	38.6	48.7	58.2	67.3	75.9	84.1	91.9	99.4	107	113	120	127	132	138	143	147
300	9.6	15.4	28.4	39.5	49.8	59.7	69.0	77.9	86.3	94.3	102	109	117	124	130	136	142	147	152
400	9.8	15.7	29.0	40.6	51.5	61.8	71.4	80.6	89.4	97.8	106	114	121	129	136	142	148	153	159
500	9.7	15.7	29.1	40.7	51.8	62.3	72.4	82.0	91.2	100	109	117	124	132	140	146	152	158	163
600	9.7	15.6	28.9	40.6	51.7	62.3	72.5	82.2	91.6	101	109	118	126	134	142	149	156	161	167
800	9.4	15.2	28.3	39.8	50.9	61.6	71.8	81.5	91.0	100	109	118	126	135	143	150	157	164	170
1000	9.2	14.8	27.6	38.9	49.8	60.4	70.5	80.2	89.6	98.8	108	117	125	134	142	150	157	163	170

Radiation Effects Letters, 1984, Vol. 86, pp. 145–151
0142-2448/84/8604-0145 $18.50/0
© Gordon and Breach Science Publishers Inc., 1984
Printed in Great Britain

A COMPARISON OF THREE VERSIONS OF SIGMUND's MODEL OF SPUTTERING USING EXPERIMENTAL RESULTS

H.J. STRYDOM and W.H. GRIES
National Institute for Materials Research, CSIR, P.O. Box 395, Pretoria 0001, South Africa

Abstract Two modifications of Sigmund's sputtering formula, viz. by Bohdansky and by Yamamura et al. are compared with an α-adaptation of Sigmund's original formula to 620 experimental sputtering yields taken from literature. Using the α-values for the comparison, it was found that the considerable scatter of these values (averaged for given M_1, Z_1, M_2, Z_2) is not reduced by either of the two modifications, except for values in the range $M_2/M_1 > 100$. In each of the three versions the scatter is systematic, however, in as far as certain target elements yield average values of α which are consistently high, low or intermediate over a wide range of M_2/M_1 ratios.

(*Received for Publication February 7, 1984*)

Two modifications of the well-known sputter yield formula for normal incidence of mono-energetic ions on single-element targets given by Sigmund[1], viz. those proposed by Bohdansky[2] and Yamamura et al.[3], have been investigated for their effectiveness in providing a better fit between theory and experiment than a simple α-adaptation of the original model. For this purpose all three formulae were subjected to a procedure whereby their α-values were calculated for 620 measured sputter yields (published in 24 papers)[4] and these values compared. Because of the scarcity of sputtering data for amorphous targets to which Sigmund's model applies, sputter yields for polycrystalline targets were used instead.

The three formulae are as follows:

Sigmund[1]

$$S = \frac{0.042\,\alpha\,S_n(E)}{U_s} \tag{1}$$

Bohdansky[2]

$$S = \frac{0.042}{U_s} \alpha \frac{R_p}{R} S_n(E)\ g(E/E_{th})$$

$$\text{with } g(E/E_{th}) = \left[1-(E_{th}/E)^{2/3}\right](1-E_{th}/E)^2 \qquad (2)$$

Yamamura et al.[3]

$$S = \frac{0.042\ \alpha}{U_s} \frac{S_n(E)}{1 + 0.35\ U_s s_e(\varepsilon)} \left[1-(E_{th}/E)^{1/2}\right]^2 \qquad (3)$$

where the symbols have their usual meaning:

- S is the sputter yield (atoms/ion),
- α is a dimensionless function of the mass ratio M_2/M_1 (where M_1 and M_2 are the mass numbers of the ion species and the target respectively), which represents the fraction of the energy available for sputtering,
- $S_n(E)$ is the nuclear stopping power (in eV.Å^2) of the well-known LSS-theory[5], which is a function of the incident ion energy E,
- U_s is the atomic surface binding energy (in eV/atom),
- R_p/R is the ratio of the projected range to the range of the ion species in the target,
- E_{th} is the threshold ion energy below which no sputtering occurs,
- $s_e(\varepsilon)$ is the dimensionless universal electronic stopping cross-section of the LSS-theory, which is a function of the dimensionless energy ε.

Each of the three equations was solved for α, with S being substituted by the 620 measured sputter yields mentioned above. To distinguish the α-values according to their origin, they were designated α_{eff} (i.e. effective α, Sigmund), α_{Bo} (Bohdansky) and α_{Ya} (Yamamura). The same standard sublimation enthalpies were used for U_s in all cases. In addition, the following special relationships were used:

(i) For E_{th} values in eqns 2 and 3, from ref. 6

$$E_{th} = \begin{cases} 8(M_1/M_2)^{2/5}\, U_s & \text{for } M_1/M_2 > 0.3 \\ U_s/\gamma(1-\gamma),\ \gamma = \dfrac{4M_1\, M_2}{(M_1 + M_2)}, & \text{for } M_1/M_2 \leq 0.3 \end{cases}$$

Another expression for E_{th}, proposed by Yamamura et al.,[3] was discarded because it gave values in the high M_2/M_1 region which were significantly higher than the energies at which sputtering was observed.

(ii) For the R_p/R ratio in eqn 2

$$R/R_p = \frac{M_2}{M_1}\psi^* + 1$$

with $\psi^* = (0.526 + 0.474\, k^{1/16})\, \psi_{k=0.2}$

where k is the well-known constant of the LSS electronic stopping cross-section $s_e(\varepsilon)$,[5] and $\psi_{k=0.2}$ is the LSS correction of the projected range for $k = 0.2$.[5]

For purposes of the present calculation $\psi_{k=0.2}$ was scaled from Fig. 8 in ref. 5, extrapolated to $\varepsilon = 0.001$, and approximated by the following set of curves

$$\psi_{k=0.2} = \begin{cases} 0.332 - 0.033 \ln \varepsilon, & 0.001 < \varepsilon \leqslant 0.4 \\ 0.301 - 0.052 \ln \varepsilon, & 0.4 < \varepsilon \leqslant 1.0 \\ 0.305 - 0.060 \ln \varepsilon, & 1.0 < \varepsilon \leqslant 20 \\ 0.574\, \varepsilon^{-0.515}, & 20 < \varepsilon \leqslant 500 \end{cases}$$

In Fig. 1 the values of R/R_p obtained by the use of this expression are compared with those from three other calculations.

For graphical display of the α-values the 620 individual values were reduced to 60 by representing those with the same (M_1, Z_1, M_2, Z_2) combination by their average value $\bar{\alpha}$. In this way values of $\bar{\alpha}_{eff}$, $\bar{\alpha}_{Bo}$ and $\bar{\alpha}_{Ya}$ were obtained which are plotted vs the ratio M_2/M_1 (in log-log form) in Figs 2 and 3. Note that the number of α-values which make up an individual average $\bar{\alpha}$ is not the same for each average. In particular, the low outlier at $M_2/M_1 = 1$ is derived from a single self-sputtering value of Zn at 0.3 keV.

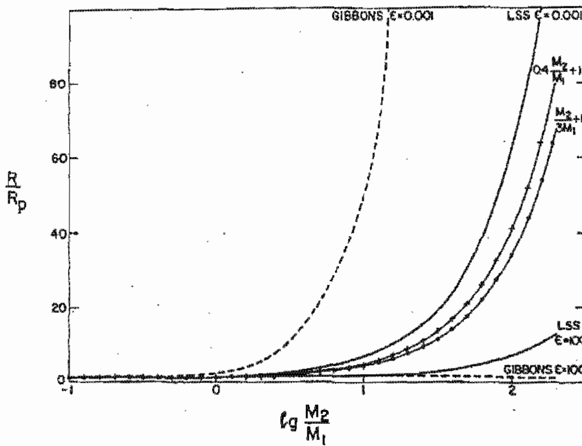

FIGURE 1 The R/R_p ratios according to

- two exact calculations by
  - Lindhard et al.[5] (solid lines for ε = 0.001 and ε = 100)
  - Gibbons et al.[7] (broken lines for ε = 0.001 and ε = 100)
- two approximations proposed by
  - Lindhard et al.[5] (dot-marked line)
  - Bohdansky[8] (cross-marked line).

The R/R_p ratios of Gibbons et al.[7] can be approximated (within 10%) by $R/R_p = (M_2/M_1)\,\psi_G + 1$, where $\psi_G = A\varepsilon^{-B}$ with $A = 0.224 - 0.082 \ln k$, $B = 0.498 + 0.163 \ln k$ and k the LSS electronic stopping constant.

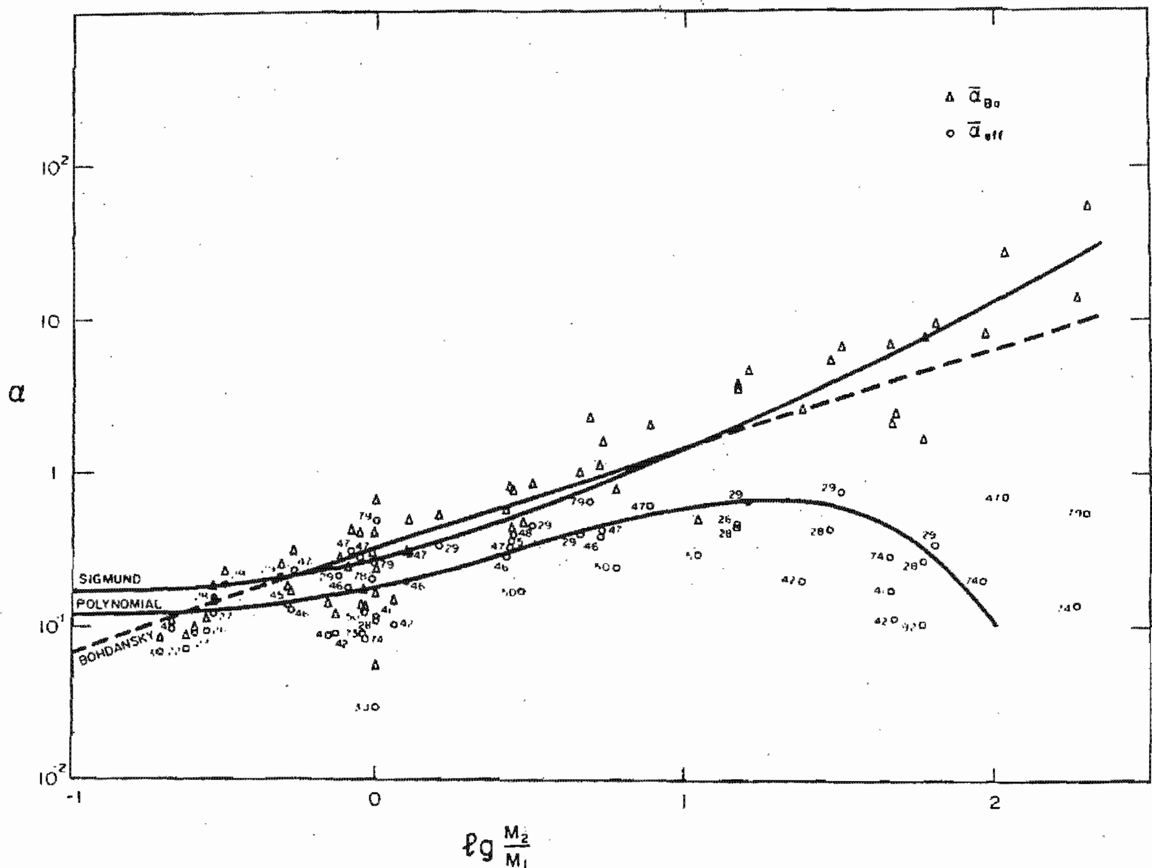

FIGURE 2 Values of $\bar{\alpha}_{eff}$ (circles) and $\bar{\alpha}_{Bo}$ (triangles) and of the associated approximating graphs $\tilde{\alpha}_{eff}$ (POLYNOMIAL) and $\tilde{\alpha}_{Bo}$ (BOHDANSKY). The graph of α-values proposed by Sigmund is also shown (SIGMUND). The $\bar{\alpha}_{eff}$ values are labelled with Z_2 numbers.

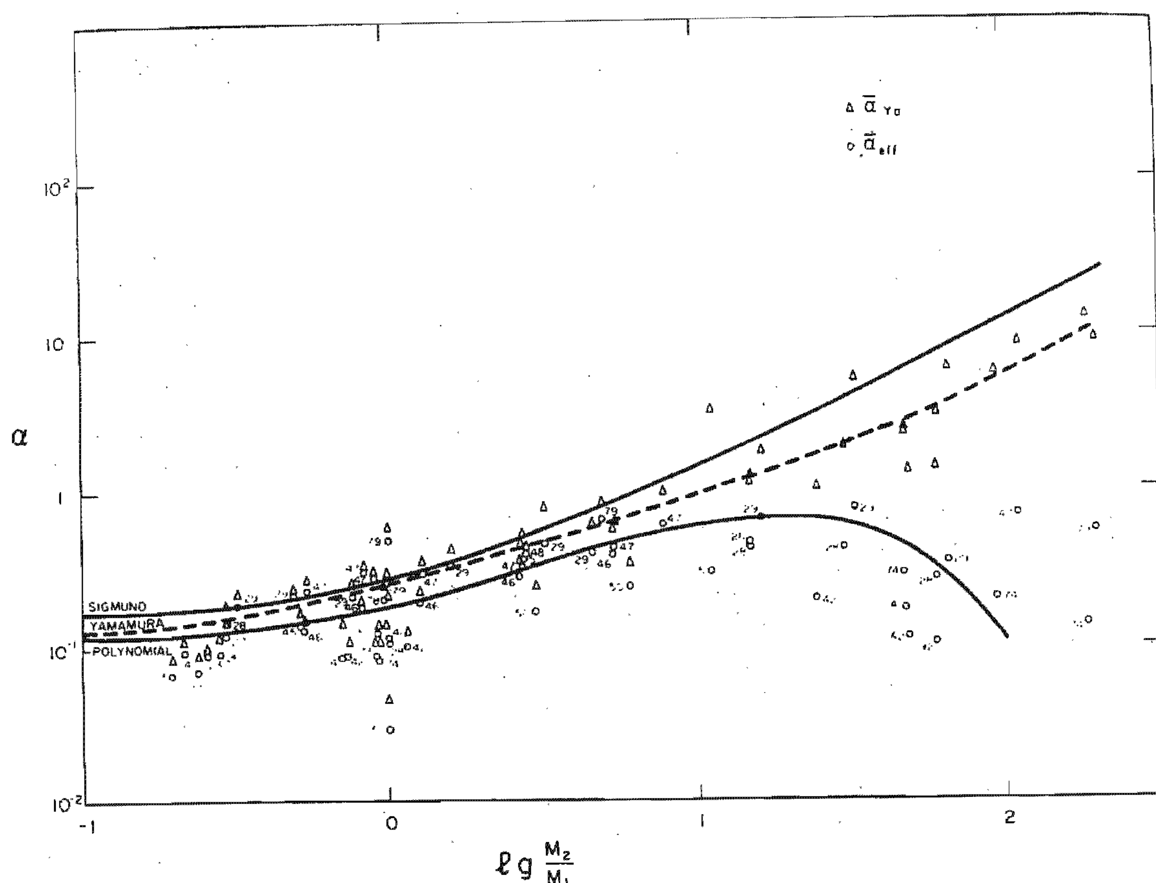

FIGURE 3 Values of $\bar{\alpha}_{eff}$ (circles) and $\bar{\alpha}_{Ya}$ (triangles) and of the associated approximating graphs $\tilde{\alpha}_{eff}$ (POLYNOMIAL) and $\tilde{\alpha}_{Ya}$ (YAMAMURA). The graph of α-values proposed by Sigmund is also shown (SIGMUND). The $\bar{\alpha}_{eff}$ values are labelled with Z_2 numbers.

From Figs 2 and 3 it is apparent that the considerable scatter of $\bar{\alpha}_{eff}$ values (note the logarithmic scale) is not reduced for either the $\bar{\alpha}_{Bo}$ values (Fig. 2) or the $\bar{\alpha}_{Ya}$ values (Fig. 3), except for the four points at the extreme high end of the M_2/M_1 scale ($M_2/M_1 > 100$). In fact, in the range $10 < M_2/M_1 < 100$ the individual values of α_{Bo} and α_{Ya} tend to have a wider relative spread (i.e. relative to the average) than the α_{eff} values. It is also seen that application of the Bohdansky or the Yamamura formulae changes the absolute positions of the $\bar{\alpha}$ points, but not in general their relative positions (with a few exceptions). The effect of the Bohdansky and Yamamura modifications on the Sigmund formula is in both cases smallest at the low end of the M_2/M_1 scale (viz. $\bar{\alpha}_{Bo} \approx \bar{\alpha}_{Ya} \approx 1.2\ \bar{\alpha}_{eff}$) and largest at the high end (viz. $40\ \bar{\alpha}_{eff} < \bar{\alpha}_{Bo} < 150\ \bar{\alpha}_{eff}$ and $15\ \bar{\alpha}_{eff} < \bar{\alpha}_{Ya} < 100\ \bar{\alpha}_{eff}$).

The fact that in the majority of cases the relative positions of the $\bar{\alpha}_{Bo}$ and $\bar{\alpha}_{Ya}$ points remain the same as for the $\bar{\alpha}_{eff}$ points indicates that none of the additional parameters in the modifications (i.e. R_p/R, E/E_{th} and $s_e(\varepsilon)$) has any significant influence on the scatter of these points. It was noticed, however, that the $\bar{\alpha}$ values of certain target elements (e.g. Au, Ag, Cu) were high at all M_2/M_1 ratios, and those of other elements (e.g. Mo, Sn, Nb) were low, while those of a third group (incl. Pd, Ni, W) were intermediate. One can speculate, therefore, that the scatter is systematic and that the $\bar{\alpha}$ values are samples from a quasi-parallel set of $\bar{\alpha}$ graphs, one for each element.

The curve marked POLYNOMIAL in Figs 2 and 3 represents a best (least squares) fit to all (620) α_{eff} values and consists of a set of three smoothly interlinking expressions (including two polynomials) as follows (cf. ref. 4):

$$\tilde{\alpha}_{eff} = \begin{cases} 0.120 & \text{for } l \leq -1.2 \\ 0.0857\, l^5 + 0.289\, l^4 + 0.402\, l^3 + 0.350\, l^2 + 0.220\, l + 0.189 & \text{for } -1.2 < l \leq -0.144 \\ 0.0449\, l^6 - 0.107\, l^5 - 0.209\, l^4 + 0.314\, l^3 + 0.207\, l^2 + 0.156\, l + 0.183 & \text{for } -0.144 < l \leq 1.8 \end{cases}$$

where $l = \lg (M_2/M_1)$. (4)

Other approximations for α have been proposed by Bohdansky[2] and Yamamura et al.,[3] each pertaining to the particular modification of Sigmund's formula. These are shown as a straight line, marked BOHDANSKY, in Fig. 2 and as a (two-segment) curve, marked YAMAMURA, in Fig. 3. The corresponding analytical expressions are

$$\tilde{\alpha}_{Bo} = 0.3 \cdot (M_2/M_1)^{2/3} \quad \text{for } 0.5 < M_2/M_1 < 10 \tag{5}$$

$$\tilde{\alpha}_{Ya} = \begin{cases} 0.010 + 0.155\, (M_2/M_1)^{0.73} & \text{for } M_2/M_1 < 50 \\ 0.321 + 0.0332\, (M_2/M_1)^{1.1} & \text{for } M_2/M_1 > 50 \end{cases} \tag{6}$$

When judging these approximations for closeness of fit to the plotted $\bar{\alpha}$ values it must be remembered that in Figs 2 and 3 equal

ordinate displacements represent equal multiplications factors and **not** equal addition terms, i.e. a symmetrical error margin appears asymmetrical in these figures. When this is taken into account, it is readily concluded that for the $\bar{\alpha}_{Bo}$ values used here the approximation $\tilde{\alpha}_{Bo}$ becomes less representative (too low) for $M_2/M_1 > 3$, while for the $\bar{\alpha}_{Ya}$ values the approximation $\tilde{\alpha}_{Ya}$ is a reasonable representation at all M_2/M_1 values.

In summary, satisfactory average results are provided by the Yamamura modification of Sigmund's model at all mass ratios (using Bohdansky's expression for E_{th}), and by Bohdansky's modification in the mass ratio range $M_2/M_1 < 3$ when compared with the 620 measured sputter yields used for this investigation. These results are not more general though, than can be obtained by use of an empirical α-approximation like the POLYNOMIAL of eqn 4 in Sigmund's original formula. This is shown by the fact that the (apparently target-related) scatter of $\bar{\alpha}$ values is not reduced by either of the two modifications.

REFERENCES

1. P. Sigmund, Phys. Rev. **184** 383 (1969).
2. J. Bohdansky, Proc. Symp. Surface Science, Obertraun (Austria) 1983, P. Braun (ed.), Institut f. Allgemeine Physik, Technische Universität Wien, Karlsplatz 13, A-1040 Vienna (Austria) p. 127.
3. Y. Yamamura, N. Matsunami and N. Itoh, Rad. Eff. Lett. **68** 83 (1982).
4. W.H. Gries and H.J. Strydom, A Table of Normalized Sputtering Yields for Monoelemental Polycrystalline Targets, Report SMAT 3 (1984), NIMR/CSIR, P.O. Box 395, Pretoria 0001, South Africa.
5. J. Lindhard, M. Scharff and H.E. Schiøtt, Dan. Vid. Selsk. Mat. Fys. Medd. **33** (14) (1963).
6. J. Bohdanksy, J. Nucl. Materials **93/94** 44 (1980).
7. J.F. Gibbons, W.S. Johnson and S. Mylroie, Projected Range Statistics, 2nd ed. (Dowden, Hutchinson & Ross Inc., Stroudsburg, Penn., U.S.A., 1975).
8. J. Bohdansky, Int. Conf. Atomic Collisions in Solids, Bad Iburg (Germany) 1983.

A Practical Table of Sputtering Yields for the Non-Expert User

W. H. Gries and H. J. Strydom

National Institute for Materials Research, CSIR, P.O. Box 395, Pretoria, South Africa

Eine Sputterkoeffiziententabelle für den Praktiker

Many users of surface analytical techniques in which sputtering by ion bombardment is used have difficulty in selecting the best conditions for a particular sputtering task. While it is generally difficult to predict sputter yields for multi-element samples, reasonable estimates can be made for mono-elemental solids. This has been done by the authors for the case of polycrystalline mono-elemental solids bombarded at normal incidence by element ions within the energy range 0.1 to 1000 keV, and the results have been tabulated [1] in a normalized form.

The predicted sputter yields were calculated from an adapted version of Sigmund's well-known sputter yield formula [2]

$$S = 0.042\ \alpha\ S_n/B\ [\text{atoms/ion}] \quad (1)$$

where α is a dimensionless number which expresses the relative availability of the deposited energy of the incident ion for sputtering, S_n is the nuclear stopping power of the target for the incident ion, and B is the average surface binding energy of the atoms to be sputtered.

In the adapted version Sigmund's α has been replaced by a best-fit graph to a plot of "effective" α values (designated

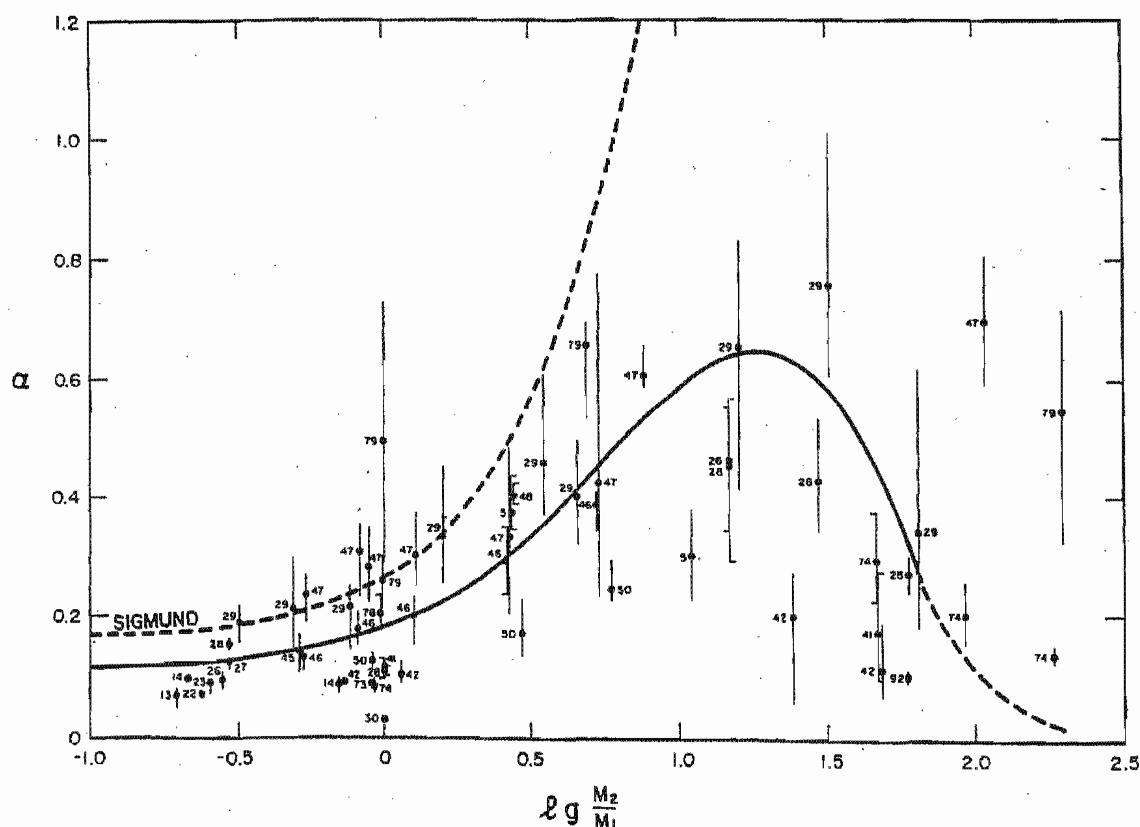

Fig. 1. Broken line: Sigmund's α. Solid line: Best-fit approximation $\tilde{\alpha}_{eff}$ used to replace Sigmund's α

Offprint requests to: W. H. Gries, Plasma-Wandwechselwirkung, Max-Planck-Institut für Plasmaphysik, Boltzmannstr. 2, D-8046 Garching b. München

© Springer-Verlag 1984

α_{eff}) obtained by substitution of 620 measured sputter yields S_{real} taken from literature into Eq. (1)

$$\alpha_{eff} = S_{real}\, B/0.042\, S_n\,. \qquad (2)$$

This best-fit graph, represented by a function $\tilde{\alpha}_{eff}\,(M_2/M_1)$, is shown in Fig. 1. The dots represent average values ($\bar{\alpha}_{eff}$) of for the same (M_1, Z_1, M_2, Z_2). where M and Z are mass numbers and atom numbers and subscripts 1 and 2 refer to ion and solid respectively. The numbers in Fig. 1 are Z_2 values. The vertical lines indicate the spread of the associated α_{eff} values.

The predicted normalized sputter yields for the table in ref. [1] were calculated as

$$SB = 0.042\, \tilde{\alpha}_{eff}\, S_n\,. \qquad (3)$$

Thus, the tabulated values are normalized to an atomic surface binding energy of 1 eV, from which real sputter yields are obtained using division by the actual atomic surface binding energy of the target solid (represented by the sublimation enthalpy).

The large scatter of experimental α_{eff} values in Fig. 1 emphasizes that the tabulated sputter yields, which are derived from the $\tilde{\alpha}_{eff}$ graph, must be regarded only as estimates.

A comparison [3] of the α-adaption used here with two modifications of Sigmund's sputtering formula, viz. by Bohdansky [4] and by Yamamura et al. [5], showed that these modifications do not lead to a reduced scatter of α_{eff} values.

However, the Z_2 numbers with which the average points $\bar{\alpha}_{eff}$ in Fig. 1 are labelled show that the scatter of experimental points is not entirely unsystematic. For certain target elements the $\bar{\alpha}_{eff}$ values are high at all M_2/M_1 ratios (e.g. Au, Ag, Cu), those of other elements are consistently low (e.g. Mo, Sn, Nb), while those of a third group are intermediate (incl. Pb, Ni, W). One can speculate, therefore, that the $\bar{\alpha}_{eff}$ values could be samples from a quasi-parallel set of $\tilde{\alpha}_{eff}$ graphs, one for each element. Until this point is proved by further evidence, the $\tilde{\alpha}_{eff}$ graph must serve as a first order general approximation.

References

1. Gries WH, Strydom HJ (1984) A table of normalized sputtering yields for mono-elemental polycrystalline targets, Report SMAT 3, NIMR/CSIR, PO Box 395, Pretoria 0001, South Africa
2. Sigmund P (1969) Phys Rev 184:383
3. Strydom HJ, Gries WH (1984) Rad Eff Lett 86:145
4. Bohdansky J (1983) Proc Symp Surface Science, Obertraun (Austria), Braun P (ed), Institut f Allgemeine Physik, Technische Universität Wien, Karlsplatz 13, A-1040 Vienna (Austria) p 127
5. Yamamura Y, Matsunami N, Itoh N (1982) Rad Eff Lett 68:83

Received May 9, 1984

Dynamic SIMS: applications to semiconductor technology

H.J. Strydom and A.P. Botha
Division of Microelectronics and Communications Technology, CSIR, P.O. Box 395, Pretoria 0001, Republic of South Africa

and

W.O. Barnard
Department of Physics, University of Pretoria, Pretoria 0001, Republic of South Africa

Presented at SASSAMA-88, Golden Gate, 21–22 October 1988

Selected features of dynamic SIMS (secondary ion mass spectrometry) and its application to semiconductor materials and devices are discussed. The differences in magnetic sector and quadrupole mass spectrometers are outlined. Applications include both types of instruments. Qualitative as well as quantitative measurements in order to obtain elemental or chemical information are reported. Examples are given to illustrate how SIMS was used to study the effect of impurities on crystal growth, diffusion during metal–semiconductor contact formation, epitaxy of quantum well structures and failure analysis in device fabrication.

Geselekteerde eienskappe van dinamiese SIMS (sekondêre-ioonmassaspektrometrie) en hul toepassing vir die analisering van halfgeleiermateriale en -toestelle word bespreek. Die verskille tussen magnetiese en kwadrupoolmassaspektrometers word uitgewys en toepassings van beide tipes instrumente word aangetoon. Kwalitatiewe sowel as kwantitatiewe metings wat elementêre en chemiese inligting bied, word bespreek. Voorbeelde word gegee om te illustreer hoe SIMS gebruik is om die effek van onsuiwerhede op kristalgroei, diffusie gedurende metaal–halfgeleierkontakvorming, epitaksie van kwantumputstrukture en falingsanalise in toestelvervaardiging te bestudeer.

1. Introduction

The rapid development of semiconductor materials and device technology over the last few years has placed increasing demands on surface and interface characterization techniques. In most cases atomic sensitivities of parts per million to parts per billion are required. The information required is either the depth distribution of dopants and/or interdiffusion and reaction of interfacial layers with high depth resolution and no significant spatial resolution, or the actual structure of a device in a plane parallel to the surface, where high spatial resolution is essential due to the small linewidths used in circuit design, or the need for surface uniformity in devices such as photodetectors.

Of all the available characterization techniques, secondary ion mass spectrometry (SIMS) has the advantage of its incredible sensitivity for small impurity concentrations, combined in some cases with a spatial resolution of less than 0.5 μm. Sensitivities down to 10^{14} cm^{-3} (less than 10 p.p.b.) have been obtained with this technique [1].

SIMS has three distinct modes of operation — static, imaging and dynamic. In static SIMS the sample is bombarded with a low energy, low flux, inert gas beam which leaves the sample surface virtually intact, allowing ample time to analyse the surface. By raster-scanning a fine focussed ion beam under static conditions across an area of surface and collecting the secondary ions at each point, a chemical image can be produced — this is referred to as imaging SIMS. Dynamic SIMS uses high flux density oxygen or caesium ions to obtain a very high yield of secondary ions. Since the surface is eroded very rapidly, very high sensitivity concentration depth profiles are produced. Typical parameters for the three modes are given in Table 1.

SIMS has been extensively reviewed in recent years, from a variety of viewpoints [2 – 7], and a repeat of that information would serve little purpose. Instead we will focus on applications of dynamic SIMS to problems encountered in the growth of semiconductor materials and device fabrication.

2. Generations of SIMS machines

Since the first construction of a double spectrometer for primary and secondary mass analysis in 1955 [8], the development of SIMS instruments followed three distinct paths [9]. The mass analyser approach, with moderate lateral resolution, utilizes high primary ion current densities to perform trace analysis and depth profiling. The microprobe approach utilizes a micro-focussed primary ion beam of micrometer dimensions that is rastered

Table 1 Modes of SIMS operation

Analysis mode	Current density	Beam diameter	Surface lifetime	Data format
Static	$< 10\,nA\,cm^{-2}$	2 – 3 mm	$> 10^3\,s$	Spectrum
Imaging	$< 10\,nA\,cm^{-2}$	< 200 nm	$< 10^3\,s$	Images or maps
Dynamic	$> 10\,\mu A\,cm^{-2}$	> 5 μm	< 1 s	Conc. depth profiles

across the sample. Lateral resolution is limited by the primary beam size. The ion microscope approach radiates the sample with a broad beam of primary ions. High lateral resolution is achieved by forming an image of the surface with the low-energy secondary ions, and transmits this stigmatically through the secondary mass spectrometer. Because the ion beam erodes the surface, the analytical front moves into the sample, allowing an in-depth analysis, or depth profiles. Lateral resolution is given by the ratio of the extraction field strength to the energy spread of the sputtered ions. Resolutions of 0.5 – 1.0 μm can be achieved.

The detection of secondary ions is achieved by either magnetic sector mass analysers or quadrupole mass analysers. The first commercial instruments were of the magnetic sector type [9]. The more recent spectrometers use quadrupole mass detection, due to a number of reasons:

(a) Magnetic stray fields rule out combinations with other surface-sensitive techniques which involve charged particles [for example, Auger electron spectroscopy (AES) and X-ray photoelectron spectroscopy (XPS)], on the same vacuum system.
(b) Up till now, magnetic sector SIMS has not been compatible with the UHV required for the sensitivity of the SIMS technique.
(c) Magnetic sector instruments suffer from memory effects, resulting in rapidly decreasing dynamic range in profiles, requiring regular cleaning of the ion optics.
(d) Negative secondary ion analysis has up till now been extremely difficult with magnetic sector instruments.
(e) Although the mass resolution of the magnetic sector is by far superior to that of the quadrupole, the loss in signal strength at high mass resolution is a disadvantage.

In this paper we will focus our attention on applications of dynamic SIMS to semiconductors. The results were obtained using a magnetic sector ARL ion microprobe mass analyser (IMMA) [10] and a quadrupole-based SIMSLAB attached to the VG ESCALAB Mk II spectrometer. The instrumental geometries have been described elsewhere [11 – 14]. In the discussions that follow, the experimental conditions are not always given in detail where reference is made to earlier published work.

3. Qualitative SIMS

All elements from hydrogen to uranium and combinations of these elements (polyatomic ions or cluster ions) can be detected. The atomic ions can be used for quantitative chemical analysis once calibration against standards has been done, while the cluster ions can be used for qualitative identification of chemical compounds or for the study of chemical structures.

In semiconductor devices the movement and location of dopants and the inertness or reaction over interfaces of alternating layered structures are of particular interest. Most of the time, the relative distribution of impurities or lattice atoms after different sample treatments (ion implantation, epitaxy, annealing, etching, etc.) is of more importance than the actual quantitative concentration levels. This is where the depth information coupled with high sensitivity in the parts-per-million to parts-per-billion range, provided by dynamic SIMS, is of the utmost importance. The following examples originate from a wide spectrum of processes and problems encountered in the development of compound semiconductor materials and failure analysis of device production processes.

3.1 Impurities in starting materials and their effect on crystal growth

Bulk $Hg_{0.8}Cd_{0.2}Te$ crystals, grown by the solid state recrystallization (SSR) technique, are used for photoconductive infra-red detectors. It is essential that the background impurity levels in n-type material should be below 5×10^{14} cm^{-3} to ensure photoconductive response of the device. In developing (HgCd)Te material, several parameters may influence the purity of the grown material, such as quality of the starting material, quenching gas or the quartz ampule used for growth.

A series of SIMS analyses was performed on SSR-grown (HgCd)Te material using raw materials from several sources and employing different types of quartz [15]. The objective was to identify elements that dominate the background doping. After extensive sputtering (to obtain bulk information), both positive and negative spectra were recorded. The free carrier concentration in the sample was determined by Hall analysis [15]. A correlation between the carrier concentration and the relative Cl density was found. In Figure 1 the average ^{35}Cl to ^{130}Te count ratio is plotted as a function of the carrier concentration at 77 K. It was concluded that the source of the Cl contamination was a combination of the Cd starting material and the silica used, as well as the cleaning (etching) of the elemental starting material.

This example illustrates a useful way of using SIMS as a 'finger-printing' technique. The question still remains: what is the total concentration of Cl impurities? This can only be determined by quantitative SIMS, and is discussed later in the paper.

3.2 Ohmic contacts

Before a semiconductor material can be used in a device application, or in order to electrically characterize it, a low resistance or ohmic contact has to be made. In contacting to compound semiconductors, the metal or metal alloy may react with any of the constituents forming the

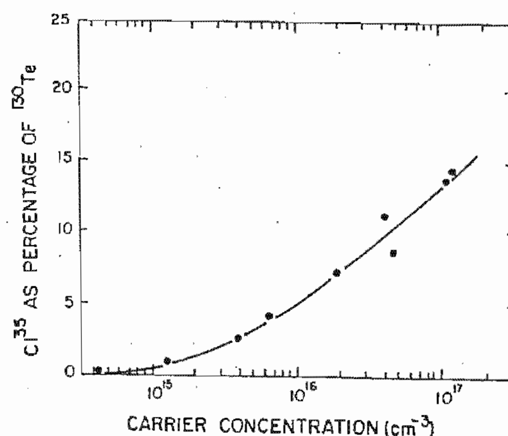

Figure 1 The Cl/Te count ratio in $Hg_{0.8}Cd_{0.2}Te$ determined by SIMS as a function of the free carrier concentration at 77 K.

compound, or diffuse into the crystal lattice.

Indium has been used for contacts on n-type (HgCd)-Te. Abnormally high carrier concentrations measured in the material using such contacts have led to the suspicion that indium diffuses into the material. SIMS analysis of evaporated indium contacts on (HgCd)Te [16] showed indium contamination deep into the bulk of the material as well as laterally in regions remote from the contacts. A schematic diagram of the sample showing the different spots profiled, as well as the SIMS indium depth profiles, are shown in Figure 2.

The indium depth profile through the evaporated indium contact shows a displacement of the $^{115}In^{+}$ maximum from the sample surface. To study this effect, the nature of the In–(HgCd)Te contact as regards oxides and other chemical species has been examined [17]. The condition of the surface after pre-contacting cleaning plays a major role in the final distribution of the species found. Chemo-mechanical polishing or etching, for example, yields Cd- and Te-rich surfaces respectively. Native oxides form on such a surface. When the indium is evaporated on top of this surface, it reacts with the oxide and semiconductor species present, and a layered structure is observed with SIMS depth profiles.

The oxide species found to be present using SIMS has been explained by a thermodynamically feasible model. This model is illustrated in Figure 3 and shows the complexity of the contact formation resulting when indium is used. The oxides explain the displacement of the $^{115}In^{+}$ signal from the surface in Figure 2 (case 1).

Ohmic contacts for source and drain metallization for GaAs MESFETs are mostly based on AuGe and Ni. Although this contact is widely used, its alloying behaviour with GaAs is not yet fully understood. One model, though, argues that Ge as a group IV element replaces Ga in the sublattice of GaAs to form an n^{+} region and in this way an ohmic contact is obtained.

The effect of an interfacial layer of Ni between the AuGe and GaAs on the Ge distribution in the contacts annealed at 450°C for 5 min was investigated [18, 19]. Figure 4 shows the SIMS depth profiles of a sample where no interfacial Ni layer was used, and one where 100 nm Ni was first deposited on the GaAs, together with a schematic representation of the most dominant elements in certain regions. These conclusions were supported by AES and Rutherford back-scattering analysis [20]. Without establishing the mechanism of ohmic contact formation uniquely in this experiment, we maintain that the second structure favours the formation of a lower resistance ohmic contact, since more Ge is present at the metal–GaAs interface. Transmission electron microscopy studies have also pointed out that low-resistance contacts are formed when a ternary Ni_2GeAs phase exists at the interface [21], a very likely situation in the sample with the interfacial Ni layer.

The non-uniformity of annealed ohmic contacts is one of the biggest problems encountered, and it is believed to be due to a thin oxide layer on the surface of the GaAs. In order to circumvent this effect, it was proposed that ion beam mixing be used to disperse the interfacial layer [22]. The morphology of contacts which have been subjected to an ion implantation step has shown great improvement [23]. SIMS and AES have been used to study (Ni–AuGe)

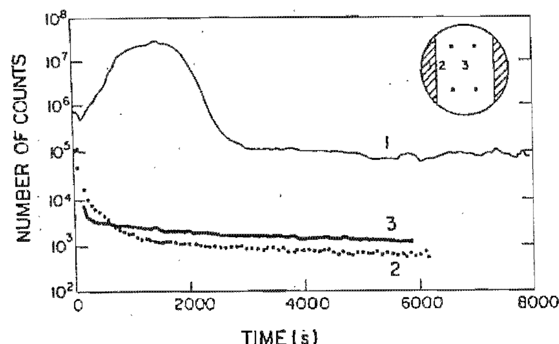

Figure 2 Schematic diagram of samples on which sputter depth profiles were done. The different spots profiled are numbered 1, 2 and 3. Hatched areas are contact areas. Shown are SIMS profiles of In on indium contact (curve 1), next to it (curve 2), and remote from it (curve 3).

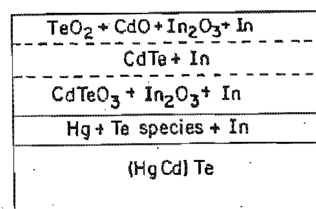

Figure 3 Proposed model for oxide formation on In–(HgCd)-Te (from ref. [15]).

contacts deposited onto GaAs after subsequent argon ion implantations [24]. From the depth profiles obtained it follows that the ion implantation step prior to annealing enhances the interdiffusion of the metallization layers.

3.3 Quantum well structures

Band-gap engineering in semiconductors is traditionally done by controlling the concentration of one of the elements in a ternary, or two elements in a quaternary compound. A novel way of confining electrons to certain regions is by introducing a new periodicity in the crystal by growing very thin (a few atoms thick) layers of alternate composition or doping. Two such families of new semiconductors are quantum wells and superlattices.

Typical quantum well structures of alternating GaAs and $Al_xGa_{1-x}As$ layers, with GaAs well thicknesses as low as 1 nm, are being grown by MBE and OMVPE techniques. The depth resolution of SIMS depth profiles through these structures are limited by atomic mixing effects and non-uniform sputtering within the analysed area due to inhomogeneous primary ion current density. It has been reported that for low energy ion bombardment, glancing incidence of the primary beam, careful focussing of the ion beam, cluster ion detection and heavy bombarding species reduce recoil mixing and increase depth resolution [25, 26]. Figure 5 shows the SIMS depth profile of an OMVPE quantum well structure consisting of alternating layers of GaAs and $Al_{0.3}Ga_{0.7}As$ grown in our laboratory. The AlGaAs layer thickness was kept constant at 60 nm, while the GaAs quantum well thicknesses were 2.5, 3.75, 5.0, 6.25, 7.5, 10, 12.5 and 15 nm respectively. In this run a specific switching sequence

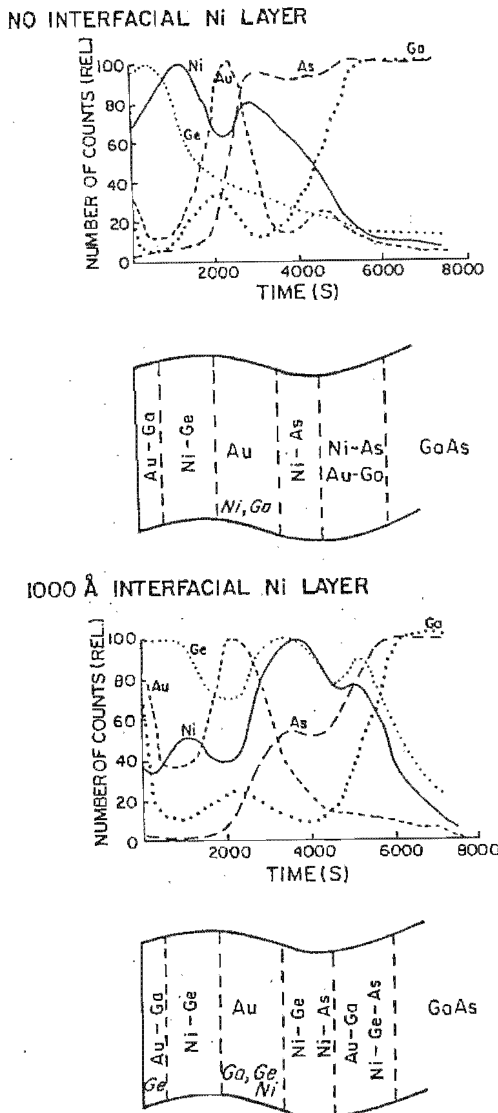

Figure 4 The SIMS depth profiles together with a schematic interpretation of the most dominant regions for a Ni–AuGe–GaAs and Ni–AuGe–Ni–GaAs contact system.

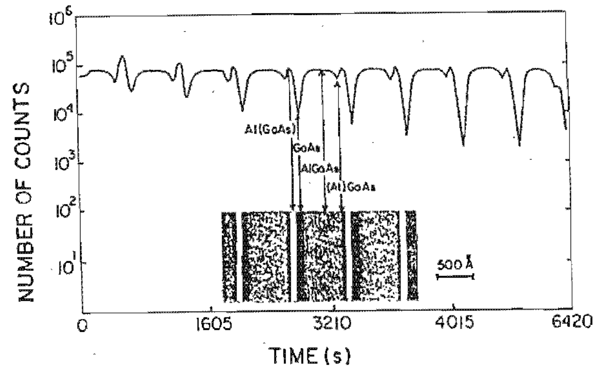

Figure 5 SIMS depth profile of the Al_2 cluster ion through a GaAs–Al_xGa_{1-x}As quantum well structure compared with a cross-sectional TEM micrograph.

was investigated and pauses in the growth sequence were varied in an attempt to calibrate growth parameters.

The SIMS depth profile of the $^{54}Al_2^+$ cluster ion was obtained using a micro-focussed gallium beam with 5 keV energy and 5 nA cm^{-2} beam current density, incident at 45°, rastered over an area of 400 × 400 μm^2, with electronic gating of the secondary signal from 20% of this area. The dynamic range between the maximum of the AlGaAs layer and the minimum of the GaAs layer varied from less than one order of magnitude for the 2.5-nm quantum well, to almost two orders of magnitude for the 15-nm quantum well.

It is clear that a periodic sequence of AlGaAs, the GaAs quantum well, Al-rich AlGaAs and Al-poor AlGaAs is obtained in the SIMS profile. Comparison with cross-sectional TEM shows the AlGaAs and Al-rich AlGaAs as the lighter contrast, with the GaAs and Al-poor AlGaAs as the darker contrast. The power of combining other structural analysis techniques with SIMS to understand some of the features obtained is clearly illustrated by this example.

3.4 Failure analysis

Bonding failure on ISO–CMOS integrated circuits has been investigated with SIMS. It was found that gold wires that were bonded to aluminium bonding pads, lifted off. In order to make them stick, the bonding pressure had to be increased to such an extent that the chips broke. It is well known [27] that Si dissolves in Al, when in direct contact, causing pitting or void formation under the contact, as well as hardening of the Al. Since this effect was suspected in this case, the amount of Si in the Al bonding pad was determined with SIMS.

A micro-focussed 10-keV Ga beam at 1 nA cm^{-2}, incident at 45°, and rastered over 60 × 60 nm^2, was used to profile for ^{27}Al and ^{29}Si. The amount of Si is expressed as a percentage of the ^{27}Al signal (and not atomic %). A CMOS chip was taken as a standard, since the Al is not in contact with poly-crystalline Si as in the case of the ISO–CMOS. The sputtered Al contained 1% Si. As illustrated in Figure 6, no bonding problems occurred on a chip having less than 3% Si in Al. However, above 3% but below 6% some bonds failed, and above 6% all bonds were unsuccessful.

It is believed that Al pads on which no bonding could be achieved were hardened by the increased amount of Si dissolved. The problem arose by having too thin a layer of Al metallization. For thicker Al bonding pads the Si does not diffuse to the bonding interface during subsequent heat treatments.

4. Quantitative SIMS

The fundamental analytical problem in SIMS is that of relating the composition of the sputtered ion flux to the composition of the sample analysed. Ionization efficiencies vary over several orders of magnitude for different elements, and likewise vary with the chemistry of the sputtered surface; thus, ion signals often vary non-linearly with concentration. Quantification of SIMS thus requires a set of standards for each new matrix to be analysed. Relative sensitivity factors (RSFs), relating the sensitivity for a specific element to the major matrix ion, are to be determined. The easiest way to prepare such samples is to implant known amounts of ions for

which RSFs are required [28].

The correlation found between the relative Cl content in $Hg_{0.8}Cd_{0.2}Te$ determined by SIMS and the residual carrier concentrations determined by Hall analysis (see discussion on impurities in starting materials and Figure 1) still needed quantitative numbers to determine the activation of impurities. The RSF for Cl was determined using a set of Cl-implanted (HgCd)Te standards at different energies (200, 300 and 400 keV) and a dose of 5×10^{13} cm^{-2} [14].

Figure 7 shows the residual Cl, now in atomic concentration, as a function of free carrier concentration. From the figure it follows that for the residual Cl impurities the activation is very low (between 3.1% and 15.7%) during SSR crystal growth. The material used in this study was compensated [15], which is believed to be the reason for the low activation percentage.

5. Conclusion

The broad range of elemental and chemical information obtained in semiconductor technology development with dynamic SIMS has been demonstrated. The immense sensitivity, coupled with the high lateral resolution, makes SIMS unique in the semiconductor characterization environment. New demands for smaller dimensions in device fabrication and enhanced complexity in heterojunction structures will always push for improvements in the limits of depth resolution and dynamic range.

In production environments, SIMS forms a powerful tool for failure analysis in many processes. Since there are inherent problems with a technique based on a sputtering process, it is always advantageous to combine it as far as possible with other surface and subsurface techniques.

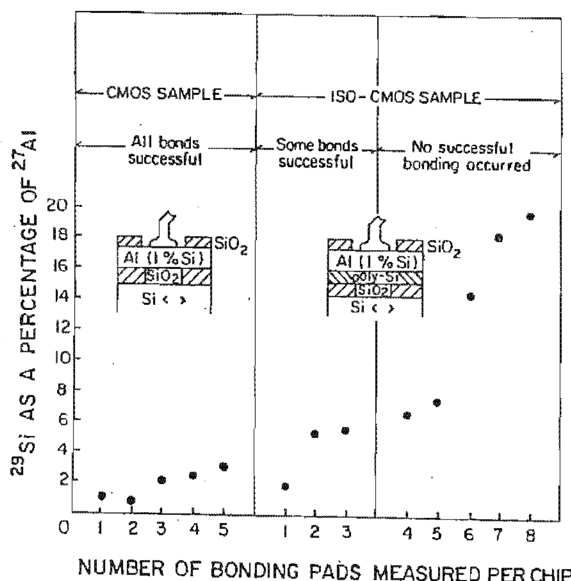

Figure 6 Schematic representation of CMOS and ISO-CMOS devices, together with the SIMS measurement of the Si signal as a percentage of the Al signal, from a number of bonding pads as indicated.

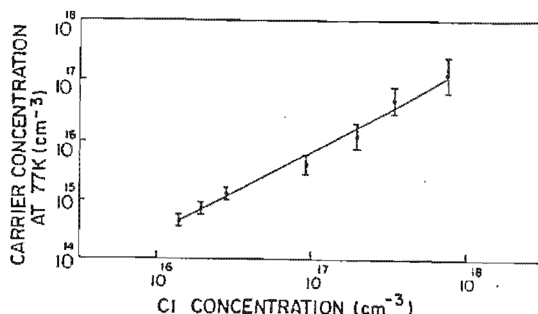

Figure 7 Residual Cl impurities measured by SIMS in $Hg_{0.8}$-$Cd_{0.2}Te$ as a function of the free carrier concentration determined by Hall analysis at 77 K.

Acknowledgements

The authors thank all their colleagues who, through numerous interactions in the past, have made this compilation of SIMS applications in the semiconductor environment possible. We also thank Dr J.C.Q. Fletcher, Dr M.W. Rautenbach and Mr R. Thavar of the Division of Microelectronics and Communications Technology (DMCT), CSIR, for growing the quantum wells, Dr J. Neethling of the Department of Physics, University of Port Elizabeth, for doing the cross-sectional TEM, and Mr M.A. Marais of DMCT for many discussions on the quantification of Cl in (HgCd)Te. We thank SAMES (Pty) Ltd for providing us with the integrated-circuit samples to illustrate the use of SIMS in failure analysis. In particular we are grateful to Mr J. Wegman for maintaining the SIMS instruments.

References

[1] P.R. Boudewijn and H.T.F. Janssen, Fresenius' Z. Anal. Chem. 329 (1987) 215
[2] H.W. Werner and A.E. Morgan, Treatise on Analytical Chemistry, Vol. 10, Part 1, eds. I.M. Kolthoff and P.J. Elving (Wiley, New York, 1983) pp.339–438
[3] A. Lodding and H. Odelius, Mikrochim. Acta Suppl. 10 (1983) 21
[4] H.W. Werner and R.P.H. Garten, Rep. Prog. Phys. 47 (1984) 221
[5] N. Winograd, Prog. Solid State Chem. 13 (1982) 285
[6] P. Williams, Appl. Surf. Sci. 13 (1982) 241
[7] P. Williams, Ann. Rev. Mater. Sci. 15 (1985) 517
[8] R.E. Honig, J. Appl. Phys. 29 (1958) 549
[9] R.E. Honig, Secondary Ion Mass Spectrometry V, eds. A. Benninghoven, R.J. Colton, D.S. Simons and H.K. Werner (Springer-Verlag, Berlin, 1986) pp.2–15
[10] H. Liebl, J. Appl. Phys. 38 (1967) 5277
[11] W.H. Gries, E.D. Rawsthorne, H.J. Strydom and K.N. Woods, Int. J. Mass Spectrom. Ion Phys. 59 (1984) 339
[12] K.N. Woods, H.J. Strydom, J.W. Wegman and W.H. Gries, Int. J. Mass Spectrom. Ion Phys. 62 (1984) 335
[13] H.J. Strydom, W.O. Barnard and A.P. Botha, S. Afr. J. Sci. 84 (1988) 685
[14] A.P. Botha, H.J. Strydom and M.A. Marais, Nucl. Instrum. Methods Phys. Res. B 35 (1988) 420
[15] M.A. Marais, H.J. Strydom, J.H. Basson, D.E.C. Rogers and H. Booyens, J. Cryst. Growth 88 (1988) 391
[16] C.M. Demanet and H.J. Strydom, Phys. Status Solidi A 90 (1985) K131
[17] C.M. Demanet, H.J. Strydom, J.H. Basson, A.P. Botha and C.M. Stander, Appl. Surf. Sci. 25 (1986) 279
[18] E. Relling, M.Sc. thesis, University of the Witwatersrand, Johannesburg (1986)
[19] E. Relling and A.P. Botha, Appl. Surf. Sci. 35 (1988/89) 380

[20] A.P. Botha and E. Relling, Mater. Res. Soc. Symp. Proc. 54 (1986) 421

[21] T.S. Kuan, P.E. Batson, T.N. Jackson, H. Rupprecht and E.L. Wilke, J. Appl. Phys. 54 (1983) 6952

[22] C.J. Palmstrøm, K.L. Kavanagh, M.J. Hollis, S.D. Mukherjee and J.W. Mayer, Mater. Res. Soc. Symp. Proc. 39 (1985) 473

[23] W.O. Barnard, J.B. Malherbe and B.M. Lacquet, Appl. Surf. Sci. 31 (1988) 437

[24] W.O. Barnard, H.J. Strydom, M.M. Kruger, C. Schildhauer and B.M. Lacquet, Nucl. Instrum. Methods Phys. Res. B 35 (1988) 238

[25] A. Brown, J.A. van den Berg and J.C. Vickerman, Surf. Interface Anal. 9 (1986) 309

[26] H.J. Strydom, W.O. Barnard and A.P. Botha, Rep. SMAT 41, Nat. Inst. Mater. Res., CSIR, Pretoria, South Africa (1984)

[27] J.M. Poate, K.N. Tu and J.W. Mayer, Thin Films – Interdiffusion and Reactions, eds. J.M. Poate, K.N. Tu and J.W. Mayer (Wiley, New York, 1978) pp.14–25

[28] L.E. Lapides, G.L. Whiteman and R.G. Wilson, Thin Films and Interface II, eds. J.E. Baglin, D.R. Campbell and W.K. Chu, Vol. 25, Proc. Mater. Res. Soc. (Elsevier, New York, 1984) pp.657–662

Second International Workshop on Physics and Modern Applications of Lasers.
6-14 September 1993, Harare, Zimbabwe.

TIME-OF-FLIGHT MASS SPECTROMETRY OF SOLIDS, GASES AND BIOPOLYMERS USING LASER IONIZATION/DESORPTION

Hendrik J Strydom, Hendrik G C Human and Christo R Green
Atomic Energy Corporation of South Africa, Pelindaba, Pretoria

Egmont R Rohwer
Department of Chemistry, University of Pretoria, South Africa

ABSTRACT

Time-of-flight mass spectrometry (TOF-MS) employs relatively simple, inexpensive instruments with high sensitivity and virtually unlimited mass range. Commercial spectrometers have been available since the early 1960's. Applications were found in vaporization and analysis of coals, elemental analysis, isotope ratio measurements and multiphoton ionization processes of organic molecules.

With the advent of matrix-assisted laser desorption (MALD) in 1988, molecular weights of biological macromolecules such as proteins, carbohydrates and oligonucleotides, exceeding 300 kDa, have been recorded. Initial success with oligonucleotide mixtures has encouraged future contributions in mapping the human genome.

An overview of the present status of the TOF-MS technique will be given. Performance characteristics of locally designed and manufactured spectrometers will be discussed. Examples in the fields of laser desorption of metals, multiphoton ionization of UF_6 and matrix-assisted laser desorption of high mass proteins will be presented.

INTRODUCTION

At the Atomic Energy Corporation of South Africa, time-of-flight mass spectrometry has been employed as a diagnostic tool in the laser isotope enrichment of uranium. From this established technology base, commercial instruments for analysis of solids and biopolymers have now become available.

Time-of-flight Mass Spectrometry (TOF-MS) operates on the principle that a packet of ions of different

mass to charge *(m/z)* ratios is rapidly accelerated through a constant electrical field V to a fixed kinetic energy. The ions will posess individual velocities u, which are inversely proportional to the square root of the m/z ratio:

$$u = \sqrt{\frac{2zV}{m}}$$

Allowing the ions to traverse a fixed distance L to the detector, they disperse in time according to their m/z ratio, the lightest ions, having the highest velocity, reach the detector first. The time-of-flight is then given by

$$TOF = \frac{L}{U} = \sqrt{\frac{L^2}{2V}} \cdot \sqrt{\frac{M}{Z}}$$

To utilize this time-of-flight dispersion the ion packets must be pulsed into the flight tube. Each packet of ions detected yields a series of output pulses at various mass dependent arrival times within the TOF time scale, typically less than 1ms. Hence each packet or ionization event yields a complete mass spectrum. The mass range is limited only by the ability of heavy ions to be created from the sample, the time available for collection and the capability of the detector to detect them.

TOF-MS has a high transmission capability and high sensitivity for single event monitoring. Since the ionization region is not confined by the presence of electric or magnetic sectors, the instrument can easily be interfaced to a whole range of analytical facilities.

TOF-MS has the following advantages:

- Ideal where ionization is pulsed/spatially confined;
- Produces a complete mass spectrum of each ionization event;
- Has high transmission;
- Has low sample consumption;
- Virtually unlimited mass range;
- Easy mass calibration;
- Simple mechanical design; and
- Low cost.

INSTRUMENTATION

Figure 1a is a diagram of a linear TOF-MS with a laser desorption ion source. The initial packet of ions is produced by a pulse of laser light absorbed by the sample. These ions are extracted and accelerated by the static electric field between the planar electrodes. The ions then pass through a field-free region and arrive at the front plane of the detector. The acceleration voltages are typically 1-40 kV (positive or negative polarity) and flight path range from 0.1 to 3m.

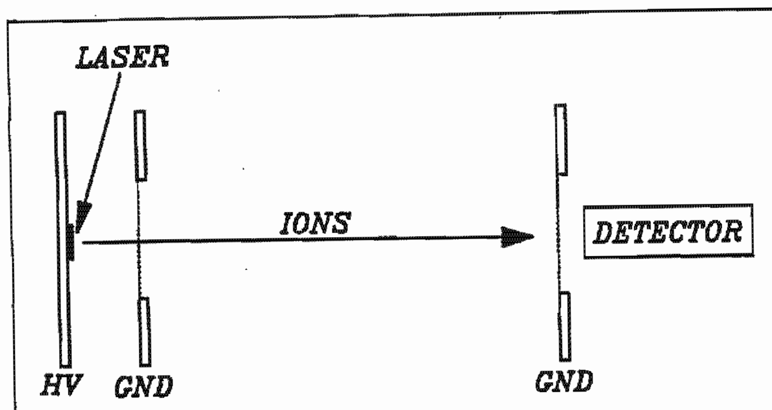

Fig. 1(a) Linear TOF mass spectrometer.

The performance of a TOF mass spectrometer is determined by its mass accuracy and mass resolution. Mass resolution

$$R = \frac{m}{\Delta m}$$

is a measure of an instrument's capability to produce separate signals from ions with adjacent masses. The practical limitations of the mass resolution are the finite ion production time, initial velocity distribution and the spatial extent of the ionized volume. Initial velocity distributions can be reduced by using a reflectron instrument as shown in Figure 1b. In this instrument, an ion mirror is placed in the flight path of the ion packets. This leads to increased mass resolution for all stable ions in the spectrum.

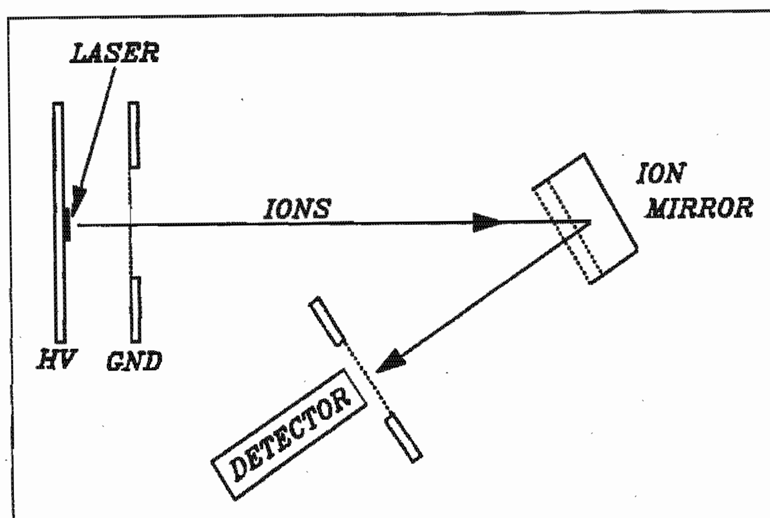

Fig. 1(b) Reflectron TOF mass spectrometer.

Laser desorption sources use pulsed lasers with pulse durations of less than 100 ns. UV lasers as well as IR lasers have been employed. The light is focused and passed through a window into the mass

spectrometer.

To be detected, the ions produced must be converted into electrons at a conversion electrode. These electrons are then used to start the electron multiplication cascade in an electron multiplier. The surfaces used for this conversion is either copper-beryllium or the lead glass surface of a microchannel plate. The transient signal produces by a single laser shot can be viewed directly on an analog oscilloscope and stored in a transient digital oscilloscope. Multiple shots are used to improve the signal-to-noise ratio and the peak shapes, thereby increasing the accuracy of the mass determination.

APPLICATIONS

MLIS OF URANIUM

The differences in isotopic mass of a particular atom in a molecule affects the frequencies of vibrations and rotations of a molecule and therefore also its infrared absorption spectrum. Spectral absorption lines of a low pressure gas are very narrow, so that even a small isotopic shift allows selective excitation

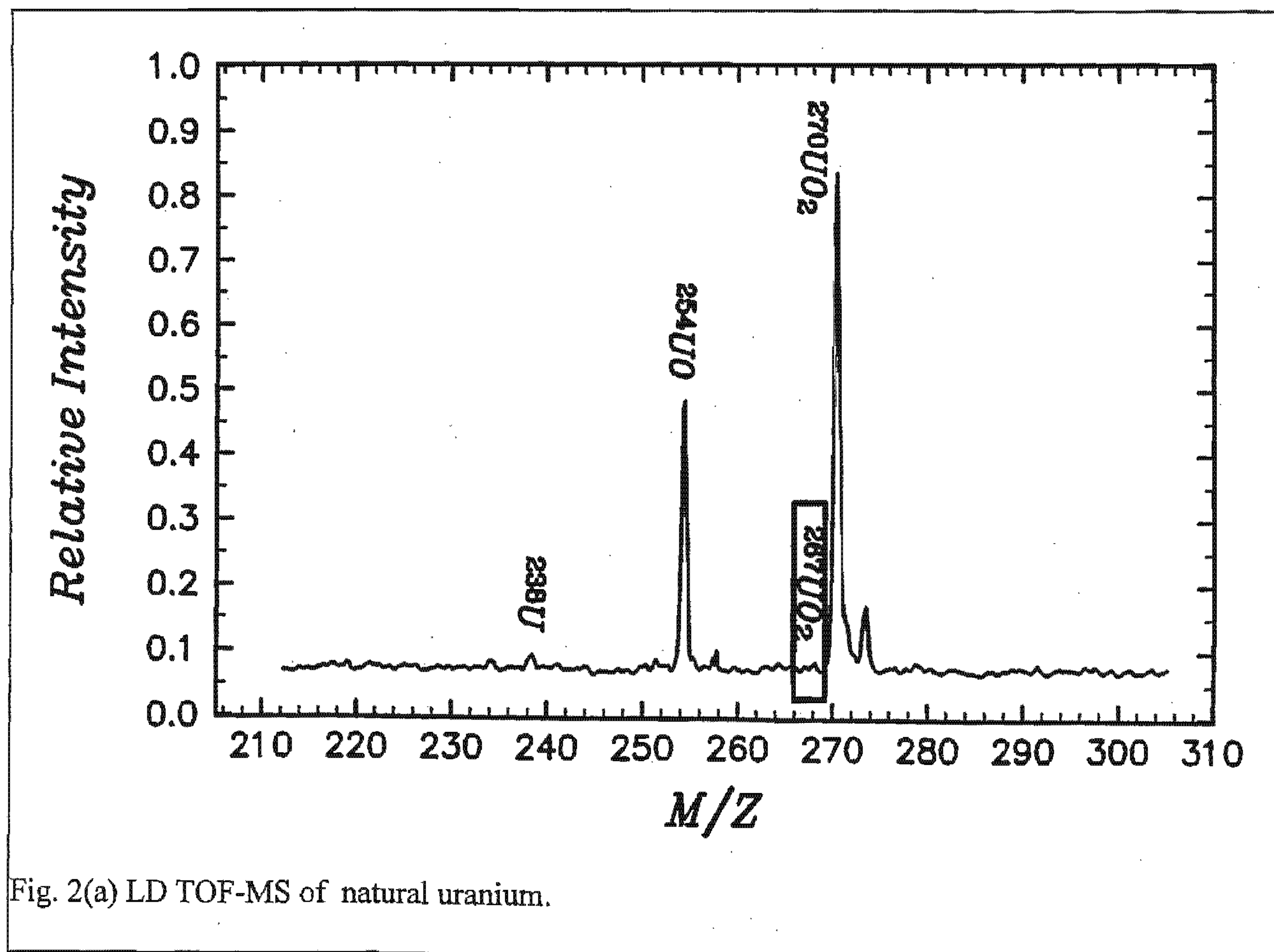

Fig. 2(a) LD TOF-MS of natural uranium.

of the chosen isotope by an appropriate infrared excitation source.

The isotopic enrichment of ^{235}U for power generation in nuclear reactors is the most economically important objective at the AEC. Molecular Laser Isotope Separation of uranium is based on multiple photon isotope selective excitation of UF_6 vibrational levels by resonant IR lasers. Excited UF6 molecules are then radiated with intense IR lasers of a different wavelenght to induce dissociation to UF_5, which precipitates as a solid.

At the AEC, UF_6 gas is flow-cooled to populate the ground states where isotope differences in absorption spectra can be utilized to selectively excite the ^{235}U isotope containing molecules. In-line time-of-flight mass spectrometry is used to optimize irradiation parameters for optimum selectivity at acceptable cut quantities, while a separate desorption TOF mass spectrometer can be used to analyse collected material. Figures 2a and b show spectra for natural and enriched standards. The laser desorption spectrum of the uranium product shows distinct peaks for UO, UF, UO_2, UF_2, UO_3 and UF_3 species. The ratio for 238:235 for the UO_2 peaks gives the natural ratio of 140:1. For the enriched standard the increase in ^{235}U can clearly be seen in figure 2b.

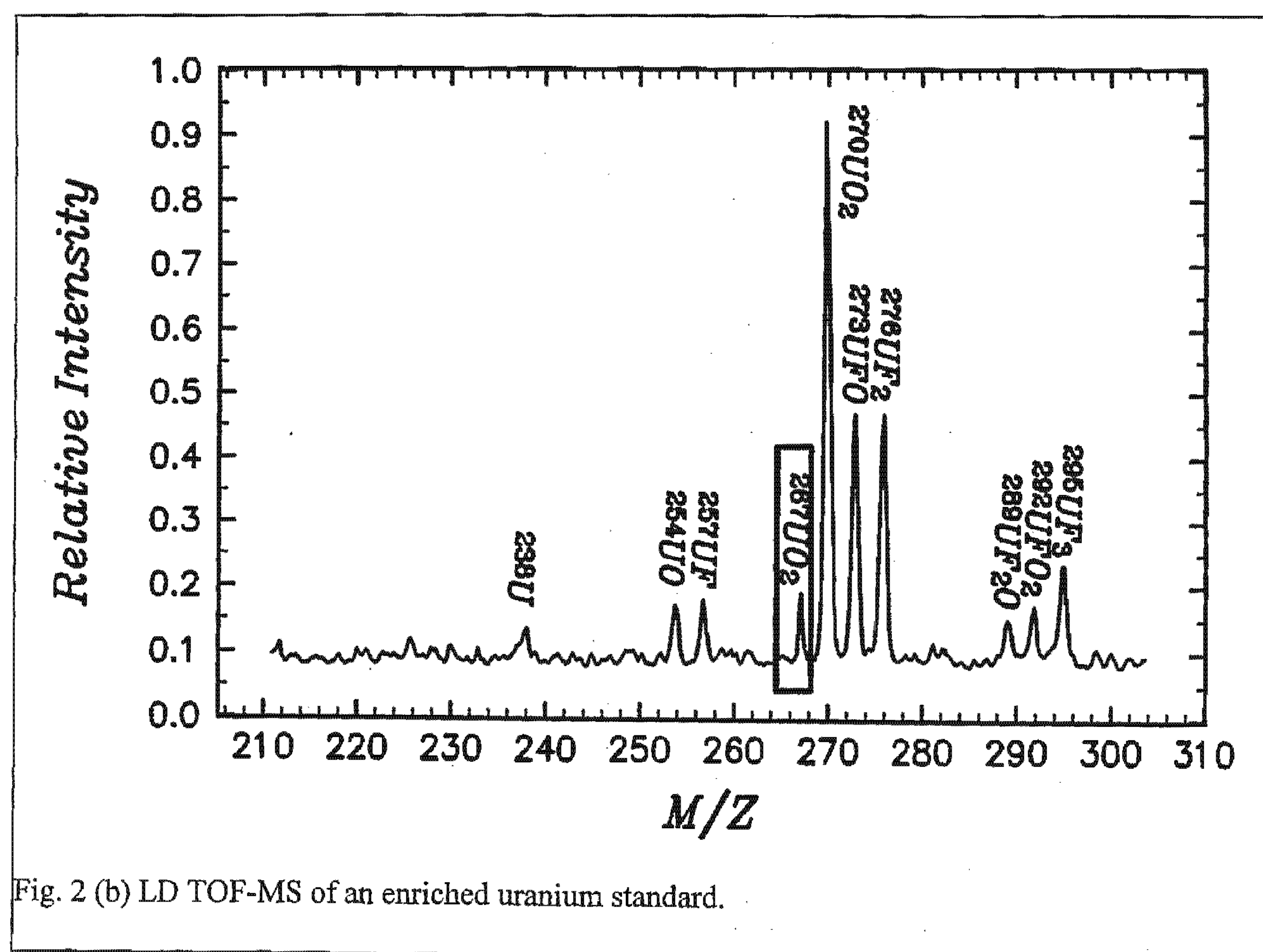

Fig. 2 (b) LD TOF-MS of an enriched uranium standard.

LASER DESORPTION OF TIN

The AEC launched its first commercial laser desorption TOF mass spectrometer in August 1992. The mass spectrometer enables isotopic and elemental information to be determined from bulk solids, near-surface layers, as well as gases. The instruments consist of either a nitrogen (337nm) laser or a Nd:YAG (1064, 532, 355 and 266nm) laser. A choice between a 1.2m linear and 2m (effective length) reflectron spectrometer is available.

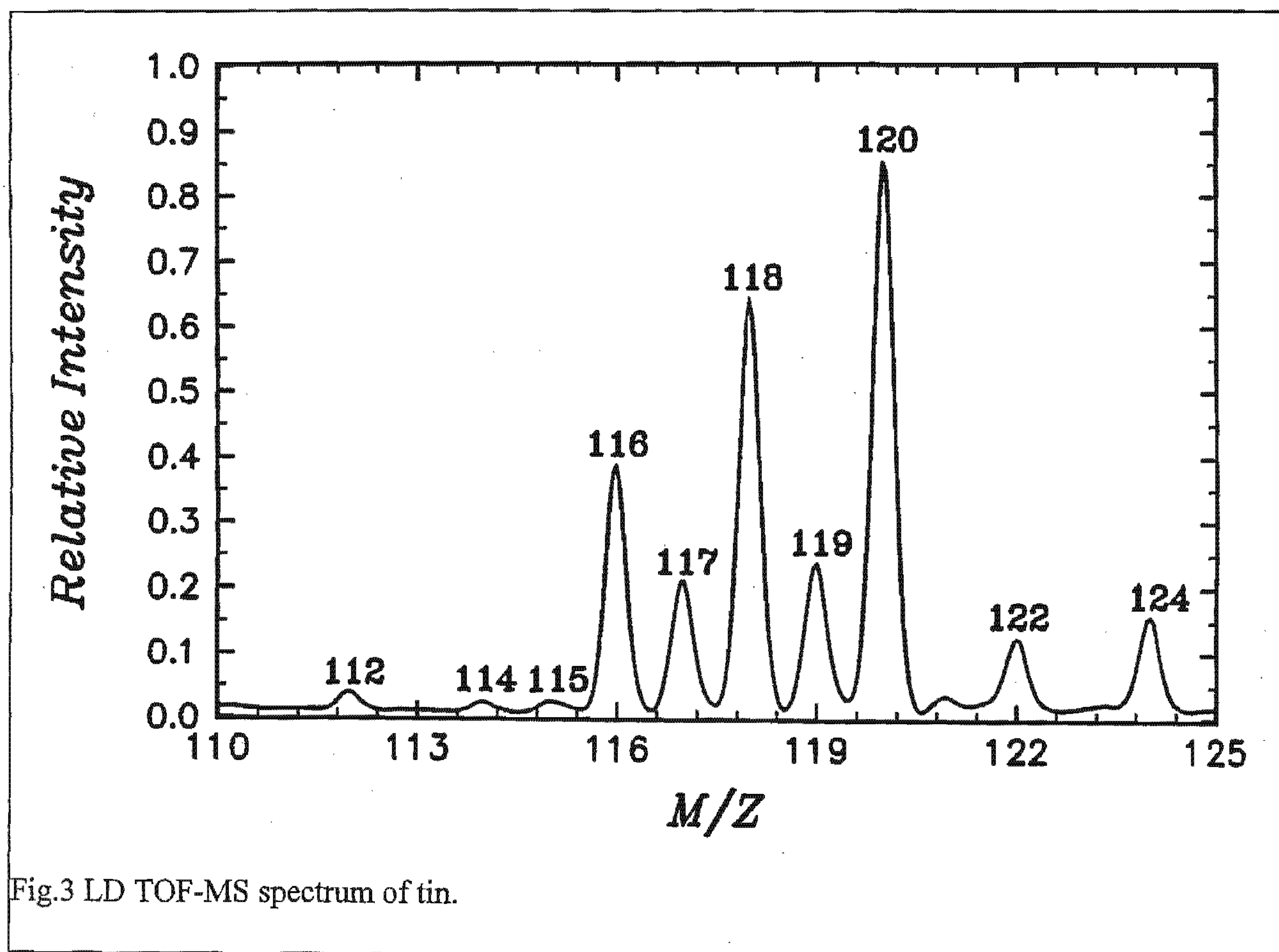

Fig.3 LD TOF-MS spectrum of tin.

Many of the limitations of isotopic abundance measurements in mass spectrometers arise from the requirement that a complete mass spectrum should be obtained from a single ionization event. The TOF-MS is well suited for this purpose. The reproducibility of measured isotopic abundance ratios of

the same element is much better than the reproducibility of relative elemental abundancies. This is because inter-isotope effects in the ionization process are much less sensitive than inter-elemental effects to variables such as laser power deposition.

Isotopic analysis of tin was performed on a commercial solder containing ~10% tin. Figure 3 shows a mass spectrum of the ten isotopes. The peak areas were measured. Table 1 gives a comparison of the natural isotopic abundances vs the laser desorption measurements. These values are in good agreement with the published values.

Sn (amu)	Natural isotopic abundance (%)	LD TOF-MS measured (%)
112	0.97	1.1
114	0.65	0.7
115	0.36	0.5
116	14.5	14.5
117	7.7	7.9
118	24.2	24.4
119	8.6	8.6
120	32.6	32.5
122	4.6	4.2
124	5.8	5.6

TABLE 1: Laser desorption TOF-MS measured values for the isotopic abundances of natural

MALD OF PROTEINS

In Matrix-Assisted Laser Desorption (MALD) a low concentration of analyte molecules is embedded in either a solid or a liquid matrix consisting of a small, highly absorbent species. The matrix therefore

retains the property of efficient and controllable energy transfer, while the analyte molecules are spared from excessive energy that would lead to fragmentation. A laser pulse with sufficient irradiance causes the mixture of matrix and analyte molecules to undergo gas phase transition. Suitable matrices enhance quasi-molecular ion formation of the analyte molecules by proton transfer reactions in the gas phase.

Figure 4a shows an MALD spectrum of horse heart cytochrome C (HHCC) with molecular mass 12360 amu. The doubly charged peak can be seen at 6280 amu. The sensitivity of the technique is shown in fig. 4b where 75 femtomoles of HHCC could still be measured with ease. A high resolution scan of the peak at 12360 is shown in 4c. A mass resolution of 320 was measured. The mass accuracy can be seen in 4d where a known mass standard bovine lung protein at 6500, was used as internal mass calibration. As a result the HHCC peaks is measured at 12364. This represents a mass accuracy of 0.03%.

ACKNOWLEDGEMENTS

The authors would like to acknowledge helpful discussions and technical assistance with colleques from the Laser Programs at the AEC.

CONCLUSION

Time-of-flight mass spectrometry has been around for some time now and has been plagued by poor mass resolution and unreliable ionization sources. Recent improvements in lasers, the introduction of the reflectron for improved mass resolution and the advent of matrix-assisted laser desorption of proteins has established TOF-MS as an indispensable analytical tool.

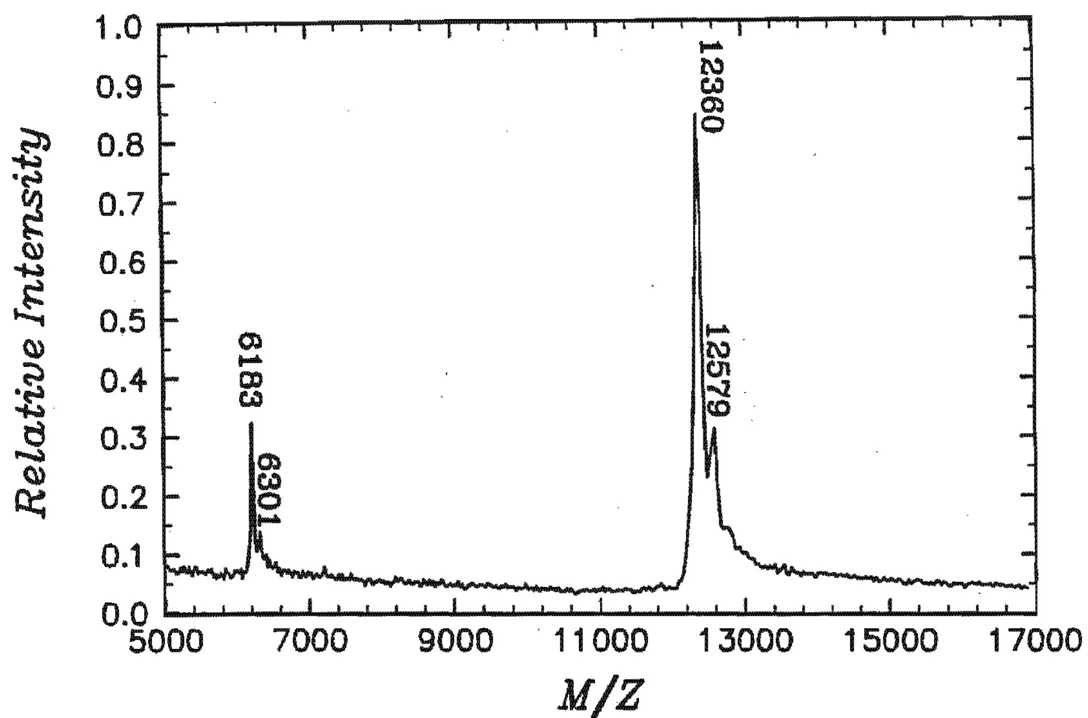

Fig. 4 (a) MALD TOF-MS of HHCC.

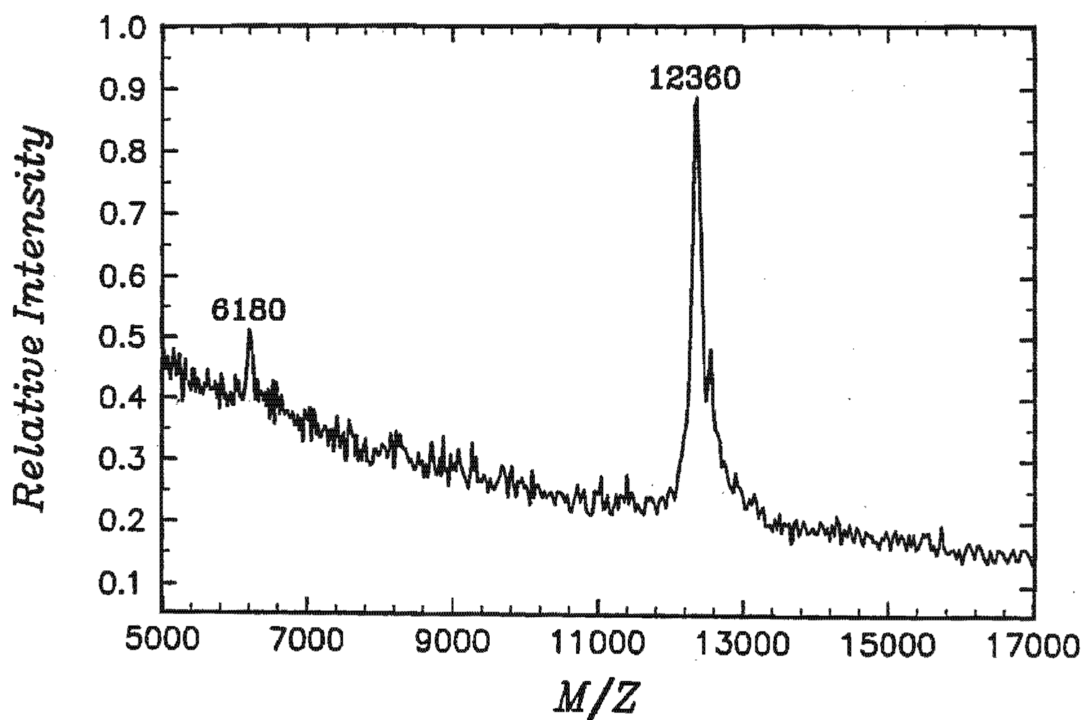

Fig. 4 (b) MALD TOF-MS of 75 Femtomole HHCC.

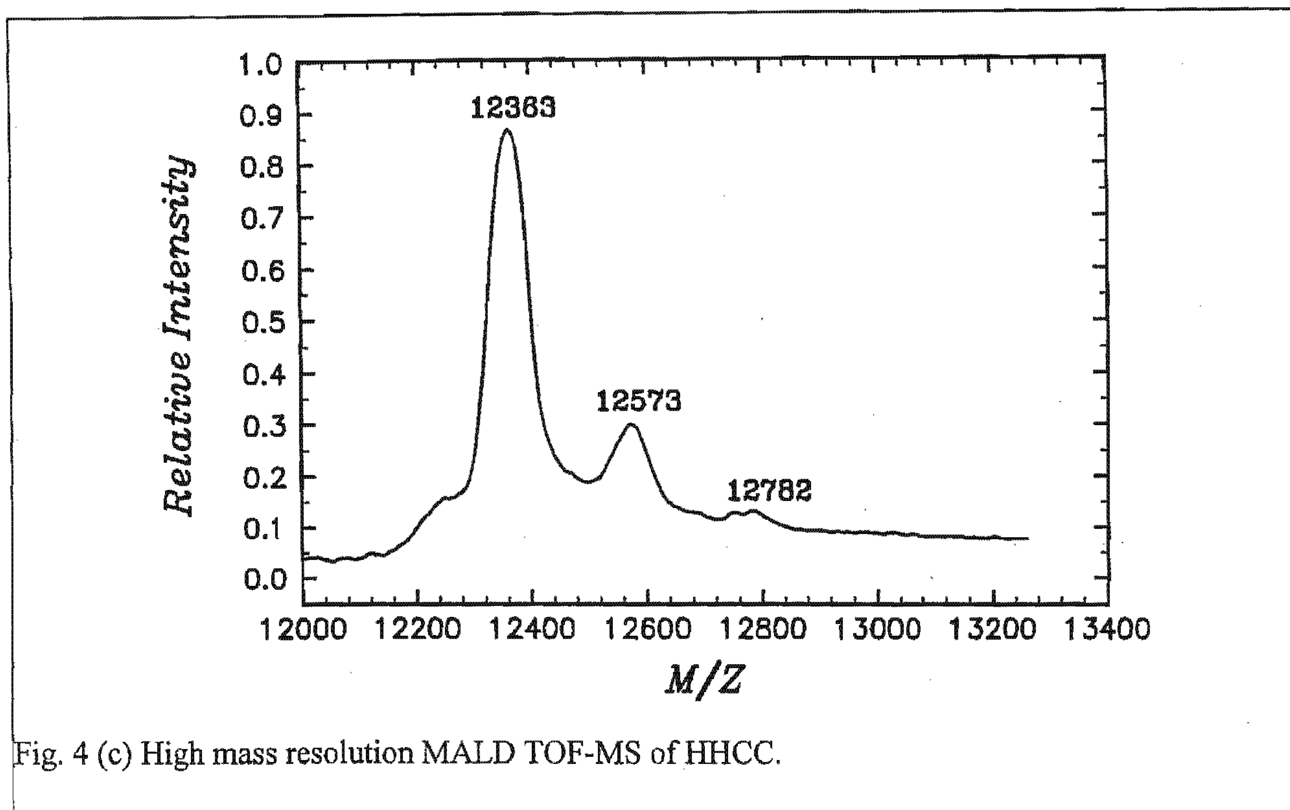

Fig. 4 (c) High mass resolution MALD TOF-MS of HHCC.

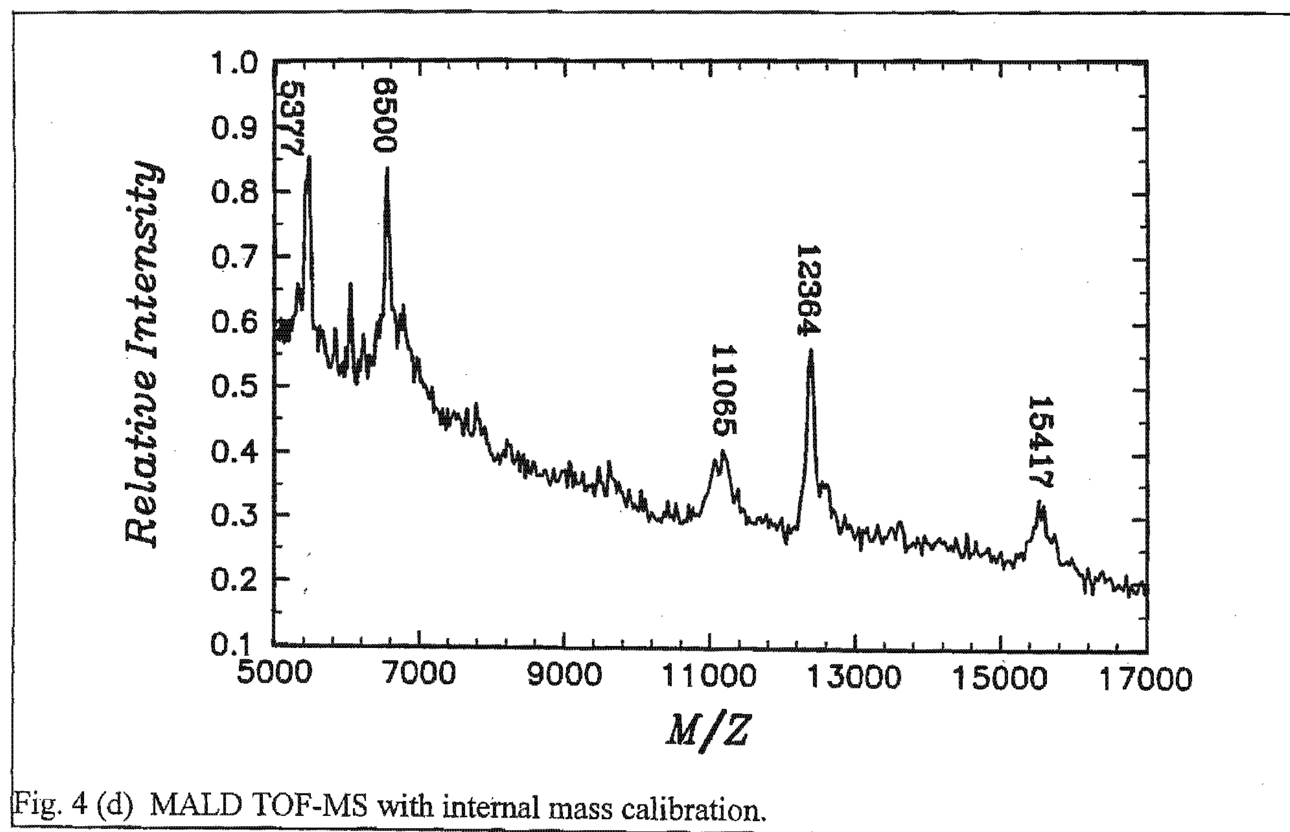

Fig. 4 (d) MALD TOF-MS with internal mass calibration.

Continuously tunable CO_2 MOPA chain for a molecular laser isotope separation pilot plant

Lourens R. Botha
Christo J. Liebenberg
Atomic Energy Corporation of South Africa
Laser Research
P.O. Box 582
Pretoria 0001, South Africa

Hubertus M. von Bergmann
Laser Systems and Applications (Pty) Ltd.
31 Wellington Road
Irene 1675, South Africa

François J. Prinsloo
Einar Ronander
Hendrik J. Strydom
Atomic Energy Corporation of South Africa
Laser Research
P.O. Box 582
Pretoria 0001, South Africa

Abstract. A continuously tunable 3-atm mixed isotope CO_2 oscillator power amplifier (MOPA) chain is developed for a molecular laser isotope separation pilot plant. The characteristics of this laser such as tunability, bandwidth, and output energy are reported. A closed loop gas flow system with a catalyst is employed and its performance is reported.

Subject terms: CO_2 lasers; isotope lasers; continuously tunable; closed loop gas flow systems; narrow bandwidths.

Optical Engineering 33(9), 2861–2865 (September 1994).

1 Introduction

A continuously tunable CO_2 laser was developed for a pilot molecular laser isotope separation (MLIS) plant. MLIS utilizes the selective excitation of the $^{235}UF_6$ isotope,[1] and for this plant, a continuously tunable TEA CO_2 laser capable of operating at pulse repetition rates of up to 50 Hz with an output energy of a few hundred millijoules per pulse in the TEM_{00} mode was required. Furthermore, the bandwidth of the laser had to be less than 1 GHz. This system was to be used in conjunction with a 1-atm TEA CO_2 laser to produce 16-μm radiation via a four-wave mixing process in a multipass Raman cell. The Raman medium was parahydrogen cooled to liquid nitrogen temperature.

Continuous tunability of a CO_2 laser can be achieved by utilizing the pressure broadening of the CO_2 lines.[2] There are a number of technical problems associated with high-pressure CO_2 lasers. The most obvious of these are (1) the high voltages required, typically 10 to 14 kV/cm atm; (2) the difficulty of obtaining a stable discharge; (3) the design and manufacturing of the pressure vessel; (4) the pumping of the high-pressure gas; and (5) the energy required to obtain a specific small-signal gain value that is directly proportional to the pressure. It is, therefore, simpler and cheaper to build a high-repetition-rate low-pressure TEA CO_2 laser. The problem is to generate acceptable continuous tunability at a reduced pressure. One solution is to use an isotopic mixture of $^{12}C^{16}O_2$, $^{12}C^{18}O_2$, and $^{12}C^{18}O^{16}O$. Gibson, Boyer, and Javan[3] investigated such an isotopic mixture and reported continuous tunability at pressures of a half to a quarter of that achieved with a single-isotope CO_2 laser. A theoretical investigation of a mixed isotope CO_2 laser was conducted by Shimada et al.,[4] and they predicted that continuous tunability could be achieved at 4 atm. The advantage of an asymmetric isotope such as $C^{16}O^{18}O$ is that it possesses both odd and even rotational lines, thus doubling the number of laser lines available. Therefore it can be expected that continuous tunability with this molecule could be achieved at a lower pressure than with a symmetric CO_2 molecule. The calculated relative gains as a function of wavelength of a 4-atm isotopic mixture and an 8-atm single-isotope gas are shown in Fig. 1. The isotopic mixture was 25% $C^{18}O_2$, 50% $C^{16}O^{18}O$, and 25% $C^{16}O_2$. The reason for this isotopic mixture was that the high cost of the isotopic gas necessitates the use of a closed-loop gas flow system with a catalyst. It was expected that if one started with an isotopic mixture of 50% $C^{16}O_2$ and 50% $C^{18}O_2$, after many cycles of dissociation and recombination the mentioned equilibrium mixture would be reached.

The characteristics of a mixed isotope CO_2 master oscillator power amplifier (MOPA) chain are reported. The MOPA chain consists of an oscillator and one amplifier with a closed-loop gas flow system and a catalyst.

2 Experiment

Excimer lasers were converted to high-pressure CO_2 lasers by manufacturing new electrodes with a different profile.

Paper SA-008 received Jan. 17, 1994; revised manuscript received Mar. 9, 1994; accepted for publication Mar. 11, 1994.
© 1994 Society of Photo-Optical Instrumentation Engineers. 0091-3286/94/$6.00.

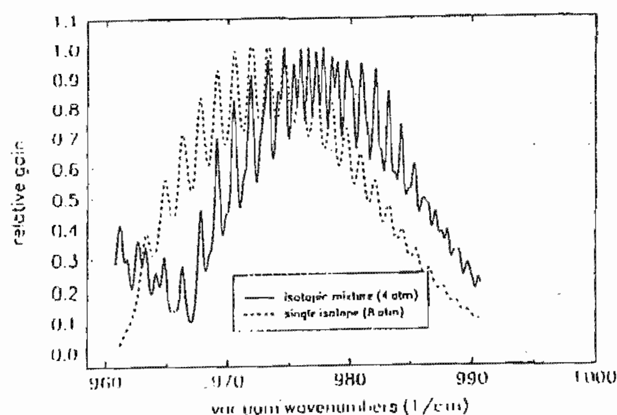

Fig. 1 Calculated relative gain of a 4-atm 25% $C^{16}O_2$, 25% $C^{18}O_2$, and 40% $C^{16}O^{18}O$ mixture compared with that of 8-atm $C^{16}O_2$.

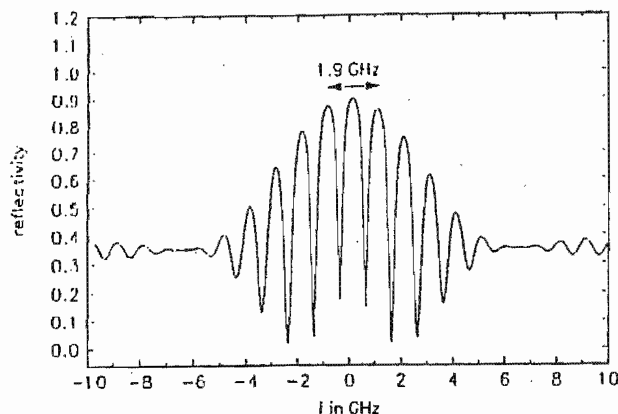

Fig. 3 Calculated wavelength-dependent reflectivity of the grazing incidence grating/mirror combination.

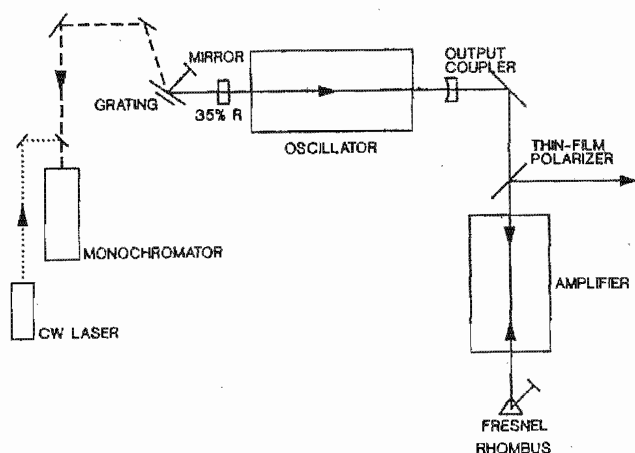

Fig. 2 Configuration of the MOPA chain. Also shown is the wavelength measurement configuration.

Because of restrictions on the power supply voltage, the electrode spacing was changed from 25 to 12 mm. The electrode length of both is approximately 900 mm. The energy loading into the gas is approximately 150 J/l atm. To ensure the specified output energy the amplifier was double passed. Because the electrode spacing was too small to enable the use of a geometric double-pass scheme, a thin film polarizer and a Fresnel rhombus were employed. This allowed the first pass to be polarized in one direction and the second pass in the other orthogonal direction. The configuration is shown diagrammatically in Fig. 2.

Narrow bandwidth was achieved with a three-mirror resonator and a 150 lines/mm grating in a near-grazing-incidence configuration. A partial reflector was installed to increase the effective reflectivity of the grating. The reflectivity of the mirror/grating combination as a function of frequency is given in Fig. 3. An intra-cavity variable aperture was installed to ensure TEM_{00} mode operation. Wavelength measurement was done with a 1.5-m Cerny-Turner monochromator with a 150 lines/mm grating. A cw CO_2 laser with wavelength stabilization provided a reference wavelength by combining its output with the zero order of the grazing incidence grating (see Fig. 2). This ensured that the wavelength of the pulsed laser could be monitored continuously without disturbing its output.

Bandwidth measurements were done with a Ge wedged étalon in combination with a pyroelectric array detector. This was used because the bandwidth of individual pulses was of interest, thus a scanning technique was not suitable. The technique was similar to that described by Izatt et al.[5] The instrument function of the wedge étalon/pyroelectric array combination was 405 MHz, as measured with a cw CO_2 laser. The measured laser bandwidth was deconvoluted with this value. The bandwidth of the laser pulse could be determined accurately to within 60 MHz.

Beam quality measurements were carried out by a modified scanning slit method and a second-order least-squares fit of the second-order moment of the beam. This fit was used to estimate the M^2 value of the beam. The beam was scanned with a slit size between 0.3 and 0.6 mm. A software knife edge was then used with 10 and 90% clip levels. The method is similar to that reported by Van Heerden et al.[6]

Because of the high cost of the isotopic CO_2, a closed-loop gas flow system with a catalyst was necessary. A catalyst was installed and the gas was circulated with a diaphragm type compressor. Flow rates of more than 1.5 l/s could be achieved. To recover the isotopic gas a cold trap was installed in the flow loop. This cold trap could be filled with liquid nitrogen to freeze trap the CO_2 in the laser gas mixture.

3 Results and Discussion

The wavelength region important for the MLIS process is between two lower gain 10-μm *R* lines of $C^{16}O_2$, and thus the tuning measurements were done in this region. With the grating in a Littrow arrangement, strong gain pulling to either of these lines was observed. When the resonator configuration was changed to a grating in near-grazing incidence with a third mirror (see Fig. 2), however, tunability between the lines could be achieved. Because wavelength measurements were done on a continuous basis using the zero order of the grazing incidence grating, tuning linearity was not important. It was, however, important to reach the correct wavelength for MLIS, and this was achieved. The tuning achieved between these *R* lines is shown in Fig. 4. Gain pulling to both the $C^{16}O_2$ lines and an *R* line of $C^{16}O^{18}O$ can clearly be seen.

Bandwidth measurements were made using the wedge étalon/pyroelectric array combination, as described in the previous section. The bandwidth measurements were made

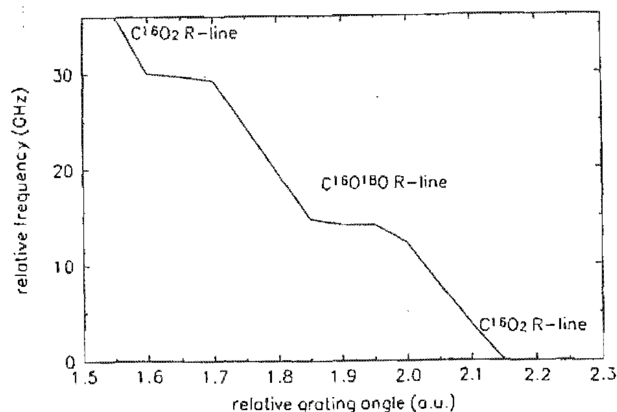

Fig. 4 Laser frequency as a function of grating angle.

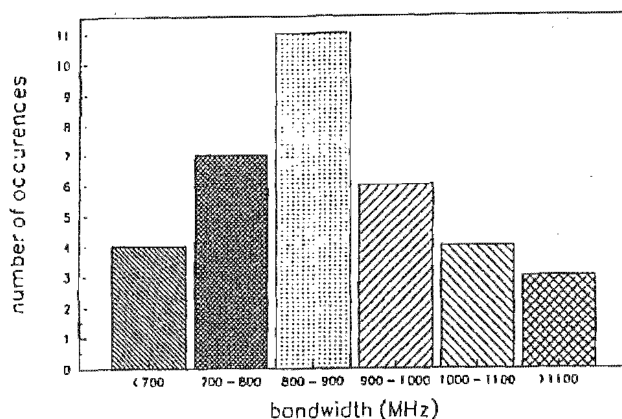

Fig. 5 Statistical distribution of the laser bandwidth as measured with a wedge étalon.

with the grating adjusted so that lasing occurred between R lines. The statistical distribution of bandwidths obtained is given in Fig. 5. The bandwidth varied between 700 MHz and 1.1 GHz. The mean value was between 800 and 900 MHz. The mode spacing of this laser was 90 MHz, thus, on average, between 8 and 10 modes were lasing simultaneously. Mode discrimination analysis has shown that a 10% difference in reflectivity between two modes with the same gain is good enough to ensure sufficient mode discrimination.[7] Keeping this in mind, and considering Fig. 3, it seemed likely that the bandwidth of this laser would be less than 1.9 GHz. However, with this isotopic mixture at a pressure of 3 atm, the gains of the modes are not the same, and the expected active bandwidth would likely be less than that of a 10-atm laser. Dyer and Raouf[8] measured a bandwidth of approximately 1.3 GHz with a grazing incidence setup with the grating at an incidence angle of 78 deg. Their measurement was made with a 10-atm single-isotope laser.

The performance of the catalyst is illustrated in Fig. 6. The pulse repetition rate was 20 Hz and the pressure 3 atm. The energy dropped to 80% of its starting value within 20 min and it was kept constant at this value for a period of 180 min, thus approximately 2.2×10^5 pulses, at which stage the test was terminated. Mass spectroscopic analysis of the gas showed that the O_2 and CO concentrations were kept at less than 0.5% for this period of time. Pulse repetition rates of up to 100 Hz were achieved. It was expected that if the starting values of the CO_2 gas mixture were 50% $C^{16}O_2$ and 50% $C^{18}O_2$, then after many cycles of dissociation and recombination an equilibrium mixture of 25% $C^{16}O_2$, 25% $C^{18}O_2$, and 50% $C^{16}O^{18}O$ would be reached, as was reported by Gibson, Boyer, and Javan.[3] However, the equilibrium mixture that was reached in our laser as measured by mass spectrometry was 33.3% $C^{16}O_2$, 33.3% $C^{18}O_2$, and 33.3% $C^{16}O^{18}O$. This is a surprising result because a statistical analysis of the dissociation and recombination reaction suggested that the 25, 25, 50% equilibrium mixture should be reached. It is possible that a different reaction scheme is involved in our laser/catalyst combination, i.e., isotopic exchange with the catalyst.

The maximum output energy of the oscillator on the required wavelength was more than 150 mJ, and this was increased to more than 450 mJ after a double pass through the amplifier. The output energy of the oscillator was kept below 100 mJ to prevent damage to the intracavity optics. It was

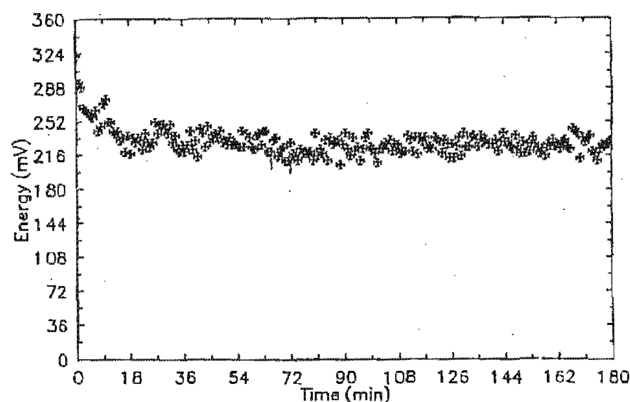

Fig. 6 Performance of the MOPA chain with a catalyst in the closed-loop flow system.

found that the insertion of the third mirror into the resonator increased the output energy by up to 40%. This is consistent with the results obtained by Deka and Zhu.[9] The M^2 value of the oscillator output beam was less than 1.3. The half width of the pulse was 220 ns with a 2σ time jitter of 100 ns. Four-wave mixing in the multipass Raman cell required that the output pulses of this continuously tunable laser and that of a line-tunable 1-atm TE laser overlap in space and time. The pulse width of the 1-atm laser was 65 ns. Because the jitter of the isotope laser was 100 ns, its long pulse width of 220 ns was advantageous; space and time overlap with the 1-atm laser pulse could still be obtained. This meant that the output 16-μm energy of both lasers was reasonably stable and fluctuated by approximately 50%, instead of the 100% if the isotope laser pulse was as short as the pump pulse.

The output energy as measured through a monochromator as a function of the power supply high voltage is shown in Figs. 7(a) and 7(b). The grating on the laser was set at a position between the R 30 and R 32 lines. As can be seen, the energy increases linearly as a function of voltage until approximately 29.7 kV for a 35% reflective partial reflector. At this stage a parasite, lasing from the partial reflector, appears. This parasite was measured to be on the 9 R 24 line. This parasitic behavior was explained in a previous publication by Botha et al.[7] Increasing the partial reflector reflectivity causes a decrease in this maximum voltage.

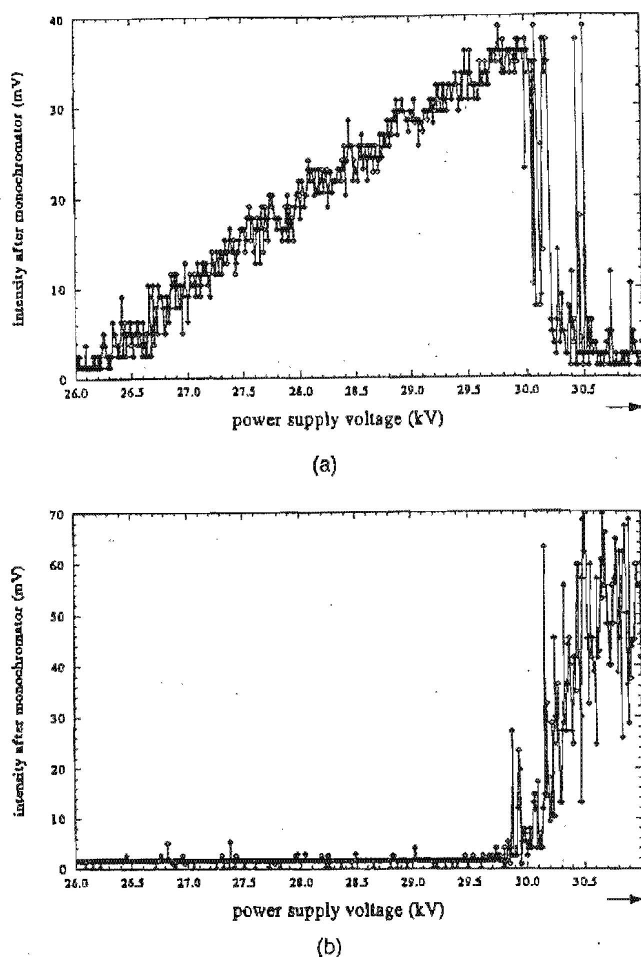

Fig. 7 (a) Oscillator output energy as function of power supply high voltage. This was measured through a 1.5-m monochromator with its grating set at a position between the *R* 30 and *R* 32 lines. The onset of the parasite, lasing from the partial reflector, can be seen. (b) The same measurement as in (a) but with the grating set to the 9 *R* 24 line.

4 Conclusion

A continuously tunable CO_2 MOPA chain was developed for an MLIS pilot plant. This system has been in operation for more than a year and was instrumental in producing macroscopic quantities of enriched uranium. Improvements that are under development are increasing the pulse repetition rate to 200 Hz and installing an automatic wavelength control system on the oscillator.

Acknowledgment

We acknowledge T. du Plooy, D. Bourne, F. Claase, N. Hugo, J. Barry, and W. Meyer for their assistance on this project.

References

1. R. L. Byer, "A 16-μm source for laser isotope enrichment," *IEEE. J. Quantum Electron.*, pp. 732–733 (1976).
2. T. W. Carman and P. E. Dyer, "Continuous tuning characteristics of a small high pressure UV preionised CO_2 laser," *Opt. Commun.* 29(2), 218–222 (1979).
3. R. B. Gibson, K. Boyer, and A. Javan, "Mixed isotope multiatmosphere CO_2 laser," *IEEE J. Quantum Electron.* 15(11), 1224–1227 (1979).
4. T. Shimada, I. J. Bigio, N. A. Kurnit, and R. F. Harrison, "Large-volume high-pressure CO_2 laser for ultrashort pulse amplification," in *Laser Beam Characterization*, P. M. Mejias, H. Weber, R. Martínez-Herrero, and A. González-Ureña, pp. 317–325, Sedo, Madrid (1993).
5. J. R. Izatt, M. A. Rob, and W. Zhu, "Two and three grating resonators for high-power pulsed CO_2 lasers," *Appl. Opt.* 30(30), 4319–4329 (1991).
6. S. P. van Heerden, T. I. Salamon, L. R. Botha, and H. M. von Bergmann, "High repetition rate TEA-CO_2 laser beam characterization," in *Proc. on the Workshop on Laser Beam Characterization*, P. Mejias, H. Weber, R. Martinez-Herrero, and A. Gonzalez-Ureña, Eds., pp. 317–324, Sociedad Española de Optica (1993).
7. L. R. Botha, R. N. Campbell, E. Ronander, and M. M. Michaelis, "Numerical investigation of a three mirror resonator for a TE CO_2 laser," *Appl. Opt.* 30(18), 2447–2452 (1991).
8. P. E. Dyer and D. N. Raouf, "Continuously tunable line-narrowed TE-CO_2 laser using a near grazing incidence grating," *Appl. Opt.* 24(19), 3152–3154 (1985).
9. B. K. Deka and W. Zhu, "Improved performance of a near grazing incidence grating continuously tunable CO_2 laser," *Appl. Opt.* 25(23), 4218–4220 (1986).

Lourens R. Botha received his MSc degree in physics from the University of Pretoria in 1984 and joined the Atomic Energy Corporation, where, until 1986, he worked on atomic vapor laser isotope separation and was involved with the development of an excimer-pumped dye laser system. Since then he has been involved with the molecular laser isotope separation process, working on high-pressure CO_2 laser development and investigating pulse-forming networks using water capacitors for use in high-pulse-repetition-rate lasers, stimulated Raman scattering, four-wave mixing using CO_2 and Nd:YAG laser systems, and the development of resonators for single longitudinal and narrow-band operation of high-pressure CO_2 lasers. This research formed part of his PhD, which he obtained from the University of Natal in 1991. Presently he is involved with beam characterization of pulsed CO_2 lasers, the development of super Gaussian resonators for high-pulse-repetition-rate CO_2 lasers, an intracavity 16-μm Raman laser, and the development of an optically pumped NH_3 laser system. He has published eight papers. Dr. Botha is a member of the IEEE Society for Quantum Electronics and the Optical Society of America.

Christo J. Liebenberg received his MSc in physics on the subject "Frequency modulation of CO_2 lasers by Ku-band microwave mixing in CdTe" at the University of Stellenbosch, South Africa, in 1990, for which he was awarded a Prof. John Todd Morrissen medal. Since 1985 he has been with the Atomic Energy Corporation at Pelindaba, South Africa, where he has been closely involved in the development phase of a molecular laser isotope separation pilot plant. He is presently specializing in multiphoton dissociation and enrichment technology of UF_6.

Hubertus M. von Bergmann: Biography and photograph appear with the paper "Short-cavity high-repetition-rate CO_2 laser" in this issue.

François J. Prinsloo: Biography and photograph appear with the paper "Limitation of CO_2 laser-induced gas breakdown" in this issue.

Einar Ronander: Biography and photograph appear with the paper "Short-cavity high-repetition-rate CO_2 laser" in this issue.

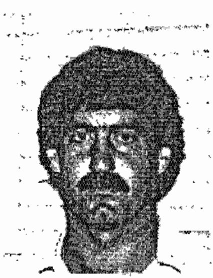

Hendrik J. Strydom graduated from the University of Pretoria with a BSc in physics and mathematics in 1981 and joined the Spectroscopy Group at the Council for Scientific and Industrial Research in 1982, where he worked with secondary ion mass spectrometry (SIMS), Auger electron spectroscopy (AES), and x-ray photoelectron spectroscopy (XPS) and conducted surface and near-surface studies of metals, ceramics, and semiconductor materials. The quantification of SIMS analysis of semiconductor materials formed part of his MSc, which he received from the University of Port Elizabeth in 1990. He then joined the Atomic Energy Corporation, where he worked on atomic vapor laser isotope separation and, in particular, ion extraction from laser-produced plasmas. In 1992 he headed the newly formed Product Development Group, which saw the successful launch of a commercial time-of-flight mass spectrometer. Since 1993 he has managed the molecular laser isotope separation (MLIS) pilot plant that is responsible for obtaining MLIS parameters of uranium. Mr. Strydom has published 25 papers.

13th International Mass Spectrometry Conference, 29 August - 2 September, 1994, Budapest, Hungary.

Uranium Isotope Analysis by Laser Desorption Time-of-Flight Mass Spectrometry and Secondary Ion Mass Spectrometry

H J Strydom, H G C Human, C R Green and E Ronander
Atomic Energy Corporation of South Africa, Pelindaba, Pretoria 0001, South Africa

E R Rohwer
Department of Chemistry, University of Pretoria, Pretoria 0001, South Africa

M M Michaelis
Department of Physics, University of Durban, Durban 4001, South Africa

ABSTRACT

A series of molecular laser isotope separation (MLIS) enriched uranium product has been investigated by laser desorption time-of-flight mass spectrometry (LD-TOFMS) and secondary ion mass spectrometry (SIMS). The uranium oxy-fluoride species, resulting from exposure to air, yielded peaks, from which the uranium isotopic distribution and enrichment factors could directly be determined. The potential of LD-TOFMS and SIMS for the analysis of enriched uranium is shown for products that contain different isotopic abundances of uranium.

INTRODUCTION

The methods of choice for measuring the isotopic abundances of uranium compounds are glow discharge mass spectrometry (GDMS), spark source mass spectrometry (SSMS) and/or thermal ionization mass spectrometry (TIMS). Problems arise, however, if the analyte is in the form of thin, nonhomogeneous layers, deposited on sample slides. We report here on the successful characterization of enriched solid uranium fluorides by laser desorption time-of-flight mass spectrometry (LD-TOFMS) and secondary ion mass spectrometry (SIMS).

At the Atomic Energy Corporation of South Africa, the commercial enrichment of ^{235}U by Molecular Laser Isotope Separation (MLIS) of uranium is researched [1]. This technique is based on multi-photon isotope selective excitation of UF_6 vibrational levels by resonant IR lasers, followed by subsequent dissociation by further non-resonant IR irradiation. The

dissociated UF_5 product has an extremely low vapour pressure and precipitate from the process gas mixture in the form of solid dust.

An in-line time-of-flight mass spectrometer (TOFMS) was developed to optimize irradiation parameters with regards to high isotopic selectivity and acceptable cut quantities [2]. TOFMS has a high transmission capability and high sensitivity for single event monitoring, ideally suited for pulsed IR radiation of UF_6. Since the ionization region is not confined by the presence of electric or magnetic sectors, the instrument can easily be interfaced to a whole range of analytical facilities. From this established technology base, commercial instruments for analysis of solids and biopolymers have now become available [3]. These successes stimulated the investigation of the solid UF_5 product with LD-TOFMS when GDMS and SSMS failed to measure small sample quantities. SIMS analysis, known for mass analysis of surfaces and near-surfaces [4], were carried out to cross check LD-TOFMS measurements.

EXPERIMENTAL

MLIS setup

UF_6 plus a carrier gas is flow-cooled via adiabatic expansion through a narrow slit [5]. At 100 Kelvin approximately 30% of the ground state is populated, where isotope differences in absorption spectra can be used for selective excitation of the ^{235}U isotope containing UF_6 molecules. $^{235}UF_6$ is selectively excited by tunable 16 µm laser energy obtained from a Raman shifted CO_2 laser.

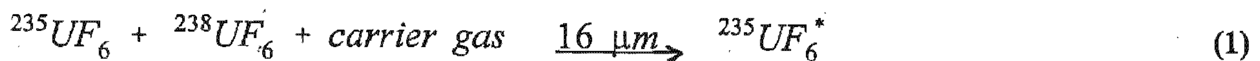

$$^{235}UF_6 + {}^{238}UF_6 + carrier\ gas \xrightarrow{16\ \mu m} {}^{235}UF_6^* \tag{1}$$

The excited species is further excited by a second 16 µm laser and finally dissociated by a 10.6 µm CO_2 laser

$$^{235}UF_6^* + photons \Rightarrow {}^{235}UF_5 + F \tag{2}$$

The fluorine radical is removed by a suitable scavenger. For the collection of macroscopic quantities of enriched UF_5 a pilot plant containing line-tuned CO_2 lasers was constructed and has been in operation for more than five years (see Figure 1). Enriched product was collected on polished metal sample slides (3x3 mm^2), situated directly under the slit. The sample slides were removed for LD-TOFMS and SIMS analysis.

LD-TOFMS Instrumental

The laser desorption time-of-flight mass spectrometer used, was a Wiley-McLaren-type [6] linear instrument with a 1.2 m flight tube. The sample slides were mounted onto a 5 mm diameter stainless-steel probe with conducting carbon adhesive. The probe design is such that when inserted into the mass spectrometer, it was aligned to produce a homogeneous acceleration field. Laser desorbed ions were accelerated in two stages with total acceleration voltage of up to ± 35 kV. Ions were detected with a micro-channel plate detector combined with a venetian blind electron multiplier in order to achieve the required sensitivity and dynamic range.

A pulsed UV laser (N_2) of 337 nm wavelength, 1.4 mJ energy per pulse and 600 ps pulse width type LN1000 (Laser Photonics) was used for ion desorption. The laser beam was focused (focal length 25 cm) onto the target surface at a 75° angle of incidence. The oval spot illuminated on the target had the approximate dimensions of 0.5x3 mm^2. The output of the laser was attenuated with a combination of neutral density filters of different transmissions, to achieve appropriate desorption rates.

The start time for the data system was determined by the laser pulse, the trigger being obtained from a beam splitter and a fast UV-grade silicon pin detector. The spectra were accumulated on a digitizing oscilloscope with a 250 MHz bandwidth, 1 GSa/s sample rate, and a time resolution as low as 1 ns. Data were read from the oscilloscope using a 386 IBM compatible computer via a IEEE interface with custom software.

SIMS Instrumental

The secondary ion mass spectrometry analysis was conducted at the CSIR, Pretoria, on a commercial Vacuum Generators ESCALAB Mk.II [7], fitted with a 0-800 amu quadrupole mass spectrometer, and a MIG 100 liquid metal ion source. The primary ions (2000 Å beam spot size) were accelerated at 10 keV at an angle of 45° off the sample surface normal and rastered over a target area of 300x300 μm^2. The beam intensity was kept below 2 nA/cm^2 to enable slow sputtering rates.

RESULTS AND DISCUSSION

Two samples of known isotopic abundances (0.68% and 2.0% enriched ^{235}U) were prepared for SIMS and LD-TOFMS analysis. Sample slides were positioned inside a gas cell, filled with UF_6 gas (of known enrichment), and left for 60 minutes to allow for UF_y product deposition. The sample slides were removed for SIMS and LD-TOFMS analysis. SIMS and LD-TOFMS spectra obtained for the 0.68% enriched ^{235}U, are shown in figures 2 and 3 respectively. Uranium oxide and fluoride species can clearly be seen. The oxide species originate from exposure to air. Fragmentation of these UO_x and UF_y products to U, UO, UF, UO_2, UOF, UF_2, UO_2F, UOF_2, and UF_3 species, were found for both SIMS and LD-TOFMS analysis. For SIMS the isotopic abundances for ^{235}U and ^{238}U can directly be obtained from measurements of the peak areas at 235 and 238 Dalton. For LD-TOFMS, however, these peaks could hardly be seen due to the "softer" laser desorption. For these analyses, the correct isotopic abundances were obtained using the corresponding uraniumdioxide ions $^{235}UO_2^+$ and $^{236}UO_2^+$ at 267 and 270. The measured 235 and 238 peak areas were normalised to 100%, to obtain the respective isotopic abundances. The SIMS and LD-TOFMS values for the two samples are compared in table1.

^{235}U Standard %	SIMS %	SIMS % error	LD-TOFMS %	LD-TOFMS % error
0.68	0.77	13.2	0.74	8.8
2.00	1.93	3.5	1.91	4.5

TABLE 1. SIMS and LD-TOFMS measured values for different enriched ^{235}U samples.

For both SIMS and LD-TOFMS the accuracies of low concentration measurements are relatively poor. This is not unexpected since the 235/238 ratio is about 1:140. For the 2% enriched ^{235}U sample the accuracy of measurements improved dramatically to better than 5%. This error margin is more than sufficient as it will be shown that the variations in concentration in the MLIS samples could be as high as 50%.

The next step was the analysis of MLIS sample slides. Enrichment experiments were carried out over three hour periods with laser pulse widths of ~50 ns at a repetition rate of 5 Hz. Because of this low duty cycle only small amounts of UF_5 product were formed. The dissociated UF_5 molecules stick to each other to form dimers that precipitate from the UF_6 gas flow. As a result of the gas phase crystal growth the product does not deposit as homogeneous layers, but rather in the form of random island growth, resulting in severe compositional changes from one spot to another.

Nuclear power plants use uranium, enriched to 3.5 - 4.2% of the 235 isotope. The single step enrichment of ^{235}U from the natural 0.71% to this reactor-grade, is important for a molecular laser isotope separation plant to be economically viable. The enrichment factor, α, between the product and feed, is defined as follows:

$$\alpha = \frac{\left[{}^{235}U/{}^{238}U\right]_{product}}{\left[{}^{235}U/{}^{238}U\right]_{feed}} \tag{3}$$

If no enrichment took place the value for α is one. Single-step enrichment for reactor-grade material, on the other hand, require alphas of between five and six. Natural feed material containing 0.71% ^{235}U and 99.29% ^{238}U was used for these measurements.

Therefore, dividing the LD-TOFMS and SIMS measured 235/238 ratios by 0.71/99.29, gave direct measurement of the enrichment alphas. Figure 4-5 shows respectively LD-TOFMS and SIMS measured alphas for consecutive measurements at different positions on a sample slide. Each LD-TOFMS measurement correspond to 16 laser shots (≤ 1 min), whilst the SIMS measurements were obtained from scanning from mass 232 to 240 (≤ 3 min). The variation in alpha from one measurement to the next is in some cases ~50%, which is much higher than the 5-10% error anticipated. This variation is not as a result of a variance in enrichment but because of the irregular deposition of the solid uranium product. The low duty cycle of radiation combined with the continuous flow of UF_6 gas over the sample slides would result in the adsorption of unenriched UF_6 on the porous sample layers. An important feature of the depth profile analysis of the deposited sample is the final measurement of the alpha of one, corresponding, to natural uranium. The reason is that unenriched UF_6 gas flows over the sample slides for ~15 minutes before laser radiation commences, during which time adsorption of unenriched UF_6 material takes place. This provides for an internal check in each spot analysed. It should be noted that other MS techniques, requiring the removal of all products from the sample disk, would only give the (lower) average alpha value of all deposits.

The potential of LD-TOFMS and SIMS for the analysis of enriched uranium was demonstrated. Average values for enrichment alphas can easily be obtained, proving single-step enrichment capability of MLIS. With higher duty cycles and an increase of uranium throughput, even better accuracy in measurements would be possible. The greater number of measurements obtained from the thin solid deposit by LD-TOFMS as compared to the SIMS, reflects the well-known TOF advantage of enhanced sensitivity by simultaneous detection of all ions originating from the desorption process.

ACKNOWLEDGEMENTS

The authors thank C J Liebenberg, H L J van Wyk, M J Gouws, P van Rhyn, T du Plooy, L E van Schalkwyk, N van der Westhuizen, F Clase, A van Dalen and C Swart for their input in obtaining these results. The authors would also like to thank Mr. C W Louw of Mattek, CSIR for conducting the SIMS measurements.

REFERENCES

[1] D M Kemp, P J Bredell, A Ponelis and E Ronander, in Proceedings of the International Symposium on Isotope Separation and Chemical Exchange Uranium Enrichment, Tokyo, Japan, 1990, Eds. Y Fujii, T Ishida and K Takeuchi, pp. 115.

[2] R C Scales, H G C Human and E R Rohwer, in Proceedings of the 12th Int. Mass Spectrometry Conf. Amsterdam, 1991.

[3] H J Strydom, H G C Human, C R Green and E R Rohwer, in Proceedings of 2nd International Workshop on Physics and Modern Application of Lasers: Harare, Zimbabwe, 1993 (in press).

[4] A Benninghoven, F G Rüdenauer and H W Werner, Secondary Ion Mass Spectrometry, John Wiley & Sons, New York, 1987; Chapter 1.

[5] C J H Thiart, G P van Zyl, E Ronander and E H Mathews, N&O Joernaal, ***9****, 31 (1993).*

[6] W C Wiley and I H McLaren, Rev. Sci. Instrum. ***26****, 1150 (1955).*

[7] H J Strydom, A P Botha and W O Barnard, S. Afr. J. Phys. ***12****, 7c (1989).*

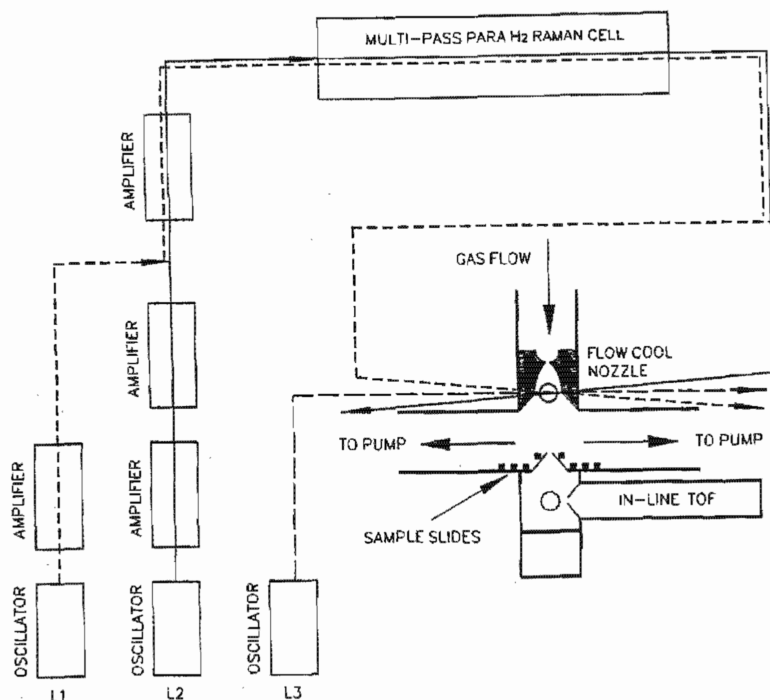

Fig 1 Layout of MLIS pilot plant.

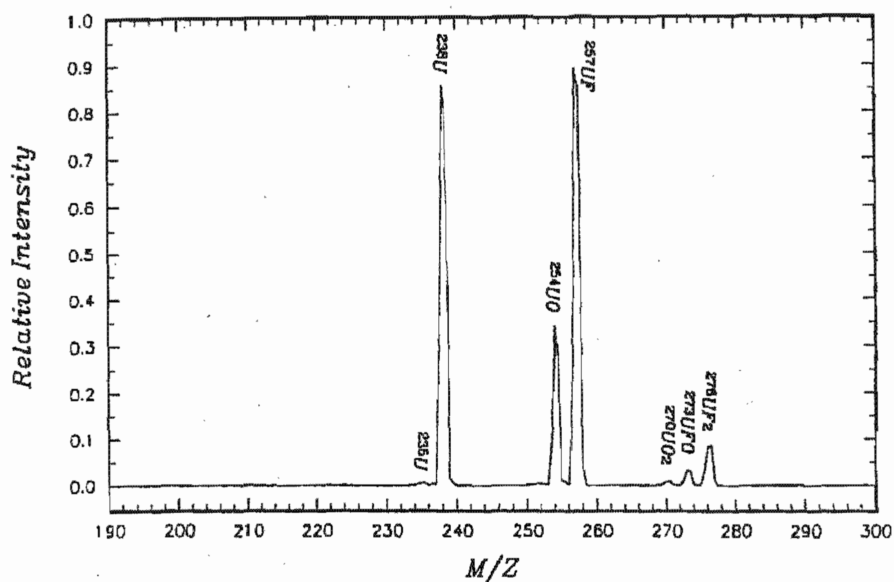

Fig 2 A SIMS spectrum of a 0.68% enriched ^{235}U sample.

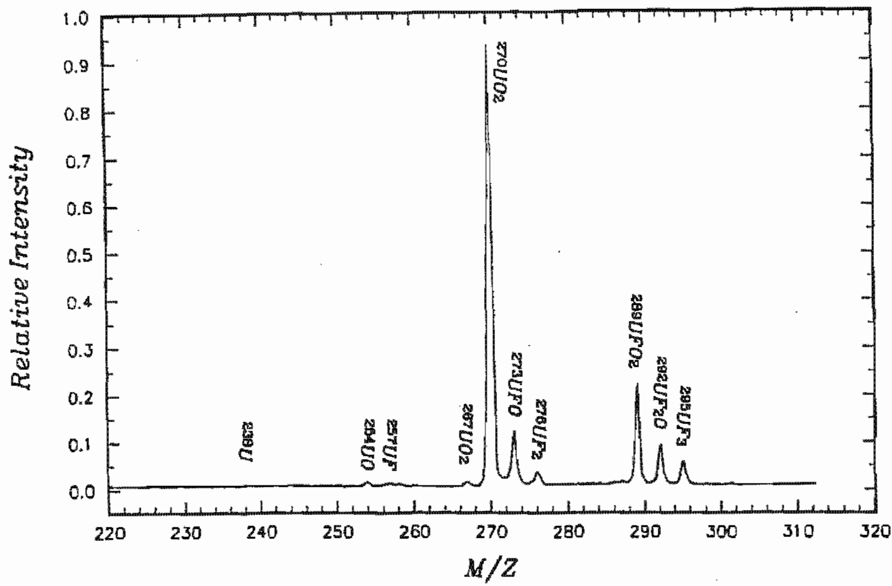

Fig 3 A LD-TOFMS spectrum of a 0.68% enriched ^{235}U sample.

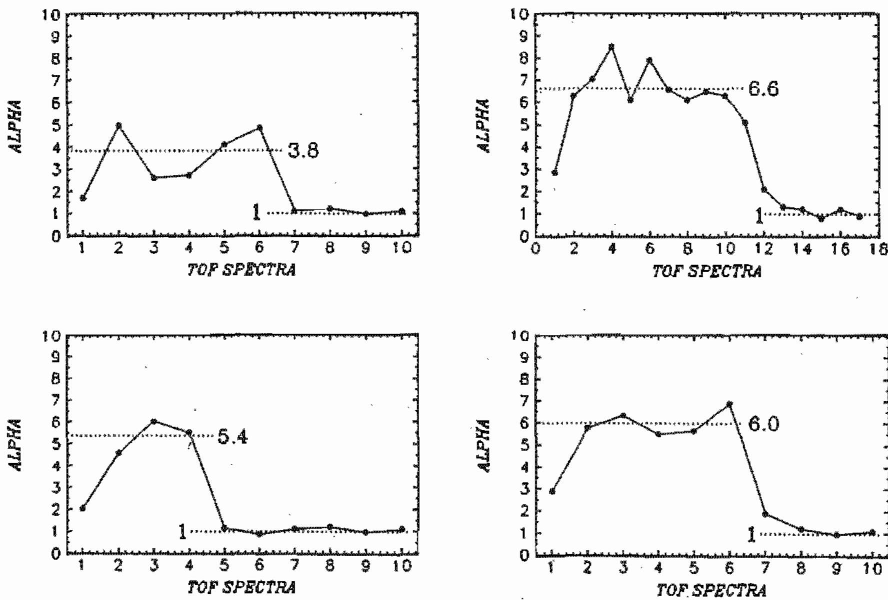

Fig 4 LD-TOFMS measured alphas for four different spots on the same sample slide.

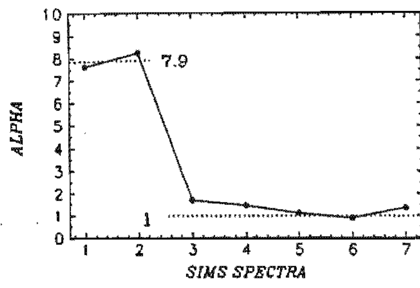

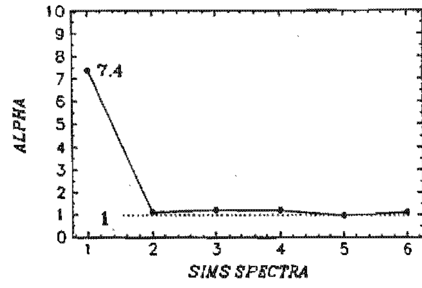

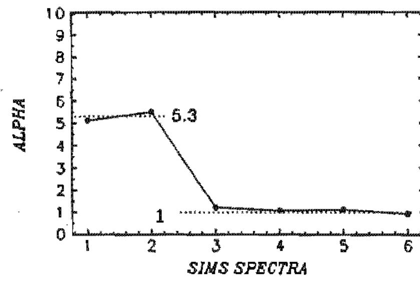

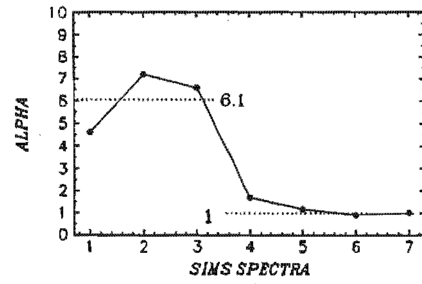

Fig5 SIMS measured alphas for four different spots on the same sample slide.